Oceanologia

Official Journal of the Polish Academy of Sciences

This journal is supported by the Ministry of Science and Higher Education, Warsaw, Poland

Indexed in: ISI Journal Master List, Science Citation Index Expanded, Scopus, Current Contents, Zoological Record, Thomson Scientific SSCI, Aquatic Sciences and Fisheries Abstracts, DOAJ

IMPACT FACTOR ANNOUNCED FOR 2019 IN THE 'JOURNAL CITATION REPORTS' IS 2.198; 5-year IF is 2.231. CITESCORE ANNOUNCED FOR 2019 IS 3.4

Publisher
Elsevier B.V.
Radarweg 29
1043 NX Amsterdam
The Netherlands

Associate Publisher
Chen Lin
c.lin@elsevier.com
+86-10-8520 8768

ISSN 0078-3234

Oceanologia (2020) 62, 413—427

Available online at www.sciencedirect.com

ScienceDirect

journal homepage: www.journals.elsevier.com/oceanologia

ORIGINAL RESEARCH ARTICLE

Observations on relations between marine aerosol fluxes and surface-generated noise in the southern Baltic Sea

Piotr Markuszewski[a,*], **Zygmunt Klusek**[b], **Ernst D. Nilsson**[c], **Tomasz Petelski**[a]

[a] *Physical Oceanography Department, Institute of Oceanology, Polish Academy of Sciences, Sopot, Poland*
[b] *Marine Physics Department, Institute of Oceanology, Polish Academy of Sciences, Sopot, Poland*
[c] *Department of Environmental Science and Analytical Chemistry, Stockholm University, Stockholm, Sweden*

Received 8 January 2020; accepted 7 May 2020
Available online 22 May 2020

KEYWORDS
Sea spray fluxes;
Underwater ambient bubbles noise;
Baltic Sea

Summary This study presents the preliminary results of combining underwater acoustic ambient noise measurements with those of in-situ sea spray fluxes (SSF). Hydroacoustic measurements (in the frequency range 80 Hz —12.5 kHz) were made using an underwater noise recording system developed at the Institute of Oceanology of the Polish Academy of Sciences which was then deployed in the southern Baltic Sea. The simultaneous measurements of coarse sea spray fluxes (with particle diameters ranging from 0.5 to 47 μm) were made on board the r/v *Oceania* using the gradient method. Observations were conducted for the duration of the passage of an atmospheric front that lasted 2.5 days (60 hours of measurements). There were significant differences in the sound pressure level (SPL) and aerosol fluxes observed between the first part of measurements (developing wave state) and the second part (developed waves). Wave parameters, such as peak period, significant wave height, wave age, and mean wave slope acquired from the WAM (WAve Model), were used to investigate the impact of wave field properties on noise and aerosol flux measurements. We observed different behaviours in the

* Corresponding author at: Physical Oceanography Department, Institute of Oceanology, Polish Academy of Sciences, Powstańców Warszawy 55, 81—712 Sopot, Poland.
E-mail address: pmarkusz@iopan.pl (P. Markuszewski).
Peer review under the responsibility of the Institute of Oceanology of the Polish Academy of Sciences.

Production and hosting by Elsevier

https://doi.org/10.1016/j.oceano.2020.05.001

power spectrum density (PSD) levels of noise for these parameters depending on the wave state development.

1. Introduction

Despite concerted efforts within the scientific community, sea spray aerosol (SSA) is still one of the less understood and parametrised components of the earth's climatic systems (de Leeuw et al., 2011; Lewis and Schwartz, 2004; Veron, 2015). With a fairly large number of concepts and approaches notwithstanding in the effort to ascertain the relations between SSA emissions, a high level of uncertainty still hovers over those estimations. According to IPCC (2013), estimation of the amount of SSA mass transport across the planet's air-sea surface ranges from 1400 to 6800 [Tg/yr], with an uncertainty level of 80% (Tsigaridis et al., 2013). Hence, different methodologies aimed at tightening this range are to be expected.

On the one hand, the most important source of the marine aerosol is the bursting of air bubbles produced for the most part by the breaking waves (e.g. Blanchard, 1963). On the other hand, it is generally accepted as fact that the wind-driven component of underwater sea noise is mainly emitted by newly-born bubbles in the whitecapping process from wind-waves (Loewen and Melville, 1991; Medwin and Beaky, 1989). An attempt at assessing the relationship between the origin of sea surface noise at frequencies below 1 kHz and the whitecaps index has been made by Wilson (1980). Based on the historical data, he showed qualitatively similar behaviour for both quantities on wind speed. The idea of monitoring sea-salt production from the sea surface to the atmosphere by measuring the underwater noise was first put forward some years ago by Wilson and Makris (2008) but with no further development since then.

In the literature, we were able to find several attempts to correlate aerosol emission with wave parameters. The most commonly used were wave phase velocity c_p and the whitecap fraction of the sea surface (inter alia Bortkovskii and Novak, 1993; Kraan et al., 1996). Stramska and Petelski (2003) first suggested a strong correlation between sea state development and whitecap fraction which points to higher aerosol emission as well. In another study by Petelski et al. (2005) based on aerosol flux measurements and the WAM (WAve Model), sea spray aerosol flux is suggested to be proportional to the rate of energy dissipation in a wave field raised to the power of 2/3. They also observed an increasing correlation between wind friction velocity (u_*) and aerosol flux in case of increasing wave age (defined as c_p/u_*). There is a wide range of parameters which can influence aerosol emission. Another very promising parameter for future research can be the turbulent kinetic energy at the sea surface interface which was investigated by Esters et al. (2017) in terms of its relations to the Schmidt number, among others.

On the other hand, it is well recognized that at frequencies above 500—800 Hz, and in the absence of anthropogenic noise, the power spectrum of underwater natural noise shows strong wind dependence. The envelopes' spectra have the same universal shape, and do not depend on salinity; however, bubble size spectra created by wave breaking differ in terms of salt and fresh water. For sea states from 3 to 7 (Beaufort), noise spectra above 1 kHz sloped within a range of −5 to −6 dB per octave (Wenz, 1962). There is evidence that the sound pressure level (SPL) is better interrelated with the wind speed than the wind waves' energy parameters (Felizardo and Melville, 1995; Vakkayil et al., 1996). Only recently, Dragan et al. (2011) have found evidence that the wind-wave component of underwater noise could be related to the wave's age.

Finding the connections between the wind-driven noise and aerosol emission is not only thought-provoking but would also open the way to monitoring aerosol fluxes from the sea surface on the basis of underwater noise measurements. Moreover, methods for measuring underwater noise could be performed autonomously with a durable and stable setup located near the sea surface without being disturbed by weather conditions on that surface. In this paper, we propose to consider the relations between two different methods typical of their respective branch of the sciences: the SSA gradient method for atmospheric science, and underwater measurements of the bubbles' ambient noise spectrum level for physical oceanography. Besides, as is well known, the usefulness of the ambient sea noise for the monitoring of aerosol fluxes is yet to be adequately studied.

In this paper, we present the results of measurements of SSA emission compared with simultaneous underwater noise recordings. The data reported here were collected on board the r/v *Oceania* during a single pass of a cyclonic weather front over the area of the Baltic Proper.

2. Background

2.1. Aerosol generation mechanisms from bubbles

Three main classes of droplets emitted from the sea surface are usually recognized: the so-called film, jet, and spume drops. The first two are closely associated with bubble bursting processes entrained to the water when the wind wave is collapsing. Film drops are emitted from the bursting of a thin bubble coat, while jet drops are injected into the air by the bubbles' cavitation, and spume drops are torn from the whitecaps' crests under strong wind conditions. All mentioned processes were originally described by Andreas (1995), Blanchard and Syzdek (1988), MacIntyre (1972), Resch et al. (1986), among others.

Using fast and precise photos of bursting bubbles (Lhuissier and Villermaux, 2012; Spiel, 1998), it was found that the size of film drops ranges from 20 nm (Sellegri et al., 2006) to hundreds of microns (Afeti and Resch, 1990). Most of these droplets are less than 1 μm. Film droplets are responsible for the transport of oceanic surface matter to the atmosphere (Blanchard, 1964).

Jet drops are emitted during the collapse of a bubble's cavern. They are injected as a narrow water stream with high acceleration. The size spectrum of such droplets is highly dependent on the parent bubble's size. It is estimated that droplet sizes are 0.13–0.15 times smaller than the bubble size (Wu, 2002). The size spectrum of such droplets covers a range of 1 μm $< r_p <$ 50 μm, with a maximum at 10 μm (Lewis and Schwartz, 2004).

The process of spume drops torn from the waves crests was first investigated by Koga (1981). Emission starts when the wind speed is higher than 7 m/s. The size range of particles emitted via this mechanism is estimated to be radii 10–500 μm, with a peak at 100 μm (Andreas, 1998, 1992; Andreas et al., 2010; Fairall et al., 1994; Smith et al., 1993; Wu, 1981, 1993).

Another emission process is indissociably linked with splash drops (Andreas, 1998). This kind of droplets is less important for emission and its observation relatively difficult. Wind waves collapsing during breaking hit the sea surface and can saltate as splash drop to air (Kiger and Duncan, 2012). Splash and spume drops' emission can depend on the wind or waves but the intensity of aerosol emission can also be fortified by rainfall (Marks, 1990).

2.2. Sea spray generation function for the Baltic Sea

The most reliable of the direct techniques for determining the marine aerosol fluxes are micrometeorological methods. Through the micrometeorology approach, fluxes of the effective SSA production are deduced from direct measurements of the fluctuation or gradient of SSA concentration in the near-water boundary layer (constant fluxes assumption). The most important techniques in this approach are the eddy covariance method (EC) and gradient method (GM).

The GM approach was first proposed by Petelski (2003). The first flux parameterisation, based on aerosol gradient measurements in the northern Atlantic Ocean using GM, was provided by Petelski and Piskozub (2006) and later modified by Andreas (2007). In the more recent literature, the usability of the GM method was confirmed repeatedly by Savelyev et al. (2014) on board the Floating Instrument Platform (FLIP) in the Pacific Ocean or on board the r/v *Oceania* in the southern Baltic Sea region (Markuszewski et al., 2017a; Petelski et al., 2014).

In order to make a parameterisation of the sea spray emission, the so-called sea spray generation function (SSGF) was used. A thorough review of the proposed SSGFs has been conducted by de Leeuw et al. (2011). All known parameterisations are highly scattered on account of the different approaches, parameters, and methodologies used.

The direct relation between aerosol flux, wind speed, and aerosol size with respect to the Baltic Sea area was given by Petelski et al. (2014) in the form of:

$$F_{p14}(U_{10}, D_p) = (1.83 \cdot 10^4 \cdot U_{10}^2 - 1.35 \cdot 10^4) \exp(-0.62 \cdot D_p), \quad (1)$$

where F_{p14} is SSGF as given by Petelski (2014), U_{10} is the wind speed at a height of 10 m above the sea surface, and D_p is the particle diameter with a particle range of 0.5 μm to 8 μm.

Another model of sea spray emission was proposed by Massel (2007). Based on dimensional analysis and deep theoretical considerations, he combined sea spray emission with wave state properties using two approaches. The first approach is the limiting steepness (LS) criterion:

$$F_{ls}(H_s, \omega_p, D_p) = F_{prod}(D_p)\left[-0.1933 a_0 \left(H_s \cdot \frac{\omega_p^2}{g}\right)^{-2}\right]. \quad (2)$$

The second is threshold vertical acceleration (TVA):

$$F_{tva}(H_s, \omega_p, D_p) = F_{prod}(D_p)\left\{1 - \Phi\left[0.447\left(H_s \cdot \frac{\omega_p^2}{g}\right)^{-1}\right]\right\}, \quad (3)$$

where, F_{ls}, F_{tva} are defined as the size-dependent SSGF, $F_{prod}(D_p)$ is a single whitecap spray emission, a_0 is the constant of spectral moment equalling 0.3048 (Massel, 2007, appendix D), Φ is the probability integral (Abramowitz and Stegun, 1975), and g is the gravitational acceleration. The peak frequency ω_p may be determined from the peak period: $\omega_p = 2\pi / T_p$.

The whitecap spray emission F_{prod} was assumed as Woolf's function (Woolf et al. 1988) determined from the Monahan model (Monahan et al. 1986), which can be formulated as follows:

$$F_{prod}(D_p) = \exp\left[16.1 - 3.43\log\left(\frac{D_p}{2}\right) - 2.49\log^2\left(\frac{D_p}{2}\right) + 1.2\log^3\left(\frac{D_p}{2}\right)\right]. \quad (4)$$

In order to obtain the total aerosol emission, all functions were integrated by the size distribution within the range D_p=(0.5 − 47 μm).

The majority of SSGFs are determined on the basis of measurements in the open ocean area. Due to the fact that the Baltic Sea is an inland-type sea with brackish water, the spectral properties of the wind-waves and mass fluxes may be different from those of the open ocean. A most pertinent comparison between sea spray flux measurements and several SSGFs (Callaghan, 2013; Massel, 2007; Petelski et al., 2014) has been provided by Markuszewski et al. (2017a).

However, the key question that remains is how to deal with the problem of the enormous spread of source function values as in the literature (some orders) and a more precise identification of the aerosols' sources, which could provide a guideline towards achieving a desirable outcome.

2.3. Noise-wind relationships

Underwater noise that is measured near the sea surface provides universal and, in principle, an ever flow of information

about dynamic processes such as wind speed, wave energy dissipation, and rain rate (Felizardo et al., 1995; Nystuen, 2001; Vagle et al., 1990; Zedel et al., 1999). These results from previous experiments have shown that the ambient noise generated at the sea surface was better parametrised by the local wind speed but not so well correlated with the height of the wind wave.

In many of the world's oceans as well as in the Baltic Sea (Klusek and Lisimenka, 2016), it was established that underwater noise in the wind-dependent frequency range, i.e. approximately above 1 kHz, shows a near-quadratic dependency with wind velocity. Consequently, underwater noise anemometers (for wind speed and air-sea fluxes estimation) were proposed and put into practice (Zedel et al., 1999, SWADE anemometer). The objective of this work is to establish the degree of dependency between SPL and aerosol fluxes for the possible implementation of monitoring by way of the more difficult-to-accomplish measurable process of aerosol production using simply measured ambient sea noise from the sea surface.

Our proposal is based on well-established facts: breaking waves entrain air bubbles under the sea surface which are the sources of underwater noise. When these bubbles return to the sea surface and burst, they emit a number of tiny droplets. Thus, both processes are contingent upon the bubble rate production so that there should be a functional relation between the investigated parameters.

In the same way, as in the source functions for aerosols, it is generally accepted that the intensity of ambient sea noise from natural sources has a broad frequency range. In particular, a strong dependency on wind ranges from some hundreds of Hz (400–800 Hz) all the way to tens of kilohertz, where wind speed above 3–4 m/s and less than 14–16 m/s grows as a power function of the wind speed (Crouch and Burt, 1972):

$$p^2(f \pm df) \propto u_{10}^{n(f)}, \tag{5}$$

where $p(f)$ is the acoustic pressure around frequency f in frequency band $f \pm df$, while the exponent of this relation $n(f)$ depends on the frequency.

Given the presence of anthropogenic sources (mainly nearby ships and traffic noise) for a relatively short time series of observations, determining the wind-dependent factor $n(f)$ in the Baltic Sea is not so simple a task. This is due to difficulties in separating and eliminating signals in which the level of noise generated by passing ships is comparable to the noise from natural sources.

2.4. Underwater noise generation

The contribution of natural noise created by bubbles in the first phase of their formation is considered a major input to sea noise with a broad frequency range. However, different variations in bubble shape are responsible for sound emission, with the main mechanism being the radial oscillation of bubbles wherein the size of the bubble determines the frequency of the emitted sound. The classical Minnaert formula (Minnaert, 1933) for the resonance frequency of gas bubbles in the fluid when the surface tension forces would be neglected is given in the form:

$$f_0 = \frac{1}{2\pi\sqrt{r_b}}\sqrt{\frac{3\gamma p_h}{\rho}}, \tag{6}$$

where, r_b is the bubble radius, ρ is the water density, p_h is the hydrostatic pressure, and γ is the heat capacity ratio.

At lower frequencies in a range of up to several hundreds of Hz, the noise originating from bubble clouds oscillates as a whole, and above 1 kHz at up to tens or even hundreds of kHz from the oscillation of single bubbles mainly at their resonance frequency. Theoretical explanations and estimates of noise from different mechanisms have been established in a couple of studies, both theoretical and experimental (Kerman, 1984; Medwin and Beaky, 1989; Prosperetti et al., 1993; Prosperetti, 1988). The bubbles' size distribution is determined by two main mechanisms. Smaller bubbles (smaller than 1 mm) are created by jet drop impact at the wind waves while the bubbles' density is proportional to the power factor −3/2 of bubble radius. Bigger bubbles are driven by turbulent fragmentation and can be described as the power factor −10/3 of bubble radius (Deane and Stokes, 2002). Thus, the spectrum of noise emitted by mechanically excited single bubbles reflects bubble size spectra, range of radii in a bubble population, and the size of bubble clouds.

3. Materials

3.1. Measurements sites

The most representative and least contaminated areas for estimating marine aerosol fluxes are the central basins of the sea. From an acoustic point of view, underwater sea noise in the Baltic Sea is highly contaminated due to the input of sounds from anthropogenic sources, mainly the high-intensity noise of marine traffic. Underwater ambient noise from wind-driven sources could be considered 'normal' or 'typical' for a given area where the influence of ship noise is observed to be minimal. Furthermore, the choice of the point of observation depends to some degree on the wind direction, research vessel's time, and the ability to recover the submersible acoustic buoy after observations in a manner that is safe. In particular, aerosol measurements must fulfil the stricter requirements of quality rather than the ones from noise. This is because it is easier to make a selection of the noise data time series during reprocessing to remove contamination by ship noise.

The data collection is carried out at a site located in the vicinity of the Słupsk Bank (55°31′N, 17°18′E). The analysed data were retrieved from deployments of the IO PAN acoustic buoy system between 21–24 October 2015. The ship was anchored at 1 NM east of the buoy's position. This distance was previously tested and found satisfactory save the uncontaminated measurements of noise from natural sources.

4. Methods

4.1. Meteorological conditions

The main measurements were conducted during 22–23 October 2015. On October 22, the region of measurements

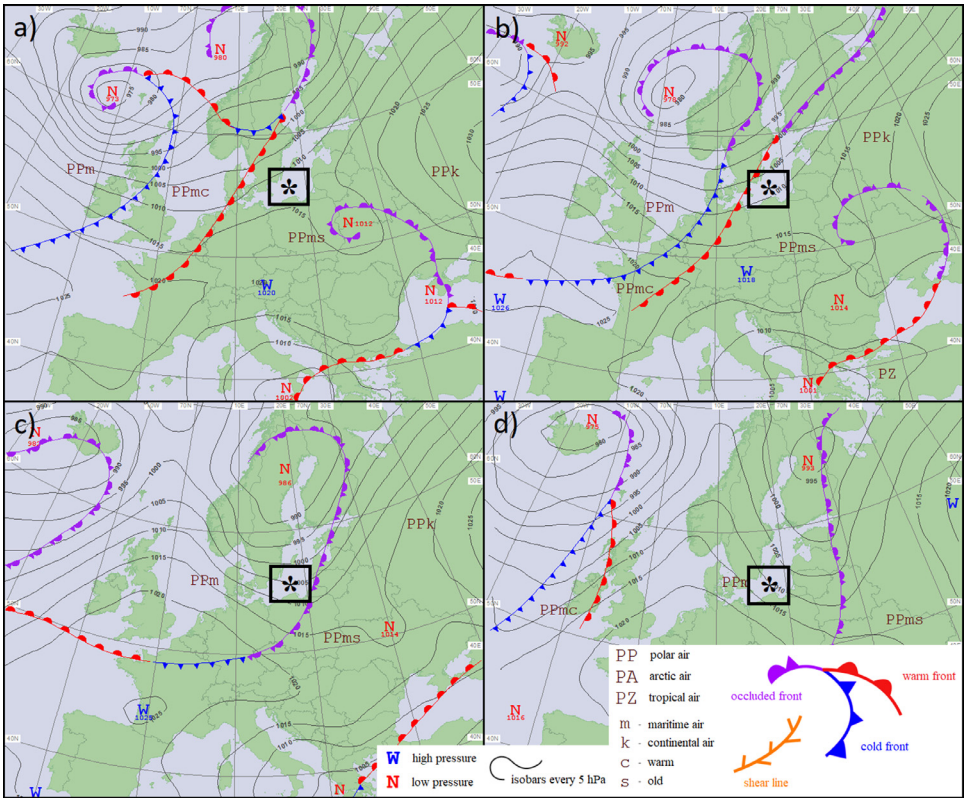

Figure 1 Synoptic charts: (a) 00 UTC on the 22nd, (b) 12 UTC on the 22nd, (c) 00 UTC on the 23rd, and (d) 12 UTC on the 23rd October. The asterisk shows the location of the measurement area (55°31′N, 17°18′E). Charts were prepared in IMGW-PIB, CBPM in Kraków (http://www.pogodynka.pl/polska/mapa_synoptyczna).

was under the influence of a weakening low-pressure system from Belarus (Figure 1a). The deep low-pressure area from Faroe Islands (973 hPa) determined the air mass oscillation in the region of measurements during the days of measurement that followed. From the west of the Baltic Sea, warm and cold fronts were approaching (Figure 1a–b) towards the ship's position. As a result, in the middle of the measurements, an occlusion front occurred. During the passage of this occlusion, there was only minor rainfall (up to 2 mm/h) observed. For the duration of the rainfall, the results of aerosol flux measurements were rejected.

During the second day of observations (Figure 1c–d), the low-pressure system moved eastward and into Scandinavia. At the same time, the occlusion front passed over the Baltic Sea. These dynamic synoptic situations determined the fresh polar-marine air masses in the measurement area.

The results of aerosol gradient flux measurements were divided into two parts, i.e. before and after the passage of the front. For safety reasons (the weather forecast predicted high winds and waves), measurements were halted just after the front had passed.

4.2. Wave and atmospheric data source

Wave parameters (wave peak period T_p, significant wave height H_s) used in this work were retrieved from the Baltic Bottom Base (BBB) database developed by the Maritime Institute in Gdańsk. The database offers a wide spectrum of parameters calculated using the third generation WAve ocean Model (WAM). The detailed physics of the model is provided in the literature (WAMDI Group 1988; Hasselmann et al., 1973; Komen, 1994). The wind data in the WAM model is taken from the Mesoscale Prediction Model COAMPS (Coupled Ocean/ Atmosphere Mesoscale Prediction System), which was provided by the Interdisciplinary Centre for Mathematical and Computational Modelling in Warsaw. Its application, discussion and comparison with measurements of such databases have been presented by Markuszewski et al. (2017a). The temporal resolution of the available data was 1 hour. The spatial resolution was 1 nm (~1.85 km).

The acoustic anemometer (OMC-118 Ultrasonic Wind Sensor of the Observator Instruments) used in measurements was placed on the bow of the ship at 10 m above the sea surface. An average of over 10-minute values of wind speed was used for further analysis. The maximum value of measured wind speed was 14.9 m/s with gusts of up to 17.5 m/s. The minimum value of the wind speed was 6 m/s. The measured air temperature and pressure during measurements oscillated from 10.2°C to 12.4°C and from 1003.9 hPa to 1017.4 hPa, respectively.

4.3. Aerosol measurements

Measurements of the sea spray concentration were taken using the classical aerosol spectrometer CSASP-100-HV of the Particle Measuring Systems. This device allows for measuring the aerosol size distribution in the range D_p=(0.5 μm, 47 μm). This type of spectrometers was widely used in many

campaigns (de Leeuw et al., 2000; Hoppel et al., 1994; Jensen et al., 2001; Markuszewski et al., 2017b; Petelski, 2005). In order to eliminate the impact of humidity on the sizes of particles, all gathered aerosol data were reduced to 80% of the relative humidity wet radius using the formula provided by Petelski (2005).

4.3.1. Gradient aerosol fluxes

To determine the aerosol flux, the gradient method was used (Petelski, 2003). According to the Monin-Obukhov theory (Monin and Obukhov, 1954), particle concentration can be considered a scalar property of the air. On that basis, we can thus define the scale of particle concentration as:

$$N_* = \frac{F_N}{u_*}, \tag{7}$$

where F_N is the aerosol flux.

In order to determine N_*, the atmospheric surface layer over the sea for the aerosol composition can be expressed as a logarithmic function of specific height z:

$$N(z) = N_* \ln(z) + C, \tag{8}$$

where C is an integration constant, and N_* is determined based on aerosol concentration measurements on five altitudes (from 8 m to 20 m above sea level). In that way, we can calculate the gradient of aerosol flux from Eq. (7). The detector was mounted in a special lift which allowed for moving it between these altitudes. The measurement at each level lasted at least 2 minutes. The overall averaging time for one aerosol flux estimation was 30 minutes. Based on the measurement channels of the aerosol spectrometer, there were partial fluxes calculated using the gradient method as well.

The gradient method used in obtaining aerosol fluxes was successfully used during several campaigns in different marine regions such as the northern Atlantic Ocean (Petelski, 2003, 2005; Petelski and Piskozub, 2006), Baltic Sea (Petelski et al., 2014), and the northern Pacific (Savelyev et al., 2014). The advantages of this method include a simple design set and the low cost of measurements (no need for fast particle counters in contrast to the eddy covariance method).

4.3.2. Error propagation of aerosol measurements

The absolute uncertainty over the particle counter can be obtained from Poisson's distribution properties which denote the standard deviation $\sigma_p = \sqrt{\mu}$, where μ is the average number of counts after multiple repetitions of measurement. Based on that fact, the relative uncertainty can be defined as $(\mu^{1/2}/\mu)^*100\%$, hence inversely proportional to the average number of counts. As such, for counts in the range $\mu \sim 10^3$, $1/(m^2 s)$ (what was typical for particle size ranging from 0.5 to 2.5 μm), the relative uncertainty is $\Delta\mu \sim 10\%$. For $\mu \sim 10^3$, $1/(m^2 s)$ (in particle size ranging from 2.5 to 7 μm), $\Delta\mu$ rises to as much as 31%. For particles, a bigger particle uncertainty has a range of 90%.

4.4. Acoustic methods

4.4.1. Setup

The acoustic setup used in the experiments is the one manufactured in the IO PAN acoustic recording systems, based on an ADC (Analog to Digital Converter) microprocessor and characterized by a low self-noise level and low power consumption. The photo of the device just before deployment along with a schematic presentation of the underwater orientation is presented in Figure 2.

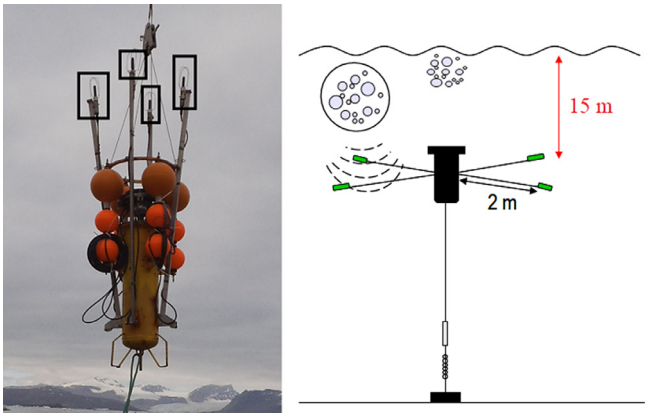

Figure 2 The acoustic recording system with four hydrophones (left panel) and its schematic underwater diagram (right panel).

The buoy is equipped with four omnidirectional Reson TC 4032-5 hydrophones placed horizontally and attached at the ends of perpendicularly distributed poles. The distances from the hydrophones to the vertically oriented cylindrical container with electronic and power supplying batteries amounted to 2 meters. So, the opposite hydrophones were at a distance of 4.4 m. Hydrophones were deployed at a depth of 15 m below the mean sea surface (the depth of deployment is measured by a pressure recorder). The deployment depth chosen was sufficiently deep so as to avoid dynamic disturbances from surface waves and yet appropriately shallow to be able to listen to single breakers. The buoy was anchored at a depth of about 40 m with sandy sediments in the area. When taking the compass sensor or inclinometer readings, we did not observe any jerks, rapid system tilts or turning.

The main task of the measuring system is to register wind or rain components of underwater noise. To avoid overdriving of preamplifiers by strong signals from marine traffic noise, the bandwidth of the tract was reduced to a frequency range of 80 Hz to 12.5 kHz. The recordings were performed with a sampling frequency of 30 kHz in each channel, in a 16-bit dynamics range. Raw data were acquired in periods of 20-second recordings with a 30-second pause.

4.5. Acoustics data analysis

The signals' recorded time series were analysed offline in a laboratory. The post-processing and statistics were performed in the MATLAB environment. Voltage was recalculated to the acoustic pressure according to the hydrophone manufacturer's sensitivity specifications. The narrow band spectra were computed from 16,384-size subsamples using the FFT (Fast Fourier Transformation) procedures, first averaging over time in 20-sec intervals and then after averaging in one-third octave frequency bands. The power spectrum density (PSD) levels of noise in each one-third octave band

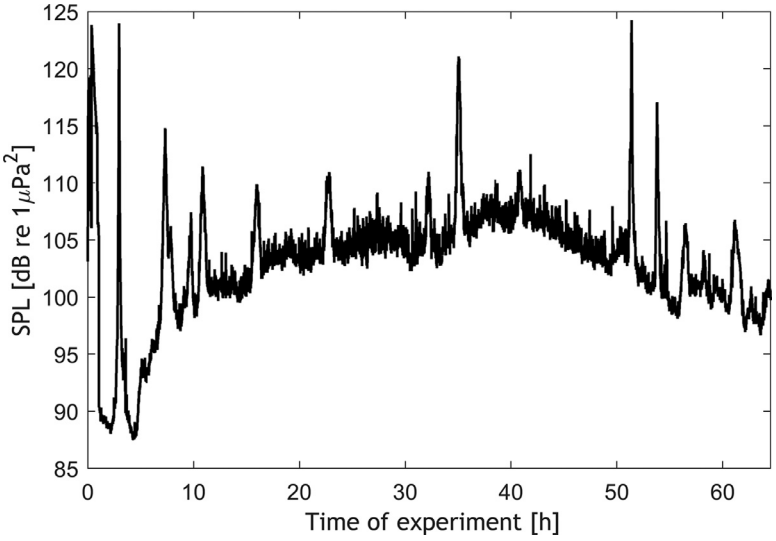

Figure 3 History of sound pressure level (SPL) observed in the entire frequency range (80 Hz–10,000 Hz) collected in subsequent 20-sec. recordings. The *x*-axis shows the time of experiment, in hours, counted from the moment of the buoy's deployment on 21 October 2015, at 14:00.

(dB re 1 μPa^2/Hz) were used as the measure of the underwater sound due to its simplicity and general use in acoustics.

Besides wind sources, commercial shipping and ferry traffic are found to be significant, however intermittent they might have been as contributors to underwater SPLs in the deployment area. The automatic algorithms aimed at the vessels' noise detection with a substantial addition to natural noise are either indefinite or time-consuming. The spectra parameters used as measures of similarity to distinguish the noise emitted by natural sources from that of ships were the centre of gravity of the individual spectra, slope of spectrum level at frequencies above 630 Hz, and most useful SPL in the whole frequency range. The last one presented in Figure 3 (as the SPL in dB re 1μPa^2) is calculated by integrating the pressure spectral density curve in narrow bands over the whole recorded frequency bands.

The time history of the broadband SPL in the analysed frequency range (i.e. between 80 and 12,500 Hz) recorded at the Słupsk Bank and extended over 60 hours is given in Figure 3. Measurements started at 14:00 21 October 2015. From the behaviour of the SPL time series, the evidence of a minimum of 14 passing ships is conspicuous, as indicated in Figure 3.

The noise data was transformed from an internal format recorded by the ADC system to the WAV (wave form audio) format to confirm the type of source via sound checking. Listening by an operator, together with further numerical processing, allows for detecting and verifying the presence of fragments of anthropogenic pollution of noise from natural sources at the sea surface.

The most important effects of the ship's noise on the form of spectra are the appearance of narrow peaks in the high-resolution spectra and relatively quick-rising SPL in the broadband range (the SPL and rate of its variation are determined by many factors such as the course of the ship in relation to the buoy, the nearest range at which the ship had passed the anchored buoy, the class of ship, sound propagation conditions, etc.). Recordings in which noise was recognised as having been emitted from ships passing by had been removed from further analysis with a simple algorithm whose design is based on the background SPL having been exceeded (Figure 4).

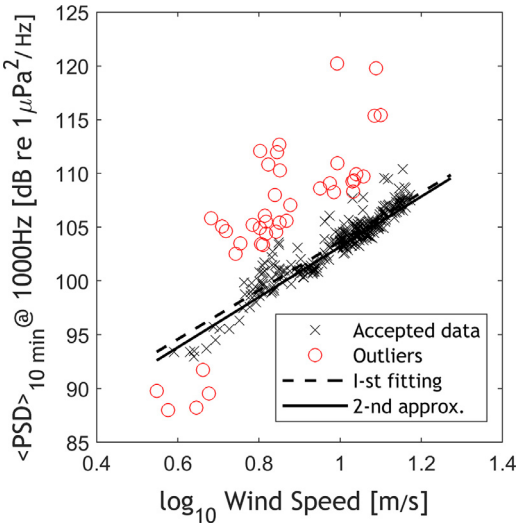

Figure 4 The example presenting the outlier removal algorithm, in which the vessel's noise exceeds the noise from natural sources. The dashed (upper) line depicts the best-fit approximation to a complete set of data. Red circles represent the data at a distance of 3 dB from the best fit line, which were removed. The process of fitting was repeated. (For the interpretation of references to colours, the reader is referred to the web version of this article.)

The principle of the exclusion algorithm of recordings when the ship's noise prevails over the noise from natural sources is presented, as an example, in Figure 4. Data are averaged in 10 minutes PSD in a one-third octave band with a central frequency of 1 kHz, i.e. the frequency band where the best correlation with the wind is observed. At the first

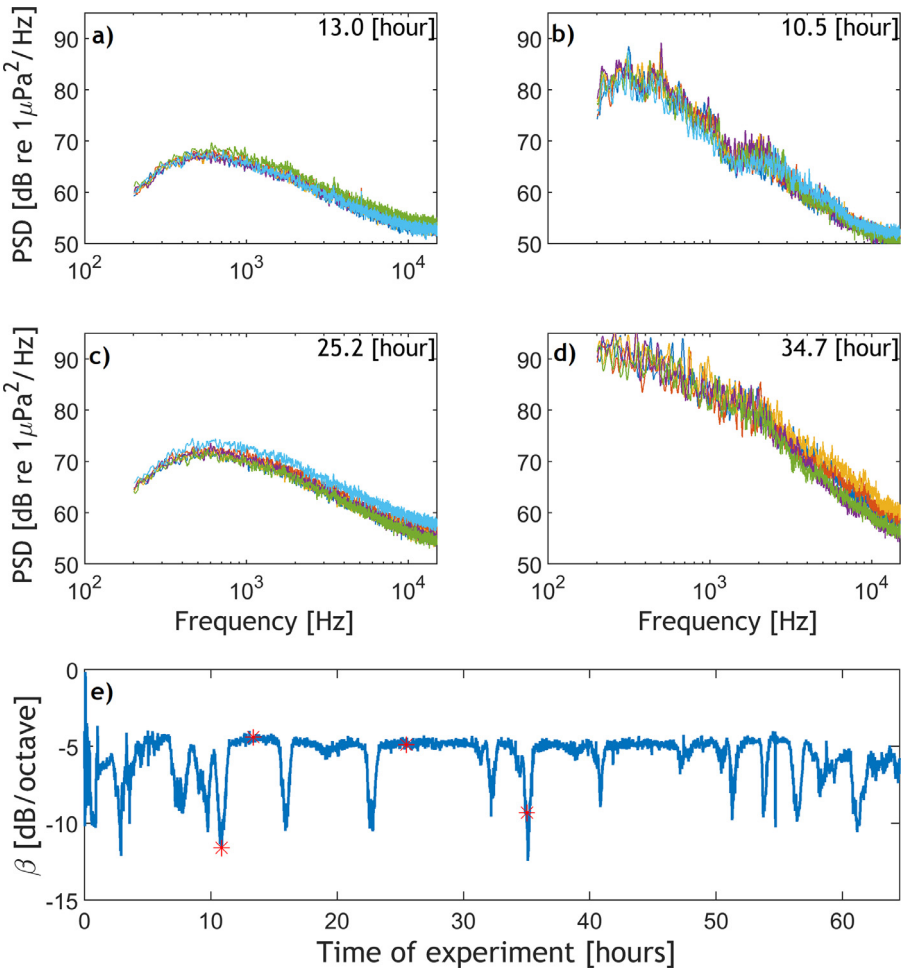

Figure 5 Examples of underwater noise spectra with no noise from ships (left panels (a) and (c)), and with a significant contribution from the shipborne component (two right panels (b) and (d)). The numbers in the upper right corner represent the position of the examples on the time axis. Time series of spectral slopes β of PSD for records collected in consecutive one-minute intervals is presented on panel e), where the asterisks indicate corresponding examples from the upper panels.

step, a best-fit approximation of Eq. (5) to an entire set of data was applied (dashed line). Using this initial guess regarding the fitting parameters, the data at a distance exceeding 3dB above the fitted curve (labelled with red open circles) had been classified as the ship's noise which was afterward removed from the database before the process of fitting was repeated. Moreover, outliers at 3dB below the first step fit line were eliminated. The presented data refer to wind speeds exceeding 3.5 m/s, i.e. when the first surface waves break.

The characteristic results of spectral analysis for records representing natural noise and with a significant contribution from ships are shown in Figure 5. Each panel a–d contains five consecutive spectra (averaged over 1 minute). The numbers in the upper right corner represent the position of examples on the noise recording timeline. Depending on the type of the noise's prevailing component, not only the sound level but also the slope of the spectrum is modified. For noise from natural surface sources at frequencies exceeding several hundred Hz, it is about a −5 dB/octave. Whereas in the presence of noise from a ship when the ship is far enough from the observation point, we can observe two ranges with different slopes of the spectrum envelope, contrary to a practically constant slope when the ship is close. In addition, in a fairly continuous and smooth noise spectrum, peaks from the ship's machinery and propeller appear. Spectral slopes β for each 1-minute record are given in Figure 5e, where asterisks represent examples from Figure 5a–d.

After removing data contaminations from the shipping noise, the final parameters of ambient noise versus wind relationships are calculated, while associations concerning underwater SPLs, wind speed, aerosol fluxes and wave parameters are analysed using the ancillary datasets.

The data were used to determine the coefficients $n(f)$ of the noise's wind dependence in different frequency bands for situations where $u_{10} > 5$ m/s when the first whitecap appears. The results of computing the values of exponent $n(f)$ in each of the 1/3-rd octave frequency bands are presented in Figure 6, wherein the x-axis is the frequency.

We notice the proximate quadratic functional dependence of the noise intensity on wind speed for frequencies above 630 Hz during the period of observation. The largest values of the set of $n(f)$ coefficients and the strongest cor-

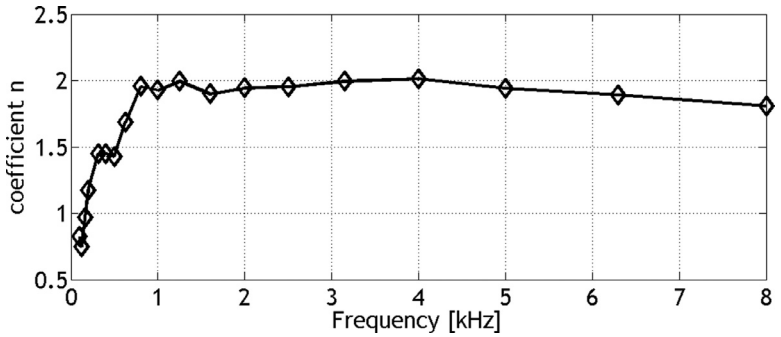

Figure 6 Values of the wind speed dependency factor $n(f)$, (Eq. (5)) in each analysed 1/3-rd octave band.

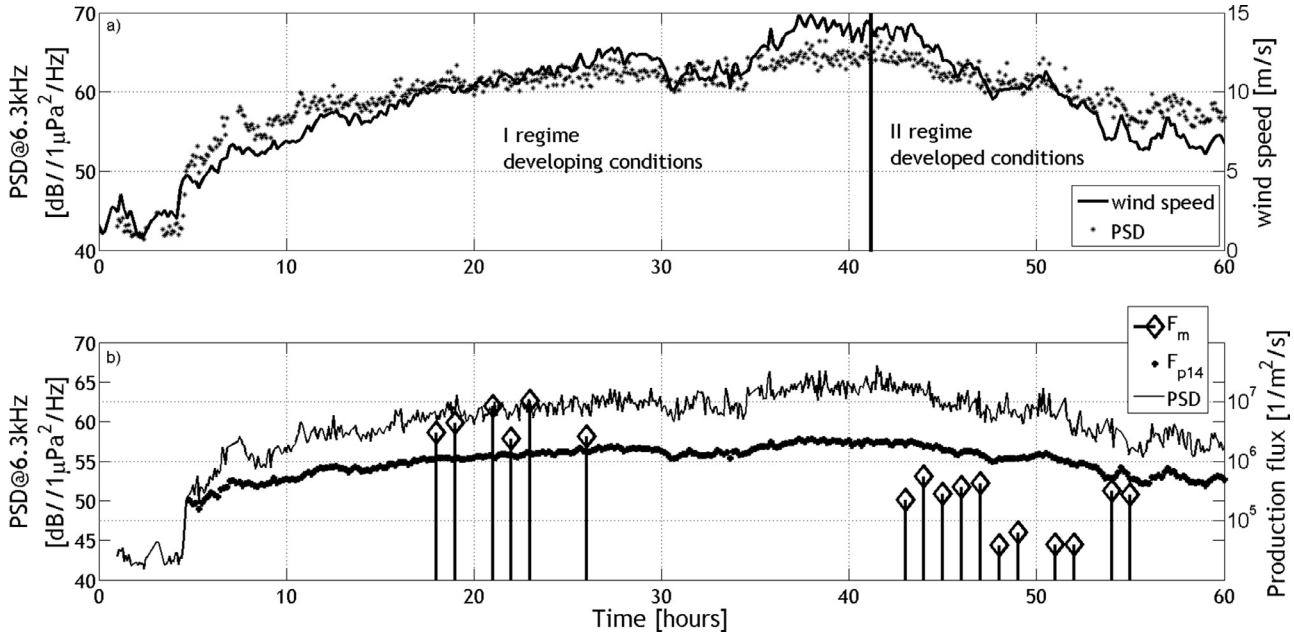

Figure 7 Concurrent time series of the Power Spectral Density of underwater noise at 6.3 kHz (PSD@6.3 kHz) and wind speed (upper panel); with PSD as the measured total aerosol gradient flux F_m and calculated fluxes based on Eq. 1 and integrated for particles' diameters ranging from 0.5 μm to 47 μm (lower panel). The x-axis shows the time of noise measurements from the start. The vertical line on the upper panel demarcates developing wind wave conditions from developed ones.

relation of noise intensity with the wind are observed in the bands between 1000 and 4000 Hz. In a lower frequency range, the noise is less dependent on the local wind speed due in part to the profound influence/input of distant noise sources on the recorded data.

The derived associations between the noise spectral density level from wind-dependent sources and wind speed seem akin to the noise-wind relations presented earlier (Klusek, 2011; Klusek and Lisimenka, 2016) in the same frequency range, with the wind speed of up to 14 m/s and for acoustic frequencies at up to 12.5 kHz. With increasing frequency, the $n(f)$ values become fixed and diminish only slightly when approaching 10 kHz.

The steadily observed trend of diminishing n value with increasing frequency is insignificant, and might be explained by the rising frequency losses in sound intensity coming from more distant sources. Thus, the use of noise in a broad frequency band as the indicator of bubble production and aerosol emission seems reasonable.

5. Results and discussion

5.1. Interconnection of noise–aerosol fluxes

A concurrent time series of the underwater SPL's power spectral density level in the 1/3-rd octave at a central frequency of 6.3 kHz, together with the wind speed, is shown in the upper panel of Figure 7, while the PSDs combined with the measured aerosol fluxes and SSGF approximation (Eq. (1)) are presented in the lower panel of Figure 7.

The noise data are given over 5-minute periods as average after removing recordings when the ship's noise makes a significant contribution to the recorded noise. The noise data are used for a relatively high-frequency band such as 6.3 kHz for the reason that at higher frequencies, the background ship component of underwater ambient noise makes smaller contributions to the summary acoustic field. The

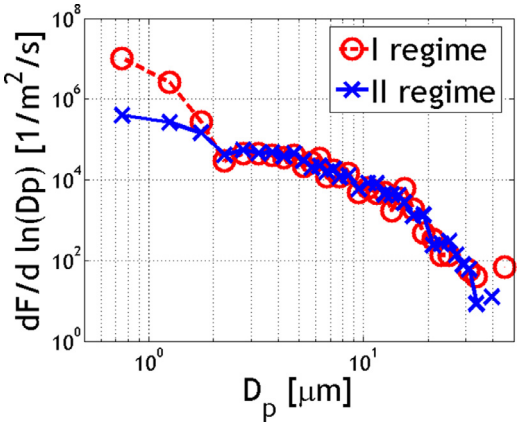

Figure 8 The averaged size distribution of particle fluxes in two emission regimes. I regime: before passing of the front, developing wave phase, wind rising up; II regime: conditions after the front, wave phase developed, decreasing wind condition. (For the interpretation of references to colour in this figure legend, the reader is referred to the web version of this article.)

correlation between measured wind speed and PSD at 6.3 kHz was high (R=0.97).

Aerosol data measurements have been conducted in the two regimes related to wave state development. The first subset was collected during the growing wind phase, while the second was performed after the occlusion front had passed. There are quite different conditions for the generation of bubbles, with the consequence for both noise and sea spray aerosols. During the first period of measurements, the wave age was below 1, while the mean wave slope was higher than a value of 0.03. In the second regime of measurements, the wave age started to increase, while the mean wave slope decreased below the 0.03 value (Figure 9b). The transition between regimes started changing after the 41st hour of measurements.

The atmospheric conditions allowed for calculating only the mean values of partial fluxes in 36 size bins (subsection 4.1.1) for both regimes of wave field development. In Figure 8, we can see the difference in the SSF size distribution. For the smaller particle diameters (D_p<2.25 μm), in the first observation regime, the aerosol flux was higher than that for the second regime. For bigger particles, the observed emission was similar.

Additionally, when wind speeds exceed 9 m/s, spume drops are produced by being torn from the wave crests (Monahan et al., 1983), part of which ascends into the air while the other part lands on the sea surface. It would be expected that spume drops striking the water surface would emit noise during the hydraulic jump or cause additional bubble generation. Nevertheless, we do not observe any growth in the SPL when wind exceeds this threshold. It indicates that the main source of noise is bubbles generated during wave breaking. It is obvious that variations in time series (presented as logarithmic quantities) almost overlap each other.

5.2. Noise — interconnections of wave parameters

There are two important parameters that inform the stage of wave field development. One is wave age which is a dimensionless parameter defined as the ratio between wave phase velocity and wind speed: c_p/U (Massel, 2018). The wave phase is determined on account of the wave peak period according to the formula: $c_p=gT_p/(2\pi)$. The other parameter that informs the development of a wave state is the mean wave slope defined as: $sl=2\pi H_s/(gT_p^2)$. We assumed that values sl>0.03 represent an undeveloped wave state, while lower values correspond to developed waves (after Bourassa et al., 2001).

Wave parameters, such as the peak period T_p and significant wave height H_s during measurements, are presented in Figure 9 (upper panel). In the analysed time series, the peak period and significant wave height increased along with the wind speed. The transition between regimes occurred when the mean slope started to decrease near the boundary value of 0.03, as shown in Figure 9 (lower panel).

Because the temporal resolution of the modelled parameters was 1 hour, the PSD values were averaged to the same resolution, with the results of the comparison shown in Figure 10. We can observe certain differences between both selected wind regimes. In the period with increasing wind conditions, significantly higher values of PSD were observed than for the period with decreasing wind conditions (Figure 10, upper panel).

5.3. Noise — comparison of sea spray models

In Figure 11, the total measured aerosol fluxes were compared with the theoretical values obtained using three different generation functions. The first was the typical experimental function and wind speed-dependent F_{p14} (obtained from Eq. (1)), while the other two were wave properties that depended only on two different wave regimes (F_{ls} — Eq. (2) and F_{tva} — Eq. (3)).

As can be seen in Figure 11a, in the first stage of measurements the regime of limiting steepness best describes the total aerosol flux. In the second stage, the function determined on the basis of wave regime and defined as the threshold vertical acceleration best predicts the aerosol emission. The last two outlier points (54 and 55 hours of measurement) can be explained as the result of unsteady dynamical wind-wave conditions. It could have been caused by local wind gusts which can be observed in several uprising episodes of PSD and wind speed between 50 and 60 hours of measurements (Figure 7). Such dynamical gusts provided additional input to the turbulence energy and thus increased the aerosol emission in this period.

The wind speed-dependent function F_{p14} was determined based on several field campaigns in different atmospheric and wave conditions (Petelski et al., 2014), so it can be treated as the average value of the measured fluxes. As can be seen in Figure 11, in the first stage of measurements, the fluxes were higher than those predicted by this function. In the case of the developed wave state, the measured fluxes were lower than the theoretical values. Similar results were also observed by Norris et al. (2012) when applying the eddy covariance method.

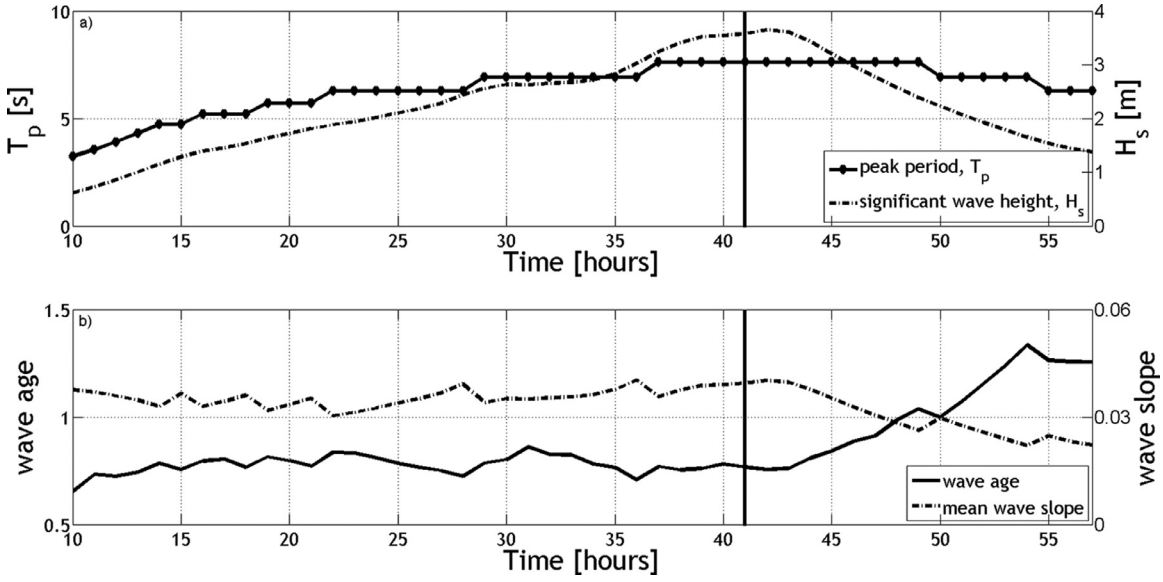

Figure 9 The upper panel shows a time series of wave parameters obtained from the Baltic Bottom Base (BBB) calculated using the WAM3 model. In the lower panel, the calculated dimensionless numbers describing the properties of wave development are shown.

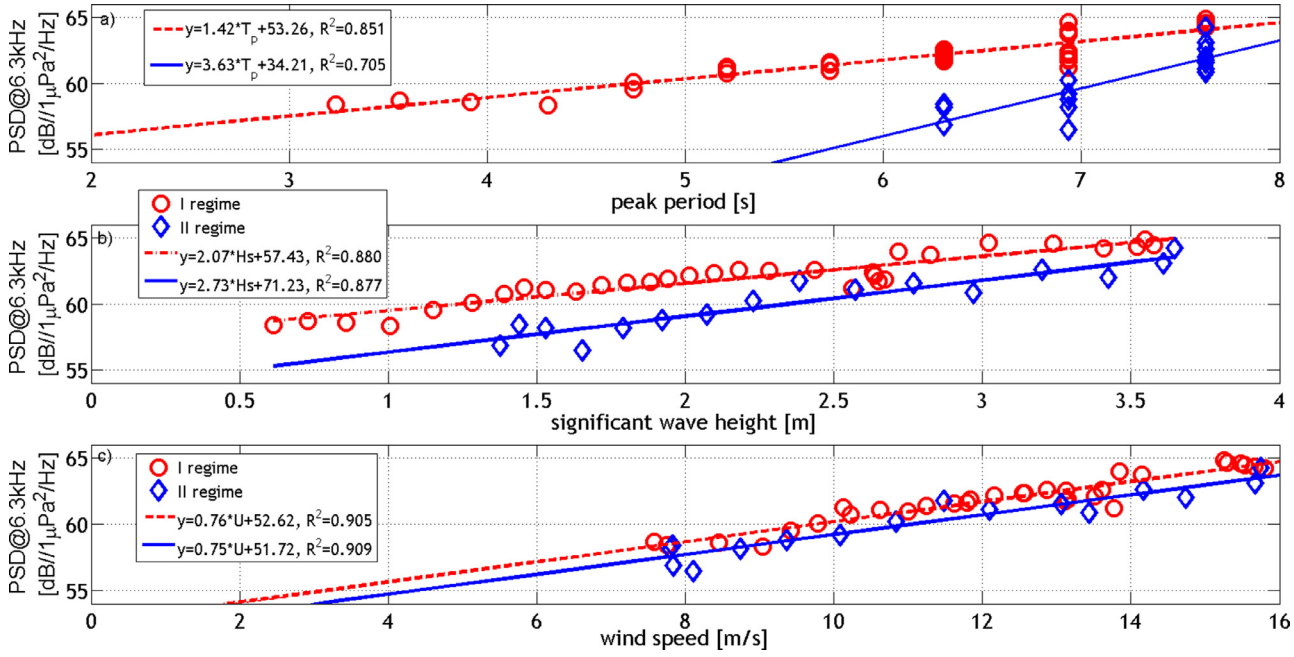

Figure 10 Comparison of 1-hour averaged Power Spectral Density at 6.3 kHz (PSD@6.3kHz) with wave parameters. The results are divided into two groups according to the wind regimes (Figure 8a, upper panel). Circles represent increasing wind regime (I regime); diamonds represent decreasing wind regime (II regime). Dotted lines represent the best linear fit to I regime data; solid lines represent the best linear fit to II regime data. (For the interpretation of references to colour in this figure legend, the reader is referred to the web version of this article.)

Correlations between PSD and theoretical values of the total aerosol emissions have been calculated (Table 1). These correlations were calculated for the complete measurement time series and the two wind regimes defined earlier. For the function $F_{p14}(U_{10})$, the correlations, as expected, were high (0.92–0.95). For the wave state-dependent functions in the first regime of developing the wind wave conditions, the correlations were rather low (~0.42). In the second regime of the developed wind conditions, the correlations increased significantly (0.89 and 0.83).

The lower correlations between PSD and SSF in the developing wind conditions may be explained by the fact that the kinetic energy flux mostly came from the wind turbulence

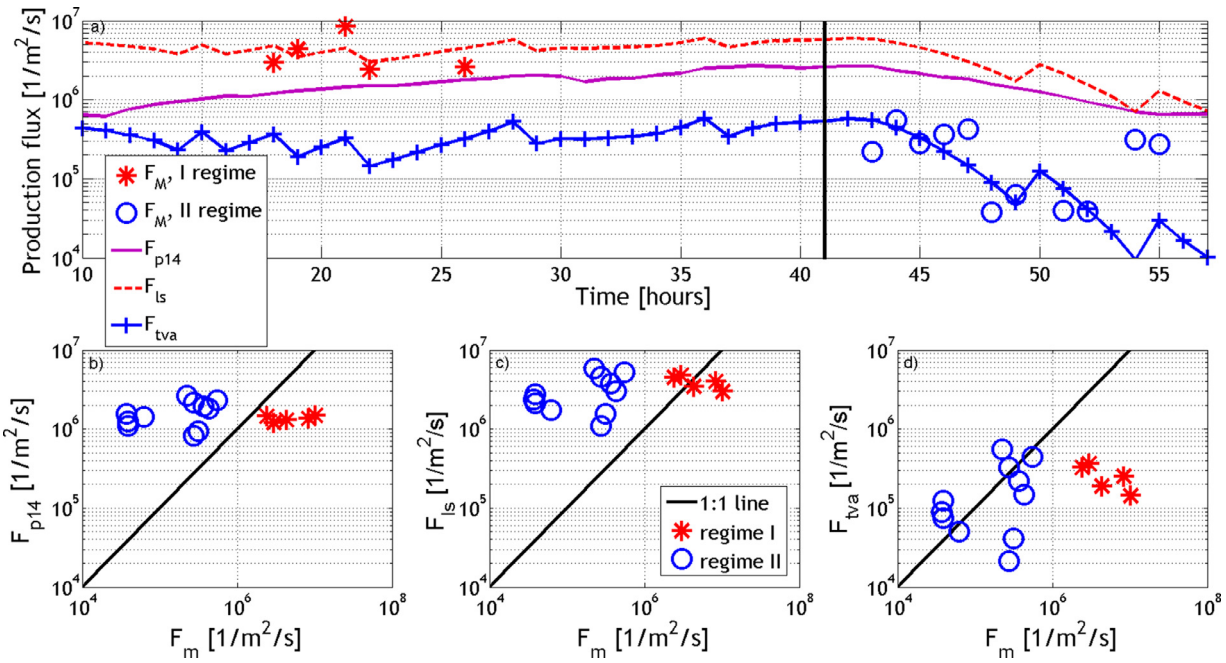

Figure 11 Comparison between the total measured production flux F_m and estimated SSF using sea spray generation functions: $F_{p14}(U_{10})$, $F_{ls}(H_s,\omega_p)$, $F_{tva}(H_s,\omega_p)$ (Eq. (1–3)). We can observe that in the first regime, the limiting steepness approach (ls, Eq. (2)) explains SSF better, while in the second regime the threshold vertical acceleration approach fits in better with the measured SSF.

Table 1 Correlation coefficients between measured Power Spectral Density (PSD) and theoretical total aerosol flux, estimated based on the three theoretical functions of Petelski et al. (2014): $F_{p14}(U_{10})$, Massel (2007) – $F_{ls}(H_s,\omega_p)$, and $F_{tva}(H_s,\omega_p)$. The total fluxes were obtained by integrating the aerosol size distribution within a range of particles D_p=(0.5, 47 μm).

	PSD@6.3 kHz		
	full time series	I regime	II regime
$F_{p14}(U_{10})$	0.92	0.95	0.94
$F_{ls}(H_s,\omega_p)$	0.71	0.39	0.89
$F_{tva}(H_s,\omega_p)$	0.69	0.42	0.83

to the wave field. So the primary factor which influenced the increase in SSF was wind speed. On the contrary, in the second period when waves were fully developed, the wind speed started decreasing, such that the SSF were more influenced by the inertia of the wave field and interference between waves. According to this, the two wave criteria of wave field description given by Massel (2007) predict quite well the two different physical phenomena of whitecaping, namely their impact on the SSF and noise of the bubbles.

During the developing wave state with increasing wind speed, there is generally an expected higher volume of air entrained to the water (Norris et al., 2013). The intensity of underwater noise caused by bubble bursting was higher as well (Figure 10). This phenomenon has to do with different energy dissipation mechanisms during both phases. That is why the increased population of bubbles influenced the total SSF by one order of magnitude higher in the first stage than in the second regime where the ambient noise was lower as well. This effect also influenced the SSF size distribution. As can be seen in Figure 8, the main difference in SSF was observed only for the submicron particles (D_p<2.5).

6. Conclusions

In this paper, we proposed and tested a method for predicting aerosol fluxes based on the underwater sound generated by local wind-dependent surface sources. The main objective of this study is to investigate the extent to which noise parameters can help estimate the aerosol sea spray source function, and our goal is to demonstrate the usefulness of using underwater sound recordings in monitoring local sources of aerosol generation.

Our attempt to ascertain these relations was motivated by the enormous progress in techniques, which allows underwater sea noise measurements to be performed for a long duration in a way that is affordable. Acoustic sensors deployed under the turbulent sea surface are durable and reliable. In contrast to the existing methods of aerosol flux measurements, the proposed method only needs a single receiver, in addition to relatively simple processing of only one-dimensional data. It would also seem promising to combine different methodologies from the various branches of marine sciences in the search for highly valuable results.

We presented an analysis of the relations between underwater noise and aerosol fluxes on the one hand, and different parameters of the wind wave field on the other. These new phenomena, explained by the limiting steepness and threshold vertical acceleration criteria, describe the SSF and bubbles noise behaviour fairly well. Compared with SSF

measurements, the generation function, based on the limiting steepness criterion, predicted the SSF in the case of the developing wave field much better. Based on the threshold vertical acceleration, the function was the best where it concerned agreement with the SSF for the developed wave field.

On that basis, the results of this study clearly indicate the possibility of being able to predict aerosol fluxes on account of underwater noise measurements. In other words, there is still the need for a more detailed inspection of wave field properties combined with bubble concentration monitoring. This study is further persuaded that for the latter to be accomplished, the focus ought to be on echo sounders anchored in areas with low-ship traffic.

Acknowledgments

This work was supported through a National Science Centre grant (BaSEAf: Baltic Sea European Arctic fluxes) id. number: 2015/17/N/ST10/02396.

We kindly thank the crew of the r/v *Oceania* for all technical assistance and safety care during the cruise. We thank two anonymous reviewers and editors of the journal for helpful comments and suggestions.

References

Abramowitz, M., Stegun, I.A., 1975. Handbook Of Mathematical Functions. Dover Publ., New York, 1045 pp.

Afeti, G.M., Resh, F.J., 1990. Distribution of the liquid aerosol produced from bursting bubbles in sea and distilled water. Tellus B 42, 378—384, https://doi.org/10.1034/j.1600-0889.1990.t01-2-00007.x.

Andreas, E.L., 2007. Comment on 'Vertical coarse aerosol fluxes in the atmospheric surface layer over the North Polar Water of the Atlantic' by Tomasz Petelski and Jacek Piskozub. J. Geophys. Res.-Oceans 112 (C11), art. C11010, https://doi.org/10.1029/2007JC004184.

Andreas, E.L., 1998. A New Sea Spray Generation Function for Wind Speeds up to 32 m/s. J. Phys. Oceanogr. 28, 2175—2184, https://doi.org/10.1175/1520-0485(1998)028⟨2175:ANSSGF⟩2.0.CO;2.

Andreas, E.L., 1992. Sea Spray and the Turbulent Air-Sea Heat Fluxes. J. Geophys. Res. 97, 11429—11441, https://doi.org/10.1029/92JC00876.

Andreas, E.L., 1995. The Temperature of Evaporating Sea Spray Droplets. J. Atmos. Sci. 52 (7), 852—862, https://doi.org/10.1175/1520-0469(1995)052⟨0852:TTOESS⟩2.0.CO;2.

Andreas, E.L., Jones, K.F., Fairall, C.W., 2010. Production velocity of sea spray droplets. J. Geophys. Res. 115, art. no. C12065, https://doi.org/10.1029/2010JC006458.

Blanchard, D.C., 1963. The electrification of the atmosphere by particles from bubbles in the sea. Prog. Oceanogr. 1, 73—112, https://doi.org/10.1016/0079-6611(63)90004-1.

Blanchard, D.C., 1964. Sea-to-Air Transport of Surface Active Material. Science 146 (3642), 396—397, https://doi.org/10.1126/SCIENCE.146.3642.396.

Blanchard, D.C., Syzdek, L.D., 1988. Film drop production as a function of bubble size. J. Geophys. Res. 93 (C4), 3649—3654, https://doi.org/10.1029/JC093iC04p03649.

Bortkovskii, R.S., Novak, V.A., 1993. Statistical dependencies of sea state characteristics on water temperature and wind-wave age. J. Mar. Syst. 4, 161—169, https://doi.org/10.1016/0924-7963(93)90006-8.

Bourassa, M.A., Vincent, D.G., Wood, W.L., Bourassa, M.A., Vincent, D.G., Wood, W.L., 2001. A Sea State Parameterization with Nonarbitrary Wave Age Applicable to Low and Moderate Wind Speeds. J. Phys. Oceanogr. 31, 2840—2851, https://doi.org/10.1175/1520-0485(2001)031⟨2840:ASSPWN⟩2.0.CO;2.

Callaghan, A.H., 2013. An improved whitecap timescale for sea spray aerosol production flux modeling using the discrete whitecap method. J. Geophys. Res. Atmos. 118 (17), 9997—10010, https://doi.org/10.1002/jgrd.50768.

Crouch, W.W., Burt, P.J., 1972. The Logarithmic Dependence of Surface-Generated Ambient-Sea-Noise Spectrum Level on Wind Speed. J. Acoust. Soc. Am. 51, 1066—1072, https://doi.org/10.1121/1.1912926.

de Leeuw, G., Andreas, E.L., Anguelova, M.D., Fairall, C.W., Lewis, E.R., O'Dowd, C., Schulz, M., Schwartz, S.E., 2011. Production flux of sea spray aerosol. Rev. Geophys 49 (2), art. no. 2010RG000349, https://doi.org/10.1029/2010RG000349.

de Leeuw, G., Neele, F.P., Hill, M., Smith, M.H., Vignati, E., 2000. Production of sea spray aerosol in the surf zone. J. Geophys. Res. Atmos. 105, 29397—29409, https://doi.org/10.1029/2000JD900549.

Deane, G.B., Stokes, M.D., 2002. Scale dependence of bubble creation mechanisms in breaking waves. Nature 418, 839—844, https://doi.org/10.1038/nature00967.

Dragan, A., Klusek, Z., Swerpel, B., 2011. Passive acoustic detection and observations of wind-wave breaking processes. Hydroacoustics 14, 29—38.

Esters, L., Landwehr, S., Sutherland, G., Bell, T.G., Christensen, K.H., Saltzman, E.S., Miller, S.D., Ward, B., 2017. Parameterizing air-sea gas transfer velocity with dissipation. J. Geophys. Res.-Oceans 122, 3041—3056, https://doi.org/10.1002/2016JC012088.

Fairall, C.W., Kepert, J.D., Holland, G.J., 1994. The effect of sea spray on surface energy transports over the ocean. Glob. Atmos. Ocean Syst. 2, 121—142.

Felizardo, F.C., Melville, W.K., Felizardo, F.C., Melville, W.K., 1995. Correlations between Ambient Noise and the Ocean Surface Wave Field. J. Phys. Oceanogr. 25, 513—532, https://doi.org/10.1175/1520-0485(1995)025⟨0513:CBANAT⟩2.0.CO;2.

Hasselmann, K., Barnett, T.P., Bouws, E., Carlson, H., Cartwright, D.E., Enke, K., Ewing, J.A., Gienapp, H., Hasselmann, D.E., Kruseman, P., Meerburg, A., Müller, P., Olbers, D.J., Richter, K., Sell, W., Walden, H., 1973. Measurements of wind-wave growth and swell decay during the Joint North Sea Wave Project (JONSWAP). Ergänzungsh, 8—12.

Hoppel, W.A., Frick, G.M., Fitzgerald, J.W., Larson, R.E., 1994. Marine boundary layer measurements of new particle formation and the effects nonprecipitating clouds have on aerosol size distribution. J. Geophys. Res. 99 (D7), 14443—14459, https://doi.org/10.1029/94JD00797.

IPCC — Intergovernmental Panel on Climate Change, 2013. Clouds and Aerosols. In: Climate Change 2013 — The Physical Science Basis: Working Group I Contribution to the Fifth Assessment Report of the Intergovernmental Panel on Climate Change. Cambridge Univ. Press, Cambridge, 571—657.

Jensen, D.R., Gathman, S.G., Zeisse, C.R., McGrath, C.P., De Leeuw, G., Smith, M.A., Frederickson, P.A., Davidson, K.L., 2001. Electro-optical propagation assessment in coastal environments (EOPACE): summary and accomplishments. Opt. Eng. 40 (8), 13 pp., https://doi.org/10.1117/1.1387985.

Kerman, B.R., 1984. Underwater sound generation by breaking wind waves. J. Acoust. Soc. Am. 75, 149—165, https://doi.org/10.1121/1.390409.

Kiger, K.T., Duncan, J.H., 2012. Air-Entrainment Mechanisms in Plunging Jets and Breaking Waves. Annu. Rev. Fluid Mech. 44, 563—596, https://doi.org/10.1146/annurev-fluid-122109-160724.

Klusek, Z., 2011. Ambient sea noise in the Baltic Sea — review of investigations. Hydroacoustics 14, 75—82.

Klusek, Z., Lisimenka, A. , 2016. Seasonal and diel variability of the underwater noise in the Baltic Sea. J. Acoust. Soc. Am, 139, art. no. 1537, https://doi.org/10.1121/1.4944875.

Koga, M., 1981. Direct production of droplets from breaking wind-waves its observation by a multi-colored overlapping exposure photographing technique. Tellus 33, 552—563, https://doi.org/10.1111/j.2153-3490.1981.tb01781.x.

Komen, G.J., 1994. Dynamics and modelling of ocean waves. Cambridge Univ. Press, Cambridge, 532 pp.

Kraan, G., Oost, W.A., Janssen, P.A.E.M., 1996. Wave Energy Dissipation by Whitecaps. J. Atmos. Ocean. Technol. 13, 262—267, https://doi.org/10.1175/1520-0426(1996)013⟨0262:WEDBW⟩2.0.CO;2.

Lewis, E.R., Schwartz, S.E. , 2004. Sea salt aerosol production: Mechanisms, methods, measurements and models — A critical review. Geophys. Monogr. Ser, 152, 413 pp, https://doi.org/10.1029/152GM01.

Lhuissier, H., Villermaux, E., 2012. Bursting bubble aerosols. J. Fluid Mech. 696, 5—44, https://doi.org/10.1017/jfm.2011.418.

Loewen, M.R., Melville, W.K., 1991. Microwave backscatter and acoustic radiation from breaking waves. J. Fluid Mech. 224, 601—623, https://doi.org/10.1017/S0022112091001891.

MacIntyre, F., 1972. Flow patterns in breaking bubbles. J. Geophys. Res. 77, 5211—5228, https://doi.org/10.1029/JC077i027p05211.

Marks, R., 1990. Preliminary investigations on the influence of rain on the production, concentration, and vertical distribution of sea salt aerosol. J. Geophys. Res. 95 (C12), 22299—22304, https://doi.org/10.1029/JC095iC12p22299.

Markuszewski, P., Kosecki, S., Petelski, T., 2017a. Sea spray aerosol fluxes in the Baltic Sea region: Comparison of the WAM model with measurements. Estuar. Coast. Shelf Sci. 195, 16—22, https://doi.org/10.1016/j.ecss.2016.10.007.

Markuszewski, P., Rozwadowska, A., Cisek, M., Makuch, P., Petelski, T., 2017b. Aerosol physical properties in Spitsbergen's fjords: Hornsund and Kongsfjorden during AREX campaigns in 2014 and 2015. Oceanologia 59 (4), 460—472, https://doi.org/10.1016/J.OCEANO.2017.03.012.

Massel, S.R., 2007. Ocean Waves Breaking and Marine Aerosol Fluxes. Atmos. Ocenaogr. Sci. Library, 38. Springer-Verlag, New York, 316 pp., https://doi.org/10.1007/978-0-387-69092-6.

Massel, S.R., 2018. Ocean surface waves: Their physics and prediction. Adv. Ser. Ocean Eng., World Sci., 800 pp., https://doi.org/10.1142/10666.

Medwin, H., Beaky, M.M., 1989. Bubble sources of the Knudsen sea noise spectra. J. Acoust. Soc. Am. 86 (3), 1124—1130, https://doi.org/10.1121/1.398104.

Minnaert, M., 1933. XVI. *On musical air-bubbles and the sounds of running water*. London, Edinburgh. Dublin Philos. Mag. J. Sci. 16 (104), 235—248, https://doi.org/10.1080/14786443309462277.

Monahan, E.C., Fairall, C.W., Davidson, K.L., Boyle, P.J., 1983. Observed inter-relations between 10 m winds, ocean whitecaps and marine aerosols. Q. J. R. Meteorol. Soc. 109, 379—392, https://doi.org/10.1002/qj.49710946010.

Monin, A.S., Obukhov, A.M., 1954. Basic laws of turbulent mixing in the surface layer of the atmosphere. Tr. Akad. Nauk SSSR Geophiz. Inst. 24 (151), 163—187.

Norris, S.J., Brooks, I.M., Hill, M.K., Brooks, B.J., Smith, M.H., Sproson, D.A.J., 2012. Eddy covariance measurements of the sea spray aerosol flux over the open ocean. J. Geophys. Res. 117 (D7), art. no. D07210, https://doi.org/10.1029/2011JD016549.

Norris, S.J., Brooks, I.M., Moat, B.I., Yelland, M.J., de Leeuw, G., Pascal, R.W., Brooks, B., 2013. Near-surface measurements of sea spray aerosol production over whitecaps in the open ocean. Ocean Sci 9, 133—145, https://doi.org/10.5194/os-9-133-2013.

Nystuen, J.A., 2001. Listening to raindrops from underwater: An acoustic disdrometer. J. Atmos. Ocean. Technol. 18 (10), 1640—1657, https://doi.org/10.1175/1520-0426(2001)018⟨1640:LTRFUA⟩2.0.CO;2.

Petelski, T., 2005. Coarse Aerosol Concentration Over the North Polar Waters of the Atlantic. Aerosol Sci. Technol. 39, 695—700, https://doi.org/10.1080/02786820500182362.

Petelski, T., 2003. Marine aerosol fluxes over open sea calculated from vertical concentration gradients. J. Aerosol Sci. 34, 359—371, https://doi.org/10.1016/S0021-8502(02)00189-1.

Petelski, T., Markuszewski, P., Makuch, P., Jankowski, A., Rozwadowska, A., 2014. Studies of vertical coarse aerosol fluxes in the boundary layer over the Baltic Sea. Oceanologia 56 (4), 697—710, https://doi.org/10.5697/oc.56-4.697.

Petelski, T., Piskozub, J. , 2006. Vertical coarse aerosol fluxes in the atmospheric surface layer over the North Polar Waters of the Atlantic. J. Geophys. Res, 111 (C6), art. no. C06039, https://doi.org/10.1029/2005JC003295.

Petelski, T., Piskozub, J., Paplińska-Swerpel, B., 2005. Sea spray emission from the surface of the open Baltic Sea. J. Geophys. Res.-Oceans, 110 (C10), art. no. C10023, https://doi.org/10.1029/2004JC002800.

Prosperetti, A., 1988. Bubble-related ambient noise in the ocean. J. Acoust. Soc. Am. 84, 1042—1054, https://doi.org/10.1121/1.396740.

Prosperetti, A., Lu, N.Q., Kim, H.S., 1993. Active and passive acoustic behavior of bubble clouds at the ocean's surface. J. Acoust. Soc. Am. 93, 3117—3127, https://doi.org/10.1121/1.405696.

Resch, F.J., Darrozes, J.S., Afeti, G.M., 1986. Marine liquid aerosol production from bursting of air bubbles. J. Geophys. Res. 91 (C1), 1019—1029, https://doi.org/10.1029/JC091iC01p01019.

Savelyev, I.B., Anguelova, M.D., Frick, G.M., Dowgiallo, D.J., Hwang, P.A., Caffrey, P.F., Bobak, J.P., 2014. On direct passive microwave remote sensing of sea spray aerosol production. Atmos. Chem. Phys. 14, 11611—11631, https://doi.org/10.5194/acp-14-11611-2014.

Sellegri, K., O'Dowd, C.D., Yoon, Y.J., Jennings, S.G., de Leeuw, G., 2006. Surfactants and submicron sea spray generation. J. Geophys. Res. 111, art. no. D22215, https://doi.org/10.1029/2005JD006658.

Smith, M.H., Park, P.M., Consterdine, I.E., 1993. Marine aerosol concentrations and estimated fluxes over the sea. Q. J. R. Meteorol. Soc. 119, 809—824, https://doi.org/10.1002/qj.49711951211.

Spiel, D.E., 1998. On the births of film drops from bubbles bursting on seawater surfaces. J. Geophys. Res.-Oceans 103, 24907—24918, https://doi.org/10.1029/98JC02233.

Stramska, M., Petelski, T., 2003. Observations of oceanic whitecaps in the north polar waters of the Atlantic. J. Geophys. Res. 108 (C3), 108 (C3), art. no. 3086, https://doi.org/10.1029/2002JC001321.

Tsigaridis, K., Koch, D., Menon, S., 2013. Uncertainties and importance of sea spray composition on aerosol direct and indirect effects. J. Geophys. Res. Atmos. 118, 220—235, https://doi.org/10.1029/2012JD018165.

Vagle, S., Large, W.G., Farmer, D.M., Vagle, S., Large, W.G., Farmer, D.M., 1990. An Evaluation of the WOTAN Technique of Inferring Oceanic Winds from Underwater Ambient Sound. J. Atmos. Ocean. Technol. 7, 576—595, https://doi.org/10.1175/1520-0426(1990)007⟨0576:AEOTWT⟩2.0.CO;2.

Vakkayil, R., Graber, H.C., Large, W.G., 1996. Oceanic winds estimated from underwater ambient noise observations in SWADE. In: OCEANS 96 MTS/IEEE Conf. Proc. The Coastal Ocean — Prospects for the 21st Century. IEEE, 45—51.

Veron, F., 2015. Ocean Spray. Ann. Rev. Fluid Mech. 47, 507—538, https://doi.org/10.1146/annurev-fluid-010814-014651.

WAMDI Group, 1988. The WAM Model. J. Phys. Oceanogr. 18, 1775—1810 , https://doi.org/10.1175/1520-0485(1988)018<1775:TWMTGO>2.0.CO;2.

Wenz, G.M., 1962. Acoustic Ambient Noise in the Ocean: Spectra and Sources. J. Acoust. Soc. Am. 34, 1936—1956, https://doi.org/10.1121/1.1909155.

Wilson, J.D., Makris, N.C., 2008. Quantifying hurricane destructive power, wind speed, and air-sea material exchange with natural undersea sound. Geophys. Res. Lett 35 (10), art. no. L10603, https://doi.org/10.1029/2008GL033200.

Wilson, P.R., 1980. The interaction of acoustic waves with flux tubes. Astrophys. J. 237, 1008—1014, https://doi.org/10.1086/157946.

Wu, J., 2002. Jet Drops Produced by Bubbles Bursting at the Surface of Seawater. J. Phys. Oceanogr. 32, 3286—3290, https://doi.org/10.1175/1520-0485(2002)032⟨3286:JDPBBB⟩2.0.CO;2.

Wu, J., 1993. Production of spume drops by the wind tearing of wave crests: The search for quantification. J. Geophys. Res. 98 (C10), 18221—18227, https://doi.org/10.1029/93JC01834.

Wu, J., 1981. Evidence of Sea Spray Produced by Bursting Bubbles Science, 212, 324—326.

Zedel, L., Gordon, L., Osterhus, S., Zedel, L., Gordon, L., Osterhus, S., 1999. Ocean Ambient Sound Instrument System: Acoustic Estimation of Wind Speed and Direction from a Subsurface Package. J. Atmos. Ocean. Technol. 16, 1118—1126, https://doi.org/10.1175/1520-0426(1999)016⟨1118:OASISA⟩2.0.CO;2.

Oceanologia (2020) 62, 428—442

Available online at www.sciencedirect.com

ScienceDirect

journal homepage: www.journals.elsevier.com/oceanologia

ORIGINAL RESEARCH ARTICLE

Study of ice cover impact on hydrodynamic processes in the Curonian Lagoon through numerical modeling

Rasa Idzelytė[a,*], **Jovita Mėžinė**[a], **Petras Zemlys**[a], **Georg Umgiesser**[b,a]

[a] *Marine Research Institute, Klaipėda University, Klaipėda, Lithuania*
[b] *CNR — National Research Council of Italy, ISMAR — Institute of Marine Sciences, Venice, Italy*

Received 27 October 2019; accepted 23 April 2020
Available online 18 May 2020

KEYWORDS
Ice cover impact;
Water circulation;
Numerical modelling;
SHYFEM;
Curonian Lagoon

Summary In this study, we present an analysis of the hydrodynamic processes under ice cover in the largest lagoon in Europe — the Curonian Lagoon. By applying a finite element numerical modelling system (SHYFEM) and remote sensing ice cover data, the residual circulation, water fluxes through specific areas of the lagoon, saltwater intrusions, and water residence time (WRT) were investigated. The results, taken over an 11 year period, show that ice cover affects the circulation patterns in the lagoon by forming and shifting different gyre systems. Different circulation patterns are observed throughout all the meteorological seasons of the year. Since ice decreases circulation, water fluxes also decrease, especially in a cross-section in the middle of the lagoon, where the ice-cover suppressed wind-stress has a higher impact on the water movement rather than it has in the north. The presence of ice cover also decreases the salinity of the water in the northern part of the lagoon. In general, the salinity in the water column averaged over different periods is vertically uniform, however, a slight increase of salt concentration can be observed at the bottom layers in the Klaipėda Strait, where the difference of >1 PSU between bottom and top layers shows up on average 130 hours per year. The ice cover also decreases the saltwater intrusions into the lagoon by nearly 14 days per year. The increase of WRT is most prominent after long ice cover periods, away from the river inlets, especially

* Corresponding author at: Marine Research Institute, Klaipėda University, Universiteto ave. 17, 92294, Klaipėda, Lithuania.
E-mail address: rasa.idzelyte@apc.ku.lt (R. Idzelytė).
Peer review under the responsibility of the Institute of Oceanology of the Polish Academy of Sciences.

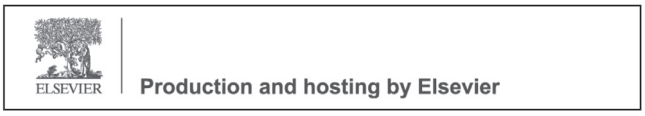

https://doi.org/10.1016/j.oceano.2020.04.006

in the southern part of the lagoon, where without the help of the wind action, water takes a longer time to renew than in the northern part.

1. Introduction

Changing ice cover conditions have a strong impact on the hydrodynamics, exchange processes, and overall ecosystem of the water body, including the fisheries and tourism sector. Ice cover formation is controlled by variations in heat exchange and mixing, as well as the heat storage capacity of the water body (Bengtsson, 2012). The initial ice formation can be rather complex with many freezing and break-up events depending on the strength of the heat loss and wind stress at the water surface.

Ice cover affects a water body in several ways. It suppresses the direct wind stress to the water surface and significantly alters the circulation and mixing (Wang et al., 2010). The movement of the water is highly regulated by thermal processes and by the vertical motion of the ice cover (Bengtsson, 2012). Convective mixing is induced when there is enough light penetrating through the ice and by heat exchange with the sediments. The latter is a very slow process capable to last throughout the whole winter (Bengtsson, 1996). Inflowing water from the rivers induce circulation near the inlets, thus it may only have a local effect on the overall circulation (Cushman-Roisin, 2019).

Freshwater bodies connected to the sea by a strait, such as the Curonian Lagoon, are prone to saltwater intrusions (Müller et al., 2018; Zemlys et al., 2013, and references therein). Although it is a natural process, it can likewise be induced by human activity, e.g., dredging in the strait area (Yuan and Zhu, 2015). This process not only alters the ecosystem of the freshwater environment (Cañedo-Argüelles et al., 2019), but also affects the freezing and melting of the ice (Idzelytė et al., 2019). It can be an increasingly more serious issue due to the climate change with increasing air and water temperatures (Jakimavičius et al., 2018; Wolanski et al., 2019), rising sea level (Carrasco et al., 2016), and the escalating number of extreme weather events (Janković and Schultz, 2017; Ummenhofer and Meehl, 2017).

Lagoons are influenced not only by salty marine water but also by freshwater input from the rivers. The average time a water parcel stays in a domain before leaving it is called water residence time (Ambrosetti et al., 2003). Ice highly affects the ability of the water to be renewed by fresh water from the river inlets, thus its residence time tends to increase, affecting the water chemical composition (Vincent, 2009), and thus affecting the time and intensity of algal blooms in early spring (Nguyen et al., 2017; Twiss et al., 2014).

Ice cover not only alters the physical properties of the water body, but it also has ecological repercussions. The magnitude of solar radiation entering the water body is highly diminished by ice and snow cover on top of it. This way, lowered temperature affects all the chemical and biological processes (Hampton et al., 2017; Wotton, 1995). In general, light provides radiation for primary production and in particularly productive water bodies, the limited light penetration causes dissolved oxygen depletion due to increased respiration of aquatic organisms and microbial decomposition (Vincent, 2009). The addition of the oxygenated water and transfer of oxygen from the atmosphere replenish its levels in the water column. Water motion is primarily responsible for reaeration. When the ice cover blocks the wind stress, there is no motion on the surface, thus oxygenated water can only come from the water inflow areas.

As the climate is changing, leading to increased temperatures, the ice cover season duration is shortening in the Curonian Lagoon (Dailidiene, 2007; Idzelytė et al., 2019). This may lead to the increased coastal erosion, because ice on the coast is a natural breakwater, protecting the shore from winter storms, and preventing the deflation of the sand (Jarmalavičius, 2007). On the other hand, when the ice breaks up and starts drifting, ice heap has a great impact on abrasion of the shoreline, which depends on the mass of the ice, direction and speed of the wind, and water currents. The ice drift affects water level fluctuations in the lagoon by damming the rivers, thus significantly increasing flooded land areas and partially or sometimes even completely changing the riverbed. In the north of the Curonian Lagoon floe clutters cause an increase of the overall water level, reducing the outflow to the sea. Moreover, the lagoon would have much higher suspended sediment concentrations in the water column if the ice cover would not be present during the winter season (Mėžinė et al., 2019).

The circulation patterns, saline water intrusions, and water residence time (WRT) in the Curonian Lagoon have been of high study interest. Ferrarin et al. (2008) showed that the main forcing affecting the circulation patterns in the northern part of the lagoon is the Nemunas River discharge and in the southern part, it is largely driven by wind forcing. The study by Zemlys et al. (2013) revealed that saline water intrusions from the Baltic Sea through the Klaipėda Strait into the lagoon are gradually decreasing and become negligible at a 20 km distance to the south of Kiaulės Nugara Island. Additionally, the results showed that the model performance during the winter season was worse, presumably because ice cover was not included in that model set up. This was improved by Umgiesser et al. (2016), producing better results by using the interpolated data of ice observations from four ground stations. Their study of water renewal time demonstrated that, overall, it is changing only slightly, although a notable increase in WRT is observed during long winters. The above-mentioned study used in situ ice observations from a limited number of

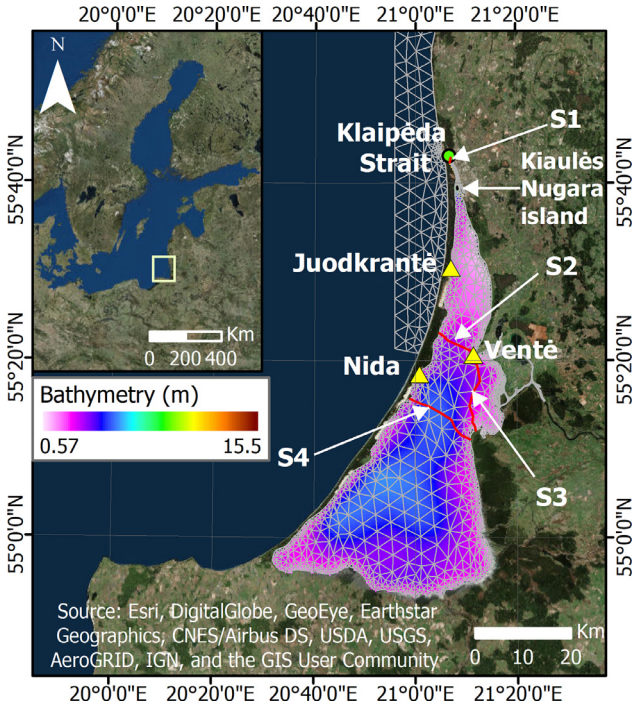

Figure 1 Location of the Curonian Lagoon with respect to the Baltic Sea. The irregular triangular network represents the computational grid, colors throughout the domain indicate the bathymetry of the lagoon, yellow triangles denote ice cover observation stations, the green circle shows a point in Klaipėda Strait for the salinity analysis, and red lines indicate cross-sections for the computation of the fluxes in the Klaipėda Strait (S1), North of Nemunas (S2), Nemunas Delta (S3), and at Lithuanian-Russian border (S4).

stations in the northern part of the lagoon, which were shown by Idzelytė et al. (2019) to not truly represent the real ice cover dynamics in the Curonian Lagoon. Furthermore, only 4 years of ice cover data were available.

With a complete set of ice data for 11 winters, it is now possible to carry out a much more complete study of the ice impact on the hydrodynamic process occurring in the Curonian Lagoon. Therefore, the aim of this paper is to analyze the ice cover effect on the circulation, water exchange capabilities, saltwater intrusions, and water residence time for the period of 2004–2015 using remote sensing ice cover data in the numerical model SHYFEM, simulating the hydrodynamics of the Curonian Lagoon.

2. Material and methods

2.1. Study site

The Curonian Lagoon is located in the southeastern corner of the Baltic Sea (between 54.9°N and 55.9°N) separated from it by a sandy spit, called Curonian Spit and connected to it by the narrow Klaipėda Strait (Figure 1). By occupying an area of around 1584 km^2 (volume 6.3 km^2) (Žaromskis, 1996), it is the largest coastal lagoon in Europe with the northern part belonging to Lithuania, and the larger southern part – to Russia. The Curonian Lagoon is a shallow water body having a mean depth of roughly 3.8 m, the maximum natural depth of 5.8 m in the southern part of the lagoon (Gasiūnaitė et al., 2008) and dredged areas in the Klaipėda Strait up to 15.5 m deep. The southern part is characterized by being freshwater, which is due to the river discharge into the lagoon of approximately 21.8 km^3 yr^{-1}, mainly supplied by the Nemunas River (Dailidiene and Davuliene, 2008; Jakimavičius, 2012). River water is the main water renewal source, especially in the northern part of the lagoon (Umgiesser et al., 2016); however, this area is characterized by a higher salinity due to the Baltic Sea water intrusions, which are determined by the water level difference of the Baltic Sea and the Curonian Lagoon. Saline water inflows along the western shoreline where the influence of Nemunas discharge is weaker (Zemlys et al., 2013). The variability of circulation patterns depends mainly on seasonal changes in hydrographic forcing and on the dominant wind regimes (Umgiesser et al., 2016). The latter are responsible also for the internal mixing and redistribution of the water masses.

Every year the Curonian Lagoon is covered by ice, however, the duration of the ice cover season is displaying a tendency to decrease with the lagoon becoming ice-free sooner. The variability of the ice cover extent throughout the season highly depends on the air temperature. If it is very low for a longer period, then a thick ice cover is able to form, which is capable to withstand positive air temperature events. However, if the negative air temperature is not very low or unstable throughout the ice season, a lot of break-up and refreezing can occur. Historical ice observation data (Baušys, 1978) show that a 10–70 cm ice thickness used to form in the lagoon, but it is steadily decreasing and is projected to be 13–15 cm or thinner by the end of the century due to the climate change (Jakimavičius et al., 2019). There is a significant trend in the final melt onset dates, denoting that ice is starting to melt sooner. Firstly, ice starts breaking in the northern part of the lagoon due to the turbid nature of this area – inflowing saline Baltic Sea water and outflow from the Nemunas River. The southern more limnic part of the lagoon is covered by ice longer than in other areas and melting there is affected more by higher temperatures and wind. Typically, ice cover starts to retreat from the western shoreline to the eastern part of the lagoon due to the prevailing westerly winds during wintertime (Idzelytė et al., 2019).

2.2. Data

For the ice cover data, we used Synthetic Aperture Radar (SAR) images received from three remote sensing missions: Envisat ASAR, RADARSAT-2, and Sentinel-1A and 1B, as well as data from spectroradiometer MODIS. Overall, 11 winter periods from 2004 to 2015 were analyzed and a total of 511 images were processed, with a frequency of 2–5 images per week. The ice polygons were manually digitized from satellite images using ArcGIS software (more about data processing techniques and results see Idzelytė et al., 2019), converted to points in the numerical model grid, and interpolated to fill in the gaps between the dates of received satellite images. The satellite data were validated with ground observations taken once per day in three coastal stations in Juodkrantė, Nida, and Ventė. Ice observation data

was provided by the Marine Research Department of the Environment Protection Agency of Lithuania. Both datasets (satellite images and ground observations) agree quite well, giving a correlation coefficient of 0.92. Some inconsistencies arise in defining the freeze onset in the lagoon, due to the temporal resolution of satellite images being not high enough to capture the fast ice formation. Nonetheless, during the melting period when ice is drifting and break-up occurs far away from the coastal stations, it is firstly detected in satellite images, likewise, the last observation of ice in the lagoon. Therefore, in most cases, satellite data are superior with respect to in situ observations for defining the key stages of ice cover formation and decay.

There are five open boundaries defined in the study domain — one for the Baltic Sea, and other four for the discharging rivers: Nemunas, Minija, Matrosovka, and Deima. Salinity, temperature and water level data at the open sea boundary for the period of 2004—2006 were obtained from the forecasts of operational hydrodynamic model MIKE21 provided by the Danish Hydraulic Institute, for the period of 2007—2009 and 2014—2016 from forecasts of the operational hydrodynamic model HIROMB (High Resolution Operational Model for the Baltic Sea) provided by the Swedish Meteorological and Hydrological Institute, and for the period of 2010—2013 from the forecasts of MOM (Modular Ocean Model) provided by Leibniz Institute for Baltic Sea Research in Warnemünde, Germany. Lithuanian Hydrometeorological Service (LHS) under the Ministry of Environment provided the daily river discharge data.

Meteorological forcings for the period of 2009—2010 were obtained from the forecasts of operational numerical weather prediction model HIRLAM (High Resolution Limited Area Model) provided by LHS, and for the rest of the years data obtained from ECMWF (European Centre for Medium-Range Weather Forecasts) were used.

2.3. Hydrodynamic model

The open source hydrodynamic finite element model for shallow water bodies SHYFEM was used to simulate ice cover effect on circulation, saltwater intrusions from the Baltic Sea, water residence time in the lagoon, and mass fluxes through sections shown in Figure 1. The model was developed at ISMAR-CNR (Institute of Marine Sciences — National Research Council, http://www.ismar.cnr.it/shyfem) and has been already successfully applied for studying hydrodynamic processes of numerous lagoons in Europe (De Pascalis et al., 2011; Ferrarin et al., 2010a, 2010b, 2013; Molinaroli et al., 2014), as well as the Curonian lagoon for which the calibration and validation of the model was done (Ertürk et al., 2015; Ferrarin et al., 2008; Zemlys et al., 2008, 2013). The results obtained by Umgiesser et al. (2016) showed that the model with a simple ice module gave much better results compared to the reference (ice-free) simulation.

SHYFEM consists of several modules: hydrodynamic, transport and diffusion, sediment transport, wave, and an ecological module. It is based on an unstructured grid, which makes it suitable for application to lagoons, coastal seas, estuaries, and lakes with complicated geometry and bathymetry. This model is able to provide 2D as well as 3D simulations; for this study we used a 3D set-up. The equations are integrated in time using a semi-implicit discretization scheme and spatial discretization is achieved using a partially modified finite element method. For salinity and temperature computations, a transport diffusion model is used that takes into account the heat fluxes from the atmosphere and input from rivers. The water residence time computation is done by transforming the near exponential decay of a conservative tracer with a logarithm application to a straight line that then can be used for estimating the WRT through linear regression (Cucco and Umgiesser, 2006).

The ice cover data in the model is represented by a number with values between 0 and 1, where marginal value 0 denotes the absence of ice and value 1 denotes water surface completely covered by ice. The presence of ice was accounted for in the model by weighting the wind drag coefficient by the fractional ice value. This is done to scale the momentum input through the surface by the area free of ice. For the areas having ice concentration equivalent to 1, the momentum transfer to the sea is completely suppressed. This study does not consider ice-ocean stress (Umgiesser et al., 2016). More explanation about the model and its equations can be found in Bellafiore and Umgiesser (2010), Ferrarin et al. (2017), Maicu et al. (2018), and Umgiesser et al. (2004).

2.4. Modelling set up and scenarios

The computational grid of the study area consists of 1309 nodes and 2027 triangular elements (Figure 1). The resolution is much finer in the Klaipeda Strait. For the vertical discretization, 10 sigma layers have been used. A part of the Baltic Sea in front of the lagoon is also included into the numerical grid, preventing the disturbances for computations of the exchanges through the Klaipeda Strait area. The Baltic Sea and Klaipėda Strait were considered ice-free for all simulations since naturally there is no landlocked ice due to intensive shipping, higher depths, and inflowing warmer water from the Baltic Sea.

Three types of simulations have been carried out: 1) ice cover artificially switched off in the model (hereafter no-ice); 2) with ice cover data obtained from the satellite observations (hereafter real ice); 3) an additional set of simulation run where the lagoon is completely covered by ice during the ice cover season, including the Klaipėda Strait area (hereafter idealized ice). The comparison of the ice and idealized ice season simulations allows a better understanding of the role of ice cover in the hydrodynamic processes in the Curonian Lagoon.

The simulation period was from 2004-01-01 to 2015-12-31. Only 11 years were analyzed as the simulation of the year 2004 was used for the model spin-up. For the analysis of ice cover impact on the velocity and direction of the water currents, water fluxes, salinity, and water residence time, the simulation results were averaged over the meteorological seasons of the year: winter (December, January, February), spring (March, April, May), summer (June, July, August), and autumn (September, October, November), as well as over the ice cover seasons, each of them having different durations (different beginning and ending dates of the ice season).

The average differences of simulation results obtained with ice switched on and switched off in the model (real

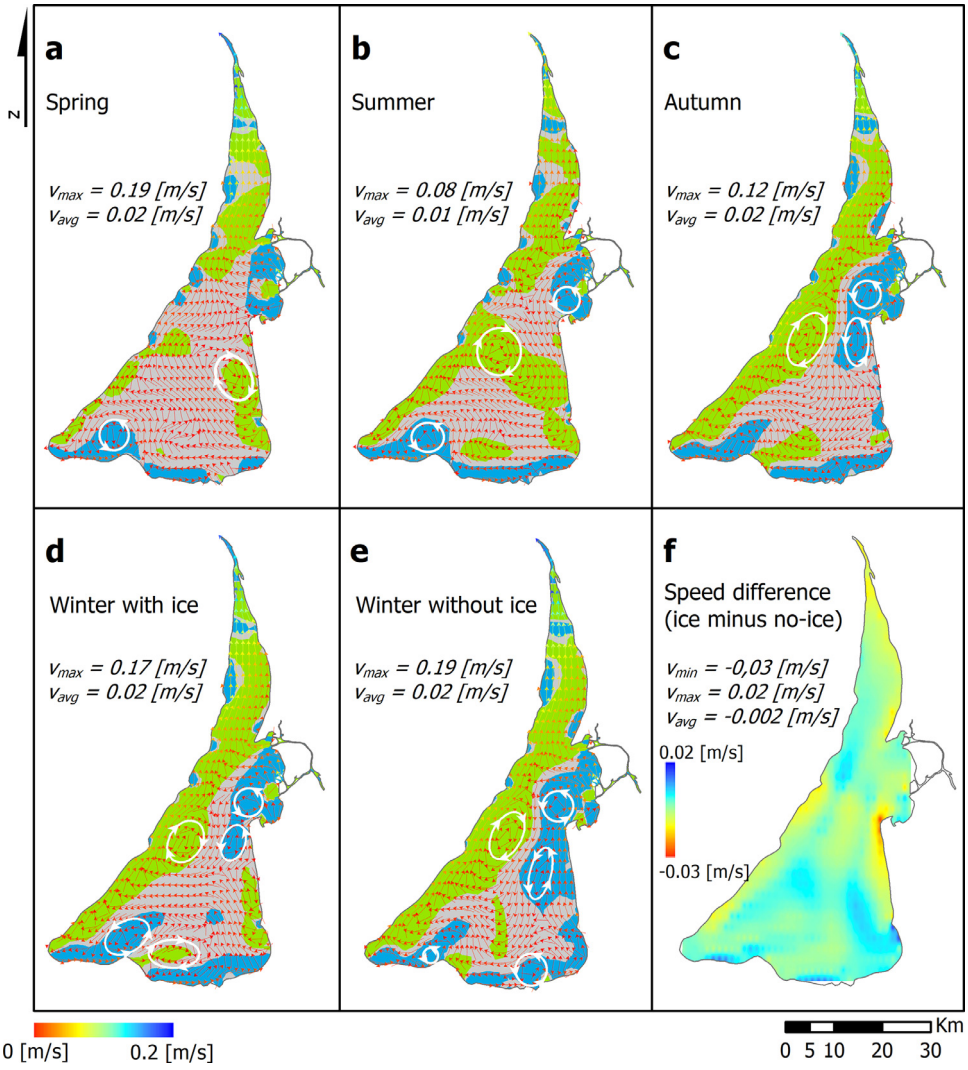

Figure 2 Water circulation (vectors are colored by the current speed in m/s) averaged over the whole simulation period of simulations with ice data in: (a) spring, (b) summer, (c) autumn, and winter seasons (d), without ice in winter (e), and the current speed difference of these winter computations (ice minus no-ice, f). White circles with arrows show gyre systems and their direction, colors in the map show positive (blue), negative (green), and irrotational (gray) vorticity, and numbers indicate the maximum (v_{max}) and average (v_{avg}) velocity of the residual currents.

ice minus no-ice and idealized ice minus no-ice) were calculated to analyze the impact of the ice cover to the above-mentioned hydrodynamic properties of the lagoon. This was done for the averaged ice cover seasons. The salinity time series difference between the bottom and top layers of the water column in Klaipėda Strait (green circle in Figure 1) were analyzed to identify the number of hours per year of salt concentration exceeding the threshold of 1 and 3 PSU. The vertically averaged salinity time series in Juodkrantė were analyzed to count the number of days when the salt concentration exceeds the 2 PSU threshold.

Simulation results of 2004–2015 period were also used for computing the water residence time (WRT) switching its calculation on in the model for the different periods: 1) for the ice-free part of the year and the ice cover season (WRT_{ice}^{real} for the real ice cover and WRT_{ice}^{ideal} for the idealized ice cover season); 2) for every meteorological season of the year defined above (WRT_{season}). All calculations were done twice — considering ice cover data and without it. The water residence time for the winter season (WRT_{winter}) was compared with WRT_{ice}^{real} and the results from Umgiesser et al. (2016). Since the northern and southern part of the Curonian Lagoon has different hydrodynamic properties, WRT was computed separately for both of these areas, as well as for the total lagoon area.

3. Results

3.1. Circulation

The behavior of water motion can be inferred through the analysis of the residual currents, which are currents averaged over a longer period, in our study, averaged over every meteorological season of the year (Figure 2). Residual currents indicate the mean flow of the water, even if much

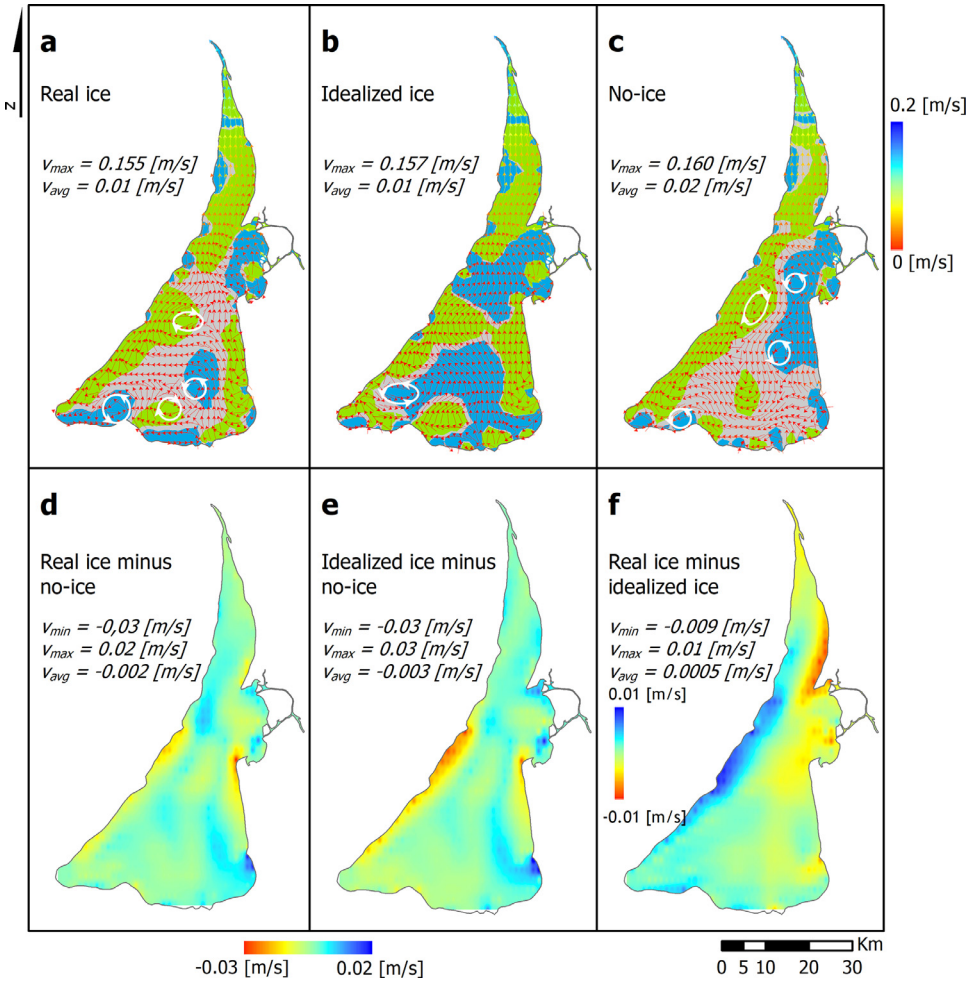

Figure 3 Water circulation (vectors are colored by the current speed in m/s) averaged over ice cover season in simulation with (a) real ice cover, (b) idealized ice cover, and (c) no-ice season set-up, as well as the current speed difference in m/s between simulations: (d) real ice cover minus no-ice, (e) idealized ice cover minus no-ice, and (f) real minus idealized ice cover. White circles with arrows in a, b, and c show gyre systems and their direction, colors in these maps show positive (blue), negative (green) and irrotational (gray) vorticity, and numbers indicate the minimum (v_{min}), maximum (v_{max}), and average (v_{avg}) velocity of the residual currents.

higher and lower instantaneous values can be detected. In the Curonian Lagoon, we can observe a strong flow from the Nemunas River northward to the Klaipėda Strait, having the highest speed throughout the year. During spring season (Figure 2a) in the southern part of the lagoon a two gyre circulation system is observed, one — anticlockwise in the southwestern corner of the lagoon, and the second — clockwise along the eastern shoreline. In summer, the latter one shifts towards the middle part of the lagoon and a third anticlockwise gyre system forms in the Nemunas Delta area (Figure 2b). In summer the current speed is much slower than in spring, with a slightly more pronounced flow along the western shoreline. In autumn (Figure 2c), the current speed slightly increases and the gyre in the southwestern part of the lagoon is not as apparent as during the previous seasons. In addition to this, another anticlockwise gyre system is observed to form in the middle of the lagoon, near the eastern shore. During the winter season under the ice cover (Figure 2d) the same gyre systems remain in the central part of the lagoon and in Nemunas Delta, however, the anticlockwise gyre in the southwestern part of the lagoon becomes more apparent and another clockwise system can be observed to form next to it. The water flow along the western part of the lagoon slightly decreases during winter and it becomes more chaotic near the eastern shoreline, where ice cover stays the longest.

The difference of the simulation results of winter circulation with and without the ice cover (Figure 2f) was computed to investigate how ice cover affects the velocity of the residual currents during the winter season. The results show that circulation under the ice cover becomes weaker by up to 0.03 m/s. Water during the winter season flows slower along the perimeter of the lagoon, especially near the eastern shoreline. As mentioned above, in the simulation with ice cover one can observe a more chaotic water movement along the southeastern shoreline (Figure 2d), compared to simulation results when the ice cover was omitted (Figure 2e). Additionally, there is a difference in gyre systems in the southern part of the lagoon, being more pronounced under ice cover.

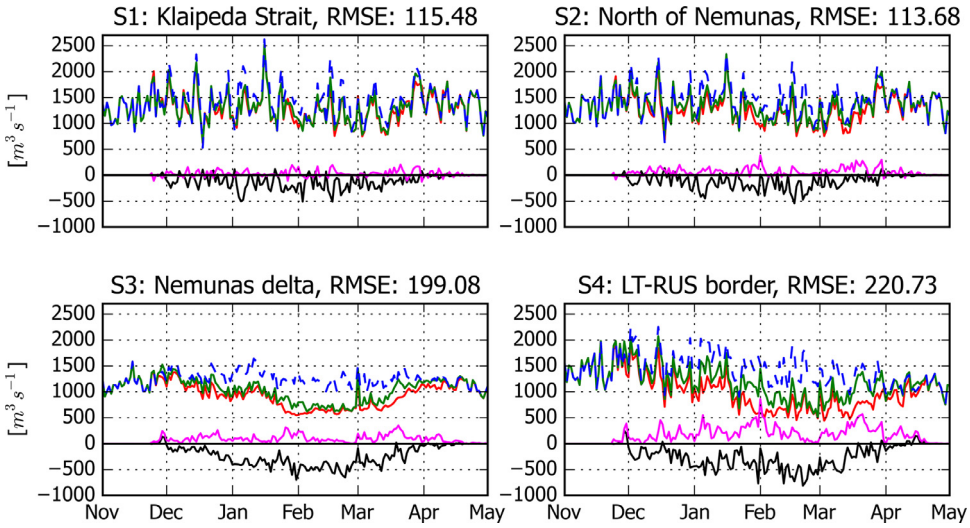

Figure 4 Average water fluxes through cross-sections at Klaipėda Strait (S1), north of Nemunas (S2), Nemunas delta (S3), and Lithuanian-Russian border (S4). The location of each cross-section is shown in Figure 1. Green solid lines indicate water fluxes of simulation with real ice, blue dashed lines – simulation without ice, the black solid line denotes the difference of these simulations (real ice minus no-ice), the red solid line shows the results of simulation with idealized ice, and the magenta solid line indicates the real ice and idealized ice simulation difference (real ice minus idealized ice). Negative values denote higher southward fluxes in the simulation without ice.

Concerning the average residual currents during the real ice cover season (Figure 3a), two gyre systems in the southern part of the lagoon, which are similar to the results averaged over the winter season, can be found (Figure 2d). However, there is a third gyre next to it and only one gyre in the middle of the lagoon during the real ice cover season. For the idealized ice cover (Figure 3b), when the lagoon is completely covered by ice throughout the whole ice season duration, only one gyre forms in the southwestern part of the lagoon. The distribution of the gyre systems in the simulation without ice (averaged over the ice season duration, Figure 3c) is similar to the results averaged over the winter season (Figure 2e), with only one gyre missing near the southern shoreline. The difference of current speed in simulations with real ice and without it (Figure 3d) is similar to the one averaged over the winter season (Figure 2f). The difference of idealized ice cover and no-ice seasons is more pronounced near the western shoreline (Figure 3e). In the idealized case, when the lagoon is completely covered by ice water flows slower along the western shoreline and it is slightly stronger along the eastern shoreline in the northern part of the lagoon, compared to the flow during the real ice cover season (Figure 3f).

By looking at the residual currents of each ice cover season separately (not shown here), it can be seen that in the southern part of the lagoon, the current speed noticeably decreases. This is due to this area being sheltered from the wind by ice cover for a longer period compared to the northern part. When the ice cover is more variable, meaning that it decomposes and refreezes several times throughout the season, it leads to slightly higher current speeds. During each ice-cover season, in the Klaipėda Strait area and approximately 5 km southward from Kiaulės Nugara island, the current speed is always higher compared to the rest of the lagoon. However, if this area is fully covered by ice for a longer period, then the current speed slightly decreases.

3.2. Fluxes

For the computation of the fluxes, four cross-sections were set – in Klaipėda Strait, north of Nemunas River, Nemunas delta, and along Lithuanian-Russian border (red lines in Figure 1). Although the water fluxes through each of the specified sections are rather the same (fluctuating around 1000–1500 $m^3\ s^{-1}$), one can clearly see the difference between simulations with ice and without it. The results show that the ice cover has a higher impact on the water fluxes in the Nemunas delta area (S3 in Figure 4) and through the borderline of the two countries (S4). The difference between simulation results with and without ice is nearly twice as high in these sections than it is in Klaipėda Strait and north of Nemunas sections. The difference is only observed during the ice cover season.

The comparison of idealized ice (fully ice covered lagoon during the ice cover season) and real ice season (ice cover from remote sensing data) simulation results shows that the prolonged full ice cover (idealized ice) has the greatest impact only in middle of the lagoon (at the cross-section along the Lithuanian-Russian border). The changes of the fluxes in the rest of the sections are much smaller.

3.3. Saltwater intrusions

Throughout the meteorological seasons of the year (Figure 5), higher salinity concentration is always observed in the northern part of the lagoon. It is especially prominent in autumn (Figure 5c), while the lowest concentration is observed in spring (D_{max} in Figure 5a). For the spatial average of the salinity over the whole lagoon area, one can see that during winter it is lower under the ice than it would be if the ice cover would not be present (D_{avg} in Figure 5d and e, respectively). The difference between

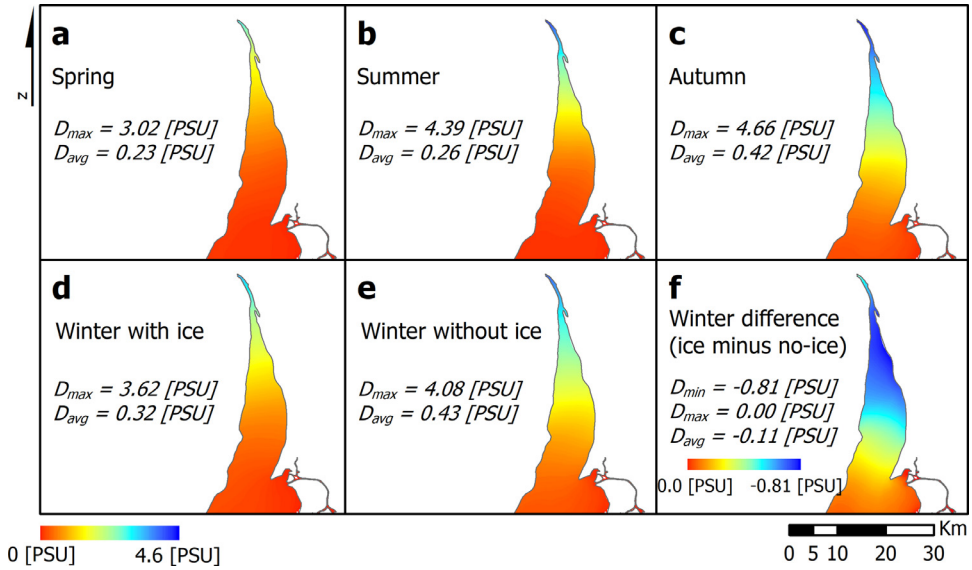

Figure 5 Distribution of salinity in the northern part of the Curonian Lagoon averaged over the whole simulation period of computations with ice data in (a) spring, (b) summer, (c) autumn, and (d) winter seasons, (e) without ice in winter, and the salinity difference of the winter simulations (ice minus no-ice, f). The numbers indicate the maximum (D_{max}) and average (D_{avg}) value of the salinity over the total lagoon area.

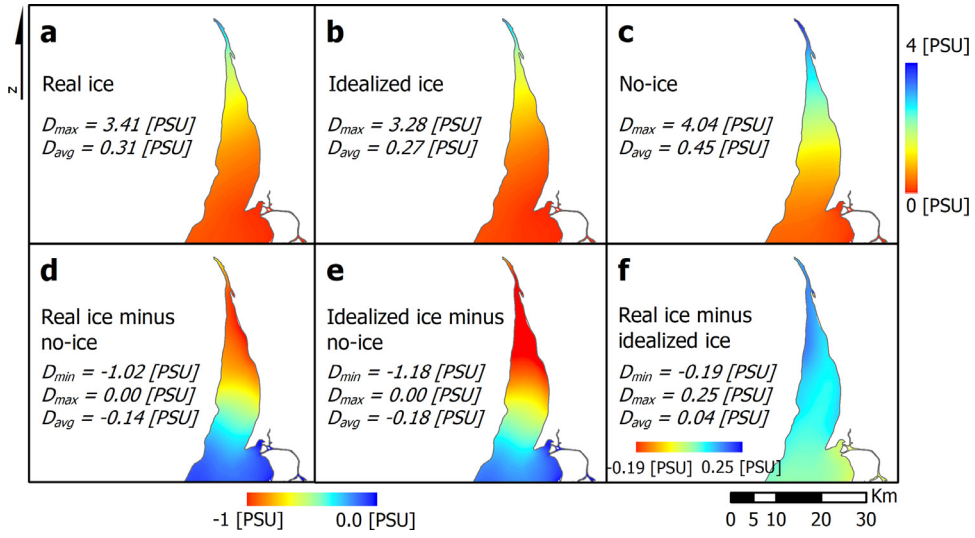

Figure 6 Salinity averaged over ice cover season in simulation with (a) real ice cover, (b) idealized ice cover, and (c) no-ice season set-up, as well as the difference between the simulations: (d) real ice cover minus no-ice, (e) idealized ice cover minus no-ice, and (f) real minus idealized ice cover. The numbers indicate the minimum (D_{min}), maximum (D_{max}), and average (D_{avg}) of salinity over the total lagoon area.

simulations considering ice and no-ice (ice minus no-ice) is negligible in the southern part of the lagoon, but in the north the salinity can be lower by up to 0.81 PSU under the ice cover (Figure 5f) than it would have been if the ice had not been present during the winter season.

The duration of the ice covering the northern part of the lagoon does not have a high impact on salinity when comparing the real and idealized ice seasons (Figure 6a, b, and f). The spatially averaged salinity of the differences between simulations with real ice cover and without it (real ice minus no-ice, Figure 6d) shows that during the real ice cover season salinity can decrease by up to 1.02 PSU, which is higher than the value averaged over the winter season (Figure 5f). During the idealized ice-cover season (Figure 6e), when the lagoon is completely shut off from the atmosphere by ice, salinity under the ice can decrease by up to 1.18 PSU, compared to a situation where ice cover is not present. It is the highest difference compared with values averaged over winter and real and idealized ice cover season, indicating that the presence of the ice and the duration of its full cover

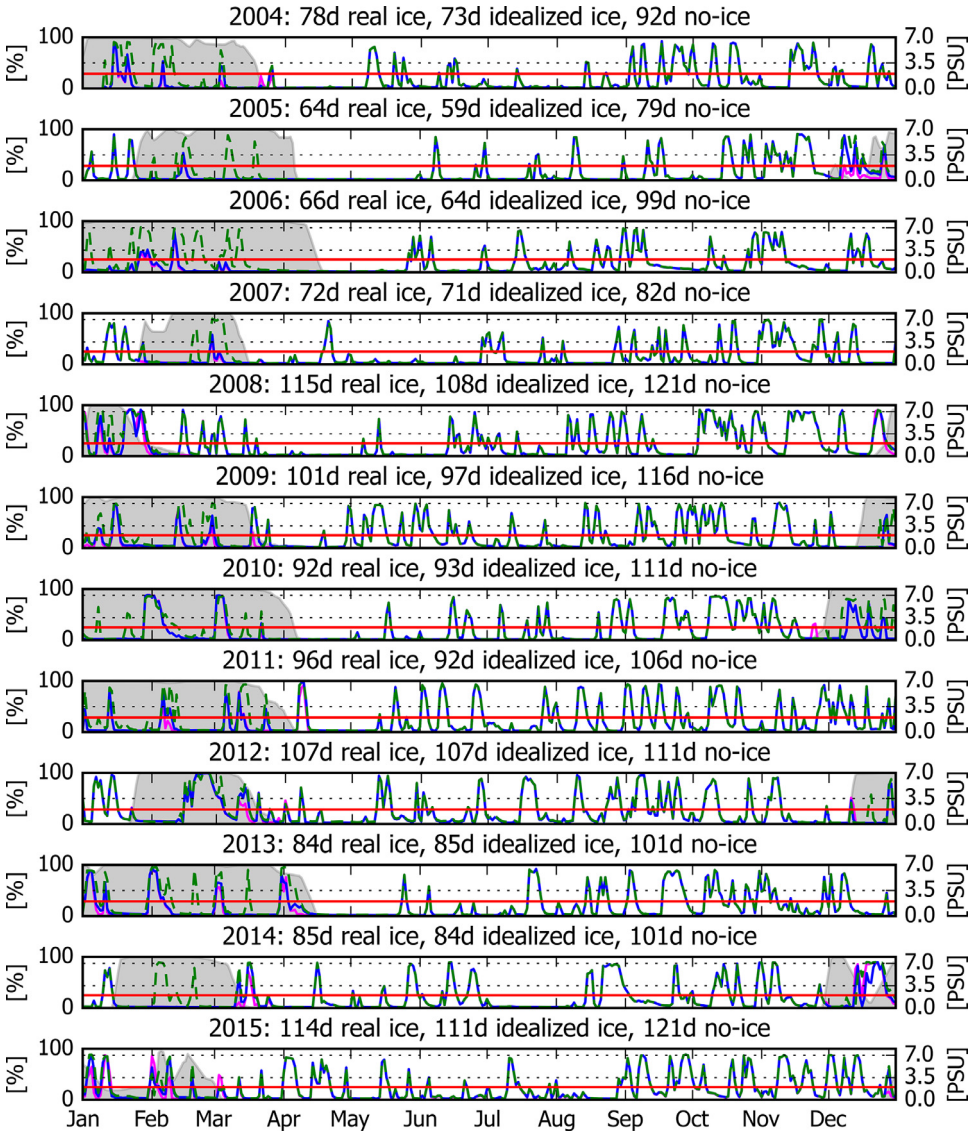

Figure 7 Vertically averaged salinity time series in Juodkrantė. Graph title indicates the year of plotted values, as well as the number of days when the salinity exceeds the threshold of 2 PSU (red solid line) when computations are done using real (real ice, blue solid line) and idealized (idealized ice, magenta solid line) ice cover data, as well as without ice (no-ice, dashed green line). Grey areas show the percentage of ice covering the lagoon, the duration of every ice cover season can be seen in Figure 8.

decreases the intensity of saline water intrusions from the Baltic Sea through the Klaipėda Strait further into the Curonian Lagoon.

The difference of salinity between the bottom and top layers of the water column in the Klaipėda Strait area (green point in Figure 1) shows a high variability throughout the years. In Table 1, the number of hours when this difference exceeds 1 PSU and 3 PSU are shown. The average number of hours is seen to be much higher when the salinity difference exceeds 1 PSU threshold in simulation with ice cover.

In Juodkrantė salinity surpasses the 2 PSU threshold nearly 90 days on average per year when the ice cover is switched-on in the model (Figure 7), this is 13.9 days less on average than in the model results of the simulation without the ice, and the difference between idealized ice cover season and no-ice simulation results is 16.3 days, clearly denoting that the highest impact is observed when the lagoon is fully covered by ice. In Klaipėda Strait salinity is exceeding the 2 PSU threshold on average for 237 days per year, when real ice cover data is used in the model, which is 10.5 days less than the records of model computations without ice. Further in the lagoon, in Nida and Ventė, differences are much lower – less than 1 and 3 days per year, respectively.

3.4. Water residence time

The average WRT values for the specified areas (north, south, and whole lagoon domain) are shown in Table 2. These values indicate that in the northern part of the lagoon the WRT is around 55 days, and in the southern – 150 days, considering the real ice cover conditions (WRT_{ice}^{real}), which are very similar to the ones averaged over the meteorological winter season (WRT_{winter}^{real}). The difference

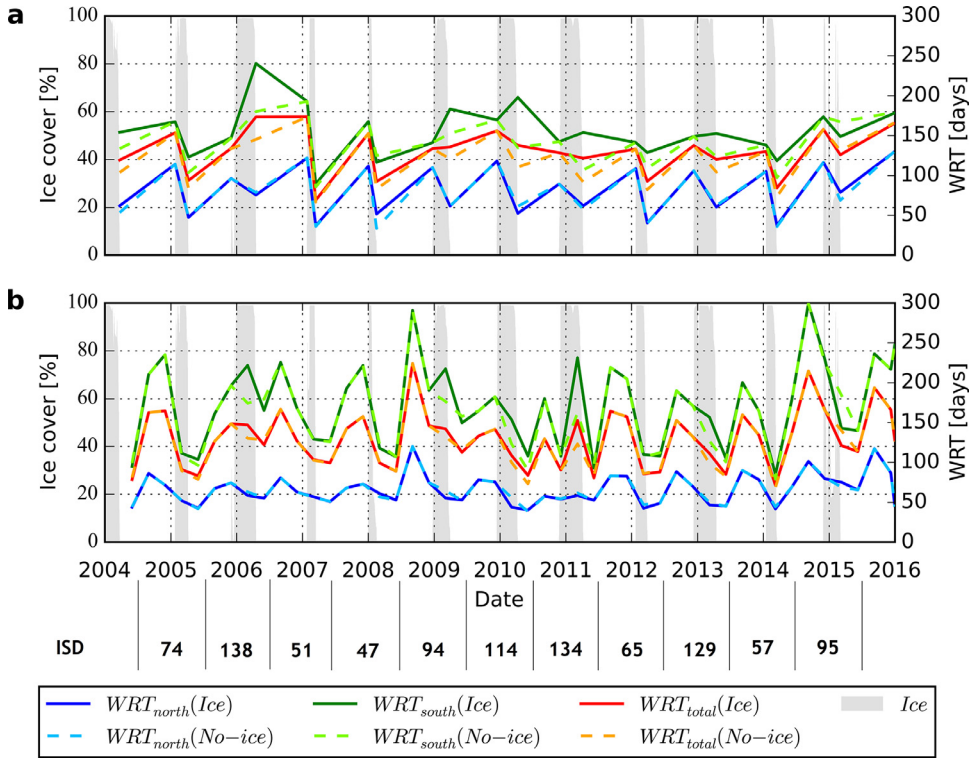

Figure 8 Water residence time in the northern (WRT_{north}), southern (WRT_{south}) parts, and in the whole lagoon area (WRT_{total}) computed with and without the real ice cover: (a) for the ice-free period of the year and the real ice-cover season, (b) seasonally every 3 months. Grey columns indicate ice cover percentage over the lagoon. At the bottom of the graph, the ice season duration (ISD) in days is shown. Please note that in panel (a) only two values per year were available due to the way the WRT was computed. In figure b four values per year were computed.

Table 1 The number of hours per year when salinity difference between bottom and top layers of the water column in the Klaipėda Strait exceeds the threshold of 1 and 3 PSU in simulations with ice and without ice.

Year	Number of hours with salinity [PSU] above threshold			
	>1 with ice	>1 without ice	>3 with ice	>3 without ice
2005	170	138	24	15
2006	190	107	20	12
2007	135	134	18	18
2008	116	114	8	7
2009	112	122	17	27
2010	156	119	12	7
2011	42	32	1	1
2012	75	90	0	12
2013	85	83	9	11
2014	202	172	15	22
2015	149	145	33	27
Mean	**130**	**114**	**14**	**14**

between WRT values in the simulations with and without real ice cover (WRT^{real}_{winter} and WRT^{no-ice}_{ice}) is around 1.5 days in the northern part and around 24 days in the southern part. Results of simulation with the idealized ice cover (WRT^{ideal}_{ice}) show that in the southern part of the lagoon the WRT increases by around 40 and 63 days compared with WRT^{ideal}_{ice} and WRT^{no-ice}_{ice}, respectively. However, in the northern part of the lagoon WRT^{ideal}_{ice} is lower.

The differences of the results averaged over the meteorological winter season (WRT^{real}_{winter} and WRT^{no-ice}_{winter}) are slightly higher in the northern part, due to the variability of the ice season duration (ISD) in this area, and the difference in the southern part is slightly smaller, compared to WRT^{real}_{ice} and WRT^{no-ice}_{ice}.

ISD and different WRT computation periods show a high correlation (from 0.71 to 0.84), denoting a significant ice cover effect on water residence time. However, when considering water residence during the meteorological winter season (WRT^{real}_{winter}), there is no correlation with ISD in the northern part of the lagoon, as mentioned, due to the fact that the ice is more dynamic in this area during the winter season.

The 11-year average water residence time in the Curonian Lagoon (averaged over all meteorological seasons, WRT^{real}_{season}) is around 130 days when the ice cover is switched on in the model, which is a ~1.5 days longer compared to the theoretical period without ice (WRT^{no-ice}_{season}). Higher WRT values can be found in the southern part of the lagoon. In the north, the difference between ice and no-ice simulations is rather small.

The variability of the WRT computation periods can be seen in Figure 8, where the difference between simulation

Table 2 Averaged water residence time (WRT) computed for the northern (WRT_{north}), southern (WRT_{south}) parts and for the total (WRT_{total}) lagoon area as well as correlation between the ice season duration (ISD) and WRT during the ice cover and winter seasons computed in simulations with real ice cover. Subscript indicates different WRT computation periods (ice – ice cover season, winter – December, January, February, and season – every meteorological season), superscript indicates the model set-up type (real – satellite ice cover data, ideal – idealized ice cover data, no-ice – without ice), all described in Section 2.4.

Simulation	WRT_{north} [days]	WRT_{south} [days]	WRT_{total} [days]
WRT_{ice}^{real}	55.48±13.72	150.54±41.10	113.79±28.68
WRT_{ice}^{ideal}	50.01±13.16	190.10±97.92	124.22±43.85
WRT_{ice}^{no-ice}	53.09±14.53	126.52±28.79	99.67±23.97
WRT_{ice}^{real} *correlation with ISD:*	*0.71*	*0.79*	*0.84*
WRT_{winter}^{real}	53.81±9.94	152.47±50.16	112.15±26.33
WRT_{winter}^{no-ice}	56.44±7.60	135.62±33.91	106.43±22.20
WRT_{winter}^{real} *correlation with ISD:*	*0.09*	*0.79*	*0.75*
WRT_{season}^{real}	66.66±18.93	170.53±52.67	129.96±36.09
WRT_{season}^{no-ice}	67.24±18.39	166.60±52.07	128.58±36.49

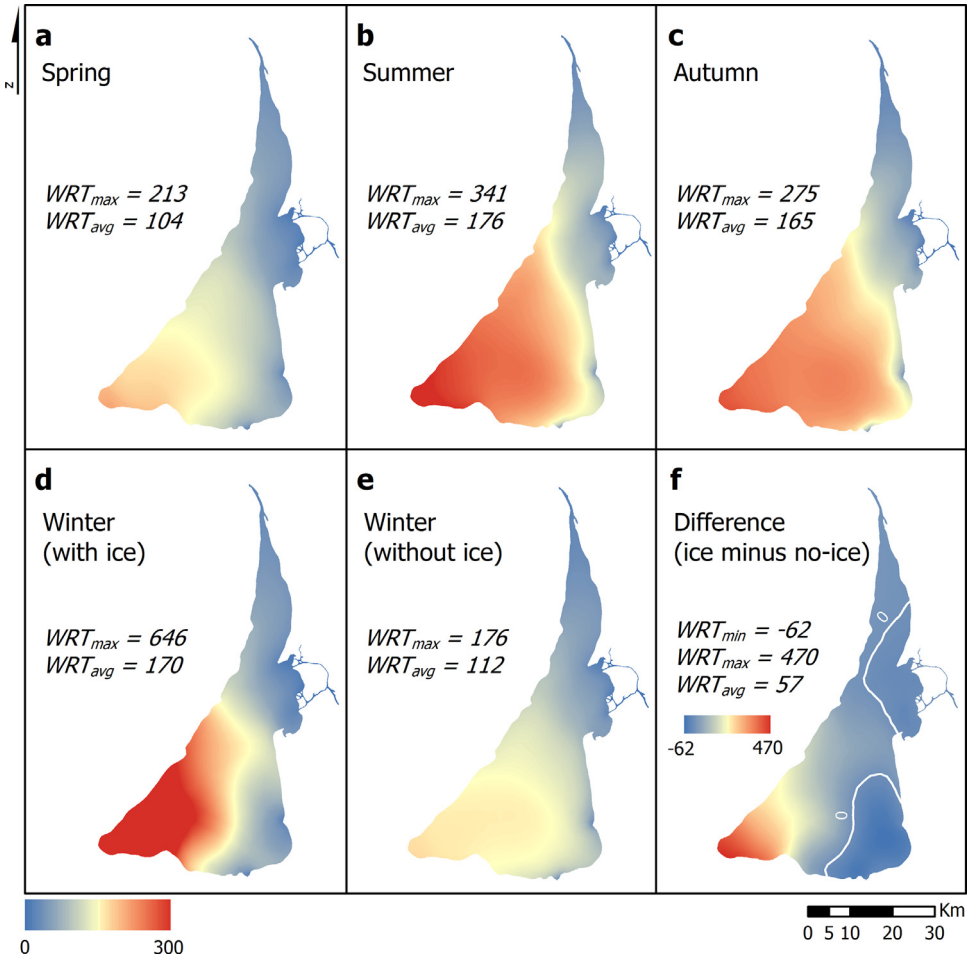

Figure 9 Seasonal water residence time maps (in days) averaged over the whole simulation period of computations with ice data (*WRTseason real*) in (a) spring, (b) summer, (c) autumn, (d) winter, and (e) without ice in winter, as well as the difference of winter simulations (ice minus no-ice, f). Contour lines in the difference map indicate the zero value (no difference) and numbers indicate the maximum (WRT_{max}) and average (WRT_{avg}) water residence time.

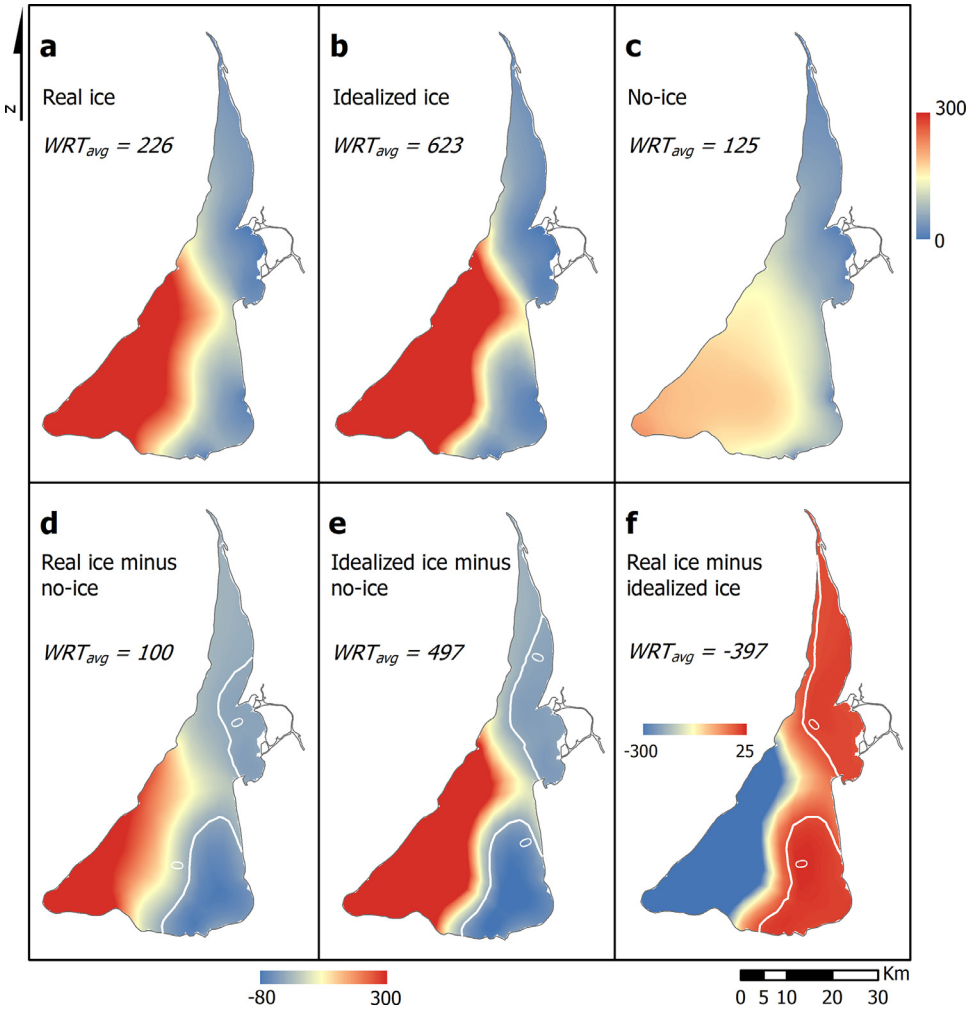

Figure 10 Water residence time distribution in days averaged over the all ice cover seasons in simulation with (a) real ice cover, (b) idealized ice cover, and (c) no-ice season set-up, as well as the difference between the simulations: (d) real ice cover minus no-ice, (e) idealized ice cover minus no-ice, and (f) real minus idealized ice cover. Contour lines indicate the zero value (no difference). The numbers indicate the spatial average (WRT_{avg}) of water residence time.

with and without ice is higher after the long and severe winters, e.g., in 2006, 2009, 2010, 2011 and 2013, when the ice season duration was the longest over the analyzed period (on average 122 days). Again, the higher difference is visible in the southern part of the lagoon, where the ice cover is less dynamic compared to the northern part.

The water residence time throughout the seasons of the year is displayed in Figure 9 (a–d). The values slightly differ throughout the ice-free season, being highest in summer, when the wind and water inflow from the rivers decrease. However, the same overall pattern is observed – high WRT values in the southern part of the lagoon and especially in the southwestern corner. During winter (Figure 9d) in the model runs with real ice the water residence time values are observed to be much higher in the southwestern corner of the lagoon (Figure 9f) than in the reference simulation without ice (Figure 9e), which is much more similar to the spring WRT distribution (Figure 9a). The residence time of nearly 2 years during the winter season means that if the ice conditions had been prolonged to two years, then the water circulation in 2 years would have renewed only 1/e of the initial concentration.

The simulation results of idealized ice cover (Figure 10b) show that the prolonged full ice cover has a much higher impact on the WRT in the southwestern corner of the lagoon compared with the simulation with real ice cover data (Figure 10a). In this area, there are no inflowing rivers, and therefore there are no additional sources of fresh water. Overall, ice affects WRT over the majority of the lagoon area. In the southeastern corner and in Nemunas Delta, where the main river outlets are situated, simulation without ice (Figure 10d and e) shows higher values, meaning that under the ice water is renewing faster than it would be if ice were not present. This difference in the northern part stretches further along the eastern shoreline compared to the no-ice simulations with the idealized ice cover (Figure 10e) than compared to the simulation with the real ice cover (Figure 10d).

4. Discussion and conclusions

The most important drivers of the hydrodynamic processes, when no ice is covering the Curonian Lagoon, is a combination of wind force and Nemunas discharge. However, when ice is present, only the Nemunas River discharge is primarily responsible for accelerating the water masses. Throughout the seasons of the year, we can observe different circulation patterns in the lagoon. In spring, a two-gyre system is observed in the southern part of the lagoon, of which one of them during summer shifts further to the center of the lagoon and another system is observed to form in Nemunas Delta, however, with much lower current speed. The increased wind conditions in autumn force one additional gyre to form near the delta area. However, the highest number of gyre systems are observed during the winter period, when the water surface is sheltered by the ice cover from the wind forcing. The rotation of the gyre systems in and near the Nemunas Delta (along the southeastern shoreline) is anticlockwise, the gyre in the central part of the lagoon is clockwise, and in the southwestern part of the lagoon it is anticlockwise. During the winter season, another clockwise gyre in the south can be observed. These results do not precisely match with the previous study of Umgiesser et al. (2016), because of the ice cover data used, which previously was interpolated from four ground observation stations and available for only for 4 years. In our study, we have used ice data from satellite images, which covered the whole 11-year simulation period.

The comparison of circulation during the real and idealized ice cover seasons reveals that the prolonged full ice cover can diminish the development of gyres in the lagoon. Ice does not only alter the structure of the circulation of the water masses, but also the speed of the currents. When ice cover decomposes and refreezes several times throughout the winter season, it leads to slightly higher current speeds, due to the wind-stress on the ice-free water surface. In the Klaipėda Strait area and approximately 5 km southward from it, the current speed is always higher compared to the rest of the lagoon, however, if this area is fully covered by ice for longer, then this difference slightly decreases.

Since the circulation decreases under the ice cover, there is less exchange between different parts of the lagoon. Therefore, all the water fluxes through the specified four cross-sections are affected by the presence of the ice cover. However, there is a lower impact observed in the northern part of the lagoon contrary to the southern part. It is noticeable that, in the northern part, the fluxes stay nearly the same, just wind is making them fluctuate. In the Klaipėda Strait area, the exchanges are mainly driven by water level fluctuations in the Baltic Sea and are much less wind-driven. However, the situation in the cross-section of Nemunas Delta and along Lithuanian-Russian border is different. Water exits the Nemunas Delta more steadily, without cycling between the delta and the lagoon and less water is diverted to the south, because, during the ice cover season, wind-driven circulation is inhibited and the prolonged full ice cover has the biggest impact on fluxes through the Lithuanian-Russian border.

In the southern part of the lagoon, salinity is small and negligible throughout the year. In the northern part, the concentration is higher, but highly depending on the season. The lowest salinity concentration is observed during spring and the highest during the autumn season when the westerly winds increase allowing for the Baltic Sea water to inflow into the Curonian Lagoon. During the period when ice is covering the lagoon, salinity decreases by up to around 1 PSU. Overall, the highest differences between the results of simulations with ice and without it are observed in the northern part of the lagoon where salinity decreases during the ice cover season, reducing the saltwater intrusion events. For instance, in Juodkrantė (approximately 20 km southward from Klaipėda Strait) saltwater intrusions (overpassing 2 PSU threshold) can be found on average around 90 days per year, which is on average nearly 14 days less when the ice cover was not considered in the model simulations. The simulation results of idealized ice cover show that this difference is even higher – 16.3 days. Thus, we can conclude that when there is ice, it markedly decreases the frequency of saltwater intrusions into the Curonian Lagoon.

The water column is uniform, however, in Klaipėda Strait a slight salt concentration increase is observed in the bottom layers. The difference of bottom and top layers of the water column can exceed the 1 PSU threshold for 130 hours per year on average, which is 16 hours more than it would be if the ice would not be covering the lagoon. Zemlys et al. (2013) have already shown that in the Klaipėda Strait area strong salinity gradients create conditions for three types of water flow: one-directional freshwater outflow to the Baltic Sea, one-directional saline water inflow into the Curonian Lagoon, and two-directional flow with a lagoon water outflow in the surface layers and saline water intrusion in the bottom. However, in their study ice cover was not taken into account, Umgiesser et al. (2016) later did this, showing the more accurate results for salinity validation; yet, they concluded that a high-resolution model used in Zemlys et al. (2013) does a better job in describing salinity variations, even if the ice cover is not included. Since in our study we wanted to present the long-term analysis of model simulation results, we also used a coarser resolution model grid, thus in the future, for a fully updated analysis of salinity variations in the Klaipėda Strait area, including the ice cover data in the model computations, a finer grid should be used.

Ice cover and its duration likewise affect the water residence time (WRT) in the Curonian Lagoon. When ice is present, it takes longer for the water to be renewed. This is especially evident after the long ice cover seasons (e.g., in 2006, 2009, 2010, 2011, and 2013) in the southern part of the lagoon. WRT computations during the ice cover season (WRT_{ice}^{real}), show a high correlation with ice season duration (from 0.71 to 0.84), however, when computing it only during the winter season (WRT_{winter}^{real}) there is no correlation in the northern part of the lagoon. This is due to the fact that the ice season duration in this area is shorter than in the southern part and the computation of WRT during the winter season is limited to only three months (Dec, Jan, Feb), while ice can be observed to start forming, often only in the middle of January and can last much longer than February.

The increased WRT under the ice is true for analyzing water residence in the whole area of the Curonian Lagoon (north, south, and the whole domain) for the real ice cover conditions (WRT_{ice}^{real}). However, computations for the meteorological winter season (WRT_{winter}^{real}) show that it is not the same in the northern part of the lagoon, where simulation results with no ice cover show longer WRT than simulation results with ice. However, the difference is quite small (just 4%), and probably does not exceed the uncertainty of the evaluation of WRT by the model. Comparing the real and idealized ice cover simulation results shows that prolonged full ice cover can lead to an increase of WRT in the southern part of the lagoon. However, in the north, it decreases due to the cutting-off the exchanges between the northern and southern part. Therefore, more water from the Nemunas River stays in the north and does not mix with water in the southern areas. This mechanism contributes to a decrease of WRTs in the northern part.

Our computed WRT values slightly differ from those described in Umgiesser et al. (2016), supposedly as a result of satellite ice cover data used in the model representing more realistic ice distribution with respect to the data interpolated from the observations from coastal stations. The melt-off occurrences during the ice cover season observed in satellite images have a small, but noticeable impact on the WRT by slightly increasing it in the norther part, and decreasing the WRT in the southern part compared to the previous study results with ice.

WRT throughout the seasons is varying. During the ice-free period, the longest time required for water to renew is in summer, due to the decreased wind speed and river water input. The pattern in summer and spring are similar, with the highest WRT being in the southern part of the lagoon. During the winter period, the WRT increases much more in the southwestern corner of the lagoon, which is far away from the rivers inflowing the lagoon, hence the water renewal is very slow. The model results with the idealized ice cover (lagoon fully covered by ice during the entire ice cover season) show that it has a much higher impact to the WRT in the southwestern part of the lagoon. Water near the river outlets — in the southeastern corner of the lagoon and in Nemunas Delta, tends to renew faster under the ice cover and the prolonged full ice cover in the northern part stretches this area further along the eastern shoreline. If ice would not be present during the ice cover season, then the WRT distribution would be much more similar to the situation during the spring.

To conclude, with this study we show how the ice data derived from satellite observations improve the representation of the real conditions of the circulation, saltwater intrusions, and water residence time in the Curonian Lagoon. Currently, an ice model is still not yet integrated in the modelling system SHYFEM, which will be done and will be presented in future publications.

References

Ambrosetti, W., Barbanti, L., Sala, N., 2003. Residence time and physical processes in lakes. J. Limnol. 62, 1—15.

Baušys, J., 1978. Ledo Režimas. In: Rainys, A. (Ed.), Kuršių Marios II. Mokslas, Vilnius, Lithuania, 34—49.

Bellafiore, D., Umgiesser, G., 2010. Hydrodynamic coastal processes in the North Adriatic investigated with a 3D finite element model. Ocean Dyn. 60, 255—273, https://doi.org/10.1007/s10236-009-0254-x.

Bengtsson, L., 2012. Ice Covered Lakes. In: Bengtsson, L., Herschy, R.W., Fairbridge, R.W. (Eds.), Encyclopedia of Lakes and Reservoirs. Springer, Netherlands, Dordrecht, 357—360.

Bengtsson, L., 1996. Mixing in ice-covered lakes. Hydrobiologia 322, 91—97, https://doi.org/10.1007/BF00031811.

Cañedo-Argüelles, M., Kefford, B., Schäfer, R., 2019. Salt in freshwaters: Causes, effects and prospects - Introduction to the theme issue. Philos. Trans. R. Soc. B Biol. Sci. 374, art. no. 20180002, 6 pp., https://doi.org/10.1098/rstb.2018.0002.

Carrasco, A.R., Ferreira, O., Roelvink, D., 2016. Coastal lagoons and rising sea level: A review. Earth-Science Rev. 154, 356—368, https://doi.org/10.1016/j.earscirev.2015.11.007.

Cushman-Roisin, B., 2019. Environmental Fluid Mechanics. John Wiley & Sons Ltd, New York, 406 pp.

Dailidiene, I., 2007. Hidroklimatinių sąlygų kaitos ypatumai Baltijos jūros Lietuvos priekrantėje ir Kuršių mariose. Klaipėda University.

Dailidiene, I., Davuliene, L., 2008. Salinity trend and variation in the Baltic Sea near the Lithuanian coast and in the Curonian Lagoon in 1984-2005. J. Marine Syst. 74, 20—29, https://doi.org/10.1016/j.jmarsys.2008.01.014.

De Pascalis, F., Pérez-Ruzafa, A., Gilabert, J., Marcos, C., Umgiesser, G., 2011. Climate change response of the Mar Menor coastal lagoon (Spain) using a hydrodynamic finite element model. Estuar. Coast. Shelf Sci. 114, 118—129, https://doi.org/10.1016/j.ecss.2011.12.002.

Ertürk, A., Razinkovas, A., Zemlys, P., Pilkaitytė, R., Gasiunaitė, Z., 2015. Linking NPZD and Foodweb Models of an Estuarine Lagoon Ecosystem. Comput. Sci. Tech. 3, 350—412, https://doi.org/10.15181/csat.v3i1.1093.

Ferrarin, C., Cucco, A., Umgiesser, G., Bellafiore, D., Amos, C.L., 2010a. Modelling fluxes of water and sediment between Venice Lagoon and the sea. Cont. Shelf Res. 30, 904—914, https://doi.org/10.1016/j.csr.2009.08.014.

Ferrarin, C., Maicu, F., Umgiesser, G., 2017. The effect of lagoons on Adriatic Sea tidal dynamics. Ocean Model. 119, 57—71, https://doi.org/10.1016/j.ocemod.2017.09.009.

Ferrarin, C., Razinkovas, A., Gulbinskas, S., Umgiesser, G., Bliudžiute, L., 2008. Hydraulic regime-based zonation scheme of the Curonian Lagoon. Hydrobiologia 611, 133—146, https://doi.org/10.1007/s10750-008-9454-5.

Ferrarin, C., Umgiesser, G., Bajo, M., Bellafiore, D., De Pascalis, F., Ghezzo, M., Mattassi, G., Scroccaro, I., 2010b. Hydraulic zonation of the lagoons of Marano and Grado, Italy. A modelling approach. Estuar. Coast. Shelf Sci. 87, 561—572, https://doi.org/10.1016/j.ecss.2010.02.012.

Ferrarin, C., Zaggia, L., Paschini, E., Scirocco, T., Lorenzetti, G., Bajo, M., Penna, P., Francavilla, M., D'Adamo, R., Guerzoni, S., 2013. Hydrological Regime and Renewal Capacity of the Microtidal Lesina Lagoon. Estuar. Coast. 37, 79—93, https://doi.org/10.1007/s12237-013-9660-x.

Gasiūnaitė, Z.R., Daunys, D., Olenin, S., Razinkovas, A., 2008. The Curonian Lagoon. In: Schiewer, U. (Ed.), Ecology of Baltic Coastal Waters. Springer, Berlin/Heidelberg, 197—215.

Hampton, S.E., Galloway, A.W.E., Powers, S.M., Ozersky, T., Woo, K.H., Batt, R.D., Labou, S.G., O'Reilly, C.M., Sharma, S., Lottig, N.R., Stanley, E.H., North, R.L., Stockwell, J.D., Adrian, R., Weyhenmeyer, G.A., Arvola, L., Baulch, H.M., Bertani, I., Bowman, L.L., Carey, C.C., Catalan, J., Colom-Montero, W., Domine, L.M., Felip, M., Granados, I., Gries, C., Grossart, H.P., Haberman, J., Haldna, M., Hayden, B., Higgins, S.N., Jolley, J.C., Kahilainen, K.K., Kaup, E., Kehoe, M.J., MacIntyre, S., Mackay, A.W., Mariash, H.L., McKay, R.M., Nixdorf, B., Nõges, P., Nõges, T., Palmer, M., Pierson, D.C.,

Post, D.M., Pruett, M.J., Rautio, M., Read, J.S., Roberts, S.L., Rücker, J., Sadro, S., Silow, E.A., Smith, D.E., Sterner, R.W., Swann, G.E.A., Timofeyev, M.A., Toro, M., Twiss, M.R., Vogt, R.J., Watson, S.B., Whiteford, E.J., Xenopoulos, M.A., 2017. Ecology under lake ice. Ecol. Lett. 20, 98—111, https://doi.org/10.1111/ele.12699.

Idzelytė, R., Kozlov, I.E., Umgiesser, G., 2019. Remote Sensing of Ice Phenology and Dynamics of Europe's Largest Coastal Lagoon (The Curonian Lagoon). Remote Sens 11 (17), art. no. 2059, 27 pp., https://doi.org/10.3390/rs11172059.

Jakimavičius, D., 2012. Changes of water balance elements of the Curonian Lagoon and their forecast due to anthropogenic and natural factors. Kaunas University of Technology.

Jakimavičius, D., Kriaučiūnienė, J., Šarauskienė, D., 2018. Impact of climate change on the Curonian Lagoon water balance components, salinity and water temperature in the 21st century. Oceanologia 60 (3), 378—389, https://doi.org/10.1016/j.oceano.2018.02.003.

Jakimavičius, D., Šarauskienė, D., Kriaučiūnienė, J., 2019. Influence of climate change on the ice conditions of the Curonian Lagoon. Oceanologia 62 (2), 164—172, https://doi.org/10.1016/J.OCEANO.2019.10.003.

Janković, V., Schultz, D.M., 2017. Atmosfear: Communicating the effects of climate change on extreme weather. Weather. Clim. Soc. 9, 27—37, https://doi.org/10.1175/WCAS-D-16-0030.1.

Jarmalavičius, D., 2007. Jūrinis krantas. In: Bukantis, A., Šinkūnas, P., Taločkaitė, E. (Eds.), Klimato Kaita: Prisitaikymas Prie Jos Poveikio Lietuvos Pajūryje. Vilniaus Universiteto Leidykla, Vilnius, 25—31.

Maicu, F., De Pascalis, F., Ferrarin, C., Umgiesser, G., 2018. Hydrodynamics of the Po River-Delta-Sea System. J. Geophys. Res. 123, 6349—6372, https://doi.org/10.1029/2017JC013601.

Mėžinė, J., Ferrarin, C., Vaičiūtė, D., Idzelytė, R., Zemlys, P., Umgiesser, G., 2019. Sediment Transport Mechanisms in a Lagoon with High River Discharge and Sediment Loading. Water 11 (10), art. no. 1970, 24 pp., https://doi.org/10.3390/w11101970.

Molinaroli, E., Sarretta, A., Ferrarin, C., Masiero, E., Specchiulli, A., Guerzoni, S., 2014. Sediment grain size and hydrodynamics in Mediterranean coastal lagoons: Integrated classification of abiotic parameters. J. Earth Syst. Sci. 123, 1097—1114, https://doi.org/10.1007/s12040-014-0445-9.

Müller, S., Jessen, S., Duque, C., Sebök, E., Neilson, B., Engesgaard, P., 2018. Assessing seasonal flow dynamics at a lagoon saltwater—freshwater interface using a dual tracer approach. J. Hydrol. Reg. Stud. 17, 24—35, https://doi.org/10.1016/j.ejrh.2018.03.005.

Nguyen, T.D., Hawley, N., Phanikumar, M.S., 2017. Ice cover, winter circulation, and exchange in Saginaw Bay and Lake Huron. Limnol. Oceanogr. 62, 376—393, https://doi.org/10.1002/lno.10431.

Twiss, M.R., Smith, D.E., Cafferty, E.M., Carrick, H.J., 2014. Phytoplankton growth dynamics in offshore Lake Erie during midwinter. J. Great Lakes Res. 40, 449—454, https://doi.org/10.1016/j.jglr.2014.03.010.

Umgiesser, G., Canu, D.M., Cucco, A., Solidoro, C., 2004. A finite element model for the Venice Lagoon. Development, set up, calibration and validation. J. Marine Syst. 51, 123—145, https://doi.org/10.1016/j.jmarsys.2004.05.009.

Umgiesser, G., Zemlys, P., Erturk, A., Razinkovas-Baziukas, A., Mezine, J., Ferrarin, C., 2016. Seasonal renewal time variability in the Curonian Lagoon caused by atmospheric and hydrographical forcing. Ocean Sci. 12, 391—402, https://doi.org/10.5194/os-12-391-2016.

Ummenhofer, C.C., Meehl, G.A., 2017. Extreme weather and climate events with ecological relevance: A review. Philos. Trans. R. Soc. B Biol. Sci. 372, https://doi.org/10.1098/rstb.2016.0135.

Vincent, W.F., 2009. Effects of Climate Change on Lakes. In: Encyclopedia of Inland Waters. Acad. Press, Elsevier, 55—60.

Wang, J., Haoguo, H., Schwab, D., Leshkevich, G., Beletsky, D., Hawley, N., Clites, A., 2010. Development of the Great Lakes Ice-circulation Model (GLIM): Application to Lake Erie in 2003—2004. J. Great Lakes Res. 36, 425—436, https://doi.org/10.1016/j.jglr.2010.04.002.

Wolanski, E., Day, J.W., Elliott, M., Ramesh, R., 2019. Coasts and Estuaries. Elsevier, Amsterdam, 726 pp.

Wotton, R.S., 1995. Temperature, Organic Matter and the Sustainability of Aquatic Systems. Freshw. Forum 5, 39—47.

Yuan, R., Zhu, J., 2015. The Effects of Dredging on Tidal Range and Saltwater Intrusion in the Pearl River Estuary. J. Coast. Res. 316, 1357—1362, https://doi.org/10.2112/jcoastres-d-14-00224.1.

Žaromskis, R., 1996. Oceans, Seas, Estuaries. Debesija. Vilnius, 293 pp., (in Lithuanian).

Zemlys, P., Ertürk, A., Razinkovas, A., 2008. 2D finite element ecological model for the Curonian lagoon. Hydrobiologia 611, 167—179, https://doi.org/10.1007/s10750-008-9452-7.

Zemlys, P., Ferrarin, C., Umgiesser, G., Gulbinskas, S., Bellafiore, D., 2013. Investigation of saline water intrusions into the Curonian Lagoon (Lithuania) and two-layer flow in the Klaipeda Strait using finite element hydrodynamic model. Ocean Sci. 9, 573—584, https://doi.org/10.5194/os-9-573-2013.

Oceanologia (2020) 62, 443—459

Available online at www.sciencedirect.com

ScienceDirect

journal homepage: www.journals.elsevier.com/oceanologia

ORIGINAL RESEARCH ARTICLE

Tidal characteristics in the Gulf of Khambhat, northern Arabian Sea — based on observation and global tidal model data

Aditi Mitra[a,b], **V. Sanil Kumar**[a,*], **Basanta K. Jena**[c]

[a] *Ocean Engineering, CSIR-National Institute of Oceanography (Council of Scientific and Industrial Research), Dona Paula, Goa, India*
[b] *Research Scholar, Bharathidasan University, Tiruchirappalli,Tamil Nadu, India*
[c] *Coastal and Environmental Engineering Division, National Institute of Ocean Technology, Pallikaranai, Chennai, India*

Received 4 September 2019; accepted 28 May 2020
Available online 7 June 2020

KEYWORDS
Gulf of Khambhat;
Semi-enclosed basins;
Tidal constituents;
Tidal propagation;
Sea-level

Summary Tidal characteristics of the Gulf of Khambhat are described based on measured and modelled sea-level data. Data were recorded at three locations inside and two locations outside the Gulf with record lengths of 6—12 months to study the tidal propagation. A northward increase in tidal amplitude is noticed from Daman (eastern side) and Diu (western side) and attains maxima at Bhavnagar. A similar trend is followed by the amplitude of the major tidal constituents, although there are discrepancies for that of the minor constituents. The non-tidal factor which influences the sea-level is the local wind, especially the alongshore component of wind. A positive correlation is obtained between the sea-level and the meridional component of wind at each location. Harmonic analysis of sea-level data shows that M2 is the major tidal constituent which propagates in a non-linear fashion inside the Gulf. Tides from two global tide models (MIKE21 and FES2014) have been compared with the measured data, which could be used for further prediction of the tides and sediment transport in the Gulf. The tide elevation derived from the MIKE21 model has further been used for the harmonic analysis of tide. The tides predicted using one-month data are up to 10% smaller than those predicted using the one-year data. The global tide model FES2014 data performs well with measured data for offshore

* Corresponding author at: Ocean Engineering, CSIR-National Institute of Oceanography (Council of Scientific and Industrial Research), Dona Paula, Goa-403 004, India. Tel.: +91 832 2450 327.
E-mail address: sanil@nio.org (V.S. Kumar).
Peer review under the responsibility of the Institute of Oceanology of the Polish Academy of Sciences.

Production and hosting by Elsevier

https://doi.org/10.1016/j.oceano.2020.05.002

locations, whereas it fails to predict the same for the inner Gulf locations. The study manifests the fact that to understand the dynamics of complex tidal areas, regional models should better be used than global tidal models.

1. Introduction

Information on tides along a coastline is vital for estimating the top level of the coastal protection structures and port structures. Ocean tides have long been thought of as a stationary process as they are driven by the gravitational forcing of Sun and Moon, whose motions are complex but highly predictable (Cartwright and Taylor, 1971). Tidal propagations in estuaries are affected by freshwater discharge and friction (Dronkers, 1964), besides changes in depths and the morphology of the channel (Carl and Aubrey, 1994; Dronkers, 1964; Godin, 1993; Lanzoni and Seminara, 1998; Shetye and Gouveia, 1998), which implies variations in the mean water level and asymmetry of the tidal wave. Tidal asymmetry in a shallow-water system could be explained through the generation of overtides and compound tides (Dronkers, 1964; Pugh, 1987). The shallow water tides contribute to differences between Mean Tide Level and Mean Sea-Level (MSL) (Woodworth, 2017); tides can also exhibit short-term variability correlated to short-term fluctuations in MSL (Devlin et al., 2014; 2017a, b). The astronomical tide is strongly distorted during its propagation from offshore into the shallow inlet/estuarine systems. This distortion could be represented as the non-linear growth of harmonics of the principal ocean astronomical constituents (Aubrey, 1985).

Measured sea-level data comprises contributions from mean sea-level, astronomical tides, vertical land movements, meteorologically and oceanographically induced water level changes and episodic water level fluctuations due to climate extremes, systematic bias and noise. The analysis of correlations between tides and sea-levels at a local or regional scale can indicate locations where tidal evolution should be considered a substantial complement to sea-level rise (Devlin et al., 2019). Removal of the tidal component from the sea-level data leaves residuals of sea-level that include contributions from atmospheric components and surface waves (Kumar et al., 2011). In the estuaries and river mouth, the river discharge also contributes to the residual component. Residual sea-level also results from the friction of the system. The combined influence of the tidal phase, amplitude and spatial gradient in MSL on the generation of the residuals of sea-level in a channel is complex and non-linear and could be predicted properly only by a non-linear numerical model (Liu and Aubrey, 1993). Unnikrishnan et al. (1999) used a barotropic numerical model based on shallow water wave equations to simulate the sea-level and circulation in the Gulf of Khambhat and surrounding areas. Sea-level variations due to surges triggered by storm winds form a noise superimposed on the highly periodic tides, which have an astronomical origin (Sundar et al., 2005). The generation of residuals of sea-level in a tidal channel is the most sensitive to the spatial gradient in MSL, less sensitive to the tidal amplitude difference and least sensitive to the tidal-phase difference. It directly influences material transport, i.e., suspended sediment, pollutants, etc. in a shallow channel. The study based on simultaneously measured sea-level data at three locations covering a distance of 100 km along the west coast of India indicates that the variations in sea-level due to tide is ~96% (Kumar et al., 2011). An understanding of the seasonal cycle of sea-level forms an important component of climate studies. It has some practical implications as well, e.g., the accurate tidal prediction tables for a coastline (Wijeratne et al., 2008).

The Gulf of Khambhat (GoK, hereafter referred to as the Gulf) is one of the highly energetic macro-tidal regimes of the north-eastern Arabian Sea and the other area in the north-eastern Arabian Sea is the Gulf of Kutch (Shetye, 1999). Although there are quality studies carried out in the Gulf from the past two decades or more, the area lags in long-term in situ datasets on hydrodynamic parameters. The previous studies mainly focused on modelled data to obtain the hydrodynamics of the Gulf. The present study utilises measured sea-level data at different locations to discern the tidal propagation in the Gulf. The observed tides have been compared with the data derived from the global tide models (MIKE21 and FES2014) to examine the behaviour of the global model at a regional scale. The study also focuses on ascertaining the major astronomical tidal constituents, which contribute to the tidal amplitude. The present study puts up an effort to determine the tidal and non-tidal components of the sea-level of the Gulf, based on numerical experiments. Even though the amplification inside the Gulf is a well-known phenomenon, a contemporary approach has been adopted in the present study. As the tidal phenomena of the Gulf are more complex than any other coastal waters of India, it is important to assess the global models to reveal their strengths and weaknesses in terms of their performances.

2. Study region

The GoK (formerly known as the Gulf of Cambay) is a funnel-shaped indentation situated between the Saurashtra peninsula and the mainland of Gujarat (Fig. 1). The western continental shelf of India varies from south to north, widens off Mumbai and leads into a strongly converging channel, the GoK. The GoK has a width of 80 km at the mouth and funnels down to 25 km over the longitudinal reach of 140 km. The Gulf has acquired significance because of its geographic proximity to two industrially important states viz. Gujarat and Maharashtra as it provides an easy opening to sea for transportation of materials to several industries around it. The tides in GoK are of a semi-diurnal type with a large diur-

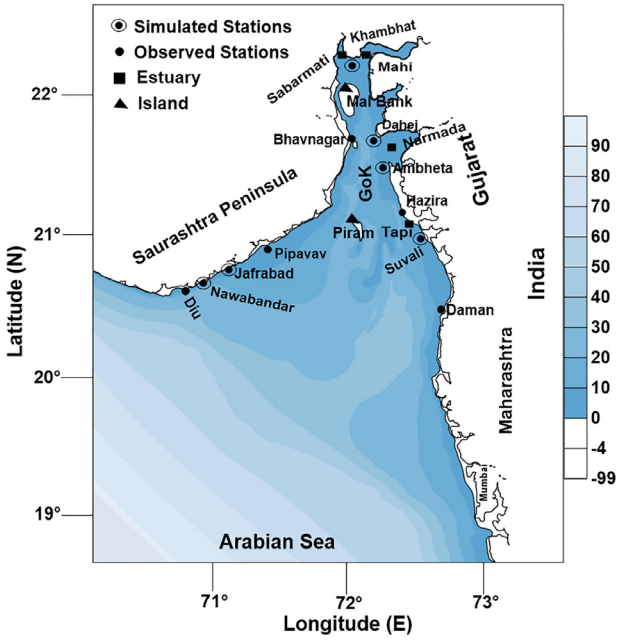

Figure 1 Study area with bathymetry of the region. The sea-level measurement locations are also shown in the figure.

nal inequality and varying amplitudes, which amplifies from the south to north along the GoK in the continental shelf and in the main Gulf (except Gulf head regions). This important characteristic of the embayment results from the quarter wavelength resonance of the tides owing to its inherent geometrical settings (Nayak and Shetye, 2003). In GoK, the tidal front experiences phase-shift due to geometric effects caused by shallow inner regions, narrowing cross-sections and uneven bottom topography. Tide gets amplified significantly inside the Gulf due to its shape and varying bottom friction coefficients (Nayak and Shetye, 2003) and the large width of the continental shelf off the north-western coast of India (Joseph et al., 2009). In the northern Arabian Sea, the maximum tidal range is found in GoK with an average tidal range of 10 m near to Bhavnagar (Kumar et al., 2006). Semi-diurnal tides in the GoK, amplify about threefold from mouth to head; in contrast, the amplification of diurnal tides is much smaller (Nayak and Shetye, 2003). It is reported that currents in the Gulf are predominantly tide-induced with speed up to 3.3 m/s and the currents are north-northwest during flood tide and south-southeast during ebb tide (Kumar and Kumar, 2010).

3. Material and methods

Time-series data of sea-level recorded with tide gauges at three locations inside and two locations outside the Gulf are used in the study. The locations and sampling periods of sea-level and wind-speed are presented in Table 1. Data were missed in a few locations for short periods due to the failure of the instrument. The observed datasets remained discontinuous (wherever used as model inputs) to avoid computational errors due to the missing datasets. The sea-level data is subjected to the standard harmonic analysis by fitting a finite set of cosine functions having frequencies at the known astronomical forcing frequencies by the least square method. Tidal Analysis Software Kit (TASK) (Bell et al., 2000) developed by the Proudman Oceanographic Laboratory, UK, is used for the harmonic analysis and to separate the tidal and residual components from the measured sea-level data. The harmonic analysis is performed using 24 major (Q1, O1, M1, K1, J1, OO1, M2, N2, L2, S2, 2SM2, MU2, MO3, M3, MK3, MN4, M4, MS4, SN4, 2MN6, M6, MSf, 2MS6 and 2SM6) and eight related (PI1, PSI1, P1, PHI1, 2N2, T2, NU2 and K2) tidal constituents in the analysis of six and twelve-monthly records. Based on their amplitude, only major 13 tidal constituents (M2, S2, K1, N2, O1, K2, P1, MU2, M4, MS4, NU2, L2 and MSf) are used in this study. The time and the phase lag reported in the paper is the local time, which is 5 hours 30 minutes ahead of the Greenwich Mean Time (GMT). Residual sea-levels are also estimated for a period of one year in Daman, Hazira and Bhavnagar and for six months in Pipavav and Diu with the help of TASK. Monthly MSL is obtained by calculating the monthly average sea-level for each month at each station. Sea-Level Anomaly (SLA) is determined by the following formula (Eq. 1):

$$SLA = \frac{1}{n}\sum_{i=1}^{n}(T_{e_i} - T_m), \quad (1)$$

where, T_e – tide elevation, T_m – mean tide.

Reanalysis data of meridional and zonal components of wind at 10 m height at 6 hourly intervals from NCEP/NCAR (Kalnay et al., 1996) is obtained for the study area corresponding to the tide gauge record period to know the influence of wind on sea-level. These data are provided by the NOAA-CIRES Climate Diagnostics Centre, Boulder, Colorado, at http://www.cdc.noaa.gov/.

The tides estimated based on the tidal constituents available with the MIKE21 Global Tide Model (DHI, 2017) at six locations covering the Gulf is also used to determine the tidal propagation inside the Gulf. The Global Tide Model is developed by DTU Space (DTU10) and is available on a 0.125 × 0.125-degree resolution grid for the major 10 constituents in the tidal spectra. The model is utilizing the latest 17 years' multi-mission measurements from TOPEX/Poseidon (Phase A and B), Jason-1 (Phase A and B) and Jason-2 satellite altimetry for sea-level residual analysis. Based on these measurements, harmonic constituents have been calculated.

Global Finite Element Solution (FES2014) (Carrere et al., 2015), which is the latest version of the FES series, is utilized to obtain the tide data at the locations where in situ data is recorded. It usually shows higher accuracy in shallow water zones because of finer bathymetry and an optimized assimilation scheme (Seifi et al., 2019). The distances of all the locations referred in the study from the Gulf mouth are presented in Table 2.

4. Results

4.1. Tide elevation

Daman is chosen as a location outside the Gulf mouth in the eastern GoK, where sea-level variation is measured for a period of one year (Fig. 2a). Maximum spring and neap tidal

Table 1 Measurement locations and period of recording of sea-level and wind.

Locations	Latitude/Longitude	Period of recording	Highest sea level measured (m)	Mean sea level from measured data (m)	Mean sea level from hydrographic chart from chart datum (m)
Daman	20.4124°N 72.8319°E	01.01.2014— 31.12.2014	6.32	2.88	3.80
Hazira	21.0860°N 72.6233°E	01.01.2014— 31.12.2014	8.42	4.19	4.50
Bhavnagar	21.8427°N 72.2562°E	01.01.2014— 31.12.2014	11.66	5.82	6.10
Pipavav	20.9163°N 71.5066°E	01.01.2014— 24.06.2014	4.85	2.47	1.80
Diu	20.7192°N 70.9952°E	01.01.2014— 31.05.2014	2.80	1.71	1.50

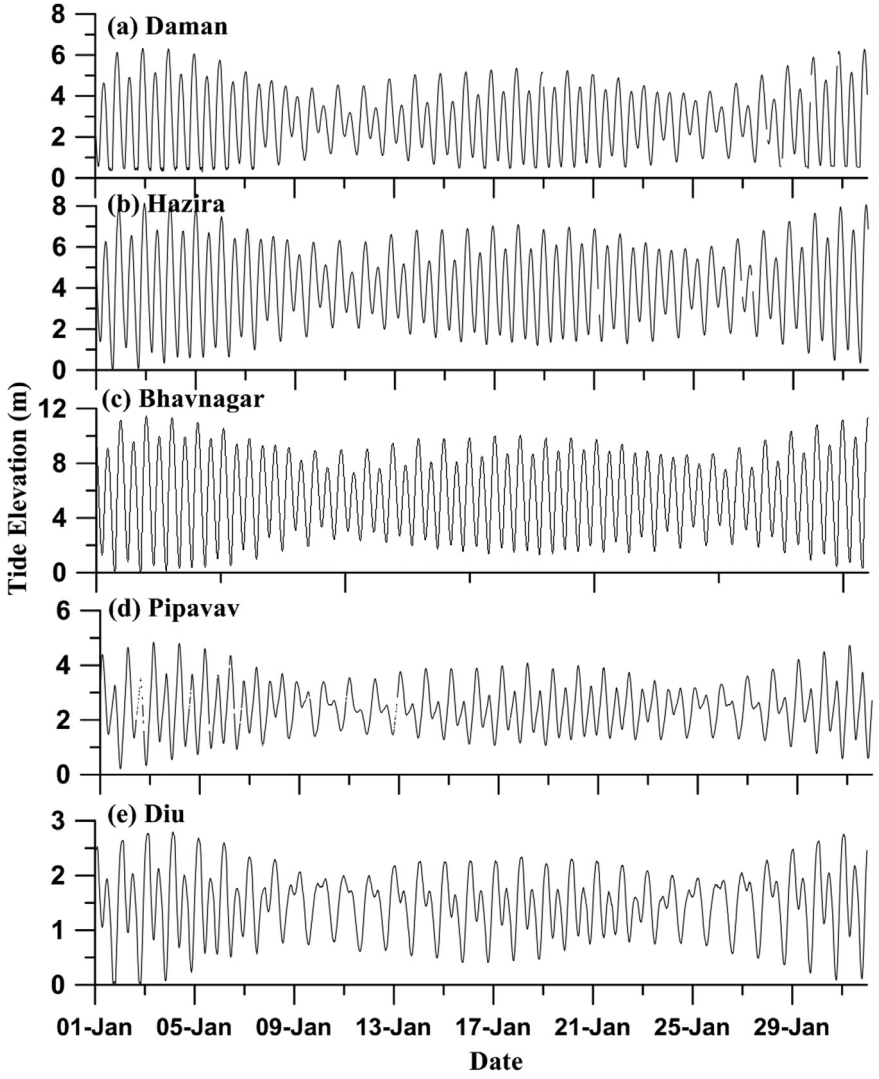

Figure 2 Time series plot of the measured tide data from 1 January to 31 January 2014 at a) Daman, b) Hazira, c) Bhavnagar, d) Pipapvav and e) Diu. Tides are presented with respect to Chart Datum.

Table 2 Locations and their distance from mouth of GoK where positive, negative and zero denotes inside, outside and Gulf mouth respectively.

Locations	Distance from Gulf mouth (km)
Daman	-51.3
Suvali	0
Ambheta	38
Hazira	55
Dahej	106
Khambhat	156.3
Bhavnagar	127
Pipavav	0
Jafrabad	-25
Nawabandar	-58
Diu	-73

elevations at Daman are 6.5 m and 5.5 m, respectively. At this location, data could not be collected continuously for one-year due to instrumental error. Hazira, a location inside GoK, is selected from the eastern coast, where observations on sea-level are taken for one year. Neap-spring variation at Hazira ranged between 7 and 8.1 m, respectively (Fig. 2b). Bhavnagar is selected inside the GoK in the western coast, where the tidal range is found to be maximum among all the locations. The maximum spring tidal height is found to be 11.6 m and the maximum neap tidal height is 10 m (Fig. 2c). Data is missed for a couple of short periods in this location due to instrumental error. Another location, selected from the western coast situated at the Gulf mouth is Pipavav, where the tide elevation is comparatively low. In situ data of sea-level is recorded for six months at Pipavav. Neap and spring tide elevations are 4 and 4.8 m, respectively, on an average (Fig. 2d). Diu is chosen outside GoK at the Saurashtra coast, where tide elevation is recorded for six months. The neap and spring variation is 2 and 2.8 m, respectively (Fig. 2e). Minimum variation in sea-level is noticed at Diu among all the five locations. Analysis of one-year-long sea-level data for three locations and six-months-long data for two locations indicates that GoK is a non-linear shallow-water system.

4.2. Comparison of model output with the measured tide

4.2.1. MIKE21 Global Tide Model

Tide elevation data are derived with the help of the MIKE21 Global Tide Model at the locations of observed data. The elevations are well-in agreement at all the locations except Hazira, where a discrete difference between modelled and the observed tide has been noticed (Fig. 3). The statistical parameters calculated based on the observed data sets and MIKE21- derived datasets are presented in Table 3. Overall, both these datasets are well in agreement with each other. Thus, this model is further used to predict tide elevations at several other locations of the Gulf.

4.2.2. FES2014 Global Tide Model

Tide elevation data are extracted from the global tidal model FES2014 for the same period of time for the locations where in situ data of tide elevation are recorded. A comparison is made between the measured and FES2014 data (Fig. 4). A good match is obtained between the measured and FES2014 data at the offshore stations, i.e., Daman and Diu. A good match could be seen even at the inner station of Pipavav. If we proceed further inside the Gulf, i.e., at Hazira and Bhavnagar, the FES2014 and measured data are not in agreement with each other. For both these locations, FES2014 data underestimated the measured tide level. The amplitudes of the major semi-diurnal and diurnal tidal constituents estimated from FES2014 are similar to the values obtained from measured data for the offshore locations, whereas, for locations like Hazira and Bhavnagar, the amplitudes of the constituents differ (Table 4).

4.3. Harmonic analysis

4.3.1. Amplitude

The major tidal constituents evaluated in the present study are grouped as diurnal (K1, O1, P1), semi-diurnal (M2. S2, N2, K2, L2) and mixed (MU2, M4, MS4, NU2, MSf). Out of the 13 major astronomical constituents used in the study based on their amplitude, five diurnal and semi-diurnal constituents are represented together in Fig. 5a. Similarly, a total of eight diurnal, semi-diurnal, compound and overtide constituents are presented together in Fig. 5b. The dominant tidal constituent is M2, with the amplitude four times greater than the major diurnal or semi-diurnal constituents. The increase in amplitude is found to be more regular from Gulf mouth to head in case of the eastern coast, while irregularity in the amplification is observed in the western coast. From Daman to Hazira, M2 has propagated a distance of 85 km, with an increase of 0.443 m (rate of 0.005 m per km). The rate increased to 0.014 m per km while moving from Hazira to Bhavnagar, covering a distance of 117 km. Minimum amplitude is noticed outside GoK at Diu (~0.48 m). The maximum amplitude is at Bhavnagar (3.33 m), which has a dramatic decrease at Pipavav with a rate of 0.02 m per km. There is a gradual increase in amplitude from Gulf mouth to head along both the coasts of GoK for the other major constituents.

Even in the case of the minor constituents, an irregular increase from Gulf mouth to head is observed. In this case, the maximum amplitude is noticed for K2, with an amplitude two times higher than the other minor constituents on an average. MSf tide is taken into consideration as this is the largest among the fortnightly constituents. It consists of both an elementary component, which is part of the equilibrium tide and a possible forced component arising from the interaction of M2 and S2 (S2-M2). It did not have a consistent trend of variation in the study region with a maximum of 0.048 m at Pipavav.

Propagation of major diurnal and semi-diurnal tide is studied with the help of tidal constituents available in the MIKE21 Global Tide Model at six locations throughout the Gulf. The trend is similar to the in situ measurements (Fig. 6a). M2 is the most dominant constituent in each of the locations. It had an amplitude of 2.057 m at Suvali, which got increased to 2.708 m at Ambheta. A sudden decrease is obtained at Dahej (1.623 m), which again increased northward at Khambhat. A similar trend of increase is obtained along the western coast towards the north and with mini-

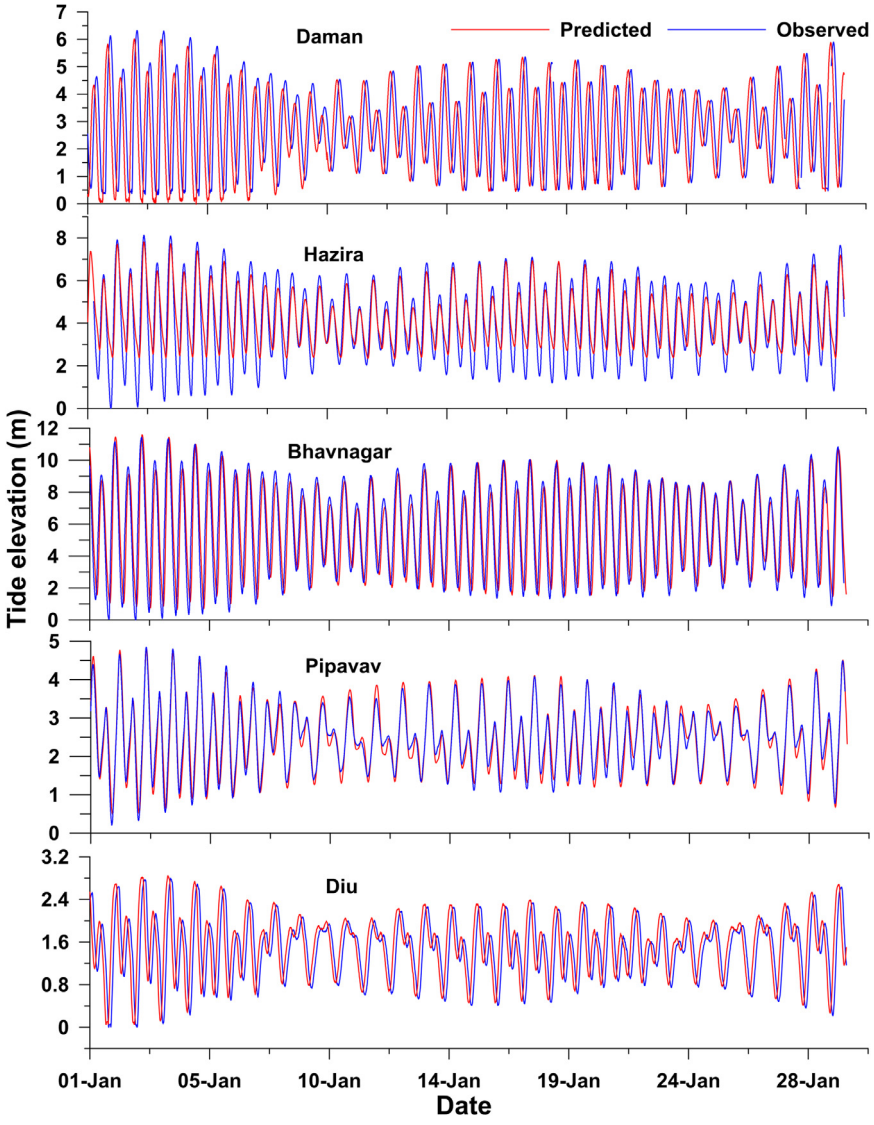

Figure 3 Comparison between predicted tide based on MIKE21 Global Tide Model and observed tide at Daman, Hazira, Bhavnagar, Pipapvav and Diu.

Table 3 Correlation (r), bias, Root Mean Square Error (RMSE) and significance level (p-value) between 2D model derived tide and observed tide in Daman and Pipavav, correlation between v-component of wind and tide residual.

Statistical Parameters	Predicted (MIKE21) and observed tide					v-component of wind and tide residual				
	Daman	Hazira	Bhavnagar	Pipavav	Diu	Daman	Hazira	Bhavnagar	Pipavav	Diu
r	0.8	0.45	0.78	0.73	0.76	0.33	0.22	0.04	0.06	0.17
Bias (m)	-0.03	-0.02	-0.04	-0.02	0.02	-	-	-	-	-
RMSE (m)	0.02	0.04	0.03	0.01	0.03	-	-	-	-	-
p-value	0.04	0.02	0.04	0.03	0.02	-	-	-	-	-

mum magnitude at Nawabandar. S2 tide had a gradual increase towards the north along both the coasts of GoK. The O1 tide follows a similar trend of propagation. There is no regularity of variation in the case of K1.

Influences of the length of the dataset and period of the data on the evaluation of the tidal constituents are studied by considering one-month-long data for January, April, July and October. Harmonic analysis is carried out and the variations in the major five astronomical constituents (M2, S2, K1, O1 and N2) are examined. The study shows monthly variation is least in the case of the diurnal constituents, i.e., K1 and O1. On the contrary, seasonal variability is noticeable in the case of the semi-diurnal constituents. The maximum amplitude of 3.418 m is recorded for M2 in April. But

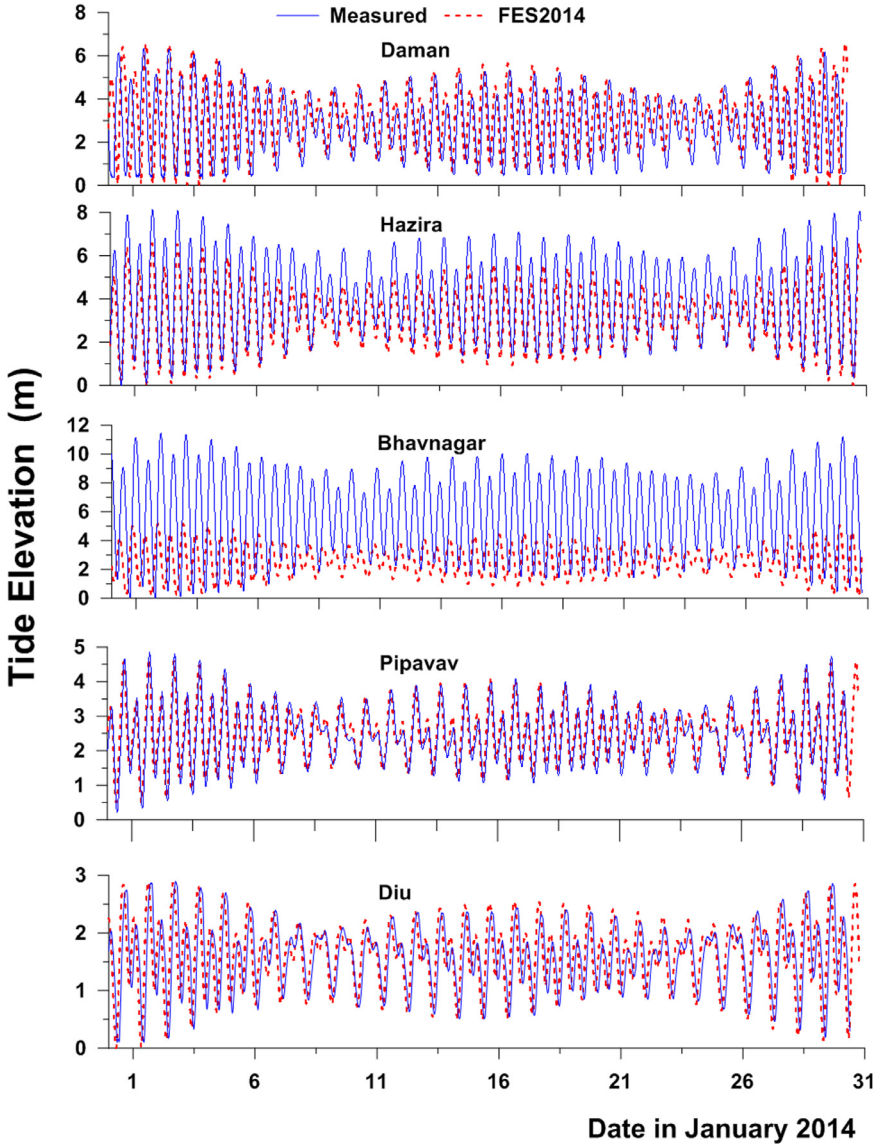

Figure 4 Comparison of FES2014 tide with the measured tide at Daman, Hazira, Bhavnagar, Pipavav and Diu.

Table 4 Comparison between major tidal constituents extracted from global model FES2014 and measured data.

Locations	M2 (m)		S2 (m)		K1 (m)		O1 (m)	
	FES2014	Measured	FES2014	Measured	FES2014	Measured	FES2014	Measured
Daman	1.65	1.72	0.74	0.64	0.55	0.54	0.22	0.24
Hazira	1.55	2.16	0.67	0.76	0.51	0.61	0.20	0.26
Bhavnagar	1.23	3.34	0.51	1.06	0.34	0.69	0.14	0.29
Pipavav	0.83	0.87	0.35	0.34	0.46	0.51	0.20	0.21
Diu	0.55	0.48	0.23	0.21	0.41	0.42	0.19	0.19

on an average, the maximum amplitude is recorded in July when the south-west monsoon is at its peak. The trend of propagation of diurnal and semi-diurnal constituents is similar, i.e., to increase from southern GoK towards the inner Gulf, reaching maxima in Bhavnagar, for every month. Still, the amplification of semi-diurnal tides is substantially high. Among the diurnal tides, the seasonal variability is prominent in the case of K1. O1 is found to be persistent for different seasons. In a nutshell, it could be noticed that the summer amplitudes are higher than the winter amplitudes and the open ocean stations have shown the least seasonal variability. The variability surmises the fact that the semi-

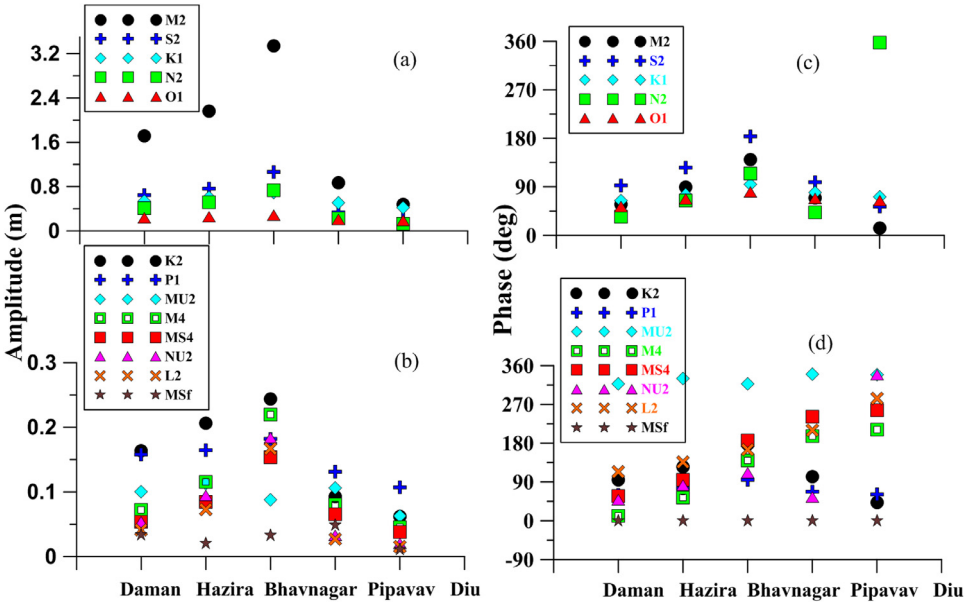

Figure 5 a) and b) Amplitude distribution of major astronomical tidal constituents at 5 locations in the study area based on measured data and the corresponding phase lag distribution is shown in c) and d).

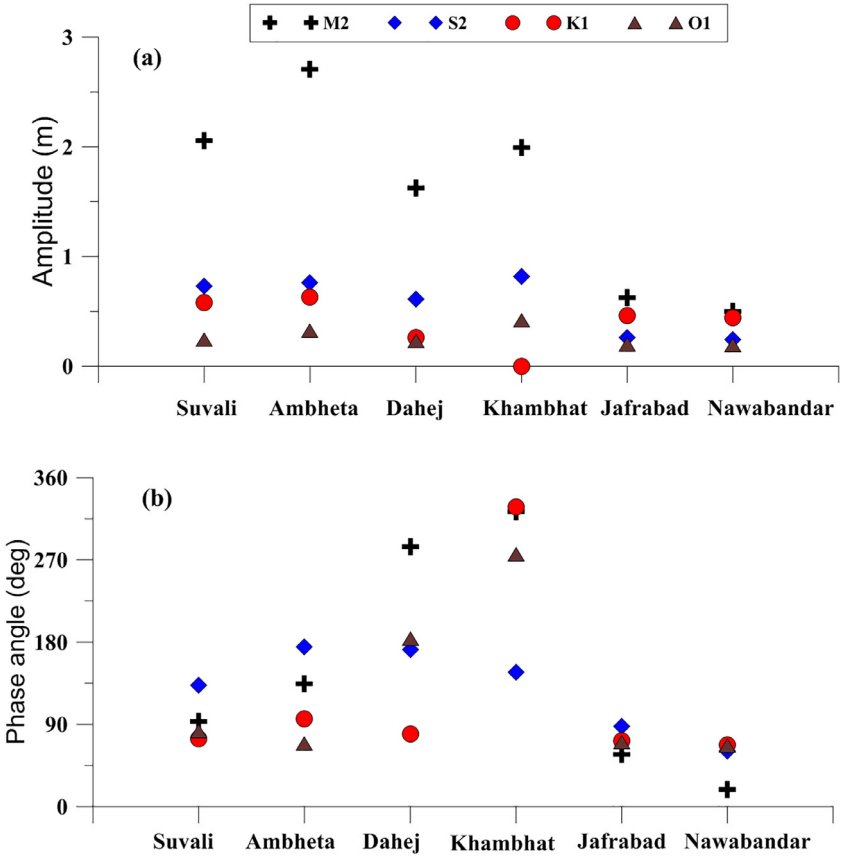

Figure 6 Amplitude and phase lag distribution of major astronomical constituents of MIKE21 Global Tide Model-derived tides in the study area.

diurnal constituents have spatial as well as temporal variation, while in the case of diurnal constituents, only the spatial variability is prominent.

4.3.2. Phase lag

Uniformity in the phase-changes for the selected locations has been obtained for all the major constituents except N2 and NU2; in these cases, a gradual increase in phase from Daman to Bhavnagar is noticed in case of eastern coast (Fig. 5c and d), but the phase got dramatically decreased from Diu to Pipavav which again increased in Bhavnagar. For all other cases, a gradual increase is observed from south to north along both the coasts. Similar trends of variation are noticed for K2 and P1. In the case of M4, MS4 and L2, a gradual increase in phase lag is obtained from Daman to Diu. There is no regular pattern of variation in the case of MU2.

A similar trend is followed in the case of MIKE21 Global Tide Model-derived data (Fig. 6b). M2 phase lag had an increase from Suvali (on the eastern coast) and Nawabandar (on the western coast) towards the north and reached the maximum at Khambhat. No other major constituents followed the same trend. The maximum phase lag is obtained in the northern-most location in the case of the diurnal constituents.

4.3.3. Spatial pattern of amplitudes and phase lags of major tidal constituents

Tide amplitudes derived at several places of the Gulf are used to determine the major tidal constituents. The MIKE21-Global Tide Model-simulated amplitudes resemble that of the observed. The spatial patterns of the amplitude of major constituents (K1, O1, M2 and S2) are presented in Fig. 7 and those of the phase lags are presented in Fig. 8. The contour lines of M2 suggest that the propagation of M2 is along the channel. The trend of propagation is similar in the case of S2, even though the amplitude of S2 is much lesser. Cross-channel propagation has been noticed in the case of the diurnal constituents (O1 and K1). Amplification of tides could easily be noticed from offshore towards the Gulf, but it is quite slower for the diurnal tide than the semi-diurnal. Gradual decreases in the phase lag are obtained from outer GoK to inner GoK for all other tidal constituents, except O1, where higher phase lag values are obtained inside the Gulf (Fig. 8).

4.3.4. Tidal form factor/tidal anomaly correlation

Tidal form factor (F) or tidal anomaly correlation, which is the ratio of the sums of the amplitudes of the two main diurnal constituents (K1 and O1) to that of the semi-diurnal constituents (M2 and S2) is estimated and presented in Table 5. The tide of a particular area could be classified according to the magnitude of the tidal form factor as; semi-diurnal ($0 < F < 0.25$), mixed and mainly semi-diurnal ($0.25 < F < 1.5$), mixed and mainly diurnal ($1.5 < F < 3.0$) and diurnal ($F > 3.0$).

There is a gradual decrease in the tidal form factor from Gulf mouth to head in the eastern and western GoK. The minimum magnitude is obtained at Bhavnagar (0.22), which gradually increased at Pipavav with a maximum at Diu on the western coast. The tidal form factor is found to increase from north to south, unlike the major tidal constituents, which increase from south to north. In addition to the mentioned locations, eight more locations are chosen throughout the Gulf, where the tidal form factor is calculated with the help of simulated tidal elevation (MIKE21 Global Tide Model-derived data). The minimum magnitude of 0.15 is obtained in the case of Khambhat (northern GoK). The maximum magnitude of the tidal form factor of 0.85 is noticed at Nawabandar, which situates at the south-western GoK in the Saurashtra coast.

Table 5 Tidal form factor at different locations.

Location	Tidal form factor
Daman (Measured)	0.33
Suvali (Simulated)	0.29
Hazira (Measured)	0.30
Ambheta (Simulated)	0.27
Dahej (Simulated)	0.22
Khambhat (Simulated)	0.15
Bhavnagar (Measured)	0.22
Jafrabad (Simulated)	0.75
Nawabandar (Simulated)	0.85
Pipavav (Measured)	0.60
Diu (Measured)	0.88

4.4. Monthly variation in MSL and SLA

Intra-annual variability in MSL is determined for the entire year from the measured as well as simulated data and is presented in Table 6. It had a gradual increase from Daman to Bhavnagar and then gradually decreased from Bhavnagar to Diu. MSL variations are more evident inside the Gulf (Bhavnagar) rather than the offshore locations (Daman and Diu). The maximum variation in the MSL (~0.25 m) is obtained in Bhavnagar. Although small variation in MSL is obtained for the entire year, maximum MSL is recorded during the south-west monsoonal months, which is associated with the monsoonal winds.

Monthly variation in SLA is observed for the entire year for each of the locations. The SLA-variability is found to be very less. Maximum SLA is observed during the monsoonal months in most of the stations, while minimum SLA is observed during pre-monsoon (Table 7).

4.5. Sea-level residual

The sea-level residual is extracted for a year at each location to obtain the inter-annual variability. The maximum residual sea-level is observed in Bhavnagar with a magnitude of around 0.7 m. Minimum tide residue of 0.17 m is obtained in Diu (Fig. 9). Even though there is a difference in the magnitude of the tidal residual, the trend of variation is similar at each location.

Wind data forJanuary 2014 is obtained and the correlation between the v-component of wind (alongshore wind) and the residual sea-level is estimated. A rise in sea-level could be noticed with an increase in the alongshore wind (Fig. 10). Even though a positive correlation between sea-level and v-component of wind is obtained for all the lo-

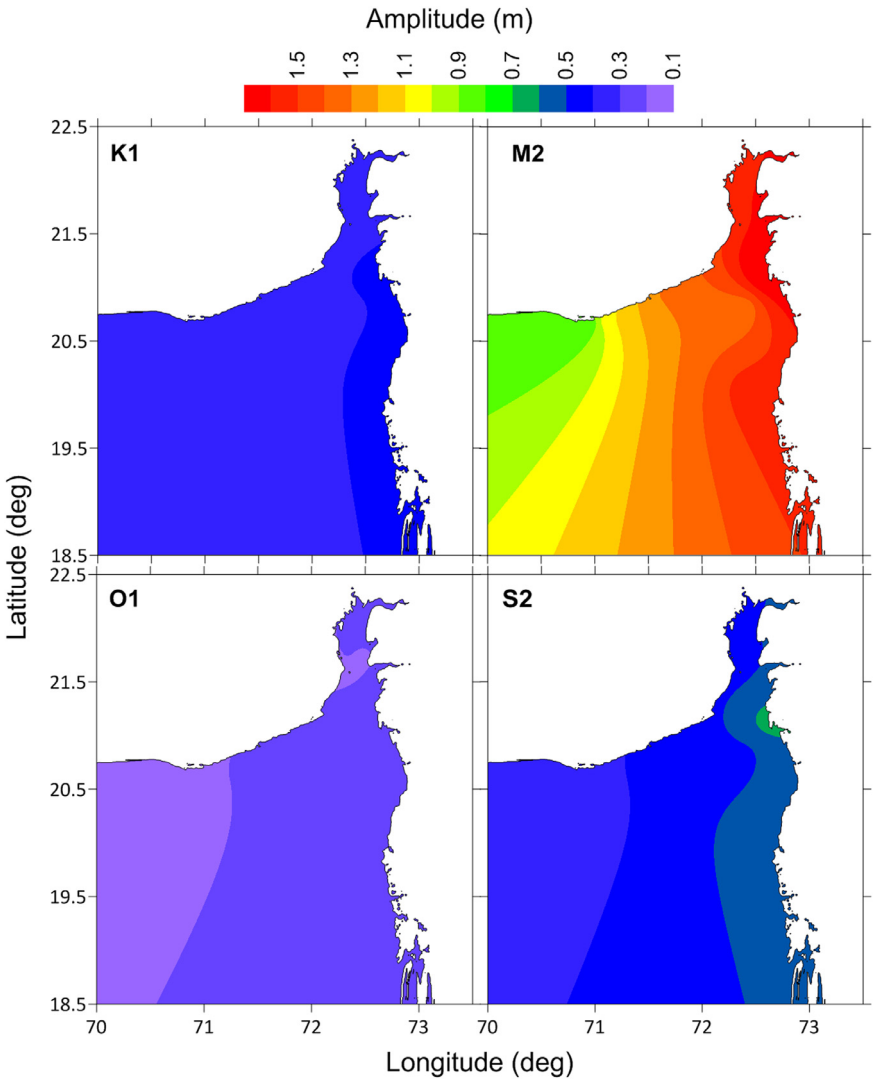

Figure 7 Contours of amplitudes of major tidal constituents (K1, M2, O1 and S2) of Gulf of Khambhat and surroundings.

Table 6 Monthly mean sea level (m) at different locations in different months.

Month	Daman	Suvali	Hazira	Ambheta	Dahej	Khambhat	Bhavnagar	Pipavav	Jafrabad	Nawabandar	Diu
Jan	2.87	3.60	4.1	4.22	4.88	4.12	5.74	2.47	1.85	1.37	1.49
Feb	2.92	3.60	4.15	4.20	4.92	4.13	5.80	2.49	1.85	1.37	1.51
Mar	2.97	3.61	4.19	4.23	4.88	4.13	5.89	2.46	1.85	1.38	1.53
Apr	2.93	3.60	4.16	4.23	4.89	4.13	5.85	2.38	1.86	1.38	1.48
May	2.95	3.60	4.19	4.23	4.89	4.13	5.87	2.37	1.86	1.39	1.47
Jun	2.90	3.60	4.32	4.22	4.90	4.13	5.99	2.50	1.85	1.38	1.70
Jul	3.03	3.60	4.23	4.22	4.91	4.13	5.84	2.47	1.85	1.37	1.70
Aug	3.03	3.60	4.23	4.21	4.92	4.13	5.83	2.47	1.84	1.35	1.70
Sep	2.97	3.60	4.16	4.21	4.91	4.13	5.85	2.47	1.84	1.37	1.70
Oct	2.93	3.60	4.17	4.20	4.92	4.13	5.76	2.47	1.84	1.35	1.71
Nov	2.95	3.60	4.24	4.21	4.90	4.13	5.85	2.47	1.85	1.37	1.70
Dec	2.88	3.59	4.15	4.21	4.90	4.13	5.72	2.46	1.85	1.37	1.70

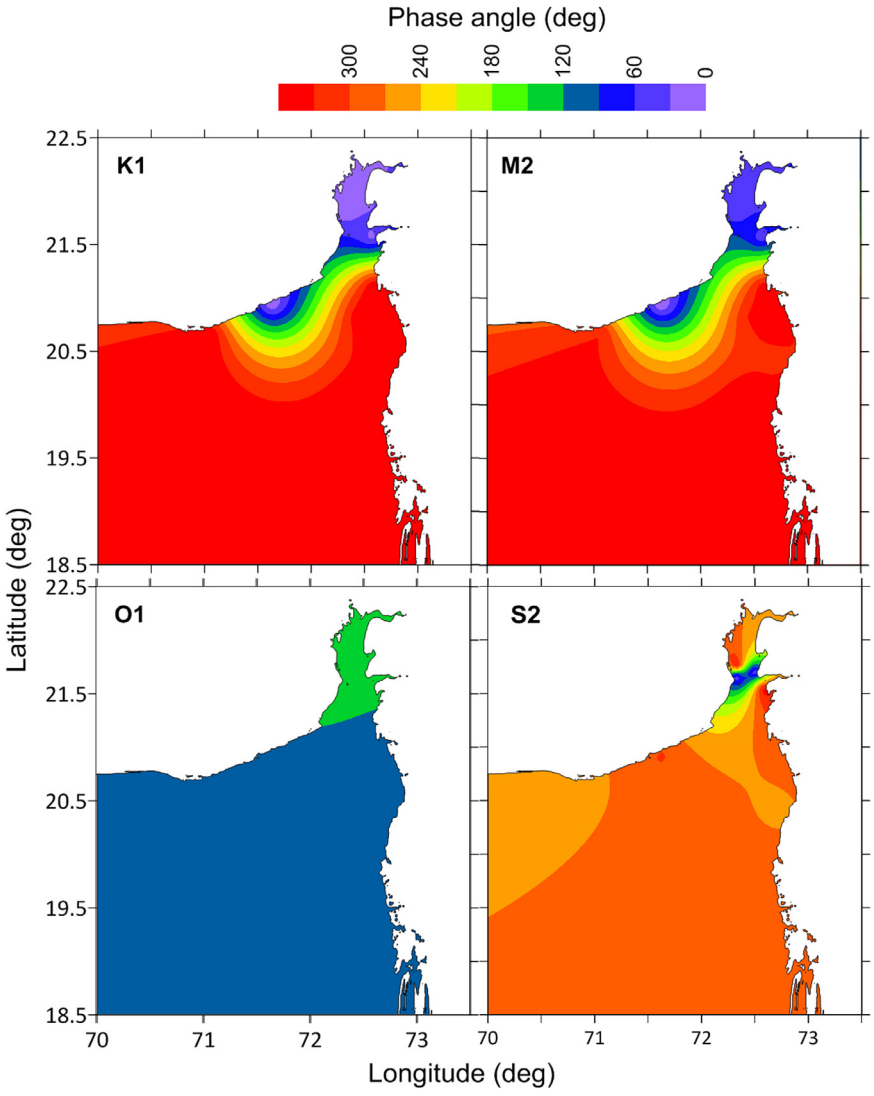

Figure 8 Contours of phase lags of major tidal constituents (K1, M2, O1 and S2) of Gulf of Khambhat and surroundings.

Table 7 Intra-annual variability of Sea Level Anomaly (SLA).

Month	Daman	Suvali	Hazira	Ambheta	Dahej	Khambhat	Bhavnagar	Pipavav	Jafrabad	Nawabandar	Diu
Jan	-0.07	0	-0.09	0	-0.02	-0.01	-0.09	0.01	0	0	-0.13
Feb	-0.02	0	-0.04	-0.02	0.02	0	-0.03	0.03	0	0	-0.11
Mar	0.03	0.01	0	0.01	-0.02	0	0.06	0	0	0.01	-0.09
Apr	-0.01	0	-0.03	0.01	-0.01	0	0.02	-0.08	0.01	0.01	-0.14
May	0.01	0	0	0.01	-0.01	0	0.04	-0.09	0.01	0.02	-0.15
Jun	-0.04	0	0.13	0	0	0	0.16	0.04	0	0.01	0.08
Jul	0.09	0	0.04	0	0.01	0	0.01	0.01	0	0	0.08
Aug	0.09	0	0.04	-0.01	0.02	0	0	0.01	-0.01	-0.02	0.08
Sep	0.03	0	-0.03	-0.01	0.01	0	0.02	0.01	-0.01	0	0.08
Oct	-0.01	0	-0.02	-0.02	0.02	0	-0.07	0.01	-0.01	-0.02	0.09
Nov	0.01	0	0.05	-0.01	0	0	0.02	0.01	0	0	0.08
Dec	-0.06	-0.01	-0.04	-0.01	0	0	-0.11	0	0	0	0.08

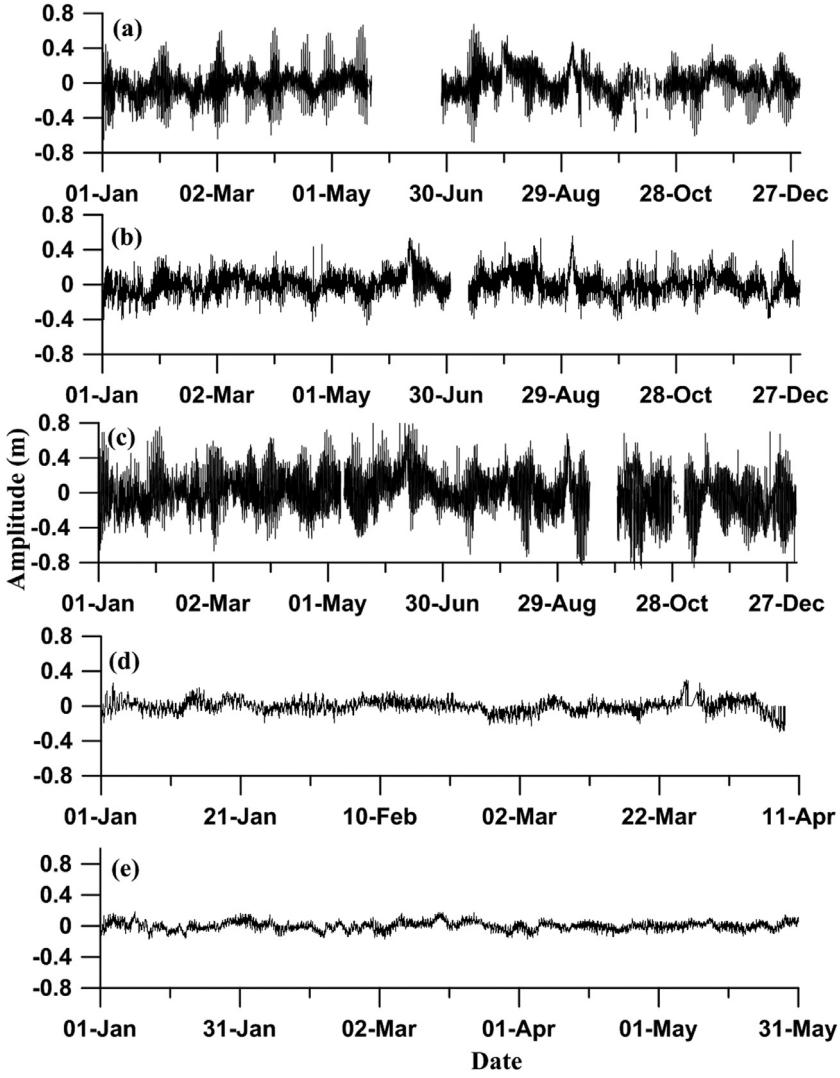

Figure 9 The non-tidal residual of sea-level at selected locations; a) Daman, b) Hazira, c) Bhavnagar, d) Pipapvav and e) Diu.

cations (Table 3), the significance level is very low for the inner Gulf locations. The maximum correlation has been noticed in the offshore stations (Daman and Diu). The seasonal wind regime of the area is portrayed in Fig. 10 for three typical months of pre-monsoon (March), southwest-monsoon (July) and northeast-monsoon (November), respectively. Maximum wind speed could be noticed inJuly, which is known as the peak monsoonal month. Wind speed reaches its maxima at the offshore locations irrespective of the seasons. Minimum wind impact could be observed inside the Gulf during March, but for other seasons, the magnitude of wind speed is considerable inside GoK.

5. Discussion

The measured and simulated tide elevation data indicates that it has a northward increase, reaches the maximum at the inner Gulf and had a slight decrease at the northernmost location. Tidal amplitude varies inside the Gulf at different rates; it is minimum for the southern stations and attains maximum inside the channel. The extremely variable channel geometry could explain these phenomena over a tidal cycle because, in a converging channel, the geometric effects amplify the incident wave and the rate of convergence depends on the channel convergence. Non-linearity in the tides could be illustrated by comparing the elevation of the Gulf-mouth (Pipavav) with that inside the Gulf (Hazira and Bhavnagar). The tidal amplification inside the Gulf resulted from the quarter wavelength resonance of the tides owing to its inherent geometrical settings (Nayak and Shetye, 2003). A similar condition was observed in the Gulf of Kachchh, west coast of India, where amplification of tidal amplitude arouse due to the convergence of the channel (Shetye, 1999). But the amplification of tides in the Gulf of Kachchh is quite smaller than that of GoK.

Tidal constituents followed a similar trend of variation as the tide elevation, which is quite evident. The amplitude maxima are found in the case of M2, which indicates the semi-diurnal dominance in the tide. The maximum M2 amplitude at Bhavnagar shows the amplification of M2 tide inside the Gulf. Amplification of semi-diurnal tide inside the Gulf is higher than that of the diurnal, which is in favour of the earlier studies. Semi-diurnal tides forced with neap

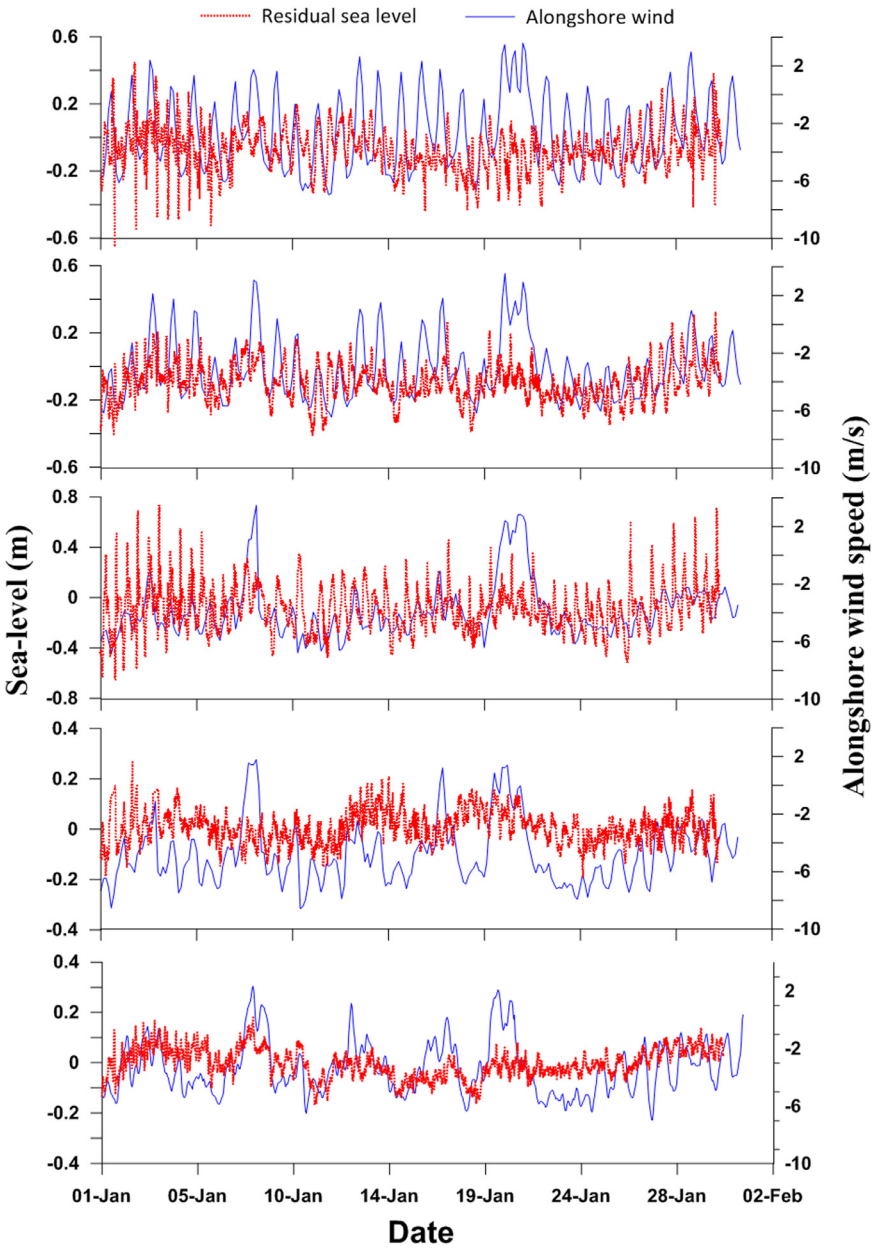

Figure 10 Comparison between the non-tidal residual of sea-level with the alongshore component of wind in January 2014.

and spring amplitudes at the estuary mouth exhibit similar properties along the upper reach, which is produced by the combined effect of reflection (that reduces friction) and enhanced morphological convergence in case of an ideal estuary (Garel and Cai, 2018); but in GoK, diurnal tides had amplification from mouth to head as resonance, together with geometric effects and friction, built up the amplification. Similar results were obtained from the study carried out by Nayak et al. (2015), where they obtained M2 amplitude of 0.40 m at the Gulf mouth, which has increased to 1.50 m inside the Gulf and decreased to 0.70 m at the Gulf head. A similar trend is followed by the other major constituents (S2, K1 and O1). The present study resembles the earlier work and reveals that amplitudes of the major tidal constituents have an increase from Daman (Gulf mouth) towards the inner Gulf and reached maxima in Bhavnagar, but had a further decrease in Khambhat (Gulf head).

The study also manifests the fact that the amplification is much higher on the western coast of the Gulf than on the eastern coast. The principal over-tide and compound tides are M4 and MU2, respectively. The trend of propagation of M4 (increasing from mouth to head) confirms the non-linearity of the system. If non-linearity is absent, the magnitudes of M4 would rapidly decrease within the channel from its small offshore values (Aubrey, 1985). M4 trend is also important for water and sediment transport purposes, which would be focussed on future research. By examining the neap/spring cycles at five stations within a month, it could be inferred that the non-linear distortion of the tide varies considerably. It is observed from the seasonal analysis that the average maximum amplitude is observed during

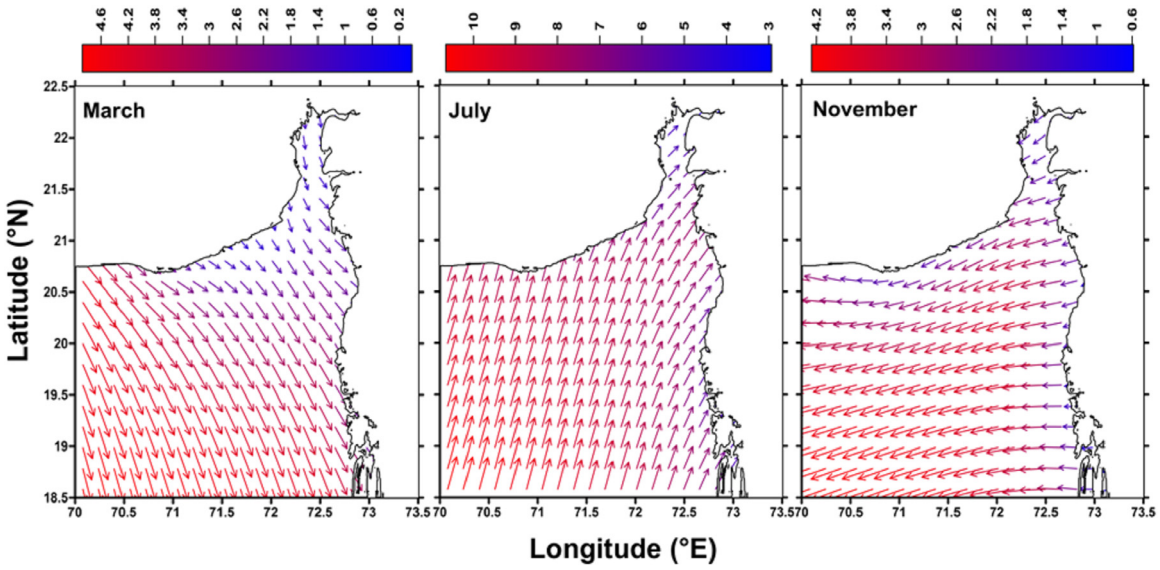

Figure 11 Seasonal wind regime of Gulf of Khambhat in March (representing pre-monsoon), July (representing monsoon) and November (representing post-monsoon).

July, which is due to the influence of peak south-west monsoon.

It should be noted that the tidal amplitude is greater during the flood flow rather than the ebb, which might accumulate sediment inside the GoK, which is known to be one of the major turbid water body of the west coast of India. Fine suspended sediment transport will be affected by the non-linear tidal distortion as well. Depending on the channel geometry, this effect becomes pronounced further in the Gulf, where the tide is more non-linear. Tidal non-linearity has implications for mass flux calculations commonly attempted in shallow water Gulf or estuaries. The numerical simulations of Lee et al. (2016) in Delaware Bay and the Chesapeake Bay concluded that the shape of estuaries and bays could also affect the tidal amplitude. Thus it could be inferred that the funnel shape of the Gulf also enhances the tidal amplification along with the other factors. The quarter diurnal compound tides include the major constituent MS4, derived from the interaction of M2 and S2, which lags the forcing tides (M2+S2). This phase relationship also enhances the tide asymmetry favouring flood. The consistency of the phase lead/lag in all over-tides and compound tides throughout the Gulf suggest it is a property of a Gulf as a whole and not just of local characteristics. If the compound tide amplitudes are much smaller than the forcing constituents, they are insignificant to the tidal energy balance. The growth of MSf inside the Gulf is not consistent; rather, its amplitude depends upon atmospheric conditions, suggesting it is not a simple compound tide. Higher value in MSf amplitude indicates atmospheric disturbances such as storms.

Tide-prediction with monthly-, semi-annually- and annually-averaged datasets has shown that the more the number of data, the less error it would be in the predicted tide. Even though the monthly analysis data could predict the tide amplitude quite accurately, the best fit is found in the case of the yearly analysis data. The contour lines of diurnal and semi-diurnal constituents are found to be along channel and cross-channel respectively inside the Gulf and the amplification of M2 tide is much higher than that of the others. The inherent geometry of the Gulf is responsible for these orientations (Nayak et al., 2015). Gradual changes in phase lag from outer to inner GoK indicate the propagation of tide inside the channel.

The magnitude of the tidal form factor is found to be less in the eastern GoK, indicating the dominance of the semi-diurnal tides. A higher value of tidal form factor is obtained in the offshore location both for the eastern and western GoK, which gradually decreased towards the inner Gulf reaching its minima at the northern-most location, Khambhat. Thus it could be inferred that the semi-diurnal components mainly contribute to the tidal amplification from southern GoK towards the north. In the western Gulf, a higher value of tidal form factor manifested comparatively better dominance of the diurnal tides. The tidal form factor calculated inside the Gulf revealed that in the eastern as well as northern GoK, the dependence of the diurnal tide on the semi-diurnal is very less. But at the south-western GoK, it is more and reaches the maximum outside the Gulf on the western coast. The values are nearly equal to 1 in Diu and Nawabandar, which indicate that even a small change in semi-diurnal tide would lead to a change in the diurnal tide vice-versa in those locations. Overall, based on the magnitudes of the tidal form factor, the tides of GoK are classified as mixed and predominantly semi-diurnal in nature. The sea-level data of the entire year shows that the astronomical tide is mainly responsible for the sea-level variation.

Tide prediction is carried out with the help of tidal constituents estimated from monthly, half-yearly and annual time series (Table 8). Tidal amplitudes are found to be 1 to 10% lower in case of the estimate based on monthly time series compared to the annual one. Tides are 1 to 6% lower in case of the estimate based on six-monthly time series compared to the annual one.

Very less variation in the MSL is observed throughout the year for each location, but an increase in MSL is recorded

Table 8 Predicted tide during spring and neap tide using tidal constituents estimated from monthly, half-yearly and annual measured time series data. The values in brackets show the percentage reduction from the longest time series.

Locations	1 month data		6 months data		1 year data	
	Neap	Spring	Neap	Spring	Neap	Spring
Daman	5.23 (5.4%)	5.95 (1.2%)	5.43 (1.8%)	6.02 (2.0%)	5.53	6.14
Hazira	7.12 (10.0%)	7.93 (2.5%)	7.45 (5.8%)	8.13 (2.2%)	7.91	8.31
Bhavnagar	10.26 (3.1%)	10.96 (1.3%)	10.44 (1.4%)	11.11 (5.9%)	10.59	11.8
Pipavav	4.16 (1.9%)	4.59 (0.7%)	4.24	4.62	-	-
Diu	2.31 (1.7%)	2.55 (1.9%)	2.35	2.60	-	-

during the monsoonal months due to strong monsoonal winds. MSL could be affected by so many factors on a regional scale, but the major role is played by the overlying atmosphere. Changes in atmospheric pressure and wind stress are the primary cause of change in the MSL (Amiruddin et al., 2015; Wouters et al., 2011), which would eventually have an impact on the wind pattern of the area. Although the non-tidal sea-levels had smooth trends throughout the year, there are some discrete undulations, which could be the effect of the atmospheric disturbance (IMD report, 2014). The positive correlation between the tide residual and the v-component manifests the dependence of the non-tidal component of sea-level on the atmospheric processes, but the atmospheric influence gets diminished inside the Gulf. Estuarine water levels are influenced primarily by astronomical tides and coastal processes and secondarily by river flow (Jay et al., 2015). Even though the river discharge could have an influence on the MSL variability of Gulfs and estuaries, its effect is found to be negligible in GoK. The major discharge is contributed by river Narmada, but its influence is found to be a purely localized phenomenon; it did not contribute to the Gulf dynamics as a whole (Mitra et al., 2020). Also, these sea-level variations, triggered by storm winds, could disturb the tide, which has an astronomical origin. Along the east coast of India, seasonal sea-level changes from atmospheric pressure variations vary from about 0.03 m at Colombo to 0.13 m at Paradip (Shankar, 2000). The impact of atmospheric pressure is not considered in the present study since there was no large variation in the atmospheric pressure as there was no cyclone during the study period. During the present study, the v-component of wind had a positive correlation with the sea-level throughout the year. Thus, in a nutshell, it could be inferred that the non-tidal sea-level rise is due to the alongshore component of wind, especially in the offshore stations. The seasonal wind regime of the area is also in accordance with this. It could be noticed well that even though the global tidal model accurately predicts the tide elevation data for the offshore locations, it fails to predict the same for the shallow areas where regional models should better be used. The global model data are less reliable in coastal zones than in the open ocean because of inaccurate geophysical corrections and noisier radar impulse responses (Deng and Featherstone, 2006). The performance of the global models in shallow water and coastal zones is inferior to their performance in the open ocean in terms of the accuracy of tidal constituent estimations and, consequently, the accuracies of tidal height predictions (Ray et al., 2011). But it is worth mentioning that neither the physics-based nor the observation-based methods can provide the exact (error-free) tide predictions (Simkooei et al., 2014).

6. Conclusion

Sea-level data collected at five locations in the Gulf revealed that the astronomical tides are mainly responsible for the sea-level variation in this area. Tide propagates from Gulf mouth to head in a non-linear fashion. The major non-tidal factor contributing to the sea-level is the alongshore component of wind, which shows a positive correlation with the sea-level for each location. The amplitude of the major tidal constituents (M2, S2, O1 and K1) at Bhavnagar is 3.33, 1.06, 0.69 and 0.28 m and at Diu is 0.48, 0.21, 0.42 and 0.19 m respectively which infers the dominance of the semi-diurnal component in the tidal amplification. The summer amplitudes of the major tidal constituents are much higher than that of the winter amplitudes and the seasonal variability of the tidal constituents is comparatively higher in the inner stations than that of the offshore stations. The tidal form factor calculated for the locations in the Gulf indicates that tides in these areas are mixed and predominantly semi-diurnal in nature. The phase lag of MS4 tide from that of M2 and S2 exhibits the dominance of flood over ebb in this area, resulting to accumulation of sediment in the Gulf. Among the two models used in the present study, the global tide model FES2014 largely underestimates the tides inside the Gulf. In contrast, the MIKE21 Global Tide Model could predict the same more accurately.

Acknowledgements

The data used in the study is measured by the National Institute of Technology, Chennai. Director, CSIR-National Institute of Oceanography, Goa and Director, National Institute of Ocean Technology, Chennai, encouraged to carry out the study. We thank Dr. Udhaba Dora, Scientist, CSIR-NIO Regional Centre, Mumbai, for helping with the MIKE21 tide data. We thank both the reviewers and the Editor for the suggestions, which improved the scientific content of the paper. We thank all colleagues for the help provided during the field data collection. This is NIO contribution 6550 and forms a part of the Ph.D. thesis of the first author registered at Bharathidasan University, Tiruchirappalli, India.

References

Aubrey, D.G., Speer, P.E., 1985. A study of non-linear tidal propagation in shallow inlet/estuarine systems part I: observations. Estuar. Coast. Shelf Sci. 21, 185—205, https://doi.org/10.1016/0272-7714(85)90096-4.

Amiruddin, A.M., Haigh, I.D., Tsimplis, M.N., Calafat, F.M., Dangendorf, S., 2015. The seasonal cycle and variability of sea level in the South China Sea. J. Geophys. Res.-Oceans 120, 5490—5513, https://doi.org/10.1002/2015JC010923.

Bell, C., Vassie, J.M., Woodworth, P.L., 2000. POL/PSMSL Tidal Analysis Software Kit 2000 (TASK-2000). In: Permanent Service for Mean Sea Level, CCMS Proudman Oceanographic Laboratory, Bidston Observatory. Birkenhead, Merseyside, U.K., https://www.psmsl.org/train_and_info/software/task2k.php (accessed on 03/10/2018).

Carl, T.F., Aubrey, D.G., 1994. Tidal propagation in strongly convergent channels. J. Geophys. Res.-Oceans 99 (C2), 3321—3336, https://doi.org/10.1029/93JC03219.

Carrere, L., Lyard, F., Cancet, M., Guillot, A., 2015. FES 2014, a new tidal model on the global ocean with enhanced accuracy in shallow seas and in the Arctic region. In: In Proceedings of the EGU General Assembly 2015. Vienna, Austria, 12—17 April 2015.

Cartwright, D.E., Taylor, R.J., 1971. New computations of the tide-generating potential. Geophys. J. Int. 23, 45—73, https://doi.org/10.1111/j.1365-246X.1971.tb01803.x.

Deng, X., Featherstone, W.E., 2006. A coastal retracking system for satellite radar altimeter waveforms: Application to ERS-2 around Australia. J. Geophys. Res.-Oceans 111, https://doi.org/10.1029/2005JC003039.

Devlin, A.T., Jay, D.A., Talke, S.A., Zaron, E., 2014. Can tidal perturbations associated with sea level variations in the western Pacific Ocean be used to understand future effects of tidal evolution? Ocean Dynam. 64, 1093—1120, https://doi.org/10.1007/s10236-014-0741-6.

Devlin, A.T., Jay, D.A., Zaron, E.D., Talke, S.A., Pan, J., Lin, H., 2017a. Tidal variability related to sea level variability in the Pacific Ocean. J. Geophys. Res.-Oceans 122, 8445—8463, https://doi.org/10.1002/2017JC013165.

Devlin, A.T., Jay, D.A., Talke, S.A., Zaron, E.D., Pan, J., Lin, H., 2017b. Coupling of sea level and tidal range changes, with implications for future water levels. Sci. Rep. 7, 17021, https://doi.org/10.1038/s41598-017-17056-z.

Devlin, A.T., Pan, J., Lin, H., 2019. Tidal variability in the Hong Kong region. Ocean Sci. 15, 853—864, https://doi.org/10.5194/os-15-853-2019.

DHI, 2017. MIKE 21 Toolbox Global Tide Model — Tide Prediction, 116, https://www.dhigroup.com/download/mike-by-dhi-tools/coastandseatools/global-tide-model (accessed on 26.02.2019).

Dronkers, J.J., 1964. Tidal Computations in Rivers and Coastal Waters. North-Holland Publ. Comp., Amsterdam, 516 pp., https://doi.org/10.1126/science.146.3642.390 .

Garel, E., Cai, H., 2018. Effects of Tidal-Forcing Variations on Tidal Properties Along a Narrow Convergent Estuary. Estuar. Coasts 41, 1924—1942, https://doi.org/10.1007/s12237-018-0410-y.

Godin, G., 1993. On tidal resonance. Cont. Shelf Res. 13 (1), 89—107, https://doi.org/10.1016/0278-4343(93)90037-X.

Jay, D.A., Leffler, K., Diefenderfer, H.L., Borde, A.B., 2015. Tidal-Fluvial and Estuarine Processes in the Lower Columbia River: I. Along-Channel Water Level Variations. Pacific Ocean to Bonneville Dam. Estuar. Coasts 38, 415—433, https://doi.org/10.1007/s12237-014-9819-0.

Joseph, A., Vijaykumar, K., Mehra, P., Unnikrishnan, A.S., Sundar, D., Prabhudesai, R.G., 2009. Observed tides at Mumbai High offshore region near the continental shelf break in the eastern Arabian Sea. Current Sci. 96 (9), 1233—1235.

Kalnay, E., Kanamitsu, M., Kistler, R., Collins, W., Deaven, D., Gandin, L., Iredell, M., Saha, S., White, G., Woollen, J., Zhu, Y., Leetmaa, A., Reynolds, R., Chelliah, M., Ebisuzaki, W., Higgins, W., Janowiak, J., Mo, K.C., Ropelewski, C., Wang, J., Roy, J., Joseph, D., 1996. The NCEP/NCAR 40-year reanalysis project. Bull. Am. Meteorol. Soc. 77, 437—471, https://doi.org/10.1175/1520-0477(1996)077%3C0437:TNYRP%3E2.0.CO;2.

Kumar, V.S., Kumar, K.A., 2010. Waves and currents in tide dominated location off Dahej. Gulf of Khambhat. Mar. Geodesy 33, 218—231, https://doi.org/10.1080/01490419.2010.492299.

Kumar, V.S., Dora, G.U., Philip, S., Pednekar, P., Singh, J., 2011. Variations in tidal constituents along the nearshore waters of Karnataka, west coast of India. J. Coast. Res. 27 (5), 824—829, https://doi.org/10.2112/JCOASTRES-D-09-00114.1.

Kumar, V.S., Pathak, K.C., Pednekar, P., Raju, N.S.N., Gowthaman, R., 2006. Coastal processes along the Indian coastline. Current Sci. 91 (4), 530—536.

Lanzoni, S., Seminara, G., 1998. On tide propagation in convergent estuaries. J. Geophys. Res.-Oceans 103 (C13), 30793—30812, https://doi.org/10.1029/1998JC900015.

Lee, S.B., Li, M., Zhang, F., 2016. The effect of sea level rise on Tidal Dynamics in Chesapeake and Delaware Bays. In: Ocean Sciences Meeting 2016. EC31A-06, 1—26 February, New Orleans, Louisiana, USA., https://agu.confex.com/agu/os16/preliminaryview.cgi/Paper93354.html.

Liu, J.T., Aubrey, D.G., 1993. Tidal residual currents and sediment transport through multiple tidal inlets. Coast. Estuar. Stud. 44, 113—157, https://doi.org/10.1029/CE044p0113.

Mitra, A., Kumar, V.S., Naidu, V.S. , 2020. Circulation in the Gulf of Khambhat- A Lagrangian Perspective. J. Mar. Sci. Eng, 8, 25 pp., https://doi.org/10.3390/jmse8010025.

Nayak, R.K., Shetye, S.R., 2003. Tides in the Gulf of Khambhat, west coast of India. Estuar. Coast. Shelf Sci. 57, 249—254, https://doi.org/10.1016/S0272-7714(02)00349-9.

Nayak, R.K., Salim, M., Mitra, D., Sridhar, P.N., Mohanty, P.C., Dadhwal, V.K., 2015. Tidal and Residual Circulation in the Gulf of Khambhat and its Surrounding on the West Coast of India. J. Indian Soc. Remote Sens. 43, 151—162, https://doi.org/10.1007/s12524-014-0387-3.

Pugh, D.T., 1987. Tides, Surges and Mean Sea Level. John Wiley and Sons, Chichester, U.K., 472 pp., http://eprints.soton.ac.uk/id/eprint/19157 .

Ray, R.D., Egbert, G.D., Erofeeva, S.Y., 2011. Tide Predictions in Shelf and Coastal Waters: Status and Prospects. In: Vignudelli, S., Kostianoy, A., Cipollini, P., Benveniste, J. (Eds.), Coastal Altimetry. Springer, Berlin, Heidelberg, 191—216.

Seifi, F., Deng, X., Andersen, O.B. , 2019. Assessment of the Accuracy of Recent Empirical and Assimilated Tidal Models for the Great Barrier Reef, Australia. Using Satellite and Coastal Data. Remote Sens, 11, 1211 pp., https://doi.org/10.3390/rs11101211.

Shankar, D., 2000. Seasonal cycle of sea level and currents along the coast of India. Current Sci 78 (3), 279—288.

Shetye, S.R., Gouveia, A.D., 1998. Coastal circulation in the North Indian Ocean — Coastal Segment (14, S—W). The Sea, 11. John Wiley and Sons, Inc., 523—772.

Shetye, S.R., 1999. Tides in the Gulf of Kutch. Cont. Shelf Res. 19, 1771—1782, http://dx.doi.org/10.1016/S0278-4343(99)00038-2.

Simkooei, A.R.A., Zaminpardaz, S., Sharifi, M.A., 2014. Extracting tidal frequencies using multivariate harmonic analysis of sea level height time series. J. Geodesy 88, 975—988, https://doi.org/10.1007/s00190-014-0737-5.

Sundar, D., Shankar, D., Shetye, S.R., 2005. Sea level during storm surges as seen in tide-gauge records along the east coast of India. Current Sci. 22, 1—10, https://www.jstor.org/stable/24104426.

Unnikrishnan, A.S., Shetye, S.R., Michael, G.S., 1999. Proc. Indian Acad. Sci. (Earth Planet Sci.) 108, 155—177, https://doi.org/10.1007/BF02842329.

Wijeratne, E.M.S., Woodworth, P.L., Stepanov, V.N., 2008. The Seasonal Cycle of Sea Level in Sri Lanka and Southern India. Western Indian Ocean. J. Mar. Sci. 7 (1), 29—43, https://doi.org/10.4314/wiojms.v7i1.48252.

Woodworth, P.L., 2017. Differences between Mean Tide Level and Mean Sea Level. J. Geodesy 91, 69—90, https://doi.org/10.1007/s00190-016-0938-1.

Wouters, B., Riva, R.E.M., Lavallée, D.A., Bamber, J.L., 2011. Seasonal variations in sea level induced by continental water mass: First results from GRACE. Geophys. Res. Lett. 38, L03303, https://doi.org/10.1029/2010GL046128.

Oceanologia (2020) 62, 460—477

Available online at www.sciencedirect.com

ScienceDirect

journal homepage: www.journals.elsevier.com/oceanologia

ORIGINAL RESEARCH ARTICLE

Physical oceanographic conditions and a sensitivity study on meltwater runoff in a West Greenland fjord: Kangerlussuaq

Dennis Monteban[a,b,*], **Jens Olaf Pepke Pedersen**[a], **Morten Holtegaard Nielsen**[c]

[a] *DTU Space, Technical University of Denmark, Lyngby, Denmark*
[b] *Norwegian University of Science and Technology, Trondheim, Norway*
[c] *Marine Science & Consulting ApS, Copenhagen, Denmark*

Received 28 November 2019; accepted 29 June 2020
Available online 11 July 2020

KEYWORDS
Arctic fjord;
Hydrodynamic model;
MIKE 3;
Water masses;
Meltwater runoff;
Kangerlussuaq fjord

Summary In this paper, we discuss the first setup of a hydrodynamic model for the fjord-type estuary Kangerlussuaq, located in West Greenland. Having such a high-fidelity numerical model is important because it allows us to fill in the temporal and spatial gaps left by in situ data and it allows us to examine the response of the fjord to changes in ice sheet runoff. The numerical model is calibrated against in situ data, and a one-year simulation was performed to study the seasonal variability in the physical oceanographic environment and the fjord's response to changing meltwater runoff. The fjord consists of two distinct parts: a deep inner part that is 80 km long with weak currents and a shallow part that covers the outer 100 km of the fjord connected to the ocean. The outer part has very fast currents (~1.3 m/s), which we suggest prevents winter sea ice formation. The dominant currents in the fjord are oriented parallel to the long axis of the fjord and are driven by tides and (during summer) freshwater inflow from meltwater-fed rivers. Furthermore, mixing processes are characterized by strong tidal mixing and bathymetric restrictions, and the deep-lying water mass is subject to renewal primarily in wintertime and is almost dynamically decoupled from the open ocean during summertime. Finally, a sensitivity study on the changing meltwater runoff was performed, showing that in-

* Corresponding author at: DTU Space, Technical University of Denmark, Lyngby, Denmark.
E-mail address: dmont@space.dtu.dk (D. Monteban).
Peer review under the responsibility of the Institute of Oceanology of the Polish Academy of Sciences.

Production and hosting by Elsevier

https://doi.org/10.1016/j.oceano.2020.06.001

creasing freshwater runoff considerably strengthens stratification in the upper 100 m of the water column in the inner part of the fjord.

1. Introduction

The largest ice mass in the Northern Hemisphere, the *Greenland Ice Sheet* (GIS), experienced a mass loss of 3,902 ± 342 billion tonnes of ice between 1992 and 2018 (Shepherd et al., 2020). The most pronounced effects of climate change, such as the increase in surface air temperature, occur in the Arctic region due to polar amplification (IPCC, 2013), which has increased the freshwater runoff (Trusel et al., 2018). The freshwater discharged from the GIS mostly transits through fjords, where it can be significantly modified before reaching the open ocean (Cottier et al., 2010). Therefore, fjords are considered to be a vital link between the inland ice and the ocean (Straneo and Cenedese, 2015), and it is essential to have a detailed understanding of fjord dynamics. Moreover, an improved understanding of the drivers of fjord circulation is required to explain regional climate changes in Greenland and how the fjord circulation may change in response to changing boundary conditions (Straneo et al., 2013).

Early studies on Arctic fjords were primarily conducted because fjords contain information on past ice sheet variability and sedimentary records (e.g., Storms et al., 2012). Another motivation was that fjord systems contain complex marine ecosystems and because local communities are dependent on fjords for fishing and hunting (e.g., Born and Böcher, 2001). It was relatively recently that the physical oceanographic environment of fjords has been the main focus (Cottier et al., 2010), and such knowledge will allow for a better interpretation of fjord-related research.

The most accurate method to obtain the physical conditions in Arctic fjords is by collecting in situ measurements. However, the harsh Arctic environment, the scale of individual fjords, the number of fjords and the range of time- and space-scales over which important processes occur make it logistically difficult and expensive to collect large amounts of in situ data that are representative of the whole fjord. Therefore, a major limitation in the Arctic is the lack of in situ data. Another approach to obtain an understanding of the physical state of a fjord is modelling. Although numerical models are a simplification of reality, they can act as an additional tool to fill in the spatial and temporal gaps in in situ data and consequently understand the physical processes at work. In addition, numerical models allow one to examine the fjords response to changes in boundary conditions.

A growing body of literature has studied Greenlandic fjord systems (see e.g., Catania et al. (2020) and Rignot et al. (2012) for an overview). These studies have looked at fjords from two different perspectives. The first perspective is that the fjord is a mixing zone where the relevant flow transports heat into the fjord and directly towards the glacier terminus (Cowton et al., 2016; Holland et al., 2008; Mortensen et al., 2011; Rignot et al., 2010; Sutherland et al., 2014), which affects glacial melting. The other view also regards fjords as mixing zones, but the focus is on the transformation and export of meltwater runoff from the GIS towards the ocean (Straneo et al., 2011), potentially influencing shelf circulation (e.g., Murray et al., 2010).

In this paper, we focus on the fjord Kangerlussuaq (also called Søndre Strømfjord), located in West Greenland. This fjord receives large quantities of freshwater from meltwater-fed rivers each year. Van As et al. (2018) found that the average discharge of the main meltwater river flowing into the fjord, i.e., the Watson River, increased by 46 percent between 2003—2017 compared to the 1949—2002 average. Moreover, the interannual variability in the meltwater runoff increased considerably. However, it is not clear how these variations in meltwater runoff have influenced the fjord Kangerlussuaq. An increase in the annual volume of freshwater runoff from the GIS influences the physical structure of the water column, including the temperature-salinity structure, the strength of the stratification (Kjeldsen et al., 2014; Mortensen et al., 2013) and the primary production (e.g., Arendt et al., 2010; Dziallas et al., 2013). To understand the fjord's response to changing meltwater runoff and the physical oceanographic conditions in general, a hydrodynamic model was established in this study. Additionally, this model is also used to perform a sensitivity analysis by changing the meltwater runoff.

The paper is structured as follows: in Section 2, the study area is described together with the available measurements and observations. Datasets of the freshwater input, the atmospheric parameters and the sea ice cover are used to force the model. In Section 3, the setup of the numerical model is presented, as well as all the model parameters and parameterizations, the model domain and the boundary conditions. We performed a one-year simulation from March 2005 until March 2006 with input data that are a combination of data from multiple years and some are somewhat idealized (meltwater runoff). Therefore, the aim is to determine the seasonal dynamics and the temperature-salinity structure of the fjord as a whole during the period of one year. To gain confidence in the model's performance, we calibrated the model against in situ data of the water level and vertical profiles of the temperature and salinity. This calibration procedure is described in Section 4 and is divided into a barotropic and baroclinic part. The main outputs of the model are presented and discussed in Section 5, which is divided into three parts: 1) the circulation pattern in the fjord, 2) the seasonal dynamics of the water masses and 3) a sensitivity study towards meltwater runoff. Finally, some concluding remarks are presented in Section 6.

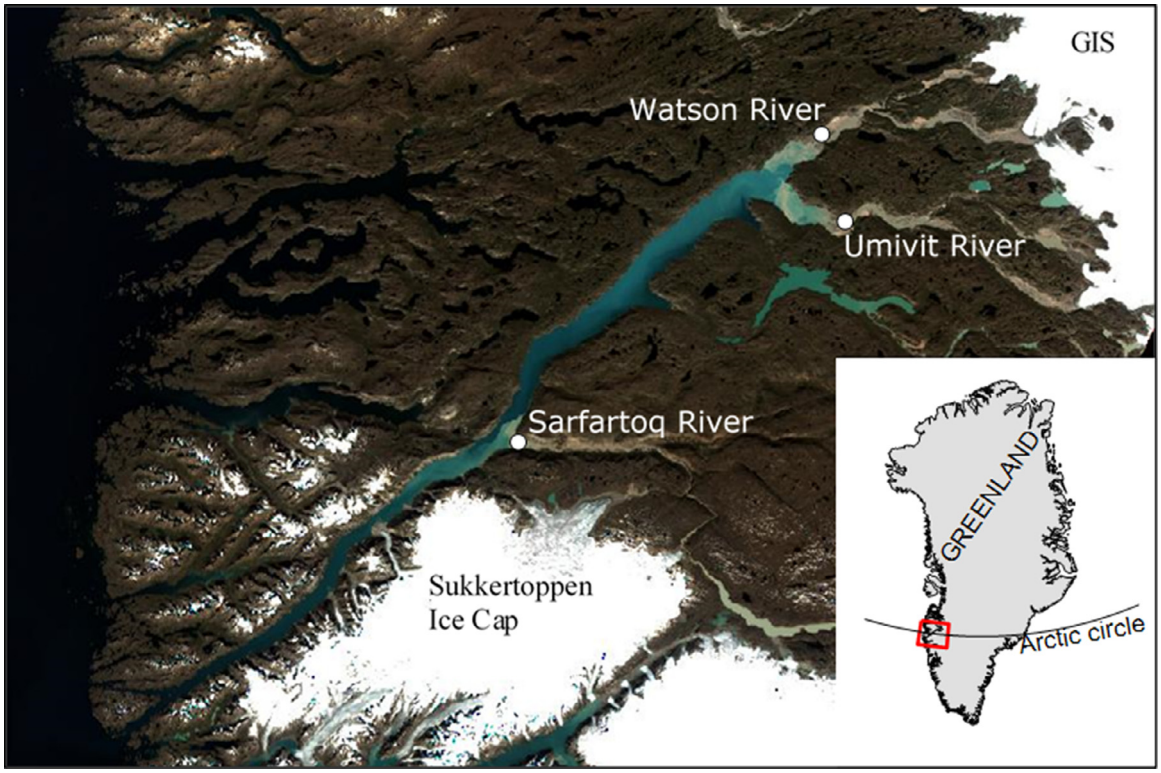

Figure 1 Sentinel-2 true-colour image of the fjord Kangerlussuaq, acquired 31 July 2017. The locations where the three main meltwater rivers enter the fjord are indicated.

2. Study area and observations

2.1. Regional setting

The fjord Kangerlussuaq is a large fjord located at the Arctic circle in West Greenland (Figure 1) and is classified as a fjord-type estuary (Lund-Hansen et al., 2010). The fjord is 180 km long, and there are two branches at the mouth of the fjord that connect the fjord with the open ocean. Further west from the mouth of the fjord at the continental slope, the West Greenland Current is located. The West Greenland Current is a continuation of the East Greenland Current and the Irminger Current, which are governed by the cold and relatively fresh water of Arctic origin and warm and salty water that originated in the Atlantic, respectively (Myers et al., 2007; Sutherland and Pickart, 2008).

In Figure 3, the bathymetry of the fjord Kangerlussuaq, which was surveyed by the Danish Geodata Agency, is presented. The fjord can be divided into two distinct parts: the outer 100 km of the fjord is shallow (30—60 m) and narrow (~1.5 km). The inner part is much deeper (up to 300 m) and wider (~5 km). A steep slope defines the transition between the two parts of the fjord where the bottom rises approximately 215 m over 13 km and is located close to the mouth of the Sarfartoq River (Figure 1).

2.2. Freshwater sources

The fjord receives freshwater from snowmelt, sea-ice melt, precipitation, local glaciers and the GIS. Large quantities of freshwater runoff enter the fjord in the summertime primarily from three rivers; the Watson River (66°57′54″N, 50°51′50″W) flows into the northeast head of the fjord, the Umivit River (66°50′2″N, 50°48′37″W) enters at the southeast head of the fjord and the Sarfartoq River (66°29′30″N, 52°1′30″W), which enters in approximately the middle of the fjord. The rivers drain meltwater from the GIS and the Sukkertoppen ice cap (Figure 1). Hudson et al. (2014) estimated the catchment area of each river based on the ice surface and basal topography, and this area is 3639 km^2, 6320 km^2 and 5385 km^2 for the Watson River, the Umivit River and the Sarfartoq River, respectively. The catchment area of the Watson River was also determined in multiple previous studies, and this value differs significantly from one study to the other. For instance, catchment areas of 9743 km^2 (Hasholt et al., 2013), 6130 km^2 (Mernild et al., 2010), 12547 km^2 (van As et al., 2012) and 12000 km^2 (Lindbäck et al., 2015) have been reported. Field measurements of the discharge of the Watson River were conducted by Hasholt et al. (2013) from 2007 to 2010. The peak discharge was usually observed in July/August, and a peak flow of 1620 $m^3\ s^{-1}$ was measured. The flow in the rivers is almost zero from October/November until April/May each year, and during 2007—2010, the average annual total discharge volume was 3.7 km^3.

2.3. Atmospheric and sea ice observations

Meteorological observations at an elevation of 50 m were obtained from the *Danish Meteorological Institute* (DMI) weather station, located at the airport of Kangerlussuaq (67°01′N, 50°42′W), which includes the wind speed and

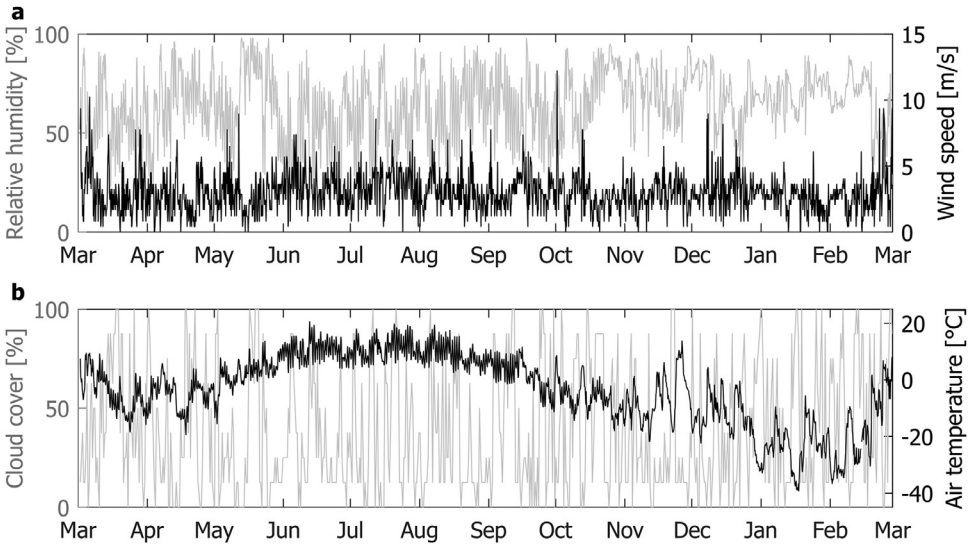

Figure 2 Observations from the DMI weather station, located at the airport of Kangerlussuaq. (a) The relative humidity (gray line) and the wind speed corrected to a height of 10 m above mean sea level (black line). (b) The cloud cover (gray line) and the dry bulb air temperature (black line). The data are taken from Cappelen (2016).

direction, relative humidity, cloud cover and air temperature (Cappelen, 2016). The wind measurements were corrected for height (from 50 m to 10 m above mean sea level) using the wind profile power law (e.g., Shore Protection Manual, 1984). The data were sampled every 1 hour, and the data used to force the model during our one-year simulation are presented in Figure 2 for the period of March 2005 to March 2006.

The mean corrected wind speed for the one-year model simulation is approximately 3 m/s, but some relatively strong winds up to 12.2 m/s were observed. The dominant wind direction is north-easterly, which corresponds to the wind blowing out of the fjord. Typical values for the relative humidity are approximately 70%. The cloud cover varies substantially with cloud-free days (0%) and days with 100% cloud cover. The recorded air temperature varied between approximately +20°C in summer and −38°C in winter. The air temperature dropped below zero degrees around October and was negative until approximately the start of May.

Sea ice formation and breakup were studied using optical imagery collected by the *Moderate-resolution Imaging Spectroradiometer* (MODIS) onboard the Terra and Aqua satellites from the NASA Worldview application during the 2009—2017 period. The sea ice extent is necessary to force the numerical model and for the winter of the one-year model simulation (2005/2006), observations were available from the *Advanced Synthetic Aperture Radar* (ASAR) instrument onboard the Envisat satellite. Generally, initial sea ice formation starts in mid-November, and the fjord is sea ice free beginning in June. Sea ice only forms in the inner part of the fjord and reaches up to approximately 1 metre thick (Hawes et al., 2012; Nielsen et al., 2010). For the winter of 2005/2006, sea ice formation started in the beginning of December 2005 and reached its maximum areal extent at the end of December. The last sea ice floes were observed on 23 May 2006.

2.4. Water level and CTD measurements

Measurements of the water level at several locations throughout the fjord (points a, b and c in Figure 3) were conducted from June 2011 until mid-September 2011 using Solinst Levelogger Gold recording devices (Solinst Canada Ltd, Georgetown, Ontario, Canada). These devices were placed under the waterline during low tide, and they measured the pressure at 5 min intervals. The water levels are computed from the pressure difference as the tidal wave passes, and a mean spring tidal range of 3.5 metres is found. Moreover, the tidal wave travels in approximately 3.5 hours from the open ocean (point a in Figure 3) to the head of the fjord (point c in Figure 3). The tidal character may be defined by the form factor, F, which is the sum of the two main diurnal components (K_1, O_1) divided by the sum of the two main semidiurnal components (S_2, M_2) and reads as follows (Courtier, 1939):

$$F = \frac{(K_1 + O_1)}{(M_2 + S_2)}. \quad (1)$$

Classical harmonic analysis using the tidal fitting toolbox (Grindsted, 2020) was used to compute the four tidal constituents in Eq. (1). Based on the form factor, four different types of tides can be distinguished. At the head of the fjord, the form factor has a value of 0.24, which means that the tidal character is classified as semidiurnal.

Conductivity, temperature and pressure data were collected during two surveys that were carried out on 3—5 August 2005 and on 26—27 February 2006. These measurements are described in Nielsen et al. (2010). During the survey in August, a total of 16 vertical profiles were made along the entire fjord using a 19plus SEACAT Profiler (Seabird Electronics, Bellevue, WA, USA). The survey in February includes 6 different vertical profiles that were made on the sea ice-covered part of the fjord; hence, only the inner part of the fjord was surveyed.

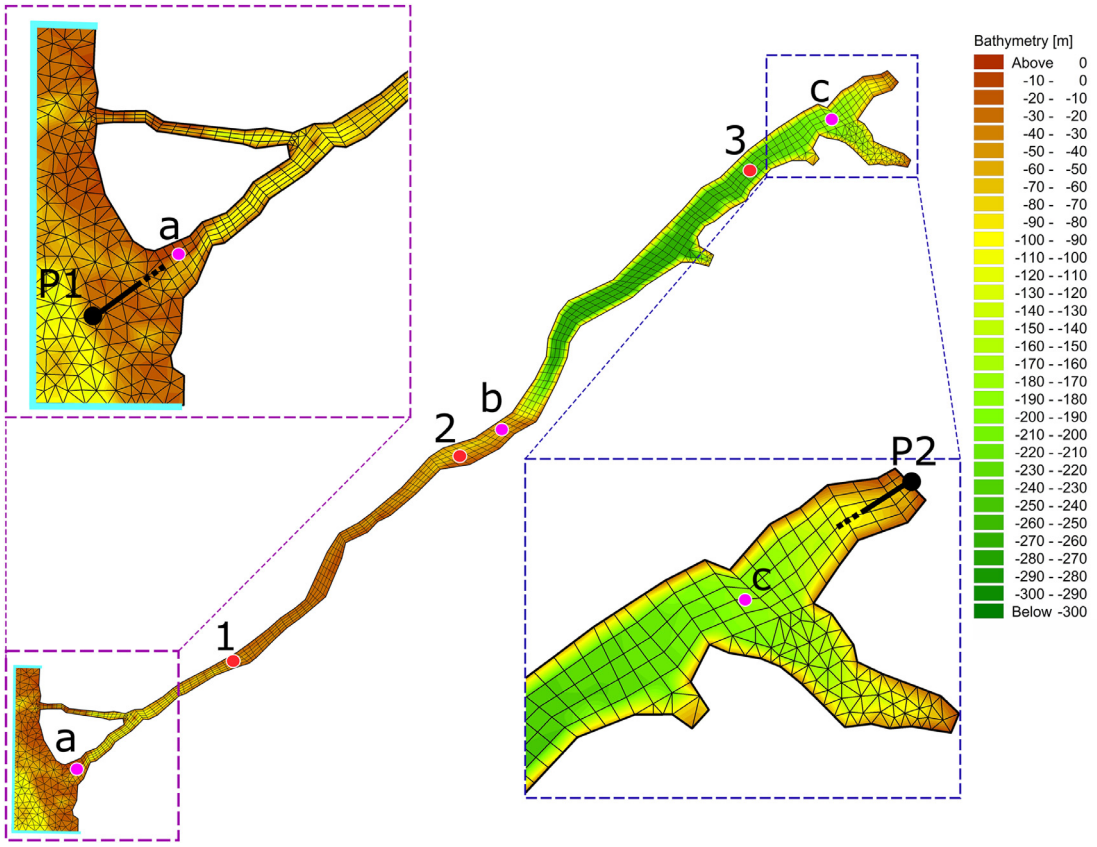

Figure 3 The model domain, bathymetry and horizontal computational mesh. The three red dots (points 1, 2 and 3) indicate the positions of the calibration points for the baroclinic part, and the three magenta dots (points a, b and c) show the calibration points of the barotropic part. The points P1 and P2 shown in the magnifications of the fjord show the beginning and end of the vertical cross sections, which are shown in multiple figures in this paper, respectively. Furthermore, the solid light blue line at the mouth of the fjord depicts the open ocean boundary.

3. Model description

The numerical model of the fjord Kangerlussuaq was implemented using the commercially available three-dimensional MIKE 3 Flow Model (2016 version) software. The MIKE 3 model is well documented, and a comprehensive description can be found in DHI 2016b. An overview of all the input parameters, the choice of the different modules in MIKE 3 and the sources of the boundary and initial conditions used in the simulations are summarized in Table 1. The model setup is described in detail in the remainder of this chapter.

3.1. Model setup

The MIKE 3 model numerically solves the *Reynolds-averaged Navier-Stokes* (RANS) equations with the assumptions of Boussinesq and hydrostatic pressure using a cell-centred finite volume method (DHI, 2017). The RANS equations are closed with a turbulent scheme by adopting the eddy viscosity concept, where the vertical and horizontal eddy viscosities are represented by the standard k-ε model (Rodi, 1984) and the Smagorinsky formulation (Smagorinsky, 1963), respectively.

The bathymetry of the modelled fjord, the model domain and the horizontal computational mesh are presented in Figure 3. The computational mesh is a combination of triangular elements and quadrangular grid cells. We anticipated a pre-dominant water flow direction along the long axis of the fjord with limited across-fjord variability. Therefore, we used quadrangular grid cells in the main part of the fjord that allow for a coarser resolution in the along-fjord direction than in the across-fjord direction; hence, the number of elements and the computation time are reduced. Moreover, the quadrangular cells simulate the flow more accurately compared to the triangular elements in this case because the elongated quadrangular cells favour water flow along the element, while the triangular elements enhance divergence in the water flow (DHI, 2016a). The computational mesh has 1984 elements (computational cells) in the surface layer. The smallest element has a characteristic length of approximately 160 m, and the largest cell has a dimension of approximately 1000 m, which is directed along the long axis. The vertical domain was discretized using 40 vertical layers with a resolution of 1 m at the surface layer down to 15 m at the bottom. The first 5 vertical layers starting at the surface are terrain-following sigma layers. The remaining vertical layers are z-layers, which do not follow the bottom terrain and are defined at fixed depths.

Table 1 Overview of the input parameters and module options used in the MIKE 3 model.

Input Parameter	Value or module option
Horizontal mesh	Resolution (min, max) = (160, 1000) m
Vertical mesh	Combined sigma/z-level; 5 sigma layers to a depth of 10 m and 35 z-layers. Resolution (min, max) = (1, 15) m
Time period	1 March 2005–01 March 2006
Maximum time step	300 s
Solution technique	Higher order scheme
Eddy viscosity	Horizontal eddy viscosity: Smagorinsky formulation Vertical eddy viscosity: k-ε model
Bed resistance	Constant roughness height: 0.05 m
Dispersion	Horizontal dispersion coefficient: 1 Vertical dispersion coefficient: 0.1
Coriolis forcing	Constant in domain
Atmospheric forcing	Observations available from the DMI weather station located at the airport of Kangerlussuaq and includes - Wind speed and direction - Air temperature - Cloud cover - Humidity
Ice coverage	Sea ice coverage derived from Envisat satellite imagery Sea ice roughness: 0.01 m
Initial conditions	Water level 0 m Velocities 0 m s^{-1} Salinity from February 2006 measurements (Nielsen et al., 2010) Temperature from February 2006 measurements (Nielsen et al., 2010)
Boundary conditions	Rivers average discharge of 2007-2010 observations (Hasholt et al., 2013) Sea water levels from DTU global tide model Sea salinity and temperature from the Global Ocean Physics Reanalysis product (Copernicus) Sea current velocities from the Global Ocean Physics Reanalysis product (Copernicus)

3.2. Initial and boundary conditions

The initial conditions (simulation started on 01 March 2005) were obtained from the CTD profiles taken on 26 February 2006. Although these measurements are from a different year, we used them because the temperature and salinity distributions throughout the fjord in wintertime are very homogeneous and relatively similar from year to year (Nielsen et al., 2010). The initial conditions in the outer, shallow part of the fjord were obtained by interpolating between the measurements of the vertical profiles in the inner part of the fjord and the values at the open ocean boundary obtained from the E.U. *Copernicus Marine Environment Monitoring Service* (CMEMS) Global Ocean Physics Reanalysis product (CMEMS, 2018). If these initial conditions were not representative of those in the outer part of the fjord, we would expect the model conditions in this region to adjust towards realistic values within a much shorter timescale than the length of the experiment. Since we do not simulate such an adjustment, we argue that this interpolation provides a close approximation to the real conditions within the outer part of the fjord. The lateral boundary condition located outside the mouth of the fjord combines the water level, current velocities, temperature and salinity. Two different sources of data for the open ocean boundary were used. The water level was predicted based on tidal constituents from the DTU10 global ocean tide model (Cheng and Andersen, 2010). This model includes 10 tidal constituents and has a resolution of 0.125° × 0.125°. The output of the DTU10 global ocean tide model compares well with the water level measurements at the mouth of the fjord, with the difference generally being less than 10 cm. The sea water velocities, temperature and salinity were taken from the CMEMS global ocean physics reanalysis product (CMEMS, 2018). This product has a horizontal resolution of 1/12°, 50 vertical layers down to a depth of 5500 metres and provides daily mean values.The lateral boundary is indicated by the solid light blue line in Figure 3. The barotropic part of the open boundary was specified using Flather's boundary condition (Flather, 1976), which is a combination of the water level and sea water velocities. The water velocities are not necessary to force the model but are imposed for stability reasons. Furthermore, the temperature and salinity were defined as Dirichlet boundary conditions.

The following atmospheric data were included in the model: wind speed and direction, dry bulb air temperature, cloud cover and relative humidity. Observations of these parameters were obtained from the DMI weather station (Figure 2), and these observations are taken as representative values for the entire fjord. The validity of this assumption was checked by comparing the atmospheric data obtained at the Kangerlussuaq airport with those at the

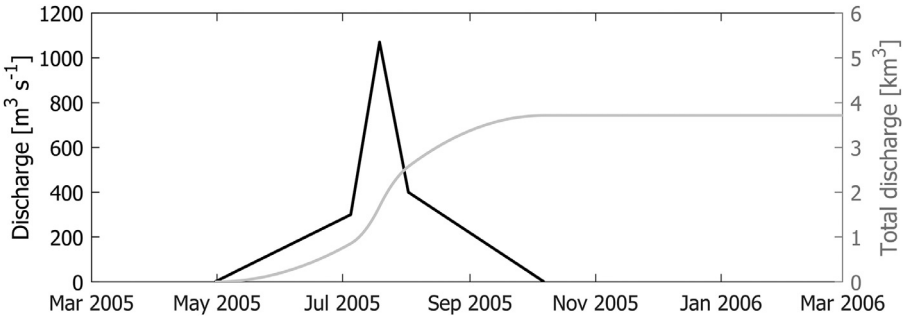

Figure 4 Estimated discharge from the Watson River used as input to the model. The solid black line shows the discharge per second, and the gray solid line shows the accumulated discharge.

Sisimiut airport, which is located further north and closer to the ocean (the comparison is not shown here). Because the inland climate is different from the coastal climate, using values from the Kangerlussuaq airport for the entire fjord may lead to a loss of realism for the atmospheric input data close to the coast. Precipitation and evaporation are neglected because they are assumed to be negligible for our study area. This is because the area of Kangerlussuaq is exceptionally dry due to orographic shielding by the Sukkertoppen ice cap (Box et al., 2006). This dryness, together with water losses from evaporation, causes the contribution of precipitation to be minimal compared to the ice sheet runoff (Hasholt et al., 2013). An input file of the ice concentration was prepared based on Envisat ASAR satellite imagery during November 2005 to May 2006. This file defines the location of the sea ice (ice concentration of 100%) and covers the inner, deep part of the fjord to approximately the Sarfartoq River from December to May.

3.3. Freshwater input

The three meltwater rivers were represented in the model as point sources, which are placed in the surface layer. A 'simple source' option was used where the source discharge only contributes to the continuity equation (DHI, 2017). The salinity was set to 0 psu (practical salinity unit) (UNESCO, 1987), and the runoff temperature was set to 1°C. The temperature as well as the discharge of the Watson River has some small-scale fluctuations, where the temperature of the Watson River typically varies between 0°C and 2°C (unpublished data). This is because of the day and night cycle and the resulting changes in air temperature. However, because we are interested in the general circulation pattern in the fjord system, we neglected all the high frequency variations found in the meltwater runoff. Furthermore, we generated an idealised time-series of the discharge, which was based on the average annual discharge of the Watson River during 2007—2010 (Hasholt et al., 2013), see Figure 4. The peak discharge is assumed to occur in late July (Julian day 200) and has a value of 1070 $m^3\ s^{-1}$. Based on our idealised time-series of runoff, the average accumulated annual discharge of the Watson River is 3.7 km^3. There are no data on the discharges of the Umivit and Sarfartoq Rivers. Therefore, we assumed the same shape as the Watson River discharge (Figure 4), but we scaled the values based on the catchment areas given by Hudson et al. (2014). Therefore, the discharge of the Watson River is multiplied by factors (6320/3639) and (5385/3639) for the Umivit River and the Sarfartoq River, respectively. The resulting total annual accumulated discharge of the Umivit River is 6.4 km^3 and 5.5 km^3 for the Sarfartoq River.

4. Model calibration

The model calibration was divided into barotropic and baroclinic parts. It was not possible to perform a validation procedure because of the lack of adequate in situ data.

4.1. Barotropic part

For the barotropic part of the calibration, the simulated surface elevation was calibrated against the water level measurements. However, these measurements (30 July 2011 to 01 September 2011) are not available for our simulated time period (March 2005 to March 2006). Therefore, we performed an additional simulation for the period when the water level measurements were taken. The model setup, sources of the boundary conditions and sources of the atmospheric forcing for the new time period were all the same (Table 1). New input data for the boundary conditions and the atmospheric forcing were generated, but the initial conditions of the salinity and the temperature were kept identical to the 2006 observations. The potential differences in the vertical profiles of salinity and temperature between the simulation periods have a very small influence on the water level variation. This was checked by running the same simulation but with a constant initial temperature of 0°C and salinity of 24 psu. The difference in water level between these simulations was less than 0.02 $\pm$ 0.025 m averaged over points a, b and c (see Figure 3).

The resolution of the horizontal computational mesh was the main parameter altered during the calibration of the barotropic part. A sufficiently fine mesh was required to reproduce the observed water levels in the fjord. The influence of the bed roughness was found to be minor and therefore kept as the default value. The model simulation is compared with the observations at points a, b and c in Figure 3. The model simulation is in good agreement with the observations (Figure 5), with a root mean square error of 0.12 m at point c. The phase of the tidal wave is very well reproduced throughout the fjord, meaning we

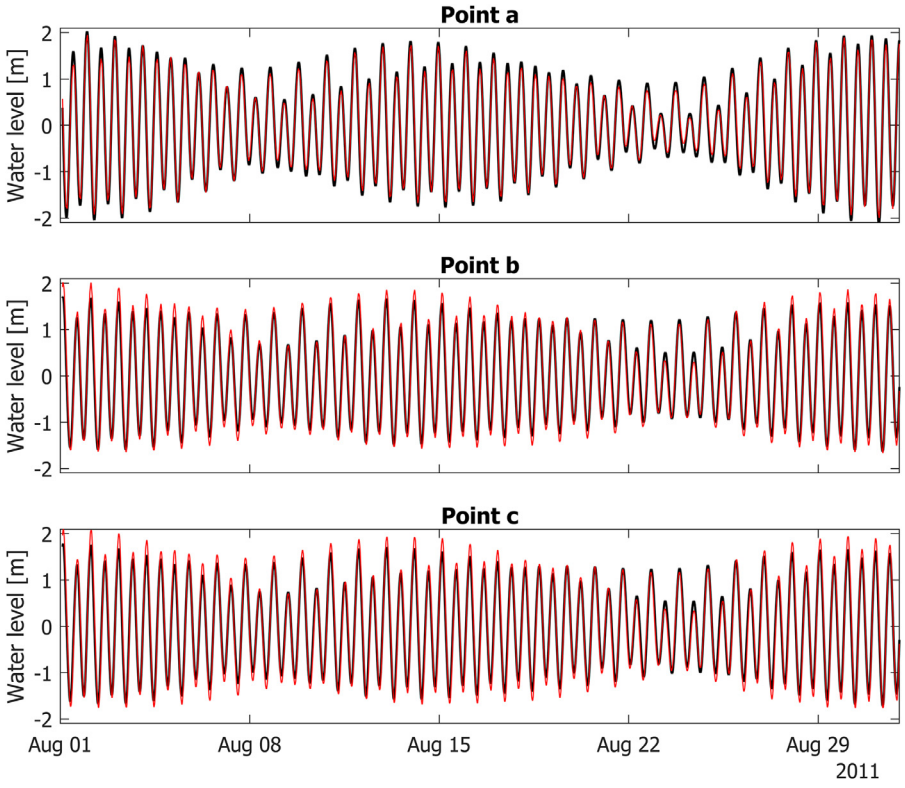

Figure 5 Observed water level (black line) and simulated water level using MIKE 3 (red line) at points a, b and c, as indicated in Figure 3, for a one-month period.

have a good representation of the bathymetry, as this is the main contributor to the phase of the simulated tidal wave. Some discrepancies are present, with a small overestimation during spring tide and an underestimation during neap tide. These minor discrepancies are already observed when comparing the input of the model (from the DTU10 global ocean tide model) at the open ocean boundary with measurements taken outside the fjord (results not shown here). Therefore, the small errors are due to the input of the model at the open ocean boundary, and the model itself reproduces the tides very well.

4.2. Baroclinic part

The second step of the calibration involved comparing vertical profiles of density, salinity and temperature at three points (points 1, 2 and 3 in Figure 3). Two main parameters were altered during this part of the calibration: the type and resolution of the vertical mesh and the vertical dispersion coefficient. Only a few terrain-following sigma layers were adopted because using more of these layers resulted in too much mixing in the deep inner part of the fjord. The reason for this excessive mixing is the very steep slope between the outer and inner parts of the fjord (see Figure 10 around cross section length 100,000 m). If such a steep slope is represented with terrain-following sigma layers, the grid cells are directed almost vertically, which causes significant mixing errors and results in unrealistic flows (DHI, 2016b).

Furthermore, we reduced the vertical dispersion coefficient to a value of 0.1. This low value was required to limit the amount of vertical mixing, which was found to be too large when using the default value of 1. The necessity of this low dispersion coefficient suggests that there is too much vertical mixing by default in the model.

The comparison between the simulated vertical density, temperature and salinity profiles from the calibrated model and the measurements at the three calibration points is presented in Figure 6. In general, there is a good agreement between the simulation and measurements, which gives us confidence that the main physics are well captured during summertime. A very good comparison is obtained at point 2 and point 3. At point 1, however, deviations are observed in both temperature and salinity. The simulated temperature is approximately 1—2°C warmer than that of the measurements. Moreover, the salinity in the depth range of 10—45 m is too saline. The reason for the deviation in temperature at point 1 is most likely because of the applied boundary condition at the mouth of the fjord. The resolution of the Global Ocean Physics Reanalysis product is much coarser than the vertical resolution of our model, which will lead to some discrepancies. Moreover, we checked the surface temperature of the applied boundary condition (taken from the Global Ocean Physics Reanalysis product) against the measurements made with the Solinst Levelogger recording devices during June—October 2011. The surface temperature taken from the Global Ocean Physics Reanalysis product is generally 0.5—2.5°C warmer than the measurements. This finding strengthens our suspicion that the observed deviations in the temperature at point 1 are due to errors in the applied boundary condition. Overall, the results of the

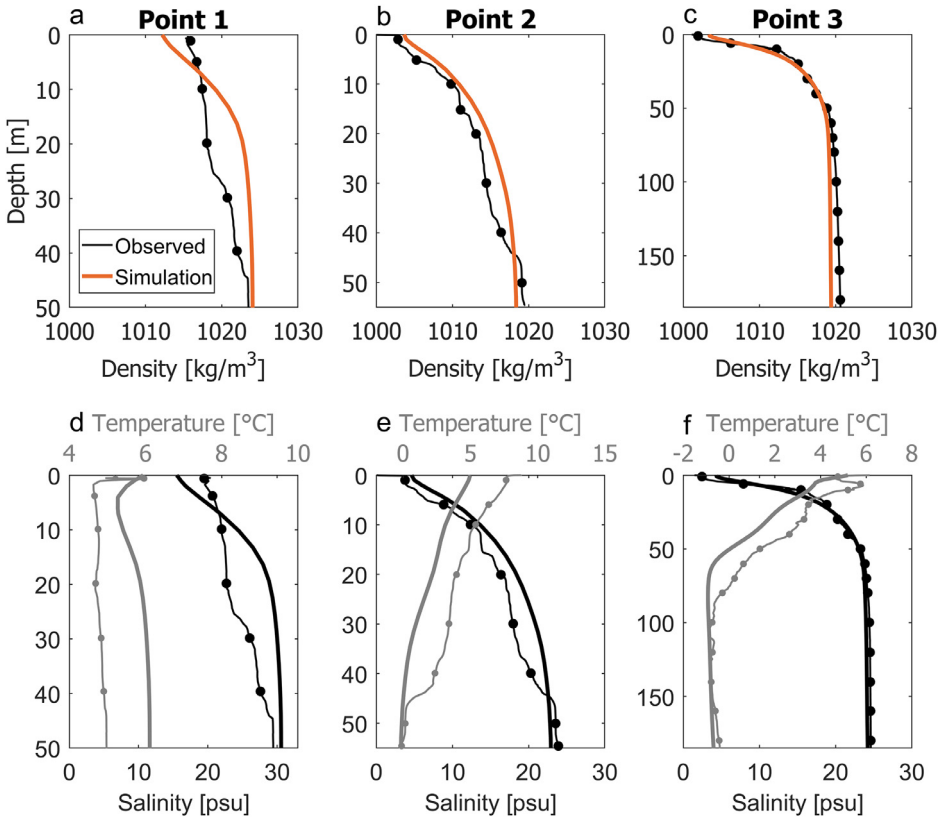

Figure 6 (a–c) Observed (black line with dots) and simulated (solid orange line) vertical profiles of the density at three locations in the fjord, as indicated in Figure 3. (d–e) Observed (line with dots) and simulated (solid line) vertical profiles of the temperature (gray) and salinity (black) at points 1, 2 and 3 for panels (d), (e) and (f), respectively. The profiles were obtained on 3 August 2005.

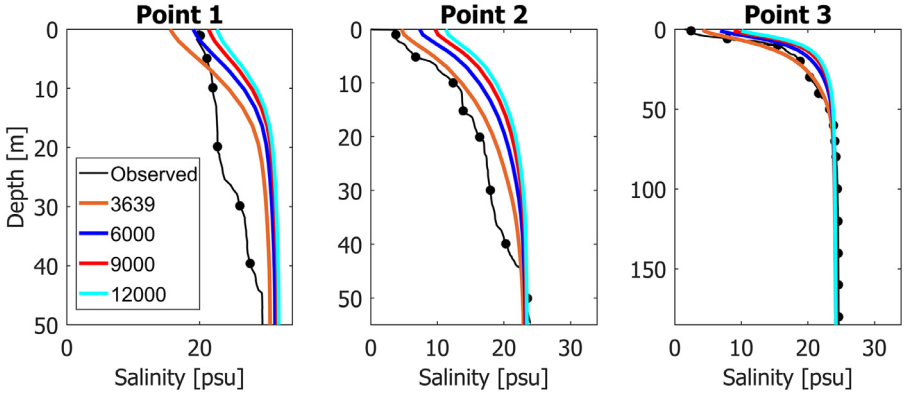

Figure 7 Sensitivity runs of varying meltwater runoff scenarios at points 1, 2 and 3, as indicated in Figure 3. The values given in the legend refer to the catchment area of the Watson River. Note that the value of 3639 km^2 is the value used in Figure 6. The profiles were obtained on 3 August 2005.

calibration are satisfactory compared with other modelling studies of Arctic fjords such as Young Sound/Tyrolerfjord (Bendtsen et al., 2014) and Hornsund (Jakacki et al., 2017).

4.3. Meltwater forcing sensitivity

As described in Section 2.2, varying Watson River catchment area values were reported in the literature, ranging from 3639 km^2 to approximately 12000 km^2. Using a larger catchment area of the Watson River would reduce the discharges of the Umivit and Sarfartoq Rivers because these values are scaled with the catchment areas. To test the accuracy of the imposed runoff forcing, additional simulations were performed using Watson River catchment areas of 6000 km^2, 9000 km^2 and 12000 km^2. The results of these simulations are presented in Figure 7 for the salinity. The temperature is not shown because the deviation between the different simulations was negligible. From Figure 7, it follows that using a larger catchment area of the Watson

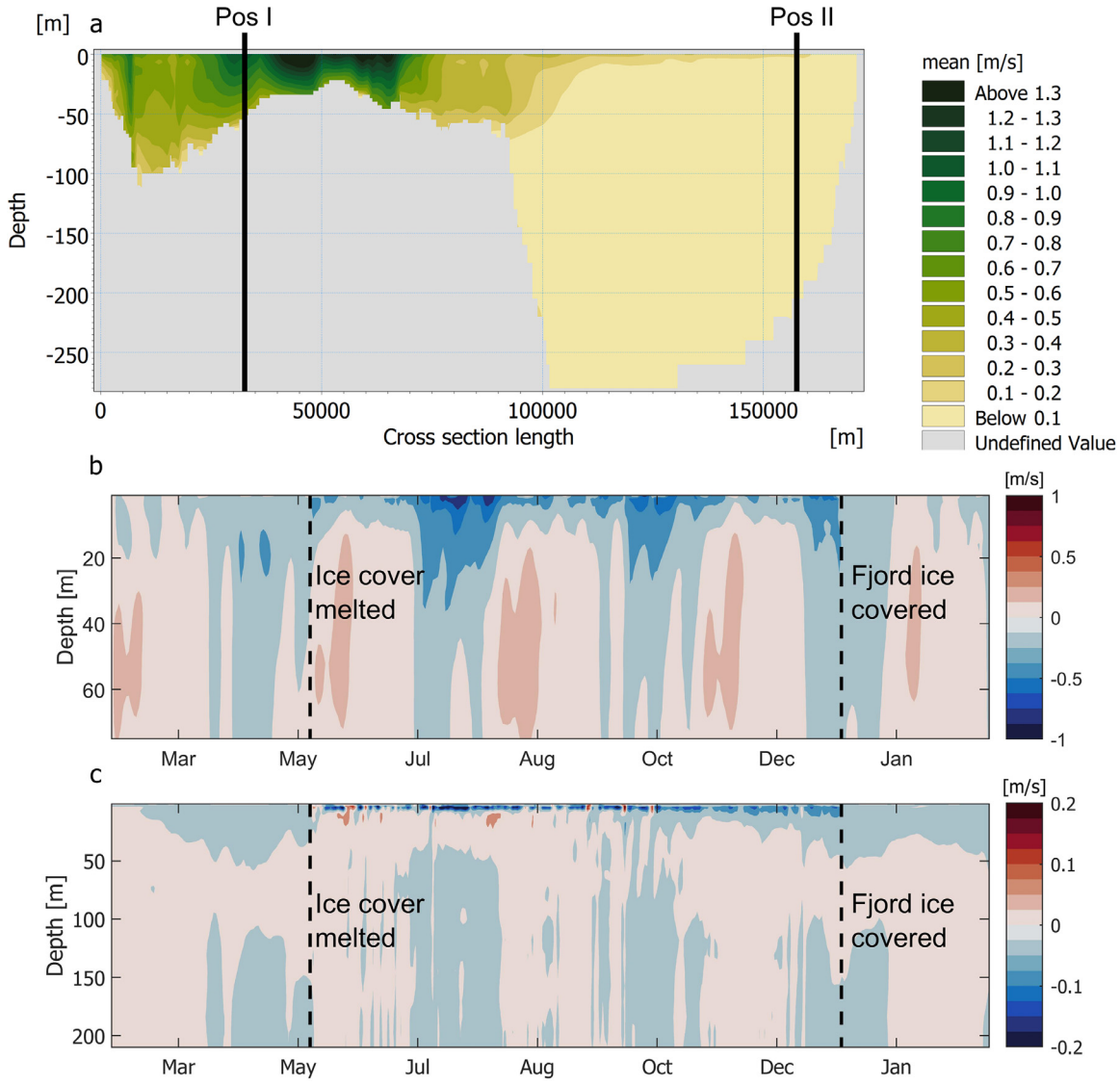

Figure 8 (a) Vertical cross section along the fjord showing the time-averaged, absolute current speed for August 2005. The start and end of the cross section along the fjord are indicated in Figure 3 with points P1 and P2, respectively. Moreover, the vertical transect follows the centreline of the fjord. Lines Pos I and Pos II indicate the locations of the vertical profiles showing the temporal variability in the mean daily currents directed into the fjord from March 2005 until March 2006 in panels (b) and (c), respectively. Note the differences in the definitions of the current speeds in (a) and (b, c); in (a), the shown values are the absolute values, while in (b and c), a positive value indicates a flow directed into the fjord.

River (and therefore a smaller discharge of the Umivit River and Sarfartoq River) results in a salinity that is too high, especially at point 2, which is close to the Sarfartoq River. The best agreement with the measurements is obtained with the used Watson catchment area of 3639 km^2, giving us confidence in the applied runoff forcing.

5. Results and discussion

5.1. Circulation pattern and currents

The circulation pattern in the fjord is primarily in the along-fjord direction, with currents in the across-fjord direction being very small. No rotational effects are observed in the fjord, which is supported by computing the internal Rossby radius (e.g., Cottier et al., 2010), which has a value of between 6–12 km at this latitude. The Rossby number is larger than the width of the fjord (approximately 5 km at its widest point), and therefore, rotational dynamics only have a minor influence on the flow. Given that the across-fjord variations are minor, the general circulation in the fjord is studied by plotting the time-averaged current speed along the length of the fjord in Figure 8a for August 2005. The currents in the deep inner part are slow, with typical time-averaged values of approximately 0.05 m/s. In the narrow and shallow middle part of the fjord, averaged values up to 1.3 m/s are observed. Moreover, extremely high instanta-

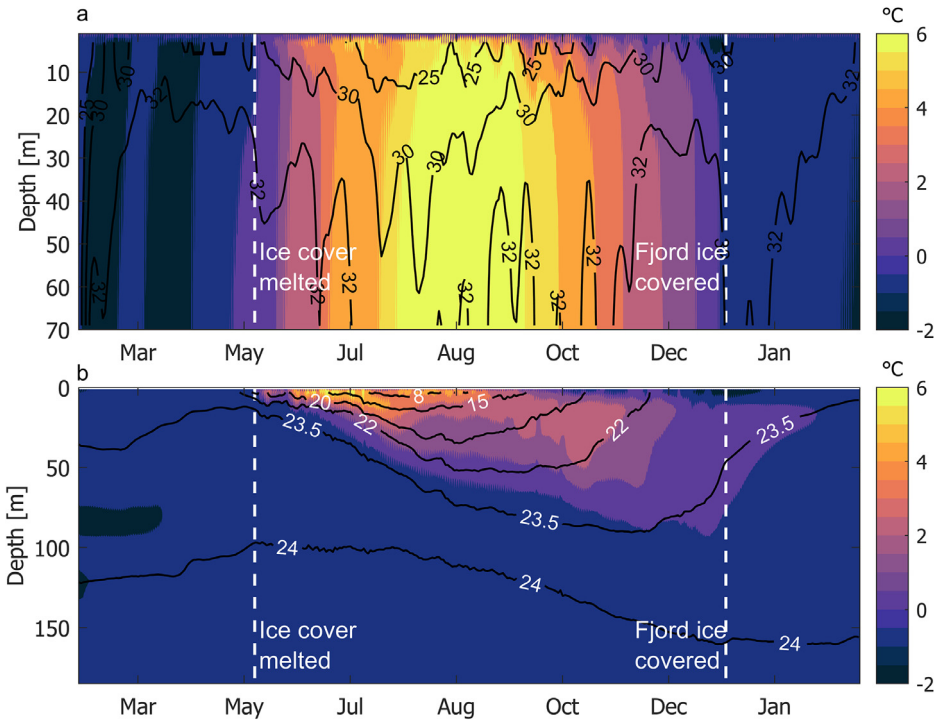

Figure 9 Simulated vertical temperature (colours) and salinity profiles (contour lines) at points 1 (panel a) and 3 (panel b) (see Figure 3) for the one-year simulation (from March 2005 until March 2006).

neous current velocities up to 3.5 m/s were found close to the Sarfartoq River (not shown here), where the width and depth of the fjord are small. The values for the month of August are higher than those in the winter months because in summertime, meltwater inflow from the rivers causes some additional barotropic currents. To show this difference, we plotted the temporal variability in the currents at a location close to the mouth of the fjord in Figure 8b and in the inner, deep part of the fjord in Figure 8c. At both locations, two different regimes are visible. From approximately May until December, there is a net outflow in the upper layer, which is the lower density freshwater-influenced water flowing out. During winter, the discharge from the meltwater rivers is negligible, and no clear vertical gradient in the currents is observed. Furthermore, the spatial variations in modelled current speed (Figure 8a) appear to be related to the spatial variations in sea ice cover in the fjord. Generally, the sea ice cover extends to the middle of the fjord around the mouth of the Sarfartoq River (Figure 1), where the currents are very strong even in winter. Therefore, we suggest that these strong currents prevent the sea ice from forming.

5.2. Seasonal dynamics of water masses

A description of the water masses in the fjord Kangerlussuaq was given by Nielsen et al. (2010), which was based on two surveys of the vertical profiles of salinity and temperature (February 2006 and August 2005) that are used as initial conditions and for the calibration of the model in this paper. By using our numerical model, we provide a more comprehensive image of the seasonal dynamics of the water masses because we can study the development of the temperature and salinity over a period of one year. The simulated seasonal variation in the vertical salinity and temperature profiles obtained at points 1 and 3 (see Figure 3) are presented in Figure 9. Cross sections of the salinity and temperature along the fjord direction during summer (01 August 2005) and winter (01 March 2006) are shown in Figure 10.

5.2.1. Mixing processes

Understanding how fjord processes modulate mixing between meltwater runoff and coastal waters is vital to understand biological processes such as primary production (Hopwood et al., 2020) and to parametrize fjords in climate models (Straneo and Cenedese, 2015). For the fjord Kangerlussuaq, the salinity and temperature structure indicate that mixing is primarily due to internal processes. The fjord is strongly stratified during summer in the inner part of the fjord. A clear layered structure of the water column is present with the salinity and temperature varying from approximately 5 psu and 7°C at the surface down to 24.5 psu and −0.5°C at the bottom, respectively (Figure 10a and Figure 10b). Wind mixing is only a relatively small contributor to mixing in the fjord because there are gradual changes observed in salinity and temperature in the upper 70 m. A well-mixed, homogeneous top layer would be present if there was strong wind-driven mixing. Therefore, the deep-lying water mass appears shielded from changes in atmospheric conditions on the time-scale of our experiments (Nielsen et al., 2010). This shielding can also be concluded from the fact that the properties of the deep-lying water masses hardly change during summer. The limited wind mixing was also found for the Uummannaq fjord system in

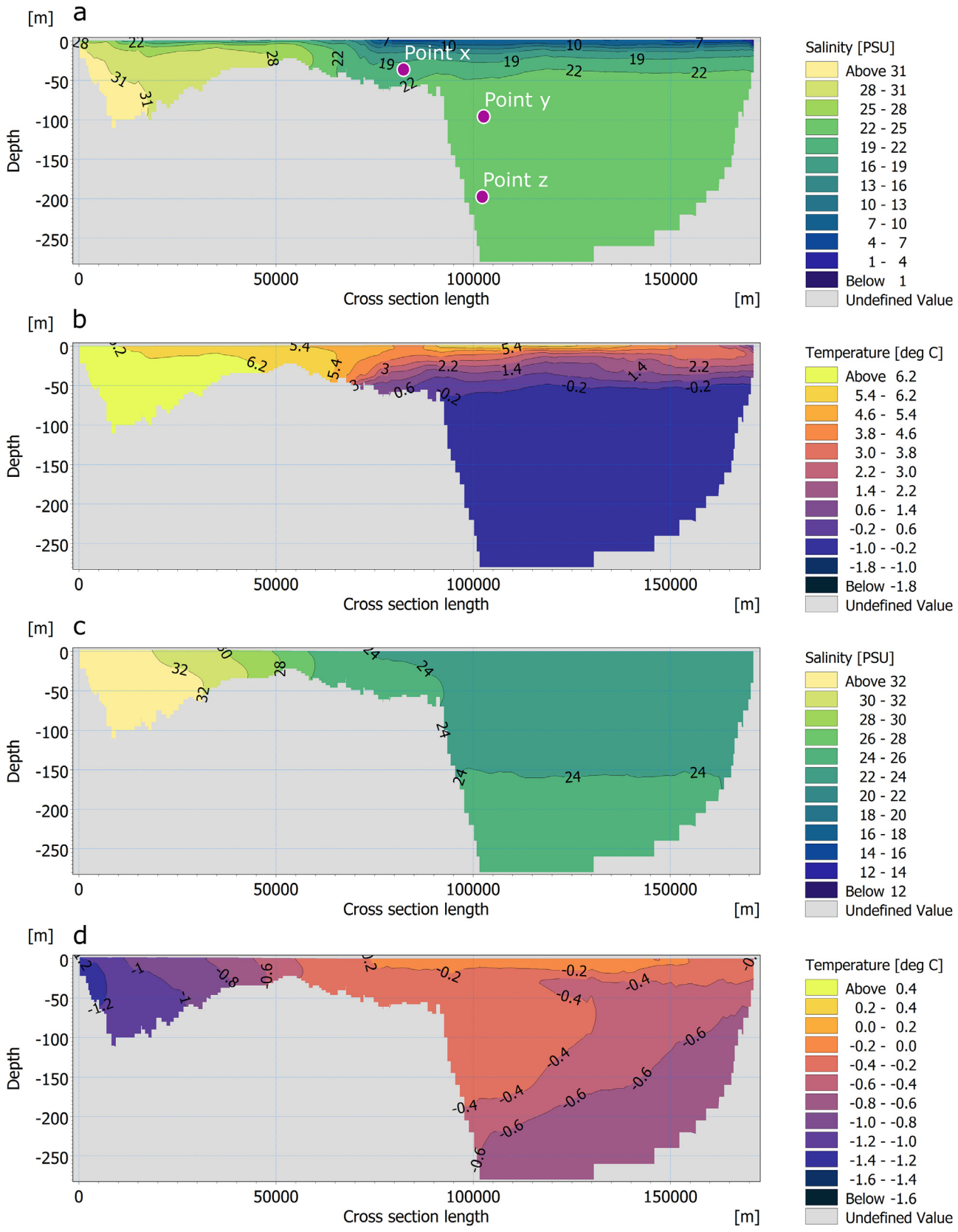

Figure 10 Vertical cross section along the fjord direction of salinity (panels a and c) and temperature (panels b and d) on 01 August 2005 (panels a and b) and 01 March 2006 (panels c and d). The mouth of the fjord is located on the left side of the figure at cross section length 0 m. The start and end of the cross section along the fjord are indicated in Figure 3 with points P1 and P2, respectively. Moreover, the vertical transect follows the centreline of the fjord. Points x, y and z are the locations where the density is extracted in Figure 11.

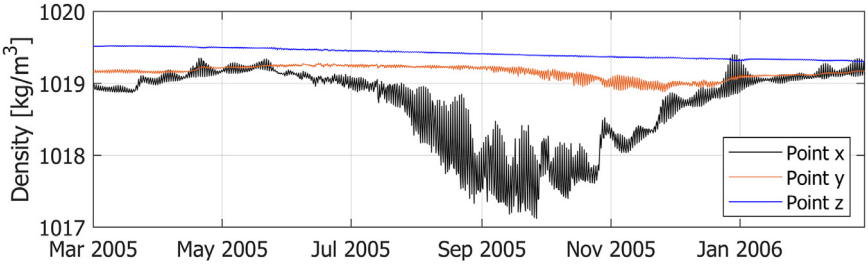

Figure 11 Seasonal density variations at three points (see Figure 10). Point x is located in the shallow inner part of the fjord at a depth of 50 m, and point y and point z are located in the inner, deep part of the fjord at depths of 100 m and 200 m, respectively.

West Greenland (Carroll et al. 2018). Both the Uummannaq fjord and the fjord Kangerlussuaq are therefore exposed to much weaker winds compared to the fjords found in southeast Greenland (Harden and Renfrew, 2012) such as the Sermilik and Kangerdlussuaq fjords (Sutherland et al., 2014). Further, the tidal currents are very fast (~1.3 m/s) over the long, shallow sill of the fjord (Figure 8). The strong tidal mixing tends to break down stratification, resulting in a relatively homogeneous water column in the shallow, outer part of the fjord in both winter and summertime (Figure 9a). Therefore, the mixing processes in the fjord Kangerlussuaq are characterized by strong tidal mixing and bathymetric restrictions (the sill).

The fjord Kangerlussuaq shows less stratified conditions in wintertime compared to summertime with salinity values ranging from 23 psu to 24 psu and temperatures from −0.1°C to 0.5°C (Figure 10c and Figure 10d). According to the observations made in February, the temperature should be close to the freezing point throughout the fjord, indicating that sea ice formation and cooling are the dominant physical processes in the winter (Nielsen et al., 2010). The MIKE 3 model is currently unable to include these processes because it does not include a sea ice module. A sea ice cover can be defined, but it is given as external data. When this cover is defined, the atmospheric conditions have no effect on the fjord's surface (sea ice acts as a barrier), and the boundary condition of salinity and temperature in the surface is defined as a Neuman boundary condition that reads as follows:

$$\frac{\partial X}{\partial z} = 0, \tag{2}$$

with X representing either the temperature or salinity, and z is the vertical coordinate. Therefore, the sea ice does not cool the water layers underneath. In addition, freshwater input due to sea ice melt and the process of brine release are not included in the model. These factors are the main drawback of the MIKE 3 model for studying Arctic fjords (Jakacki et al., 2017).

5.2.2. Water masses

Three different water masses are observed in summertime. At the mouth of the fjord, the coastal water is found, which has a salinity of approximately 33 psu and a temperature of 5°C during summer (e.g., Myers et al., 2009). In the inner deep part of the fjord, a runoff-influenced top layer reaching down to approximately 70 m is found lying on top of a deep, relatively cold and saline water mass (Figure 10a and Figure 10b). The top 20 m of this surface layer has a high temperature of 6°C. Surface insolation may generate such a small warm surface layer during summer, which is observed in many other deep Greenlandic fjords (e.g. Inall et al., 2014; Straneo et al., 2010). The lower part of the runoff-influenced water layer (depth range of 20–70 m) is less dense than the deep-lying water mass but significantly denser than the water found at the surface. From a visual analysis of Figure 9b it follows that this intermediate body of water has a salinity between 15 psu and 23.5 psu and a temperature ranging from 0°C to 4°C This water was formed between May and August 2005 in our model, when the meltwater runoff was still relatively small (see Figure 9b). The deep-lying water mass has a salinity of approximately 24 psu (Figure 10a) and a temperature of −0.5°C (Figure 10b) and is, therefore, notably different than the water mass found along the coast. This is unusual in comparison with many other Arctic fjords as the coastal water can usually be found in the inner deep basin of the fjord (Carroll et al., 2018; Gladish et al., 2015; Mortensen et al., 2018, 2011). The reason for this is that these fjords have a small sill that allows for a relatively fast exchange between the ocean and the deep-water basin. The fjord Kangerlussuaq, however, has a long shallow sill where the tidal currents are fast, which results in well-mixed conditions causing a dampened exchange between the open ocean and the water mass in the fjord.

5.2.3. Deep-lying water mass

It was suggested by Nielsen et al. (2010) that the dampened exchange between the open ocean and the water mass in the fjord causes the deep-lying water mass to be barely subject to any renewal in summer, which is confirmed by our model results. To check the density of the inflowing water over the sill, we plotted the seasonal variations in density at multiple locations in Figure 11. One point is located in the shallow part of the fjord (directly over the sill) at a depth of 50 m (point x in Figure 10a) and two points in the inner deep part of the fjord at depths of 100 m and 200 m (points y and z in Figure 10a, respectively). All points are close to the steep slope in the bathymetry near the Sarfartoq River (Figure 1). There is barely any change in density at points y and z during the year, while the density at point x shows a variation between summertime and wintertime. This variation is because the incoming water mass of the West Greenland Current at the mouth of the fjord is significantly modified (i.e., mixed with the outflowing freshwater) before reaching the deep inner part of the fjord during summertime. The result is a smaller

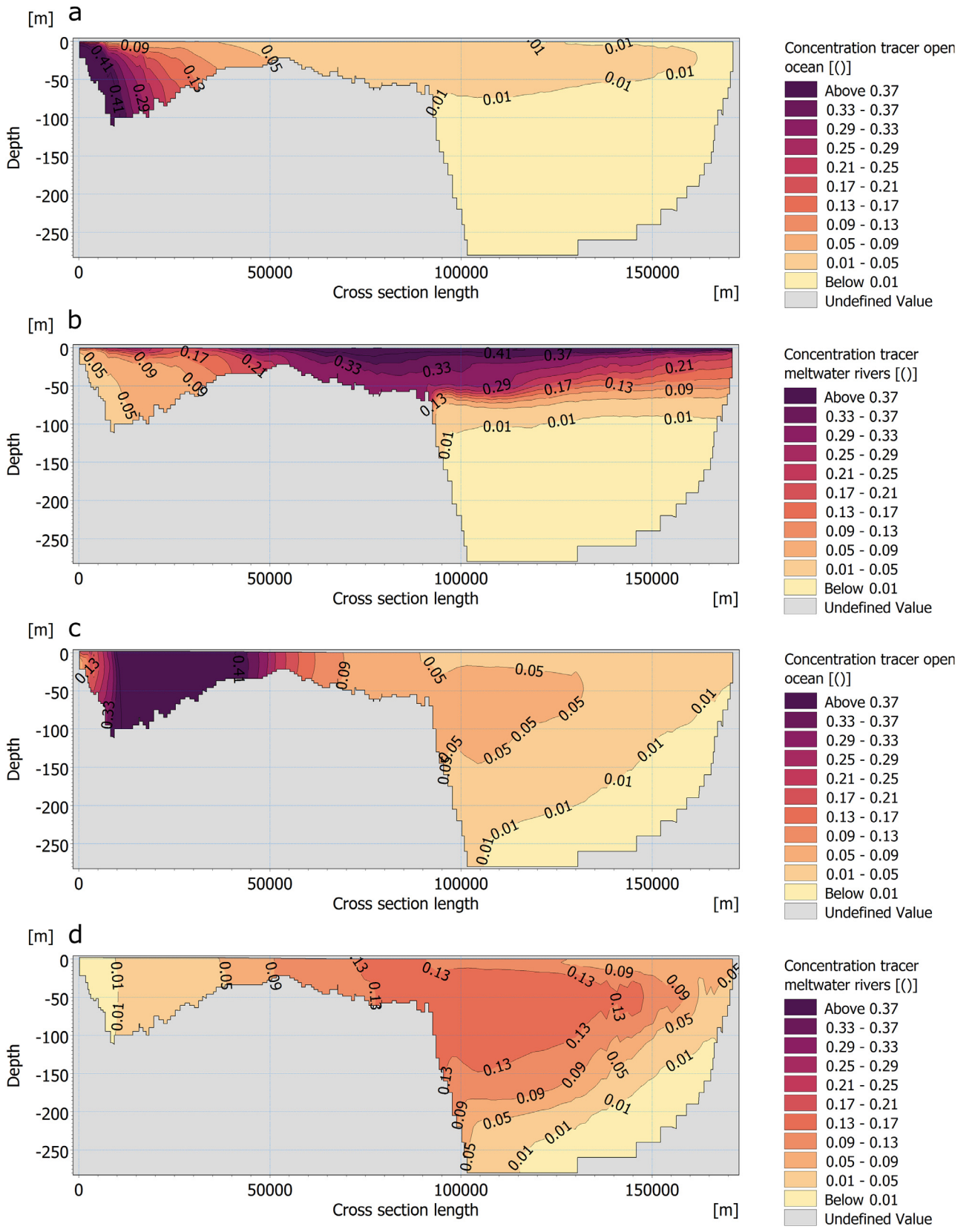

Figure 12 Vertical cross section of the tracer concentration released at the open ocean boundary (a) and (c) and of the tracer concentration released at the meltwater river sources (b) and (d) along the fjord. Subfigures (a) and (b) were obtained on 01 October 2005, (c) and (d) are from 01 March 2006.

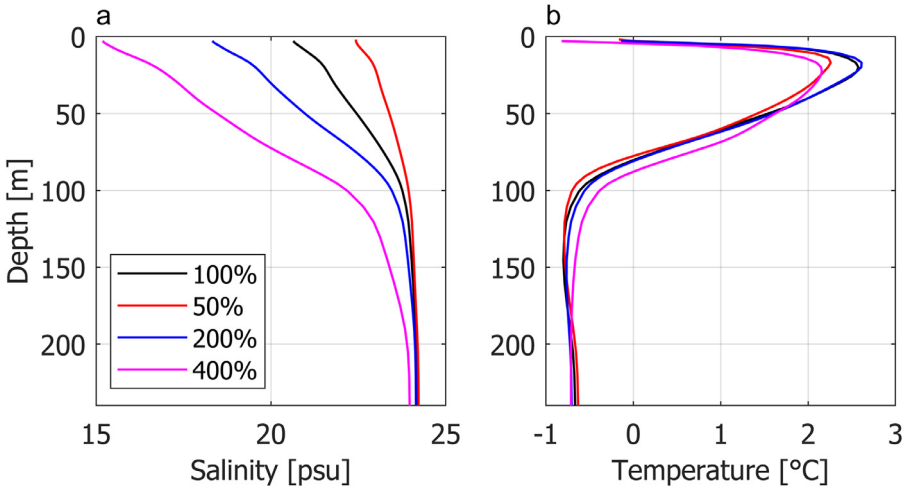

Figure 13 Vertical profiles of the salinity (panel a) and temperature (panel b) at point 3, as given in Figure 3, for the four meltwater runoff scenarios on 01 November 2005.

density at point x than at point y from approximately June to December, which suggests that there is hardly any mixing between these layers during summertime. In addition, the deep part appears to be largely dynamically decoupled from the open ocean during summertime. In other words, changes in temperature and salinity of the coastal water do not propagate into the inner, deep part of the fjord.

To investigate this further, we performed a tracer investigation using the transport module in MIKE 3 (DHI, 2016c). Conservative passive tracers with a concentration of 1 were continuously included, with one tracer at the open ocean boundary and one tracer at the three meltwater river sources. The along-fjord vertical distribution of the tracer's concentration is given in Figure 12. It follows that the deep-lying water mass is hardly influenced by the water mass of the West Greenland Current (Figure 12a) or meltwater runoff (Figure 12b) during the summertime, with tracer concentrations of approximately 0 in the deep part. The deep-lying water mass is (very slowly) renewed by the West Greenland Current water mass (Figure 12c) and meltwater runoff (Figure 12d) during wintertime. Moreover, the meltwater runoff tracer that is present in wintertime (Figure 12d) originated during summertime. This observation is in striking contrast to the typical renewal of deep basin waters, which occurs when the dense coastal water flows over the sill and replaces the deep lying-water mass in fjords (e.g., Carroll et al., 2018; Edwards and Edelsten, 1977; Gladish et al., 2015; Skogseth et al., 2005).

5.3. Meltwater runoff sensitivity analysis

We studied the fjord's response to different meltwater runoff scenarios by running three additional simulations for the March-December period. The total volume of meltwater entering the fjord was either halved, doubled or multiplied by a factor of four compared to the reference case shown in Figure 4, and these cases are referred to as the '50% case', the '200% case' and the '400% case', respectively. In terms of the total annual discharge, the 'base case' has a value of 15.66 km^3 (all three meltwater rivers combined). For the 50% case, the total annual discharge is 7.83 km^3, the 200% case has a value of 31.32 km^3, and the value for the 400% case is 62.63 km^3. For comparison, the maximum observed total annual discharge of the Watson River corresponds to an approximate multiplication of the reference case by a factor of three (van As et al., 2018); therefore, only the 400% case lies outside the range of observations.

The vertical profiles of the temperature and salinity at one location in the fjord are presented in Figure 13. The surface temperature only shows a small deviation among the four scenarios ($<$0.3°C). In contrast, the different runoff scenarios have a substantial impact on the surface salinity, where it increases by 1.8 psu for the 50% case and reduces by 2.3 psu and 5.5 psu for the 200% and 400% cases, respectively. Similar values are found throughout the inner, deep part of the fjord (not shown here). The stratification in the inner part of the fjord is considerably strengthened with an increase in total meltwater runoff in the upper 100 m of the water column. Furthermore, the deep-lying water mass (below 100 m) only becomes fresher in the 400% case, while it is hardly influenced in the 50% and 200% cases.

It is very likely that the meltwater runoff into the fjord Kangerlussuaq will increase in the future due to climate change, which may have a severe impact on primary production. Lund-Hansen et al. (2018) found that meltwater runoff is the main driver of the variations in optical conditions, inorganic nutrients and primary production during summertime. The increase in meltwater runoff will have two effects on the fjord because the meltwater supplies nutrients and particle matter into the fjord. The increase in nutrient supply will increase productivity, while an increase in particle matter will increase light attenuation, thereby reducing productivity (Murray et al., 2015). However, as Arctic fjords without marine terminating glaciers are generally associated with suppression of primary production (Hopwood et al., 2020), we expect that the net effect of increasing meltwater runoff will reduce primary production in the fjord. This is because stratification impedes the vertical nutrient supply from mixing, and together with light limitation, a reduction of primary production is expected.

6. Conclusions

The commercially available MIKE 3 hydrodynamic model was set up for the fjord Kangerlussuaq to understand its seasonal variability and to study the response to changing freshwater runoff. The model was calibrated against in situ data of the water level and transects of temperature, salinity and density. The main findings are described as follows:

- The general circulation pattern is primarily oriented along the long axis of the fjord, and there is minimal across fjord variations because the fjord is too narrow to be influenced by the Earth's rotational dynamics.
- Two general current regimes are present. The first regime is observed in the summertime, where there are down-fjord currents in the upper 20 m of the water column and up-fjord currents below. The other regime is present during winter, when the freshwater content is negligible and small vertical gradients in the currents are observed.
- The tides are semidiurnal with a mean spring tidal range of 3.5 m.
- The deep inner part of the fjord is characterized by weak currents (~0.05 m/s) and is sea ice covered during wintertime. Very fast tidal currents (~1.3 m/s) are present in the shallow, outer part of the fjord. We suggest that these fast currents prevent winter sea ice formation in the outer part.
- The mixing processes in the fjord are characterized by strong tidal mixing and bathymetric restrictions.
- The inner part of the fjord is strongly stratified during summer. In the outer part of the fjord, strong tidal mixing tends to breakdown stratification, and smaller vertical gradients in temperature and salinity are observed.
- The deep-lying water mass is hardly subject to any renewal during summertime and is almost dynamically decoupled from the open ocean. The latter is because the water of the West Greenland Current flowing into the fjord over the long shallow sill is heavily modified before reaching the inner part of the fjord, resulting in a density smaller than that of the deep-water mass. This is different compared to many other Arctic fjords, where renewal of deep basin waters occur when dense coastal water flows over the sill and replaces the deep-lying water mass.
- A sensitivity study on meltwater runoff revealed that the surface salinity decreases by approximately 2.3 psu and 5.5 psu when the total discharge flowing into the fjord is doubled or multiplied by a factor of 4, respectively. Moreover, the most severe changes are observed in the upper 100 m in the inner, deep part of the fjord, and shows significant strengthened stratification when the total volume of runoff is increased. Therefore, the predicted increase in meltwater runoff will most likely result in a reduction of primary production.

The main drawback of using the MIKE 3 model to study Arctic fjords is the lack of a sea ice module. Therefore, processes such as cooling, brine release and freshwater release during sea ice melt cannot be included in the model. For the fjord Kangerlussuaq, this means that important physics during wintertime are not captured. For future studies, it is highly recommended to add a sea ice module to the model, thereby making the model suitable for studying sea ice-covered fjord systems during wintertime. Furthermore, it appears that the model overestimates vertical mixing when the default parameter values are used, and it is highly recommended to investigate this further.

Acknowledgements

We thank and acknowledge DHI for providing access to MIKE 3 and for their assistance implementing the model. We also like to thank Morten Rugbjerg from DHI for his assistance and feedback regarding the model setup. Further, we would like to acknowledge DMI for kindly providing the Envisat data. The Sentinel-2 image used in Figure 1 is available from the ESA and can be downloaded freely from the Sentinel data hub (https://scihub.copernicus.eu/). Finally, for the MODIS images used to study the sea ice cover, we acknowledge the use of imagery from the NASA Worldview application (https://worldview.earthdata.nasa.gov), which is part of the NASA Earth Observing System Data and Information System (EOSDIS).

References

Arendt, K.E., Nielsen, T.G., Rysgaard, S., Tönnesson, K., 2010. Differences in plankton community structure along the Godthåbsfjord, from the Greenland Ice Sheet to offshore waters. Mar. Ecol. Prog. Ser. 401, 49—62, https://doi.org/10.3354/meps08368.

Bendtsen, J., Mortensen, J., Rysgaard, S., 2014. Seasonal surface layer dynamics and sensitivity to runoff in a high Arctic fjord (Young Sound/Tyrolerfjord, 74N). J. Geophys. Res. Ocean. 119, 2439—2461, https://doi.org/10.1002/2013JC009622.

Born, E.W., Böcher, J., 2001. The Ecology of Greenland. Atuagkat, Nuuk, 429 pp.

Box, J.E., Bromwich, D.H., Veenhuis, B.A., Bai, L.S., Stroeve, J.C., Rogers, J.C., Steffen, K., Haran, T., Wang, S.H., 2006. Greenland ice sheet surface mass balance variability (1988—2004) from calibrated polar MM5 output. J. Clim. 19, 2783—2800, https://doi.org/10.1175/JCLI3738.1.

Cappelen, J., 2016. DMI Report 16-08 Weather observations from Greenland — Observation data with description. 1—31.

Carroll, D., Sutherland, D.A., Curry, B., Nash, J.D., Shroyer, E.L., Catania, G.A., Stearns, L.A., Grist, J.P., Lee, C.M., de Steur, L., 2018. Subannual and Seasonal Variability of Atlantic-Origin Waters in Two Adjacent West Greenland Fjords. J. Geophys. Res. Ocean. 123, 6670—6687, https://doi.org/10.1029/2018JC014278.

Catania, G.A., Stearns, L.A., Moon, T.A., Enderlin, E.M., Jackson, R.H., 2020. Future Evolution of Greenland's Marine-Terminating Outlet Glaciers. J. Geophys. Res. Earth Surf. 125, 1—28, https://doi.org/10.1029/2018JF004873.

Cheng, Y., Andersen, O.B., 2010. Improvement in global ocean tide model in shallow water regions. Altimetry for Oceans & Hydrology. OST-ST Meeting, Lisbon.

CMEMS, 2018. Global Ocean Physical Reanalysis product. Product Identifier: GLOBAL_REANALYSIS_PHY_001_030. E.U. Copernicus Marine Service Information.

Cottier, F.R., Nilsen, F., Skogseth, R., Tverberg, V., Skarthhamar, J., Svendsen, H., 2010. Arctic fjords: a review of the oceanographic environment and dominant physical processes. Geol. Soc. London, Spec. Publ. 344, 35—50, https://doi.org/10.1144/SP344.4.

Courtier, A., 1939. Classification of tides in four types. Int. Hydrogr. Rev.

Cowton, T., Slater, D., Sole, A., Goldberg, D., Nienow, P., 2016. Modeling the impact of glacial runoff on fjord circulation and submarine melt rate using a new subgrid-scale parameterization for glacial plumes. J. Geophys. Res.-Ocean. 120, 796—812, https://doi.org/10.1002/2014JC010324.

DHI, 2017. MIKE 3 Flow Model — Scientific Documentation. DHI, Hørsholm, Denmark.

DHI, 2016a. MIKE zero — Mesh Generator — Step-by-step training guide. DHI, Hørsholm, Denmark.

DHI, 2016b. MIKE 21 & MIKE 3 Flow Model FM — Hydrodynamic and Transport Module — Scientific Documentation. DHI, Hørsholm, Denmark.

DHI, 2016c. MIKE 3 FLow Model FM — Transport Module — User guide. DHI, Hørsholm, Denmark.

Dziallas, C., Grossart, H.P., Tang, K.W., Nielsen, T.G., 2013. Distinct communities of free-living and copepod-associated microorganisms along a salinity gradient in Godthåbsfjord, West Greenland. Arctic, Antarct. Alp. Res. 45, 471—480, https://doi.org/10.1657/1938-4246.45.4.471.

Edwards, A., Edelsten, D.J., 1977. Deep water renewal of Loch Etive: A three basin Scottish fjord. Estuar. Coast. Mar. Sci. 5, 575—595, https://doi.org/10.1016/0302-3524(77)90085-8.

Flather, R.A., 1976. A tidal model of the north-west European continental shelf. Mem. Soc. R. Sci. Liege 10, 141—164.

Gladish, C.V., Holland, D.M., Rosing-Asvid, A., Behrens, J.W., Boje, J., 2015. Oceanic Boundary Conditions for Jakobshavn Glacier. Part I: Variability and Renewal of Ilulissat Icefjord Waters, 2001—14. J. Phys. Oceanogr. 45, 3—32, https://doi.org/10.1175/JPO-D-14-0044.1.

Grindsted, A., 2020. Tidal fitting toolbox Aslak Grinsted (2020). Tidal fitting toolbox. MATLAB Central File Exchange, https://www.mathworks.com/matlabcentral/fileexchange/19099-tidal-fitting-toolbox (accessed on May 12, 2020).

Harden, B.E., Renfrew, I.A., 2012. On the spatial distribution of high winds off southeast Greenland. Geophys. Res. Lett. 39, 1—6, https://doi.org/10.1029/2012GL052245.

Hasholt, B., Bech Mikkelsen, A., Holtegaard Nielsen, M., Andreas Dahl Larsen, M., 2013. Observations of Runoff and Sediment and Dissolved Loads from the Greenland Ice Sheet at Kangerlussuaq, West Greenland, 2007 to 2010. Zeitschrift für Geomorphol. 57 (Suppl. Iss. 2), 3—27, https://doi.org/10.1127/0372-8854/2012/S-00121.

Hawes, I., Lund-Hansen, L.C., Sorrell, B.K., Nielsen, M.H., Borzák, R., Buss, I., 2012. Photobiology of sea ice algae during initial spring growth in Kangerlussuaq, West Greenland: Insights from imaging variable chlorophyll fluorescence of ice cores. Photosynth. Res. 112, 103—115, https://doi.org/10.1007/s11120-012-9736-7.

Holland, D.M., Thomas, R.H., De Young, B., Ribergaard, M.H., Lyberth, B., 2008. Acceleration of Jakobshavn Isbr triggered by warm subsurface ocean waters. Nat. Geosci. 1, 659—664, https://doi.org/10.1038/ngeo316.

Hopwood, M.J., Carroll, D., Dunse, T., Hodson, A., Holding, J.M., Iriarte, J.L., Ribeiro, S., Achterberg, E.P., Cantoni, C., Carlson, D.F., Chierici, M., Clarke, J.S., Cozzi, S., Fransson, A., Juul-Pedersen, T., Winding, M.H.S., Meire, L., 2020. Review article: How does glacier discharge affect marine biogeochemistry and primary production in the Arctic? Cryosphere 14, 1347—1383, https://doi.org/10.5194/tc-14-1347-2020.

Hudson, B., Overeem, I., McGrath, D., Syvitski, J.P.M., Mikkelsen, A., Hasholt, B., 2014. MODIS observed increase in duration and spatial extent of sediment plumes in Greenland fjords. Cryosphere 8, 1161—1176, https://doi.org/10.5194/tc-8-1161-2014.

Inall, M.E., Murray, T., Cottier, F.R., Scharrer, K., Boyd, T.J., Heywood, K.J., Bevan, S.L., 2014. Oceanic heat delivery via Kangerdlugssuaq Fjord to the south-east Greenland ice sheet. J. Geophys. Res.-Oceans, 119, 631—645, https://doi.org/10.1002/2013JC009295.

IPCC, 2013. Climate Change 2013: The Physical Science Basis. Contribution of Working Group I to the Fifth Assessment Report of the Intergovernmental Panel on Climate Change. Cambridge Univ. Press, Cambridge, UK, New York, USA, 1535 pp.

Jakacki, J., Przyborska, A., Kosecki, S., Sundfjord, A., Albretsen, J., 2017. Modelling of the Svalbard fjord Hornsund. Oceanologia 59 (4), 473—495, https://doi.org/10.1016/j.oceano.2017.04.004.

Kjeldsen, K.K., Mortensen, J., Bendtsen, J., Petersen, D., Lennert, K., Rysgaard, S., 2014. Ice-dammed lake drainage cools and raises surface salinities in a tidewater outlet glacier fjord, west Greenland. J. Geophys. Res. 119 (6), 1310—1321, https://doi.org/10.1002/2013JF003034.

Lindbäck, K., Pettersson, R., Hubbard, A.L., Doyle, S.H., Van As, D., Mikkelsen, A.B., Fitzpatrick, A.A., 2015. Subglacial water drainage, storage, and piracy beneath the Greenland ice sheet. Geophys. Res. Lett. 42, 7606—7614, https://doi.org/10.1002/2015GL065393.

Lund-Hansen, L.C., Andersen, T.J., Nielsen, M.H., Pejrup, M., 2010. Suspended Matter, Chl-*a*, CDOM, Grain Sizes, and Optical Properties in the Arctic Fjord-Type Estuary, Kangerlussuaq. West Greenland During Summer. Estuar. Coast. 33, 1442—1451, https://doi.org/10.1007/s12237-010-9300-7.

Lund-Hansen, L.C., Hawes, I., Holtegaard Nielsen, M., Dahllöf, I., Sorrell, B.K., 2018. Summer meltwater and spring sea ice primary production, light climate and nutrients in an Arctic estuary, Kangerlussuaq, west Greenland. Arctic Antarct. Alp. Res, 50, art. no. e1414468, 11 pp., https://doi.org/10.1080/15230430.2017.1414468.

Mernild, S.H., Liston, G.E., Steffen, K., Van Den Broeke, M., Hasholt, B., 2010. Runoff and mass-balance simulations from the Greenland Ice Sheet at Kangerlussuaq (Søndre Strømfjord) in a 30-year perspective, 1979-2008. Cryosphere 4, 231—242, https://doi.org/10.5194/tc-4-231-2010.

Mortensen, J., Bendtsen, J., Motyka, R.J., Lennert, K., Truffer, M., Fahnestock, M., Rysgaard, S., 2013. On the seasonal freshwater stratification in the proximity of fast-flowing tidewater outlet glaciers in a sub-Arctic sill fjord. J. Geophys. Res.-Oceans 118, 1382—1395, https://doi.org/10.1002/jgrc.20134.

Mortensen, J., Lennert, K., Bendtsen, J., Rysgaard, S., 2011. Heat sources for glacial melt in a sub-Arctic fjord (Godthåbsfjord) in contact with the Greenland Ice Sheet. J. Geophys. Res.-Oceans 116, (C1), art. no. C01013, 13 pp., https://doi.org/10.1029/2010JC006528.

Mortensen, J., Rysgaard, S., Arendt, K.E., Juul-Pedersen, T., Søgaard, D.H., Bendtsen, J., Meire, L., 2018. Local Coastal Water Masses Control Heat Levels in a West Greenland Tidewater Outlet Glacier Fjord. J. Geophys. Res.-Oceans 123, 8068—8083, https://doi.org/10.1029/2018JC014549.

Murray, C., Markager, S., Stedmon, C.A., Juul-Pedersen, T., Sejr, M.K., Bruhn, A., 2015. The influence of glacial melt water on bio-optical properties in two contrasting Greenlandic fjords. Estuar. Coast. Shelf Sci. 163, 72—83, https://doi.org/10.1016/j.ecss.2015.05.041.

Murray, T., Scharrer, K., James, T.D., Dye, S.R., Hanna, E., Booth, A.D., Selmes, N., Luckman, A., Hughes, A.L.C., Cook, S., Huybrechts, P., 2010. Ocean regulation hypothesis for glacier dynamics in southeast Greenland and implications for ice sheet mass changes. J. Geophys. Res. 115, 1—15, https://doi.org/10.1029/2009JF001522.

Myers, P.G., Donnelly, C., Ribergaard, M.H., 2009. Structure and variability of the West Greenland Current in Summer derived from 6 repeat standard sections. Prog. Oceanogr. 80, 93—112, https://doi.org/10.1016/j.pocean.2008.12.003.

Myers, P.G., Kulan, N., Ribergaard, M.H., 2007. Irminger water vari-

ability in the West Greenland Current. Geophys. Res. Lett. 34, 2—7, https://doi.org/10.1029/2007GL030419.

Nielsen, M.H., Erbs-Hansen, D.R., Knudsen, K.L., 2010. Water masses in Kangerlussuaq, a large fjord in West Greenland: the processes of formation and the associated foraminiferal fauna. Polar Res. 29, 159—175, https://doi.org/10.1111/j.1751-8369.2010.00147.x.

Rignot, E., Fenty, I., Menemenlis, D., Xu, Y., 2012. Spreading of warm ocean waters around Greenland as a possible cause for glacier acceleration. Ann. Glaciol. 53, 257—266, https://doi.org/10.3189/2012AoG60A136.

Rignot, E., Koppes, M., Velicogna, I., 2010. Rapid submarine melting of the calving faces of West Greenland glaciers. Nat. Geosci. 3, 187—191, https://doi.org/10.1038/ngeo765.

Rodi, W., 1984. Turbulence models and their application in hydraulics. Internat. Assoc. Hydraulic Res. Delft.

Shepherd, A., Ivins, E., Rignot, E., Smith, B., van den Broeke, M., Velicogna, I., Whitehouse, P., Briggs, K., Joughin, I., Krinner, G., Nowicki, S., Payne, T., Scambos, T., Schlegel, N., A, G., Agosta, C., Ahlstrøm, A., Babonis, G., Barletta, V.R., Bjørk, A.A., Blazquez, A., Bonin, J., Colgan, W., Csatho, B., Cullather, R., Engdahl, M.E., Felikson, D., Fettweis, X., Forsberg, R., Hogg, A.E., Gallee, H., Gardner, A., Gilbert, L., Gourmelen, N., Groh, A., Gunter, B., Hanna, E., Harig, C., Helm, V., Horvath, A., Horwath, M., Khan, S., Kjeldsen, K.K., Konrad, H., Langen, P.L., Lecavalier, B., Loomis, B., Luthcke, S., McMillan, M., Melini, D., Mernild, S., Mohajerani, Y., Moore, P., Mottram, R., Mouginot, J., Moyano, G., Muir, A., Nagler, T., Nield, G., Nilsson, J., Noël, B., Otosaka, I., Pattle, M.E., Peltier, W.R., Pie, N., Rietbroek, R., Rott, H., Sandberg Sørensen, L., Sasgen, I., Save, H., Scheuchl, B., Schrama, E., Schröder, L., Seo, K.W., Simonsen, S.B., Slater, T., Spada, G., Sutterley, T., Talpe, M., Tarasov, L., van de Berg, W.J., van der Wal, W., van Wessem, M., Vishwakarma, B.D., Wiese, D., Wilton, D., Wagner, T., Wouters, B., Wuite, J., 2020. Mass balance of the Greenland Ice Sheet from 1992 to 2018. Nature 579, 233—239, https://doi.org/10.1038/s41586-019-1855-2.

Shore Protection Manual, 1984. Shore Protection Manual. US Army Corps of Engineergs, Washington DC.

Skogseth, R., Haugan, P.M., Jakobsson, M., 2005. Watermass transformations in Storfjorden. Cont. Shelf Res. 25, 667—695, https://doi.org/10.1016/j.csr.2004.10.005.

Smagorinsky, J., 1963. General Circulation Experiments With the Primitive Equations. Mon. Weather Rev. 91, 99—164, https://doi.org/10.1175/1520-0493(1963)091⟨0099:gcewtp⟩2.3.co;2.

Storms, J.E.A., de Winter, I.L., Overeem, I., Drijkoningen, G.G., Lykke-Andersen, H., 2012. The Holocene sedimentary history of the Kangerlussuaq Fjord-valley fill, West Greenland. Quat. Sci. Rev. 35, 29—50, https://doi.org/10.1016/j.quascirev.2011.12.014.

Straneo, F., Cenedese, C., 2015. The Dynamics of Greenland's Glacial Fjords and Their Role in Climate. Ann. Rev. Mar. Sci. 7, 89—112, https://doi.org/10.1146/annurev-marine-010213-135133.

Straneo, F., Curry, R.G., Sutherland, D.A., Hamilton, G.S., Cenedese, C., Våge, K., Stearns, L.A., 2011. Impact of fjord dynamics and glacial runoff on the circulation near Helheim Glacier. Nat. Geosci. 4, 322—327, https://doi.org/10.1038/ngeo1109.

Straneo, F., Hamilton, G.S., Sutherland, D.A., Stearns, L.A., Davidson, F., Hammill, M.O., Stenson, G.B., Rosing-Asvid, A., 2010. Rapid circulation of warm subtropical waters in a major glacial fjord in East Greenland. Nat. Geosci. 3, 182—186, https://doi.org/10.1038/ngeo764.

Straneo, F., Heimbach, P., Sergienko, O., Hamilton, G., Catania, G., Griffies, S., Hallberg, R., Jenkins, A., Joughin, I., Motyka, R., Pfeffer, W.T., Price, S.F., Rignot, E., Scambos, T., Truffer, M., Vieli, A., 2013. Challenges to Understand the Dynamic Response of Greenland's Marine Terminating Glaciers to Oceanic and Atmospheric Forcing. Bull. Am. Meteorol. Soc. 94 (8), 1131—1144, https://doi.org/10.1175/BAMS-D-12-00100.1.

Sutherland, D.A., Pickart, R.S., 2008. The East Greenland Coastal Current: Structure, variability, and forcing. Prog. Oceanogr. 78, 58—77, https://doi.org/10.1016/j.pocean.2007.09.006.

Sutherland, D.A., Straneo, F., Pickart, R.S., 2014. Characteristics and dynamics of two major Greenland glacial fjords. J. Geophys. Res.-Oceans 119, 3767—3791, https://doi.org/10.1002/2013JC009786.

Trusel, L.D., Das, S.B., Osman, M.B., Evans, M.J., Smith, B.E., Fettweis, X., McConnell, J.R., Noël, B.P.Y., van den Broeke, M.R., 2018. Nonlinear rise in Greenland runoff in response to post-industrial Arctic warming. Nature 564, 104—108, https://doi.org/10.1038/s41586-018-0752-4.

UNESCO, 1987. International oceanographic tables. Unesco Tech. Pap. Mar. Sci. 3, 195 pp.

van As, D., Hasholt, B., Ahlstrøm, A.P., Box, J.E., Cappelen, J., Colgan, W., Fausto, R.S., Mernild, S.H., Mikkelsen, A.B., Noël, B.P.Y., Petersen, D., van den Broeke, M.R., 2018. Reconstructing Greenland Ice Sheet meltwater discharge through the Watson River (1949—2017). Arctic, Antarct. Alp. Res. 50 (1), art. no. e1433799, 10 pp., https://doi.org/10.1080/15230430.2018.1433799 .

van As, D., Hubbard, A.L., Hasholt, B., Mikkelsen, A.B., van Den Broeke, M.R., Fausto, R.S., 2012. Large surface meltwater discharge from the Kangerlussuaq sector of the Greenland ice sheet during the record-warm year 2010 explained by detailed energy balance observations. Cryosphere 6, 199—209, https://doi.org/10.5194/tc-6-199-2012.

Oceanologia (2020) 62, 478—488

Available online at www.sciencedirect.com

ScienceDirect

journal homepage: www.journals.elsevier.com/oceanologia

ORIGINAL RESEARCH ARTICLE

Argo floats in the southern Baltic Sea

Waldemar Walczowski*, Małgorzata Merchel, Daniel Rak, Piotr Wieczorek, Ilona Goszczko

Institute of Oceanology, Polish Academy of Sciences, Sopot, Poland

Received 1 April 2020; accepted 25 July 2020
Available online 7 August 2020

KEYWORDS
Argo floats;
Baltic Sea;
Dissolved oxygen;
Inflows

Summary This work aims to familiarize the reader with issues related to modern oceanographic measurement techniques performed by Argo autonomous profiling floats. The opportunity for this is the three years of innovative activity on the part of Argo-Poland in the Baltic Sea. Based on the experience and results acquired by the Institute of Oceanology of the Polish Academy of Sciences (IO PAN), we can say that a revolution in the Baltic Sea monitoring is underway. During three years of activity, the floats launched by IO PAN provided more than 1600 CTD profiles, including 600 O_2 profiles. Together with synoptic data from ships, data from moorings and surface buoys, the Argo float measurements are an important part of the southern Baltic monitoring system. Two Argo floats launched by IO PAN collected enough data to determine the dynamics of the oxygen content in various layers, the extent of hypoxic and anoxic zones, and to detect small baroclinic inflows to the Gotland and Gdańsk Deeps.

1. Introduction

Rapidly progressing climate change has focused the interest of climatologists and weather services on the ocean. There was a need to create a system that, in place of thinly spaced oceanographic stations, would provide near-real-time information about the thermal state of the ocean from a global network of monitoring instruments. The assumption underlying the Argo Programme was that the use of autonomous, free-drifting profiling floats would meet this need. Following its implementation in 1999, Argo achieved global coverage of the upper 2000 m of the oceans in 2006. Nowadays, a global array of 4000 floats covers the oceans (Fig. 1). Argo floats provide the most important in situ ob-

* Corresponding author at: Institute of Oceanology, Polish Academy of Sciences, Powstańcow Warszawy 55, 81—712 Sopot, Poland.
E-mail address: walczows@iopan.pl (W. Walczowski).
Peer review under the responsibility of the Institute of Oceanology of the Polish Academy of Sciences.

Production and hosting by Elsevier

https://doi.org/10.1016/j.oceano.2020.07.001

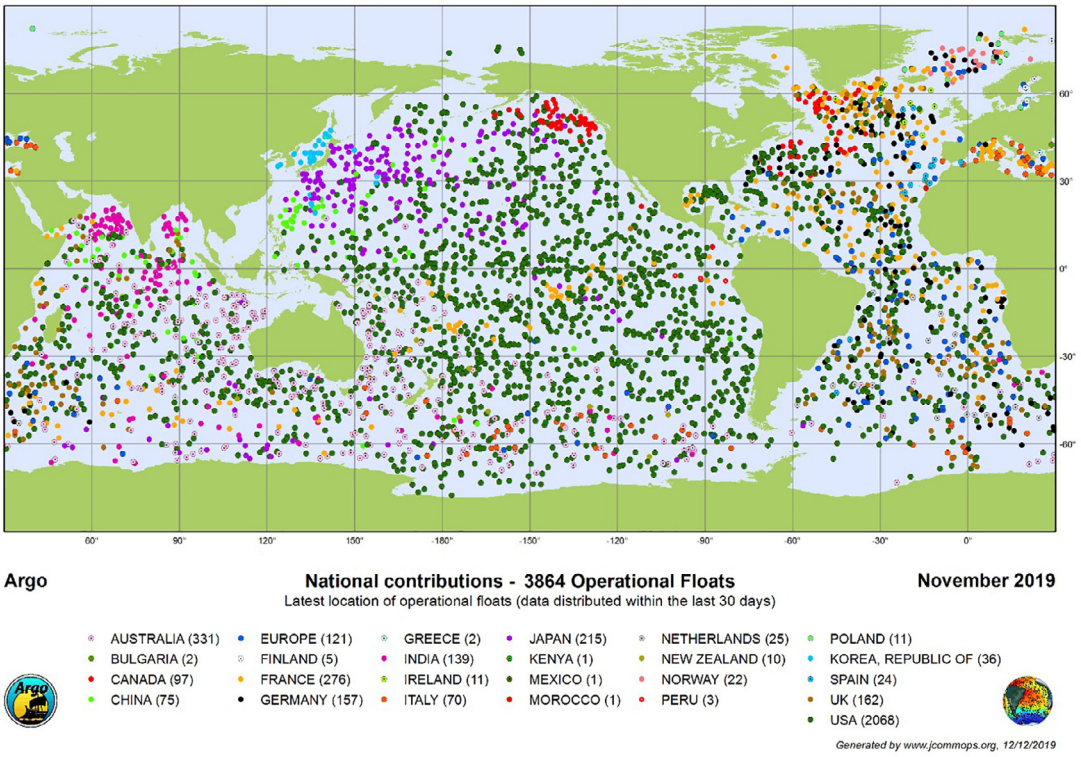

Figure 1 Location of operational floats and national contributions in November 2019.

servations for monitoring and understanding the influence of the ocean on Earth's climate and for operational oceanography (Le Traon, 2013). The Argo system is the main component of the Global Ocean Observing System (GOOS) and the Global Climate Observing System (GCOS) (Roemmich et al., 2019). The freely available Argo data are used mainly in atmospheric, oceanographic and climate research. Since the programme's inception to October 2018, the floats have provided 2 000 000 profiles from the surface to 2000 m depth and a comparable amount of information on drift speed estimated at a depth of 1000 m. Floats deliver continuous observations of ocean temperature and salinity vs pressure. Data are transmitted by satellite to receiving centres and are available to users in near-real-time (NRT). The development and maintenance of a global array of profiling floats delivering NRT in situ data has been an outstanding achievement and revolution in oceanography. In fact, there have been three revolutions in world oceanography (Le Traon, 2013): 1) the development and introduction of high-resolution satellite altimetry; 2) the array of Argo floats; 3) the development of global operational oceanography, closely linked to the first two revolutions. In Baltic Sea research the second revolution — "Argo time" — has now begun.

The exchange of water between the North Sea and the Baltic through the narrow, shallow Danish Straits is very important for the entire Baltic Sea environment (Elken and Matthäus, 2008). This very limited exchange maintains brackish water conditions in the Baltic (HELCOM, 1986). Major Baltic Inflows (MBI) are the main source of deep-water ventilation in the central Baltic basins and govern environmental conditions below the halocline to a significant extent (Mohrholz, 2018). These inflows are barotropic, driven mainly by wind forcing and the water level difference between the Kattegat and western Baltic. MBIs occur mostly in the autumn and winter. Smaller, baroclinic inflows, occurring mostly in summer, are driven by the salinity gradient between the North and Baltic Seas. The importance of MBIs, smaller barotropic inflows and baroclinic inflows in Baltic Sea hydrography continue to be a matter of debate (Mohrholz, 2018).

The Polish Exclusive Economic Zone (Polish EEZ) includes part of the Bornholm Basin, the Słupsk Furrow, part of the Eastern Gotland Basin and the Gdańsk Basin. The Słupsk Furrow is the only deep connection between the Bornholm and Gotland basins (Fig. 2) and the only pathway for eastward deep-water advection. The dynamics of eastward water transport is governed by the interaction of bottom topography and external forcing: currents can be interrupted, and mesoscale processes play an important role (Piechura et al., 1997). Therefore, regular observations and a coherent system utilizing observational data and modelling are needed in order to thoroughly understand inflow processes and how they affect the Baltic Sea. The inclusion of Argo floats in the southern Baltic Observing System was proposed by Walczowski et al. (2017). They suggested using various data sources, including hydrographic sections from synoptic surveys, Eulerian data from a moored buoy and Lagrangian data provided by Argo floats to monitor the properties and dynamics of deep inflows of saline, oxygenated water from the North Sea. After three years of work, all the signs are that these ideas are feasible.

The aim of this paper is to briefly describe the Argo float technology, network organization and data potential

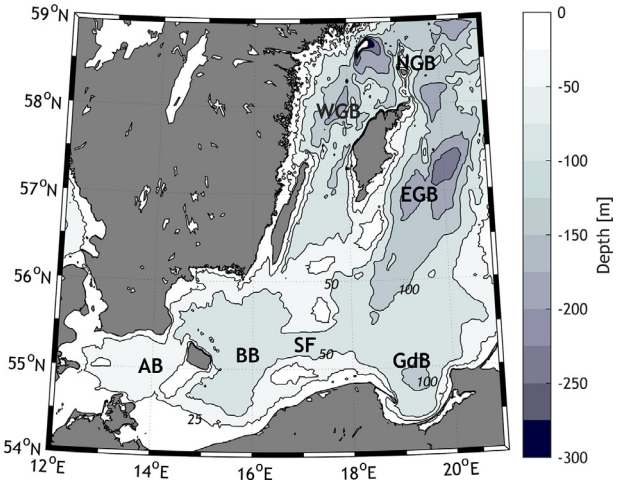

Figure 2 Main basins of the Baltic Proper: Arkona Basin (AB), Bornholm Basin (BB), Gdańsk Basin (GdB), Eastern Gotland Basin (EGB), Western Gotland Basin (WGB), Northern Gotland Basin (NGB) and Słupsk Furrow (SF).

because we are going through a second, Argo revolution in the Baltic Sea. Just a few years ago, the thinking was that this deep-ocean technology was unsuitable for use in the small, shallow Baltic Sea. But in fact, Argo floats work well here and provide valuable data that should be used in Baltic Sea monitoring and forecasting systems, as well as in comprehensive analyses of the state of the Baltic Sea. Finnish oceanographers have shown that Argo data are very useful for monitoring and hydrographic analyses in the Bothnian Sea (Haavisto et al., 2018; Roiha et al., 2018) and Gotland Basin (Siiriä et al., 2019). Data obtained by the Institute of Oceanology Polish Academy of Sciences during the three years of Argo Poland activity in the Baltic Sea are presented. Our intention is not to carry out a thorough analysis of all the data, rather familiarize the reader with the operation of the Argo system, to describe southern Baltic Argo data, to highlight their value, usefulness and potential, and to encourage their utilization. Looking for and collaborating with end-user communities in order to improve the utilization of Argo data is an important aspect of the Argo programme.

2. Argo technology and data

Argo floats were developed for oceanic measurements. The most commonly-used Argo float type (Core Argo) is a small, autonomous underwater platform that measures the temperature and conductivity of seawater vs pressure. The maximum profiling depth is 2000 m. The float is about 1.60 m tall, weighs 20 kg, and has neutral buoyancy in the water. The sensors and antenna of the satellite data transmission system are located in the upper part of the float (Fig. 3 a). It does not have its own propulsion but drifts freely in the sea. Depth changes are enforced by altering the float's buoyancy: this is done by pumping the oil from the inside of the float into the outer rubber bladder or sucking it back inside.

The typical deep-ocean work cycle of such a float is shown in Fig. 3 b. Floats are programmed to dive to a 'parking depth' of 1000 m and to drift for approximately nine days. They then descend to the profiling depth of 2000 m for Core Argo and 6000 m for Deep Argo. Temperature, conductivity, pressure and other water properties are recorded during the drift and ascent (six to sixteen hours). Once back at the surface, the float transmits data via satellite in near-real-time. The rapid transmission of observational data to data centres enhances the usefulness of Argo floats for numerical ocean forecasts. The large amount of data collected and good ocean coverage has made Argo floats an invaluable source of information about changes in ocean heat content, and the surfacing positions provide information on ocean dynamics.

Older devices used the Argos one-way satellite transmission system. The progress that has taken place in the construction of Argo profilers over the past 20 years is best demonstrated by the fact that with the first Argo, 12 hours were needed to transmit the data set from one cycle; now

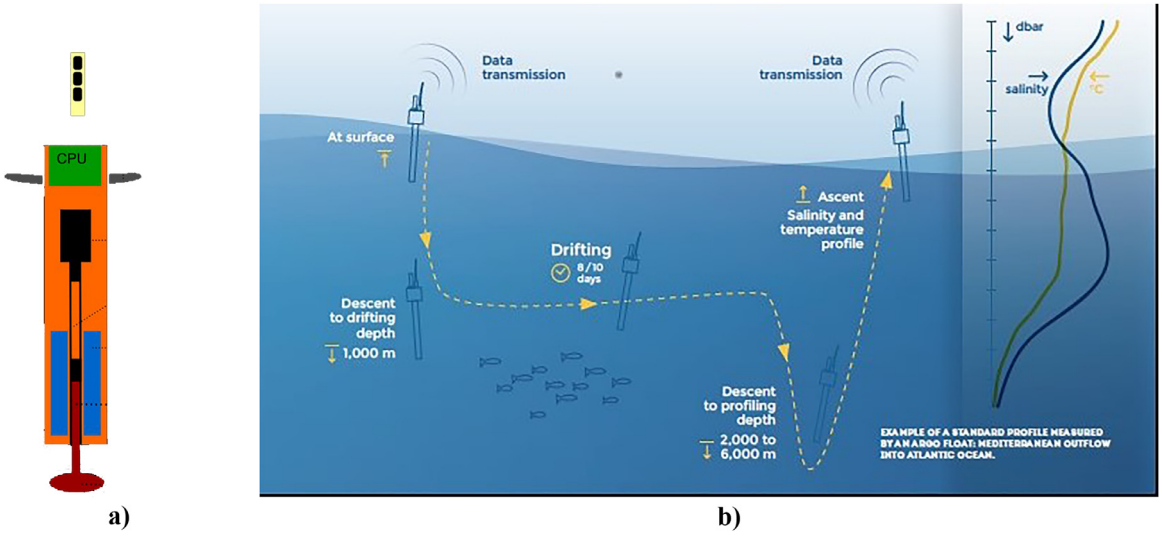

Figure 3 Argo float scheme (left) and deep ocean cycle (right).

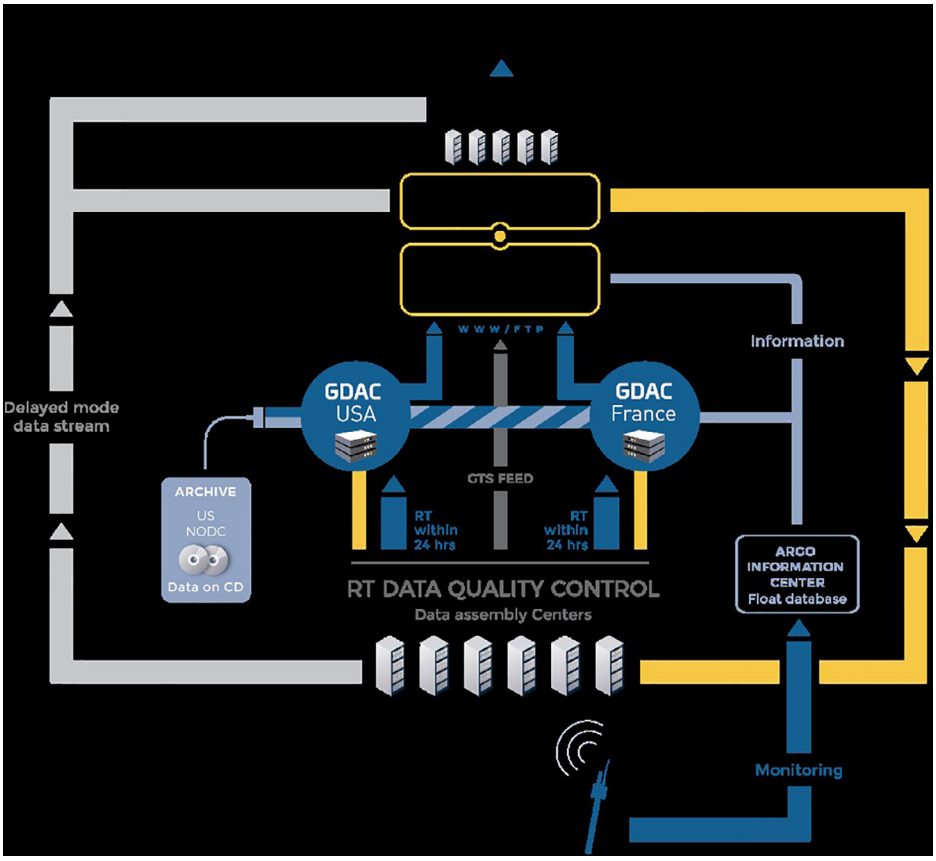

Figure 4 Argo data management system. The pathways of Argo near-real-time and delayed-mode data are illustrated. (Copyright: by courtesy of Euro-Argo ERIC).

this can be done in 20 minutes. The majority of modern floats use the two-way transmission Iridium or Argos system; such floats can work up to 4 years with 10-day cycles. The bidirectional transmission allows float settings to be altered during the mission. A float's operating time depends on its battery capacity and the stability of its sensors; once the battery runs out, the float sinks. This sometimes raises doubts and questions about the environmental legitimacy of such a procedure. Unfortunately, the recovery of spent floats from the ocean is still unprofitable and at present environmentally unjustified. The amounts of fuel consumed and CO_2 emitted by the vessel recovering the float would be incomparably greater than the economic and environmental gains resulting from its recovery.

Each Argo float has a unique World Meteorological Organization (WMO) number, such as are allocated to ocean platforms reporting in the Global Telecommunications System (GTS). When float surfaces, data are transmitted within 12 hours to Data Assembly Centres (DACs), where they are submitted to preliminary control using an agreed set of real-time quality control tests, where uncorrected data are flagged. The data are then transmitted to the Global Data Assembly Centres (GDACs) in Brest, France and Monterey, California (Fig. 4), where the freely available data can be obtained from the Internet within 24 hours of transmission. Within one year of data being collected, these are subjected to delayed-mode quality control via GDACs. All this work is coordinated by the Argo Data Management Team (ADMT).

3. Argo-Poland project

The Institute of Oceanology of the Polish Academy of Sciences, being the only scientific institution in Poland carrying out systematic research in the deep ocean, was designated by the Ministry of Sciences and Higher Education (MNiSW) to be the national representative in the European Argo programme. IO PAN has been participating in this programme since 2009. In 2014, the Euro-Argo European Research Infrastructure Consortium (ERIC) was established with the aim of maintaining one-quarter of the international Argo network. Poland joined the consortium as an observer. Initially, Euro-Argo interests were focused mainly on the Atlantic Ocean, the Nordic Seas and the Mediterranean Sea. Also, the initial deployments by IO PAN were made in the Nordic Seas during Arctic expeditions of its research vessel r/v *Oceania*, organized within the framework of the long-term AREX research program. However, the experience of Finnish oceanographers has shown that it is possible to operate Argo floats even in the shallow Baltic Sea; they began their activity on the Baltic Sea in 2011. That is why Polish and Finnish oceanographers have jointly expanded Euro-Argo's interests to include marginal seas such as the Baltic and the Black Sea (Euro-Argo ERIC, 2017). The recommendation for the Baltic Sea is to keep seven floats active at all times, deployed within its several basins. Float recovery is planned, with redeployment after maintenance and calibration.

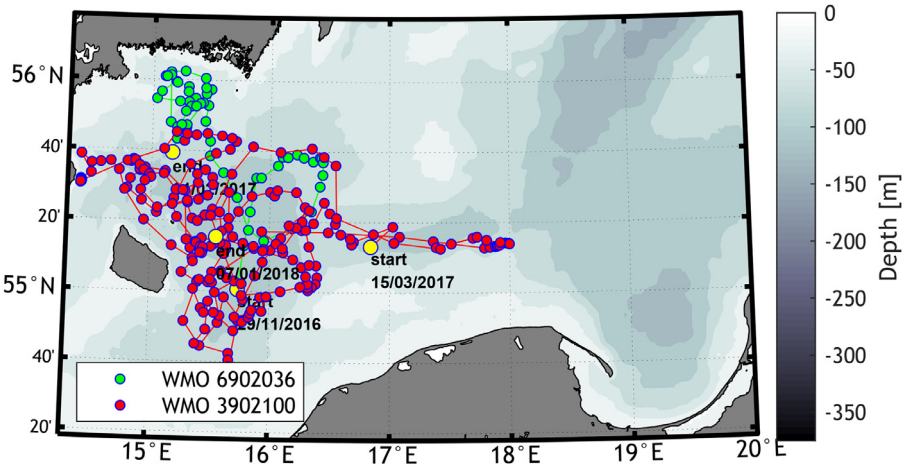

Figure 5 Pathways of the first Polish Argo float in the Baltic Sea during two deployments, as WMO 6902036 and WMO 6902100.

IO PAN, the Polish representative in the Euro-Argo ERIC and Global Argo organizations, provides data from Polish floats to GDACs and participates in the data validation. All the data are available on the webpages of GDACs and the IO PAN Argo-Poland project.

4. Float deployments in the Baltic Sea

Because of its specific properties, the Baltic Sea sets somewhat different requirements for Argo floats than the deep ocean. The Baltic is a small, shallow, semi-enclosed body of water. The structure of the water column is characterized by a strong permanent pycnocline, a separation zone between local, brackish surface waters and more saline waters originating from the North Sea. The vertical density gradient between the surface and deep waters is much larger in the Baltic Sea than the typical gradient for oceanic waters. This applies mainly to the deeps of the southern and central Baltic, and to a lesser extent to the Gulfs of Bothnia and Finland. In addition, ship traffic in the Baltic Sea is heavy and its waters are intensively exploited for fish.

In 2011, the first floats in the Baltic Sea were deployed by Finnish oceanographers (Purokoski et al., 2013). They used the most popular APEX floats produced by Webb (USA). The first Polish float was deployed in the Baltic Sea on 21 November 2016. This was also an APEX float, ballasted in accordance with the southern Baltic Sea water density. It was an experimental mission, aimed at testing the float in southern Baltic Sea conditions and training the issuing of commands for remotely controlling the float settings. In addition, the possibilities of indirectly controlling float drift were tested by altering the 'parking depth' or forcing the float to stay at the surface. The course of this first mission (WMO 6902036) was dramatic, coinciding as it did with the passage of hurricane 'Barbara' across the Baltic Sea region. The wind strength reached 11° B. During this time the float got very close to the Swedish coast (Fig. 5), entering shallow waters. Ongoing weather forecasts and the results from a numerical model working in real-time at IO PAN were used to adjust the float's settings, enabling it to drift away from the shore. The float survived, transmitting data on a daily basis and was recovered during a cruise of r/v *Oceania* in January 2017.

This first mission yielded 56 CTD profiles and provided valuable experience regarding the behaviour of Argo floats in the Baltic Sea in general and the APEX float in particular. But even so, the mission met with limited success: the strong pycnocline prevented the float from reaching the sea bed, 'false grounding' occurred during every descent, the float stopped at a maximum depth of 60 m, and the float's small bladder capacity made it incapable of adjusting its buoyancy to the southern Baltic deep's steep vertical density gradients.

The procedure to recover the float was also a valuable experience. Following the practice of our Finnish colleagues, we decided to re-use Baltic Argo floats many times. Unlike the deep ocean, the small dimensions of the Baltic Sea make float recovery cost-effective. Additional advantages for IO PAN are the numerous cruises of r/v *Oceania*, during which floats can be recovered and re-launched. Only the weather can hamper this practice. Strong winds and high waves make it hard to pick out the float: as it drifts across the water surface, only its antenna and a small part of the sensors protrude from the water surface.

The recovered float from the first mission (WMO 6902036) was redeployed as WMO 3902100 during the *r/v Oceania* cruise in March 2017. It worked for almost a year until January 2018, data transmission ceasing a week before its planned recovery. In both missions, this APEX float produced 280 profiles, providing valuable data on the hydrography of the upper layer and the pycnocline of the Bornholm Basin. Interestingly, this float was trawled by an Estonian fishing boat near Władysławowo in the summer of 2019.

In 2017, in cooperation with Euro-Argo ERIC, two floats belonging to the Monitoring the Ocean Climate Change with Argo (MOCCA) project were tested in the Polish EEZ. They were ARVOR-type floats made by the French company NKE. In comparison with APEX, this kind of float has a larger hydraulic bladder capacity (800 ml), which offers a wider range of float buoyancy changes and better chances of crossing the pycnocline. The floats were adapted to the Baltic Sea's water density by removing 250 g of ballast from the hull. The first ARVOR float was launched in the Gdańsk

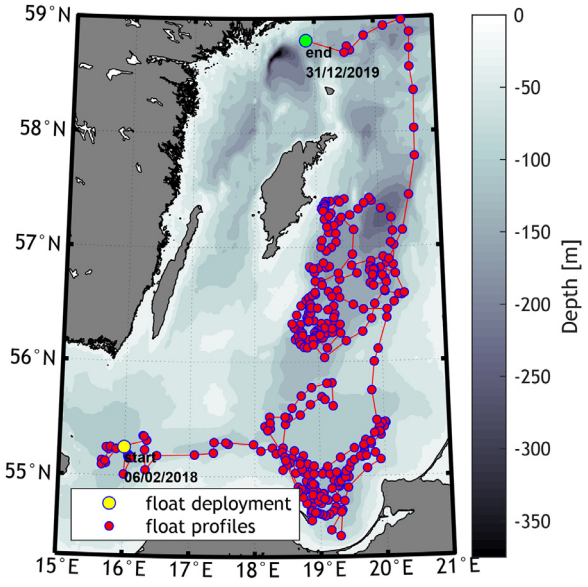

Figure 6 Pathways of the first Polish Argo Arvor float in the Baltic Sea, WMO 3902101.

Deep in September 2017, but after a few days, because it was approaching dangerously close to the shore, float WMO 3901940 was recovered by r/v *Oceania*. It was redeployed in November 2017 as WMO 3902133. The second MOCCA project float was deployed in September 2017 with the WMO number 3901941. This one was recovered by r/v *Oceania* in summer 2019 after having performed the impressive number of 382 profiles. It was subsequently sent to the manufacturer for maintenance, sensor calibration and battery exchange. This opened a new era of re-usable ARVOR floats.

In the initial phase of the floats' activity, experiments were performed to improve their operation. Various grounding algorithms, drifting depths and communication procedures were tested. Increasing parking depth accuracy improved float behaviour during the drifting phase, changing the grounding strategy and allowing touching bottom eliminated the 'false bottom' effect. Optimization of float settings meant that the devices were now able to reach the sea bed, where water with salinity higher than 17 was observed; previously tested APEX floats were able to reach depth occupied by water with salinity up to 12. Such profiling is particularly important for investigating water inflows from the North Sea and deep-water properties. The profiling period was also changed during float missions. Initially, profiling was daily, but ultimately we settled on a two-day profiling period in most missions. The usual parking (drifting) depth was 50 m.

As a result of the invaluable experience gained with ARVOR in the Baltic Sea, IO PAN decided to purchase such devices for the needs of the Argo-Poland project. With funds from the Ministry of Science and Higher Education, we acquired two floats with additional dissolved oxygen (DO) concentration sensors, as monitoring dissolved oxygen dynamics is very important from the point of view of Baltic Sea ecology. Floats with DO sensors belong to the Biogeochemical (BGC) float class. The first Polish ARVOR BGC float (WMO 3902101) was deployed in the Bornholm Basin in February 2018 (Fig. 6), operating in a two-day cycle. During two months, it drifted from the Bornholm Basin to the Gdańsk Deep. The transit through the Słupsk Furrow, the main pathway of eastward deep-water advection, took 20 days. On the fastest section between profiles 29 and 30, the mean drift speed was higher than 20 cm s^{-1}, which was much faster than mean drift speed in the Bornholm Basin. The float remained in the Gdańsk Deep until January 2019, performing 130 dives, after which it drifted away to the Gotland Deep. In this case, too, the transit between deeps was fast, with mean velocities between profiles of up to 18 cm s^{-1}. In December 2019 the float was still operational, having performed 350 dives up to that moment.

The second Polish ARVOR BGC float (WMO 3902104) was deployed in the Bornholm Basin in May 2018. For three months it drifted eastwards (Fig. 7). In September 2018 it was recovered and redeployed back in the Bornholm Basin. As before, this operation required a change of WMO number, so that after redeployment the float was renumbered WMO 3902106. Most of the time, it remained in the Bornholm Basin, but in June 2019 it began drifting eastwards (Fig. 7).

During a three-year period (November 2016—December 2019), the Argo floats deployed by IO PAN in the southern

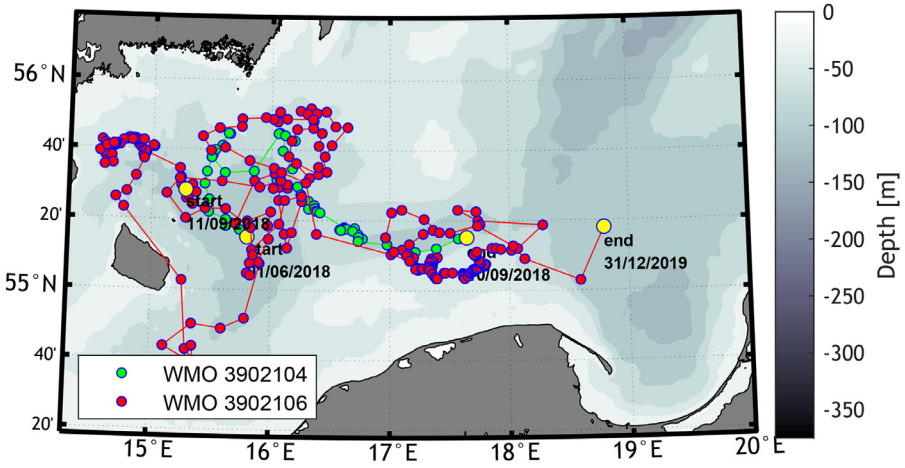

Figure 7 Pathways of the ARVOR float WMO 3902104, and after redeployment WMO 3902106.

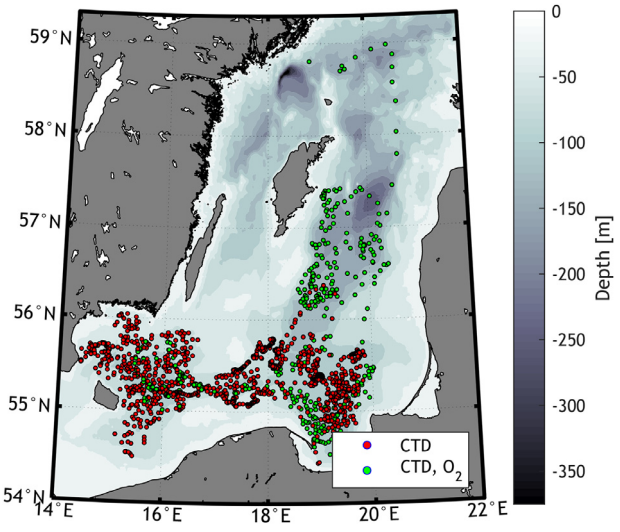

Figure 8 Positions of IOPAN Argo float profiles in the Baltic Sea between November 2016 and December 2019.

Baltic performed 1600 CTD profiles (including 600 of DO). The measurements covered the Bornholm Basin, Słupsk Furrow, Gdańsk Deep and Gotland Basin (Fig. 8). Most of the time, the floats remained in deep regions, only occasionally drifting into shallow water or coming dangerously close to the shore. The mean drift speed did not exceed 8 cm s^{-1}, but during the transition between deeps, maximum speeds, calculated as the mean speed along a straight line between profiles, were in excess of 20 cm s^{-1}. Although eastward movements were prevalent, some westward drift was observed even in the Słupsk Furrow. As they drifted, the floats moved in loops: the radius of the smallest of these loops was of the order of 4 km, which is close to the baroclinic Rossby deformation radius for the Baltic Sea basins in question (5–7 km) (Osiński et al., 2010). The direction of circulation was both cyclonic and anticyclonic.

5. Importance of Argo data

The balance of oxygen dissolved in the Baltic seawater column is different for the surface and deep layers. Mixing of these two water masses is restricted by the halocline/pycnocline barrier. The primary source of oxygen in the upper layer is the atmosphere, whereas in the deep layer it is oxygen-rich water flowing in through the Danish Straits. The west-to-east advection of North Sea water provides this life-giving element to Baltic deep waters, which suffer from hypoxia (O_2 < 2 ml l^{-1} or ~90 μmol kg^{-1}) and even anoxia (no oxygen at all). Owing to the strong stratification of the water column, the layers below the permanent pycnocline cannot be efficiently ventilated by convection, so the oxygen dynamics depends mainly on lateral advection.

The significant reduction in Major Baltic Inflows recorded in the early 1980s led to a decline in deep-water renewal (Fischer and Matthäus, 1996). In recent decades, too, the frequency of these large, barotropic inflows has dropped. On the other hand, Mohrholz (2018) showed that MBI frequency does not display a consistent trend. Other studies indicate that smaller baroclinic inflows may be playing a greater role than previously thought in the oxygenation of the southern Baltic deeps (Meier et al., 2006). Even so, the Baltic Sea is one of the largest dead zones in the world (Conley et al., 2009; Diaz and Rosenberg, 2008). Worse still, the zones of hypoxia and anoxia are expanding in all parts of the Baltic Sea. Despite the MBI in 2014, approximately 16% of the bottom area was affected by anoxia and 29% by hypoxia in 2015 (Hansson and Andersson, 2015). Oxygen in deep waters is consumed mostly during the decomposition of organic matter sinking from the surface layer, where it

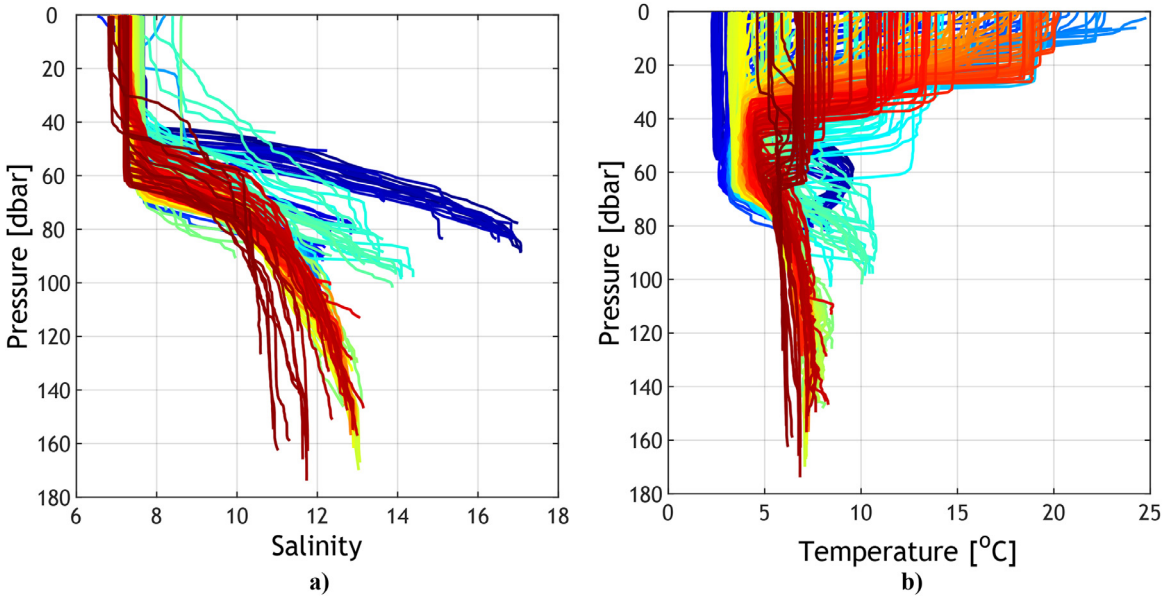

Figure 9 Salinity and temperature profiles recorded by float WMO 9202101 (February 2018–December 2019). The colour scale indicates the time of measurements, as in Fig. 10.

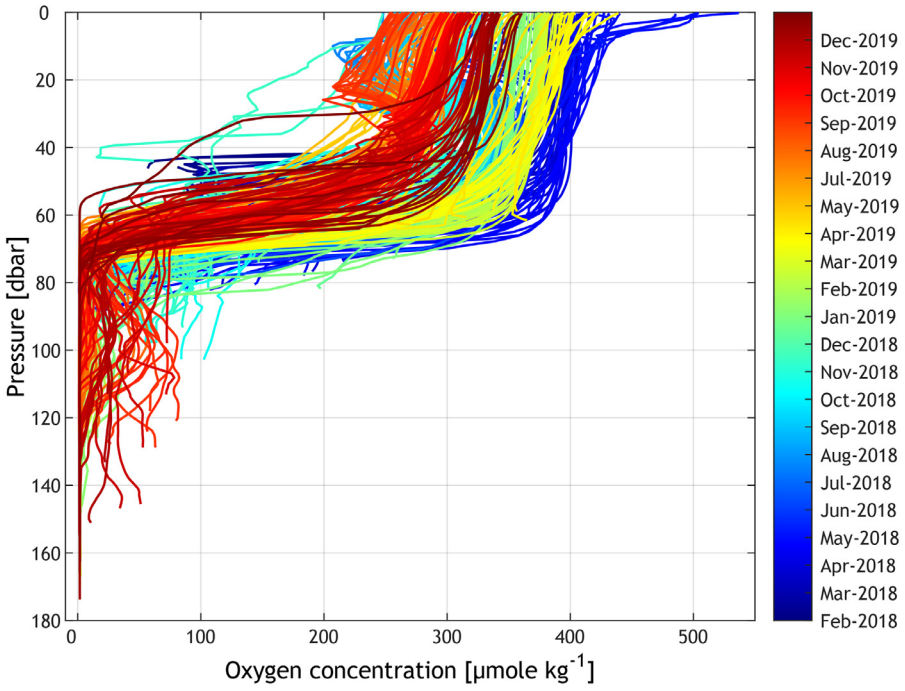

Figure 10 Dissolved oxygen concentration profiles recorded by float WMO 9202101 (February 2018—December 2019).

is produced (Stigebrandt, 2017). In the long term, the consumption of oxygen is greater than its supply, so it becomes depleted and is replaced by toxic hydrogen sulphide in the near-bottom layer (Stigebrandt et al., 2015).

In light of these facts, the monitoring of inflows is clearly a matter of urgency. Deep-water dynamics and variability of dissolved oxygen concentrations are crucial phenomena in the Baltic Sea and heavily dependent on the advection of water from the North Sea. In the western Baltic, data on inflows are gathered by permanent MARNET stations, moored in the Danish Straits (Darss Sill) and the Arkona Basin (Mohrholz et al., 2015). Data from these stations are transmitted in real-time. Unfortunately, there are no real-time data from the Polish EEZ. The measurements currently being made by IO PAN are sufficient for investigating the seasonal and long-term variability of southern Baltic water masses (Rak and Wieczorek, 2012) and for monitoring MBIs (Piechura and Beszczyńska-Möller, 2004; Rak, 2016), but not for analysing or even detecting baroclinic inflows. Also, low-resolution models are incapable of analysing these phenomena (Meier et al., 2006). To improve inflow monitoring, more measurements are needed, especially since a large proportion of the water exchange takes place during smaller barotropic and baroclinic inflows, which are more difficult to detect. That is why extensive and frequent measurements of dissolved oxygen concentrations in parallel with temperature and salinity are particularly important in the Baltic Sea.

Argo floats make such measurements possible. Unlike the 10-day measurement period of deep-ocean Argo floats, the IO PAN Baltic Sea floats usually operate in one- or two-day measurement cycles. The water is shallow, so profiling times are short, with a better spatial resolution of measurements. Within a relatively short time, CTD/O_2 floats collected data showing a range of hypoxic/anoxic zones in the Bornholm Basin, Gdańsk and Gotland Deeps, baroclinic inflows of better-oxygenated water in winter 2018 and summer—autumn 2019, the seasonal cycle of oxygen in the upper layer of the water column, and the oxycline dynamics. All the data were made available online in NRT. This provides an additional opportunity to send research vessels to certain regions, where process-oriented studies can then be carried out.

6. Selected results

The study below demonstrates the opportunities offered by Argo observations for diagnosing the dynamics of dissolved oxygen in the southern Baltic.

The profiles of properties from the whole measurement period (Fig. 9) show a seasonal variability of temperature in the upper layer as well as spatial variability of salinity in the deeper layers in various regions of the southern Baltic. Near-bottom salinity was the highest (up to 17) in the Bornholm Basin (blue lines), lower in the Gdańsk Deep, and the lowest in the Gotland Deep (red lines). The DO profiles (Fig. 10) show well-oxygenated surface waters, a strong oxycline and anoxic waters in the Gdańsk and Gotland Deeps. The temporal increase of DO in August—September at the 100 m level indicates a weak baroclinic inflow to the Gdańsk and Gotland Deeps.

The time series constructed from the raw data demonstrate the considerable seasonality of temperature (Fig. 11a) and DO concentration (Fig. 11b) in the upper layer (0—40 m) and the lack of seasonality in the deep layer (Fig. 11d). In upper layer DO is negatively correlated with water temperature. Both patterns of temperature

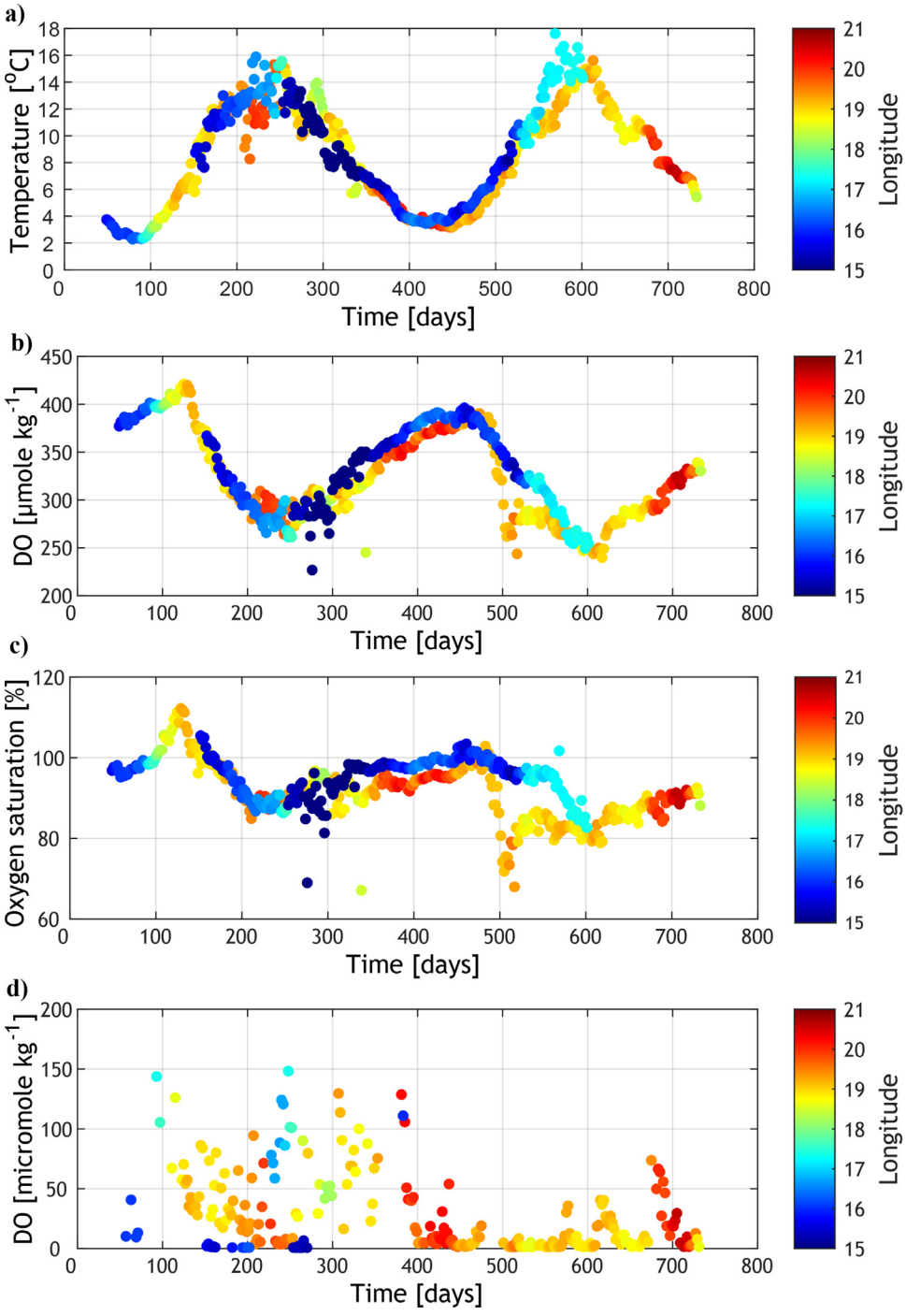

Figure 11 Time series of mean temperature for the 0–40 m layer (a), dissolved oxygen concentration for the 0–40 m layer (b), oxygen saturation [%] for the 0–40 m layer (c) and dissolved oxygen concentration for the 70–90 m layer (d) recorded by floats WMO 9202101, WMO9202104 and WMO9202106 from February 2018 to December 2019. The colour scale indicates the longitudes of the measurements. The time axes begin on 1 January 2018.

and DO are similar in the western and eastern parts of the investigated area. The time series of oxygen saturation O_{2sat} (Fig. 11c) reveal supersaturation of the Gdańsk Basin surface waters in mid-May 2018 and in May–June 2019 and region of low surface waters saturation east of Gotland. Seasonality of surface waters layer saturation is not so pronounced as in the case of DO. Pronounced shift between minimum temperature and maximum saturation and high level of saturation in spring 2018 show that oxygen delivery related to primary production in photosynthetic zone plays an important role in the surface waters oxygen budget.

Calculated seasonal distribution of the oxygen concentration in the upper layer shows the highest DO concentration in April and the lowest in the August–September period

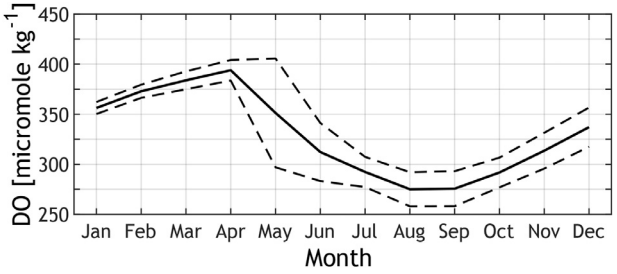

Figure 12 Seasonal distributions of mean dissolved oxygen concentration in the 0—40 m layer as recorded by floats WMO 9202101, WMO9202104 and WMO9202106 from February 2018 to December 2019. The standard deviation of the data is indicated.

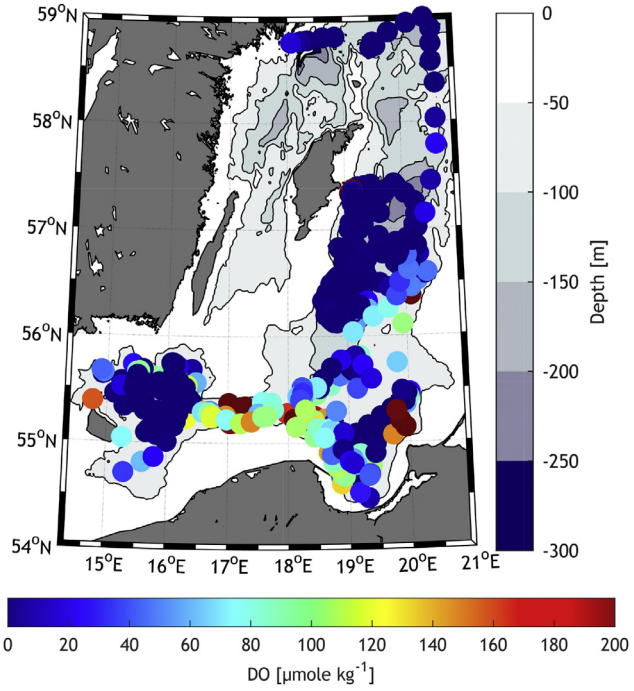

Figure 13 Near-bottom dissolved oxygen concentration. Data for regions deeper than 60 m.

(Fig. 12). High standard deviation in May arise from various dynamics of processes in springs 2018 and 2019 and the occurrence of low DO region east of Gotland in May 2019.

The absence of seasonal variability in DO in the deeper layers means that all the data can be used for investigating the bottom-layer oxygen content (Fig. 13). The deeper parts of the Bornholm Basin, Gdańsk and Gotland Deeps are mostly affected by hypoxia and anoxia. Other phenomena are discernible, like the previously mentioned small inflow reaching the Gotland Basin, and the advection pathways of oxygen-rich water. The sequence of salinity and DO rising was observed in summer—autumn 2019: at the end of June 2019 the water with extraordinary high salinity (12.8—13.9) and DO concentration (85—135 µmole kg^{-1}) in near-bottom layer (80 m depth) was observed in the central part of Słupsk Furrow at longitude 17.2°—17.4°N by float 3902106, at the beginning of September 2019 increasing of dissolved oxygen concentration in level 80—120 m was observed in the eastern Gotland Basin by the float 3902101. At 100 m depth DO concentration raised from 1 to 80 µmole kg^{-1} (Fig. 10). Another increasing of DO level and salinity (100 µmole kg^{-1} at 100 m) was noticed in Gdańsk Deep in November—December 2018.

7. Conclusions

In open-ocean oceanography, the importance of autonomous devices in measurements is increasing. Argo floats are a reliable and cheap source of oceanographic real-time data, and the global Argo array is well-organized and maintained. As a result of the coordinated work of the countries involved in global Argo, the data are freely available in the Coriolis Service. The Euro-Argo ERIC is an important part of this system, and a big advantage of Euro-Argo is that it covers the shelf seas.

The possibility of using Argo floats as part of a comprehensive southern Baltic monitoring system was postulated by Walczowski et al. (2017). Various sources of data, such as Argo floats, cruises and moorings can provide extensive, complementary data for the better monitoring of the Baltic Sea, the improvement of numerical models and validation of satellite observations.

Our three-years' experience with Argo floats in the Baltic Sea, in conjunction with the even longer work of Finnish oceanographers, shows that shallow shelf seas can also be explored with these floats. Contact with the sea bed (grounding), proximity to the shore and collisions with ships are not as dangerous for the float as had seemed earlier. In small seas like the Baltic, floats — mostly the sophisticated and expensive BGC floats — can be profitably recovered, refurbished and redeployed. The numbers and importance of BGC floats in the Baltic Sea are set to increase. Even the use of the simplest BGC float, equipped with just an oxygen sensor, significantly enhances the opportunities for recording important processes and data interpretation. According to Euro-Argo's preliminary estimates, seven continuously working floats should be adequate for the basic monitoring of Baltic deep waters, although their recovery, redeployment and relocation may be necessary. Additional sensors and the implementation of full BGC floats raises the value of the data. The competent, meaningful use of all the data requires the cooperation of multidisciplinary teams of scientists and technicians on the one hand and countries on the other. Despite some initial teething troubles, there is no doubt that the second, Argo revolution in oceanography has arrived in the Baltic Sea.

Acknowledgements

The Argo-Poland project is funded by the Polish Ministry of Science and Higher Education [grant number DIR/WK/2016/12].

This publication was also financed by the Euro-Argo Research Infrastructure Sustainability and Enhancement (EA-RISE) project funded by the European Union's Horizon 2020 research and innovation program [grant agreement No 824131].

The MOCCA project provided two floats for use in the Baltic Sea.

Thanks to the Euro-Argo ERIC, especially to Romain Cancouët for consultation and help in tuning the floats for the Baltic Sea conditions.

We would like to express our gratitude to Henry Bittig for help in oxygen data calibration. We would also like to thank the crew of r/v *Oceania* for their support and help at sea.

References

Conley, D.J., Björck, S., Bonsdorff, E., Carstensen, J., Destouni, G., Gustafsson, B.G., Hietanen, S., Kortekaas, M., Kuosa, H., Meier, M., Müller-Karulis, B., Nordberg, K., Norkko, A., Nürnberg, G., Pitkänen, H., Rabalais, N.N., Rosenberg, R., Savchuk, O.P., Slomp, C.P., Voss, M., Wulff, F., Zillén, L., 2009. Controlling Eutrophication: Nitrogen and Phosphorus. Environ. Sci. Tech. 43 (10), 3412—3420.

Diaz, R.J., Rosenberg, R., 2008. Spreading dead zones and consequences for marine ecosystems. Science 321 (5891), 926—929, https://dx.doi.org/10.1126/science.1156401.

Euro-Argo ERIC, 2017. Strategy for evolution of Argo in Europe, v3.2., EA-2016-ERIC-STRAT, https://dx.doi.org/10.13155/48526.

Elken, J., Matthäus, W., 2008. Physical system description. In: von Storch, H. (Ed.), Assessment of Climate Change for the Baltic Sea Basin. Series: Regional climate studies. Springer-Verlag, Berlin, Heidelberg, 379—398.

Fischer, H., Matthäus, W., 1996. The importance of the Drogden Sill in the sound for major Baltic inflows. J. Marine Syst. 9, 137—157, https://dx.doi.org/10.1016/S0924-7963(96)00046-2.

Haavisto, N., Tuomi, L., Roiha, P., Siiriä, S.-M., Alenius, P., Purokoski, T., 2018. Argo floats as a novel part of the monitoring the hydrography of the Bothnian Sea. Front. Mar. Sci. 5, art. 324, https://dx.doi.org/10.3389/fmars.2018.00324.

Hansson, M., Andersson, L., 2015. Oxygen Survey in the Baltic Sea 2015: Extent of Anoxia and Hypoxia, 1960—2015. The major inflow in December 2014. Report Oceanography No. 53, SMHI, Norrköping, 24 pp.

HELCOM, 1986. Water Balance of the Baltic Sea. Baltic Sea Environment Proceedings No. 16. HELCOM, 97 pp.

Meier, M., Feistel, R., Piechura, J., Arneborg, L., Burchard, H., Fiekas, V., Golenko, N., Kuzmina, N., Mohrholz, V., Nohr, V., Paka, V.T., Sellschopp, J., Stips, A., Zhurbas, V., 2006. Ventilation of the Baltic Sea deep water: a brief review of present knowledge from observations and models. Oceanologia 48 (S), 133—164.

Mohrholz, V., Naumann, M., Nausch, G., Krüger, S., Gräwe, U., 2015. Fresh oxygen for the Baltic Sea — An exceptional saline inflow after a decade of stagnation. J. Marine Syst. 148, 152—166.

Mohrholz, V., 2018. Major Baltic Inflow Statistics — Revised. Front. Mar. Sci. 5, art. 384, https://doi.org/10.3389/fmars.2018.00384.

Le Traon, P.Y., 2013. From satellite altimetry to Argo and operational oceanography: three revolutions in oceanography. Ocean Sci. 9 (5), 901—915, https://doi.org/10.5194/os-9-901-2013.

Osiński, R., Rak, D., Walczowski, W., Piechura, J., 2010. Baroclinic Rossby radius of deformation in the southern Baltic Sea. Oceanologia 52 (3), 417—429, http://dx.doi.org/10.5697/oc.52-3.417.

Piechura, J., Walczowski, W., Beszczyńska-Möller, A., 1997. On the structure and dynamics of the water in the Słupsk Furrow. Oceanologia 39 (1), 35—54.

Piechura, J., Beszczyńska-Möller, A., 2004. Inflow waters in the deep regions of the southern Baltic Sea — transport and transformations. Oceanologia 46 (1), 113—141.

Rak, D., 2016. The inflow in the Baltic Proper as recorded in January—February 2015. Oceanologia 58 (3), 241—247, http://dx.doi.org/10.1016/j.oceano.2016.04.001.

Rak, D., Wieczorek, P., 2012. Variability of temperature and salinity over the last decade in selected regions of the southern Baltic Sea. Oceanologia 54 (3), 339—354, https://doi.org/10.5697/oc.54-3.339.

Purokoski, T., Aro, E., Nummelin, A., 2013. First long-term deployment of Argo float in Baltic Sea Argo's inaugural operation in shallow, low-salinity water. Sea Technol. 54, 41—44.

Roemmich, D., Alford, M., Claustre, H., Johnson, K., King, B., Moum, J., Oke, P., Owens, Brachner, B., Pouliquen S., Purkey, S., Scanderbeg, M., Suga, T., Wijffels, S., Zilberman, N., Bakker, D., Baringer, M., Belbeoch, M., Bittig, H.C., Boss, E., Calil, P., Carse, F., Carval, T., Chai, F., Conchubhair, D.Ó., d'Ortenzio, F., Dall'Olmo, G., Desbruyeres, D., Fennel, K., Fer, I., Ferrari, R., Forget, G., Freeland, H., Fujiki, T., Gehlen, M., Greenan, B., Hallberg, R., Hibiya, T., Hosoda, S., Jayne, S., Jochum, M., Johnson, G.C., Kang, KiR., Kolodziejczyk, N., Körtzinger, A., Le Traon, P.-Y., Lenn, Y-D., Maze, G., Mork, K.E., Morris, T., Nagai, T., Nash, J., Naveira Garabato, A., Olsen, A., Pattabhi, R.R., Prakash, S., Riser, S., Schmechtig, C., Schmid, C., Shroyer, E., Sterl, A., Sutton, P., Talley, L., Tanhua, T., Thierry, V., Thomalla, S., Toole, J., Troisi, A., Trull, T.W., Turton, J., Velez-Belchi, P.J., Walczowski, W., Wang, H., Wanninkhof, R., Waterhouse, A.F., Waterman, S., Watson, A., Wilson, C., Wong, A.P.S., Xu, J., Yasuda, I., 2019. On the Future of Argo: A Global, Full-Depth, Multi-Disciplinary Array. Front. Mar. Sci. 6, 1—28, art. 439, https://doi.org/10.3389/fmars.2019.00439.

Roiha, P., Siiriä, S.M., Haavisto, N., Alenius, P., Westerlund, A., Purokoski, T., 2018. Estimating currents from Argo trajectories in the Bothnian Sea. Baltic Sea. Front. Mar. Sci. 5, art. 308, https://doi.org/10.3389/fmars.2018.00308

Siiriä, S., Roiha, P., Tuomi, L., Purokoski, T., Haavisto, N., Alenius, P., 2019. Applying area-locked, shallow water Argo floats in Baltic Sea monitoring, J. Oper. Oceanogr. 12 (1), 58—72, http://dx.doi.org/10.1080/1755876X.2018.1544783.

Stigebrandt, A., 2017. Processes and factors influencing the through-flow of new deep water in the Bornholm Basin. Oceanologia 59 (1), 69—80, http://dx.doi.org/10.1016/j.oceano.2016.09.001.

Stigebrandt, A., Rosenberg, R., Råman, L., Ödalen, M., 2015. Consequences of artificial deepwater ventilation in the Bornholm Basin for oxygen conditions, cod reproduction and benthic biomass — a model study. Ocean Sci. 11 (1), 93—110.

Walczowski, W., Wieczorek, P., Goszczko, I., Merchel, M., Rak, D., Beszczynska-Möller, A., Cisek, M., 2017. Monitoring the salt water inflows in the southern Baltic Sea. In: Proceedings of the Eighth EuroGOOS International Conference 3—5 October 2017, Bergen, Norway, 165—169.

Oceanologia (2020) 62, 489—500

Available online at www.sciencedirect.com

ScienceDirect

journal homepage: www.journals.elsevier.com/oceanologia

ORIGINAL RESEARCH ARTICLE

The impact of Klaipėda Port entrance channel dredging on the dynamics of coastal zone, Lithuania

Gintautas Žilinskas, Rasa Janušaitė, Darius Jarmalavičius, Donatas Pupienis*

Nature Research Centre, Institute of Geology and Geography, Vilnius, Lithuania

Received 20 May 2020; accepted 3 August 2020
Available online 15 August 2020

KEYWORDS
Southern Baltic;
Sediment transport;
Port jetties;
Entrance channel dredging

Summary Dredging entrance channels to ports on open littoral drift seashores often causes major morphological changes to the shoreline. This study aims to assess the impact of dredging the Port of Klaipėda's entrance channel and the construction of the jetties on the coastal zone. Based on an analysis of cartographic material collected between 1835 and 2017, and on field data (bathymetric surveys and cross-shore profile levelling), changes to the coastal zone in the area nearest to the port were evaluated. The dominant longshore sediment transport on the Lithuanian nearshore runs from south to north. Thus, based on established patterns, intensive accretion could have been expected to take place on the southern side of the port jetties and erosion on their northern side. However, in the case of the Port of Klaipėda, in the area nearest to the port on the updrift side of the port jetties, where accretion would have been expected to take place, the nearshore depth increased throughout the 20th century (when the length and configuration of the jetties did not change). The shoreline shifted landward instead of moving further out to sea. The present study shows that the intensive dredging of the entrance channel caused nearshore and shore erosion on the updrift side of the port jetties, even while a sufficient sediment load was being transported by the longshore drift.

* Corresponding author at: Nature Research Centre, Institute of Geology and Geography, Akademijos str. 2, LT-08412 Vilnius, Lithuania.
E-mail addresses: gintautas.zilinskas@gamtc.lt (G. Žilinskas), rasa.janusaite@gamtc.lt (R. Janušaitė), darius.jarmalavicius@gamtc.lt (D. Jarmalavičius), donatas.pupienis@gamtc.lt (D. Pupienis).
Peer review under the responsibility of the Institute of Oceanology of the Polish Academy of Sciences.

Production and hosting by Elsevier

https://doi.org/10.1016/j.oceano.2020.08.002

1. Introduction

The depth of ports is an important factor with regard to competition in container shipping. In order to accommodate the largest cargo carriers, port water areas must be dredged to remove excess sediments (Demir et al., 2004; HELCOM, 2015; Mohanty et al., 2012; Žaromskis, 2008).

The fact that nearshore dredging causes shore erosion has been known for a long time (Blackman, 1951; Kojima et al., 1986; McLoughlin, 2000; Shaw, 1978; Simons and Hollingham, 2001; Šuiskyj et al., 1987; Work et al., 2004). The impact of dredging on the shoreline usually depends directly on the distance between the shoreline and the dredging site, the depth of the dredged pit and the amount of extracted marine sediments (Marine Habitat Committee, 2000).

An overview of the processes taking place in the dredging environment and the results of laboratory investigations and numerical modelling are given in Demir et al. (2004). It was determined that offshore dredging has both a direct and indirect impact on the coastal zone. According to Demir et al. (2004), the amount of erosion is in proportion to the amount of dredged sediments if the depth of the pit is smaller than the depth of closure. When the dredging pit is beyond the limits of the depth of closure, dredging has no direct impact on the shore. Wave field changes that are predetermined by changes in the bottom relief are regarded as an indirect impact (Demir et al., 2004). The sediment transport models change depending on changes in the wave energy's alongshore distribution.

The impact of port dredging on the state of the adjacent shores is not as easily determined when entrance channels are protected by jetties and when water and sediment transport takes place between a river delta or estuary and the sea via a channel (Healy et al., 2002; Kudale, 2010; Mohanty et al., 2012; Tsinker, 2004). The influence of the Klaipėda Port jetties on the state of the adjacent coastal area has been analyzed in a number of studies (Knaps, 1965; Pupienis et al., 2013; Žaromskis and Gulbinskas, 2016; Žaromskis, 2008; Žilinskas, 1998). These studies focused on the impact of the port jetties and emphasized coastal zone erosion processes on the downdrift side. The impact of entrance channel dredging on the coastal zone was not taken into consideration.

The aim of the present study is to show the impact of entrance channel dredging on the adjacent shore and to prove that its intensive dredging and cleaning have caused coastal erosion on the updrift side of the port jetty even while a sufficient sediment load was being transported by the alongshore drift.

2. Study area and methods

The Port of Klaipėda is located in the south-western part of the Baltic Sea across the Klaipėda Strait (Figure 1). It is the northernmost ice-free port (even in the coldest winters) in the East Baltic. At present, the water area of the port (6.5 km^2) covers almost the entire Klaipėda Strait. The length of the water area is approximately 11.5 km, and its width ranges between 3 m at the port gates in the north and 1350 m in the southern part of the Strait. The average depth of the entrance channel is 15.2–15.5 m and the average depth of the navigation channel near most of the quays is 14.5 m.

The number of stormy days (with a wind velocity of over 15 m/s) per year is between 50 and 60. Storms usually occur in the autumn and winter. The wind velocity during storms reaches 25–28 m/s, while during extreme storms it can even reach 30–40 m/s. The maximal recorded wave height on the nearshore exceeded 6 m and the maximal sea level rise reached 185 cm. The most frequent storm wind directions are south-westerly (35.6%) and westerly winds (24.3%) (Kriaučiūnienė et al., 2006). Up to 57.7% of the waves on the Lithuanian shoreline are from a westerly direction: SW, W and NW (Jakimavičius et al., 2018). The high volumes of river runoff into the Curonian Lagoon (about 23 km^3/yr) are responsible for outflowing currents dominating the Klaipėda Strait (80% of the surface and 60% of the near-bottom currents). The water level in the Lagoon is on average 12 cm above sea level. The average velocity of the outflowing currents is 0.3–0.4 m/s. During spring tides, this velocity can reach 2 m/s. Inflowing currents develop in W, NW and N storm wind conditions. As the tide-ebb amplitude on the south-eastern Baltic coast only reaches 3.5–4.0 cm (Jarmalavičius et al., 2020), the wind-generated waves, the south to north alongshore sediment transport (Žilinskas et al., 2018) and the aeolian processes (Jarmalavičius et al., 2019) are the main beach-forming agents on the Lithuanian shore. The Baltic sea level rise on the Lithuanian shore (0.16±0.02 cm/yr) has so far not had any noticeable impact on the shoreline's dynamics (Jarmalavičius et al., 2017).

The impact of dredging the Klaipėda Port entrance channel on the shore zone was analyzed using charts during a number of years, in 1835, 1845, 1878, 1910, 1993, 1955, 1961, 1991, 1998, 2003 and 2017. Also used were bathymetric plans of the port (1:10 000 and 1:5 000), material that had accumulated in the Klaipėda Port archives, and measurements taken on the shore and nearshore. The investigation area included approximately 1500 m-long sectors on both sides of the port jetties to 15 m isobaths (the data before the 20th century was collected to 10 m isobaths).

A bathymetric survey was carried out in 2017 using a Humminbird Helix 9 SI GPS multibeam echo sounder on both sides of the port jetties. Morphological investigations of the shore in the Klaipėda Port sector (3000 m-long sectors on both sides of the port) have been carried out since 1995. Cross-profiles of the coast are levelled (using a TOPCON GTS 229 electronic tachometer) once a year in the first week of May in calm weather (fair weather) conditions and when the sea level is close to the mean long-term average (Jarmalavičius et al., 2012). Shoreline dynamics and nearshore bathymetry changes for different periods are analyzed using ArcMap 10.7 software.

3. Results

Before the port jetties were constructed, the depth of the Klaipėda Strait was maintained by outflowing spring tidal waters from the Curonian Lagoon. The dominant depth was 5 m. The tidal waters from the Lagoon transported sediments of varying composition (mud, aleurite and sand).

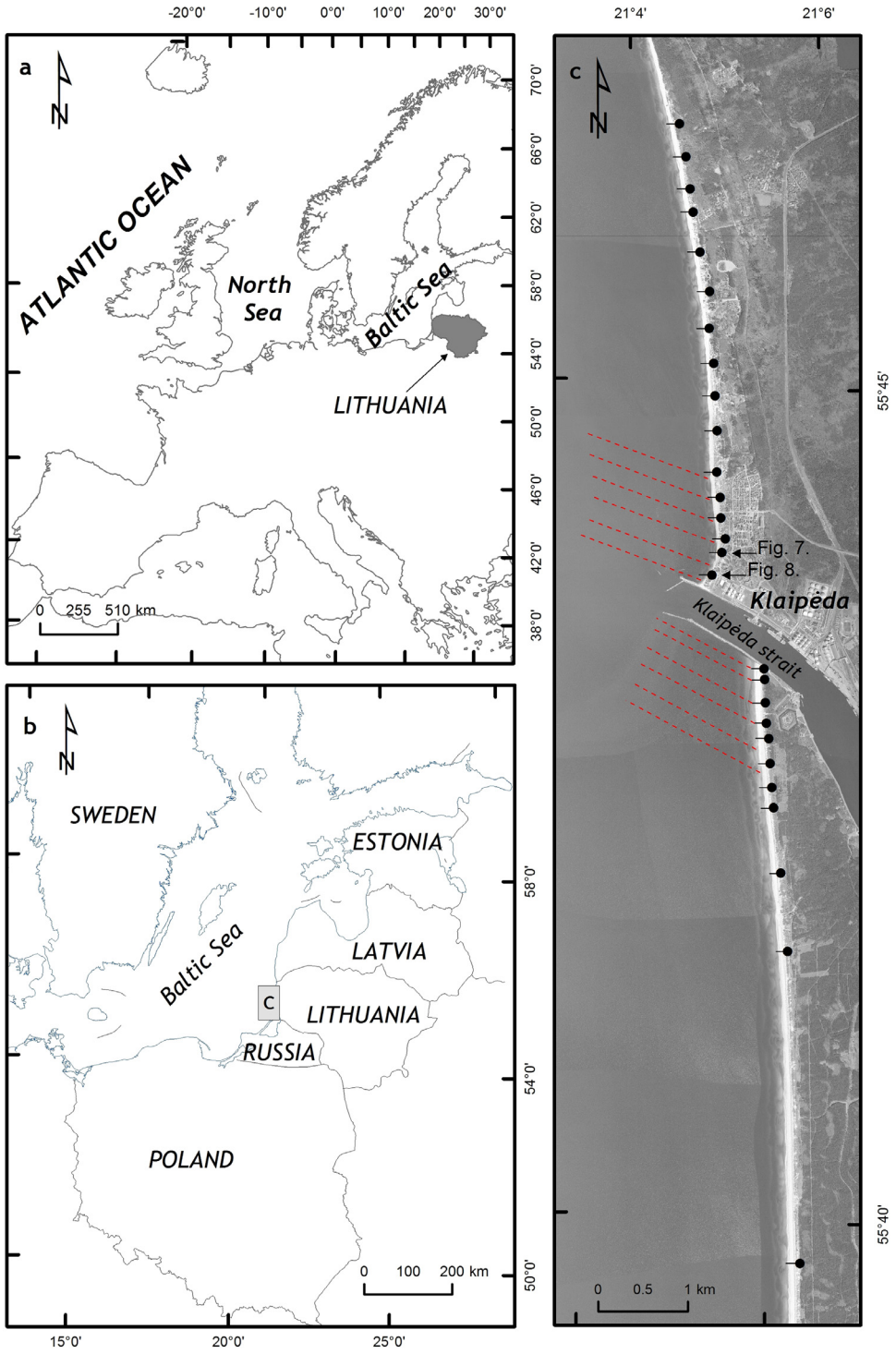

Figure 1 Study area. Black dots indicate locations of cross-shore levelling, red doted lines — locations of nearshore cross-section measurements.

These sediments, as well as sediments transported by the sea from south to north, form three bars: southern, central and northern. At the end of the 18th century and the beginning of the 19th century (Figure 2), an intensive accumulation of sand took place at the distal end of the Curonian Spit. Between 1796 and 1820, the distal end shifted approximately 640 m northward (Veit, 1821), i.e. 8.5 m per year on average. The pressure of the water flowing out of the Curonian Lagoon and onto the mainland shore due to the extension of the Curonian Spit caused the mainland shore to erode. Between 1796 and 1820, the mainland shore retreated by 180 m (Veit, 1821), i.e. by 7.2 m per year. In 1773, 1784, 1797 and 1801, in order to protect the entrance channel from silting, wooden piles with stone fillings were embedded at the distal end of the Curonian Spit.

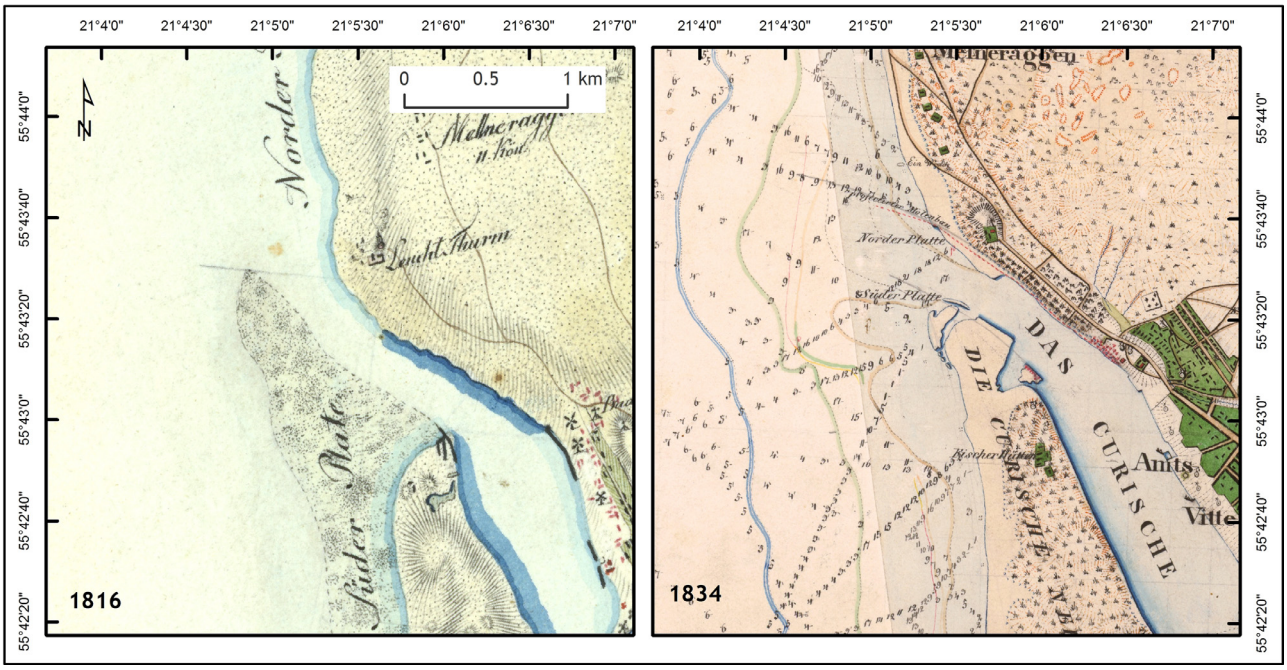

Figure 2 The Klaipėda Strait before the beginning of port jetties construction in 1816 and 1834.

However, during and even after the end of the construction work, the jetties were destroyed over and again by strong storms or spring tides (Žilinskas, 1998). Only a 152 m-long jetty, constructed in 1806 and stretching approximately 46 m out to sea (Figure 3a), was not destroyed (Veit, 1921). After 10 years, due to a rapid accumulation of sand, this jetty became part of the shore and by 1821 it was totally covered with sand. Sand flowing into the Klaipėda Strait impeded navigation.

The analysis of the Klaipėda Port jetties and entrance channel deepening impact on adjacent coastal environments was split into three specific periods: 1834—1902; 1902—2000; 2000—2017.

3.1. Construction of the port jetties (1834—1902)

In 1834, in order to ensure favourable conditions for navigation and to stop the erosion of the Klaipėda Strait's mainland shore, the construction of the northern jetty was started (Figure 3). The finished (1878) jetty was 1158 m in length. The construction of a new southern jetty was started in 1847 50—60 m to the north of the jetty built in 1806 (Figure 3). The construction work finished in 1902. The new jetty was 1227 m in length.

The jetties acted as barriers against sediment drift; the northern and southern bars verged onto the shore, and on the nearshore on both sides of the jetties (at a depth of 0—3 m) intensive accumulation took place. However, at depths below 3 m, isobath bed erosion set in (Figure 4). Part of the central bar shifted out to sea due to intensified outflows from the Curonian Lagoon after the jetties were constructed. The remaining part was removed while the navigation channel was being dredged. At the end of the 19th century, the maintained depth in the entrance channel was 6 m (Figure 5). Due to the inefficient mechanics of the time, the annual amounts of dredged material did not usually exceed several thousand cubic metres (Hagen, 1885).

During the construction work, the shoreline in the adjacent sectors migrated rapidly in a seaward direction (Figures 3—4, Table 1). Large-scale changes took place alongside the jetties in particular. Further to the north or south of the jetties, these displacements were consistently less noticeable.

Between 1835 and 1878, the shoreline near the northern jetty (at a distance of 50 m) migrated 544 m in a seaward direction. Moving northward at distances of 250 m, 500 m, 750 m, 1000 m and 1250 m from the jetty, the shoreline's displacements toward the sea were 403, 265, 211, 144 and 122 metres, respectively. A similar pattern of shoreline dynamics within the same timespan could be seen in the area along the southern jetty. 50 m from the jetty, the shoreline migrated by 422 m. Further from the jetty, at distances of 250 m, 500 m, 750 m, 1000 m and 1250 m, the displacements were 284, 173, 120, 76 and 58 m, respectively.

Between 1835 and 1978, the mainland shore's area 1300 m from the northern jetty increased by approximately 326 000 m^2 and the Curonian Spit shore's area increased by just 169 000 m^2 at the same distance from the southern jetty. During the same timespan, two circumstances were responsible for the rapid seaward migration of the shoreline beyond the updrift northern jetty and for the increase in the land area being almost as twice as large as on the side of the southern jetty:

- The construction of the southern jetty only started in 1847, i.e. 13 years later than the construction of the northern jetty, behind which the shoreline had migrated markedly seaward during this timespan (Figure 3).
- Until the beginning of the 20th century, the dredged sand from the port had been dumped behind the northern jetty at shallow depths, causing an accumulation of sand

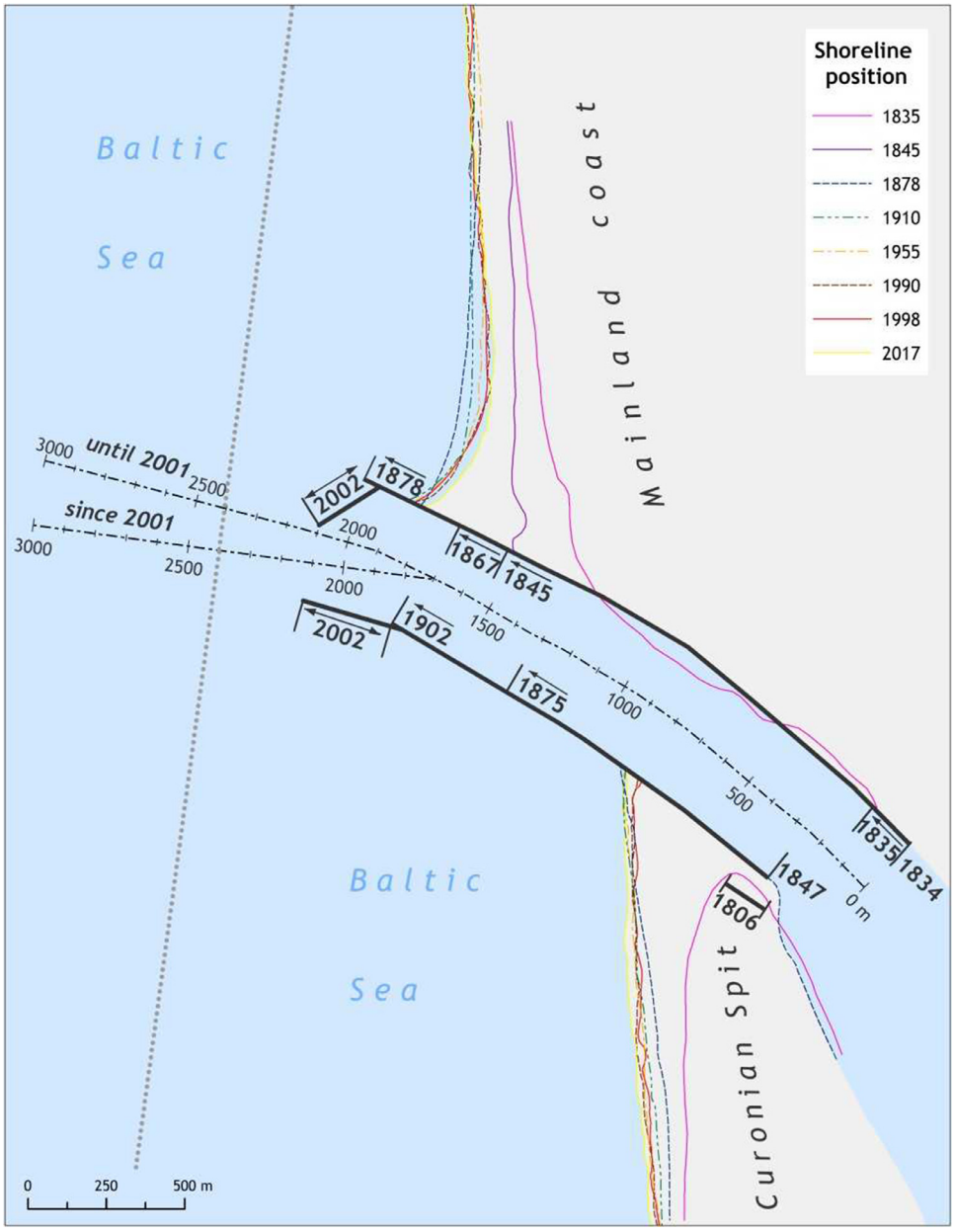

Figure 3 The stages of construction of the Port of Klaipėda's jetties and shoreline dynamics during the period 1835—2017.The dashed-dotted line indicates the fairway axis. The dotted line indicate nearshore depth dynamics showed in Figure 9. The scheme was compiled based on R. Knaps's data (1965): 1835, 1845, 1878, and on those of the authors: 1910, 1955, 1990, 1998, 2017.

on the shore. Later, when it was observed that some of the sand dumped behind the northern jetty had returned to the navigation channel, the dredged sand was dumped 10—20 m farther from the port at depths of 20—25 m from 1963 and 25—35 m from 1994.

The accumulation of large amounts of sand on the shore caused wide beaches (65—85 m) to form. In order to stop the intensive blowing of sand toward the town on the mainland shore and into the Curonian Lagoon, foredune ridge formation was started in as early as the first half of the 19th century (Musset, 1916). At the beginning of the 20th century, the foredune height beyond the northern jetty ranged from 3.8 m at a distance of 50 m from the jetty to 10.5 m at a distance of 1620 m (Figure 6a). Even larger amounts of sand accumulated beyond the southern jetty: the height of the foredune ridge 50 m from the jetty was 6.0 m and at a distance of 1750 m it even reached 13.1 m (Figure 6b).

The maximal seaward shift of the shoreline on both sides of the jetties almost coincided with the end of the construction work (Figure 3).

3.2. Intensive dredging of the entrance channel (1902—2000)

Throughout the 20th century, the length and configuration of the port jetties remained the same (Figures 3, 4a—b). They were only heightened, widened and repaired. How-

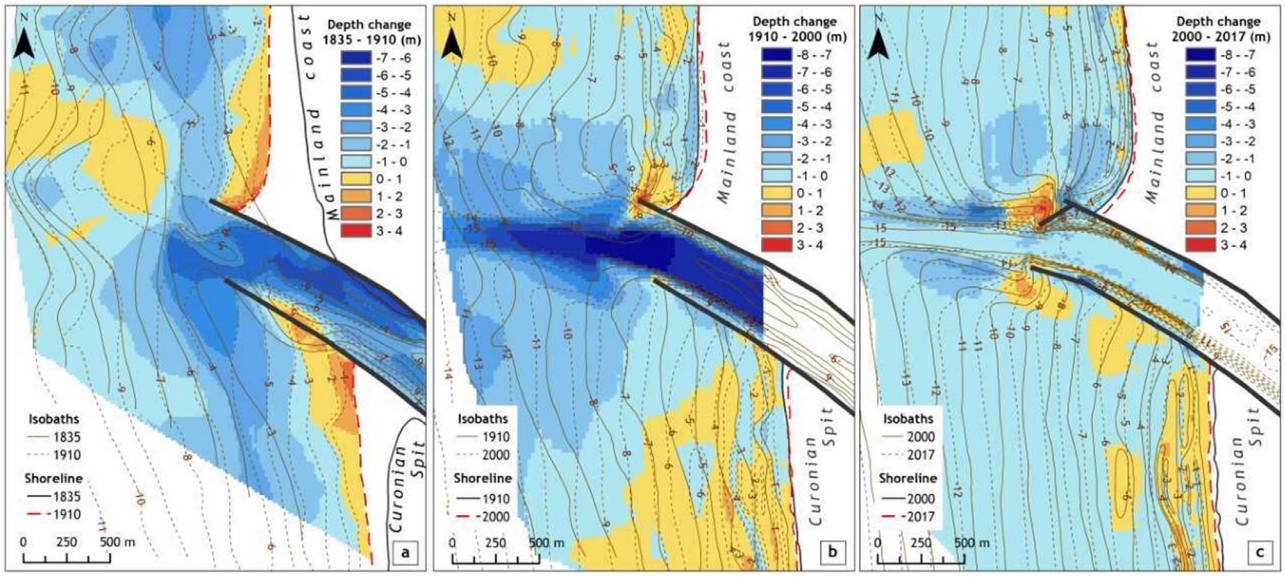

Figure 4 The coastal zone dynamics during the period 1835–2017. The positive depth change values indicate accumulation and the negative values indicate erosion.

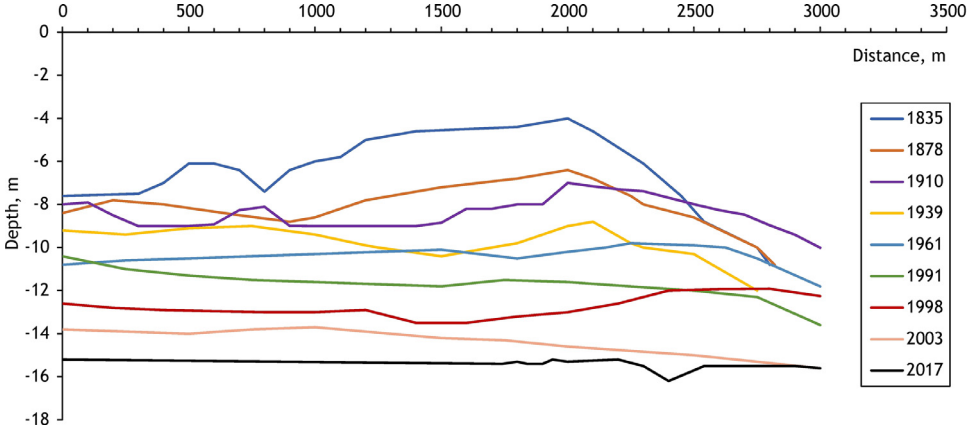

Figure 5 Depth dynamics along the fairway axis of the entrance channel from the start of Klaipėda Port construction to these days. The profile location is shown in Figure 3.

Table 1 Shoreline dynamics (m/yr) in 1835–2017 at both sides of the Klaipėda Port jetties.

Period		Shoreline displacement, m/year					
The distance from jetty, m		1835–1878	1878–1910	1910–1955	1955–1990	1990–2004	2004–2017
Northern	**1250**	2.83	0.22	0.40	1.09	0.15	0.39
jetty	**1000**	3.35	0.91	−0.62	−0.14	0.38	−0.63
	750	4.91	−0.09	−0.87	−0.29	0.00	−1.69
	500	6.16	−0.72	−0.69	−0.71	0.40	−1.94
	250	9.37	−1.22	−0.24	−0.43	0.02	−2.43
	50	12.7	0.38	−0.22	−0.46	0.12	−1.95
Southern	**50**	9.81	0.22	−0.09	−1.29	−0.21	0.23
jetty	**250**	6.61	0.84	−0.09	−0.46	−0.37	1.78
	500	4.02	0.81	0.27	−0.12	−0.22	2.45
	750	2.79	1.41	0.36	0.17	−0.12	2.16
	1000	1.77	1.72	0.58	0.29	0.03	2.20
	1250	1.35	1.13	0.82	0.23	0.37	1.96

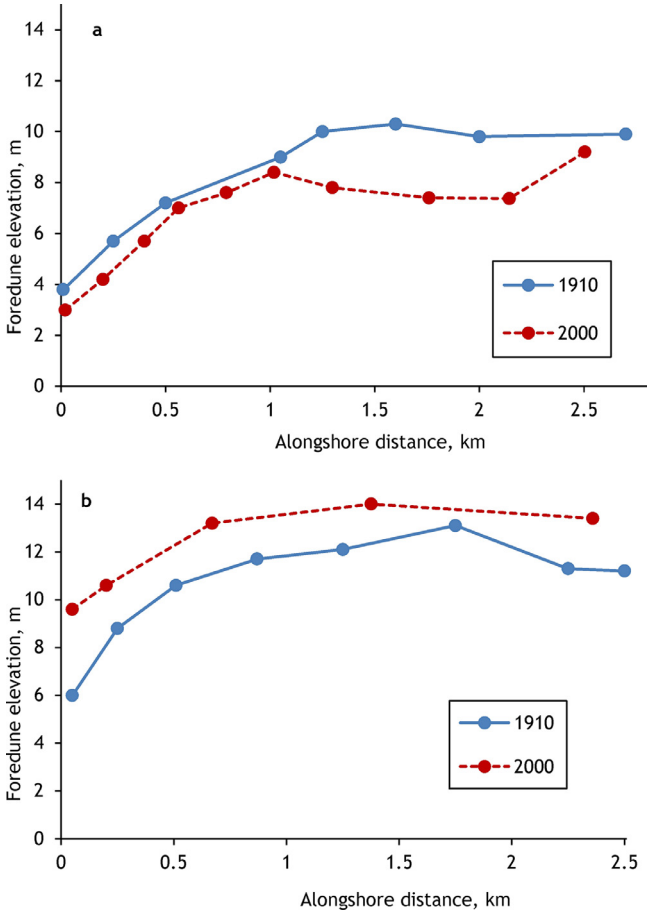

Figure 6 Dynamics of the foredune height in 1910–2000: a – northward, b – southward from the jetties.

ever, this timespan was marked by particularly significant changes in the parameters of the entrance channel. Since the beginning of the 20th century, efforts have been made to maintain a depth of 6 m in the entrance channel. In 1927, the depth was increased to 6.5 m, in 1928 to 8 m and in 1939 to 9.5 m. During and after the Second World War (1941–1958), the dredging works were irregular and the depth of the entrance channel varied from 6 to 8 m (Žilinskas, 1998). In 1958, regular dredging was resumed and in 1962 the depth reached 11 m and the channel was completely straightened for the first time. In order to accommodate ships with the deepest drafts, the dredging work continued: in 1974, the depth of the entrance channel had already reached 12 m, in 1986 it was 12.5 m and in 1997 it was 14.5 m (Figure 5).

The channel was simultaneously deepened and widened. Before the 20th century, judging from the bathymetric plans, the width of the entrance channel meandering between the bars ranged from 20 to 35 m. At the beginning of the 20th century it was 30–50 m. Between 1928 and 1939, the maintained width of the channel was 50 m, from 1945 it was 80 m, from 1957 it was 100 m and from 1997 it was 130 m. Beginning in 1960, in order to compensate for the rapid filling in of the channel during storms, the slopes of the channel were formed with smaller angles and sediment traps were constructed beyond the port gates. The entrance channel was widened to almost 260 m along an approximately 200 m sector beyond the port gates. This wider cross-section of the navigation channel reduced the speed of the currents in the sediment traps along the channel and moderated any sudden changes in depth.

Deepening and widening the entrance channel increased the amount of dredged soil at the same time. Between 1930 and 1960, up to 100 000 m^3/yr of soil was removed to maintain a depth of 8–9 m (Žaromskis and Gulbinskas, 2016). On average, approximately 210 000 m^3/yr of soil had to be removed to maintain a depth of 10.5–11.0 m (1960–1970) and approximately 330 000 m^3/yr to maintain a depth of 12–13 m (1970–1997). Based on data from the Klaipėda Port archives, between 1950 and 2000 over 10 million m^3 of sediment was removed from the channel during the deepening and widening work.

It should be noted that the internal water area of the port was deepened and expanded at the same time the navigation channel was being deepened and widened. As a result, transitory coarse-grained sediment from the rivers and Curonian Lagoon accumulated in the inner water area of the port, and since the 1980s this has not had any effect on the filling in of the navigation channel (Gulbinskas, 1999; Mėžinė et al., 2019). At present, silt (0.01–0.0 mm) and clay (<0.01 mm) particles dominate the lagoon water (Remeikaitė-Nikienė et al., 2018).

In the 20th century, with the increasing amounts of dredged sediment, widening the entrance channel and dumping the dredged sand at greater depths in the water area adjacent to the entrance channel also increased. The nearshore erosion also increased significantly (Figure 4b). A comparison of the morphometric data from the bathymetric plans from 1910 and 2000 showed that during this timespan, while the entrance channel was being deepened and widened, approximately 3.7 million m^3 of sediment was removed (the sediment removed during cleaning was not included). Due to sea bottom erosion, the nearshore to the north of the entrance channel has lost 1.3 million m^3 of sediment and to the south 1.8 million m^3.

The shallowing of the sea bottom (since the 1990s) at the distal end of the northern jetty can be explained by shipwrecks. On November 21 1981, a 170 m-long tanker from Gibraltar named “Globe Asimi” crashed at the distal end of the northern jetty, broke into two parts and sank. On September 25 1988 during a fierce storm, a German freighter named “Rudolf Breitscheid” (142.2 m long) crashed and sank in almost the same place. These ships are lying on the sea bottom (with their upper parts protruding a few metres above the surface) almost parallel to the shore along the northern jetty in a south-north direction and act as a barrier against the waves, thus creating the right conditions for the accumulation of sediment.

Ever since the jetties were finished, the shoreline on either side of them has been retreating (Figure 3). Near the northern jetty, a bay has developed with its central part at a distance of 500 m from the jetty (Figures 3, 4b). It is interesting to note that there was also maximal shore erosion 500 m from the downdrift side of a jetty in Gopalpur Port on the east coast of India (Mohanty et al., 2012). Between 1910 and 1990, the average rate of shoreline retreat in the central part of the bay was 0.63 m/yr (Table 1). Shoreline erosion took place in a sector stretching 1 km north of the jetty. In this sector, approximately 45.2 thousand m^2 of land

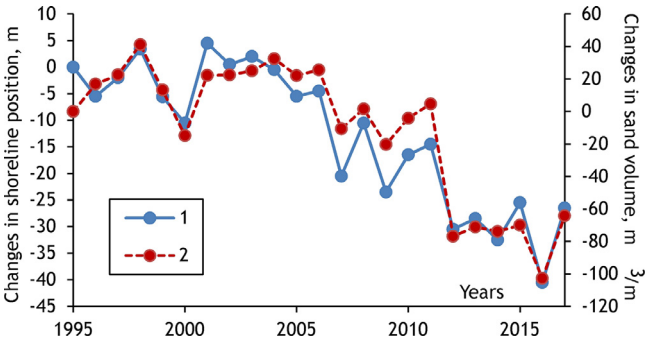

Figure 7 The shoreline dynamics (1) and the volume of sand (2) at a distance of 500 m north of the jetty during the period 1995–2017. The positive values indicate shoreline accretion and the amount of accumulated sand, and the negative values indicate shoreline erosion and the amount of eroded sand. The profile location is shown in Figure 1.

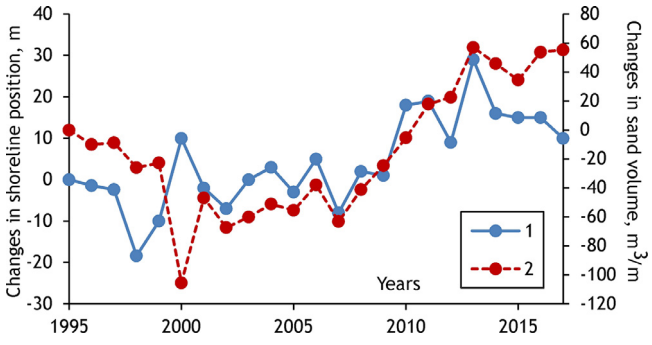

Figure 8 The shoreline dynamics (1) and the volume of sand (2) at a distance of 200 m north of the jetty during the period 1995–2017. The positive values indicate shoreline accretion and the amount of accumulated sand, and the negative values indicate shoreline erosion and the amount of eroded sand. The profile location is shown in Figure 1.

was washed away. During the analyzed timespan, the spatial position of the shoreline further to the north remained stable or even migrated slightly out to sea. This shoreline retreat has markedly changed the shore's morphology. The average width of the beach decreased from 60–75 m in 1910 to 35–45 m in 2000. Due to these narrow beaches, storms could reach and erode the foredune ridges. In the sector closest to the jetty, the foredune ridge has disappeared altogether (Figure 6a).

The last decade of the 20th century and the beginning of the 21st century can be viewed as an exception. During this timespan, the spatial position of the shoreline stabilized and in some places even moved out to sea. This phenomenon can be explained by the impact of the above-mentioned shipwrecks on hydro-lithodynamic processes. In 1995 work got underway to salvage the shipwrecks. The final wrecks were removed in 2005 and precisely at that time the shoreline retreat resumed and its intensity increased (Figure 7, Table 1).

South of the jetties, in the sector closest (250–300 m) to the jetties, the shoreline retreated throughout the 20th century (Figures 3, 4b, Table 1). In this sector, approximately 13.1 thousand m^3 of land has washed away. Further to the north, the shoreline has been migrating seaward (with small fluctuations caused by extreme storms) since the port was first built. On the southern side of the port jetties, the changes to the beach width have not been as significant: from 65–75 m in 1910 to 40–60 m in 2000 within a 250–300 m-long sector. Further to the south, the beach width has remained almost unchanged (Žilinskas et al., 2001). The height of the foredune ridge has increased along the entire sector, but its spatial position in the 250 m-long sector closest to the southern jetty has changed (Figure 6b). As the shoreline has retreated (Figure 3) the foredune ridge has eroded. Some of the sand has washed away out to sea and some has been blown further to the leeward side of the foredune. Beyond this shore sector (Figures 3, 4b), where the dynamic trend of the shoreline changes (the shoreline's regression is replaced by transgression), not only has the height of the foredune ridge increased, but between 1910 and 2000 a new ridge developed 40–50 m from the foredune ridge closer to the sea. Its height in 2000 was 5–6 m (Žilinskas et al., 2001).

3.3. Reconstruction of the port jetties (2000–2017)

In 2001–2002, the jetties were lengthened (the northern one by 205 m and the southern one by 278 m), turning them SW. The port gates were narrowed in order to slow down the filling in of the entrance channel at the distal end of the jetties. The direction of the fairway axis was also changed (Figure 3). The entrance channel was deepened to 15.5 m, and to 16.2 beyond the port gates (Figure 5). The width of the entrance channel reached 150 m in 2004. Moreover, the slopes of the channel were made twice as flat (1:6, $tg\alpha = 0.166$) as before (1:3, $tg\alpha = 0.333$) in order to prevent the rapid filling in of the entrance channel during storms. In 2001–2002, new sediment traps approximately 200 m long and 125 m wide (on both sides of the channel) were dug around 200 m from the ends of the lengthened jetties.

Although relatively little time (15 years) has passed since the jetties were reconstructed, it is evident (Figure 4c) that the nearshore to the north of the deepened entrance channel and beyond the northern jetty has also deepened. A rather intensive accumulation of sediment has been observed at the end of the northern jetty. This is related to the ongoing filling in of the pits that were left after the shipwrecks were salvaged. Moreover, while the northern jetty was being lengthened, the northern sediment trap was filled in. After the jetties were lengthened, the retreat of the shoreline (av. 2.5 m/yr) beyond the northern jetty intensified (Figures 3, 7; Table 1). The foredune ridge along a 450 m sector stretching from the jetty was completely washed away.

After the jetties were reconstructed, there was an increase in the depth of seabed south of the deepened entrance channel, while on the adjacent nearshore an accumulation of sediment was also observed (Figure 4c). The shallowing of the nearshore affected the shoreline's dynamic trend (Figure 8).

Since around 2004, the shoreline has been migrating seaward (at a rate of approximately 1.5 m/yr) (Table 1). These changes could have been predetermined by a few factors: mitigated wave impact after lengthening the jetty and turning it westward, a smaller nearshore slope angle and filling in the former sediment traps. Moreover, in 2013, over

Table 2 Dynamics of the nearshore slope (up to a depth of 8 m) at both sides of Klaipėda Port jetties in 1835–2017.

Year		Nearshore slope (tgα)					
The distance from jetty, m		1835	1910	1955	2000	2017	1835–2017
Northern jetty	**1250**	–	–	–	0.1000	0.0109	–
	1000	–	–	0.0086	0.0094	0.0102	–
	750	0.0054	0.0087	0.0089	0.0088	0.0097	0.0043
	500	0.0049	0.0087	0.0076	0.0081	0.0094	0.0045
	250	0.0054	0.0076	0.007	0.0086	0.0121	0.0067
	50	0.0057	0.008	0.0072	0.0104	0.0163	0.0106
Southern jetty	**50**	0.0029	0.0065	0.0066	0.0082	0.0082	0.0053
	250	0.0038	0.006	0.0061	0.0074	0.0075	0.0037
	500	0.004	0.0059	0.0062	0.0074	0.0075	0.0035
	750	0.0046	0.0057	0.0061	0.0071	0.0074	0.0028
	1000	0.0047	0.0063	0.0062	0.0072	0.0073	0.0026

3000 m^3 of sand was poured onto the beach along a 150 m sector. Presumably, the shoreline's advance is a temporary phenomenon related to the above-mentioned circumstances. The 2018–2020 data show the shoreline retreating in the sector under consideration.

On generalizing the above investigation results, it can be stated that between 1834 and 1902, and between 2000 and 2017, morphological changes to the coastal zone were caused by the construction and reconstruction of the port jetties. Between 1902 and 2000, when the spatial positions of the jetties remained stable, there was a significant impact on the morphological changes in the port environment from deepening, widening and cleaning the entrance channel.

4. Discussion

The intensive expansion of ports on open littoral drift seashores that started in the 19th century is considered one of the most dramatic human interventions in coastal processes (Port Engineering II., 1990). It was determined that port jetties and breakwaters had a profound effect on the natural equilibrium of shore zones. An area of accretion forms on the updrift side of port jetties and an area of erosion on their downdrift side (Bakker, 1968; Bruun, 1995; Johnson, 1957; Komar, 1976; Kudale, 2010; Mohanty et al., 2012). These processes also are characteristic of south-eastern Baltic ports: Władysławowo in Poland (Szmytkiewicz et al., 2000), Baltijsk in Russia's Kaliningrad Region (Babakov and Chuburenko, 2019), and Liepaja and Ventspils in Latvia (Eberhards and Lapinskis, 2008).

Alongshore sediment transport from south to north dominates the Lithuanian shore (Knaps, 1965; Krek et al., 2016; Ostrowski et al., 2014; Pupienis et al., 2017; Žilinskas et al., 2018). This has been proven by investigations into the impact of the hydrotechnical constructions to the north of the Port of Klaipėda (there are no dredging works in their environment). Intensive accretion has taken place on the updrift (southern) side and erosion on the downdrift (northern) side of Palanga pier, which is located 22 km north of the Port of Klaipėda (built in 1878) (Žilinskas et al., 2010) and the unfinished Port of Šventoji (construction started in 1924) (Kriaučiūnienė et al., 2013), which is located 34 km from the Port of Klaipėda.

Shore zone erosion had already set in by the end of the 19th century to the north of the finished northern jetty in the Port of Klaipėda (Figures 3–4, Table 1). The changes in the coastal zone fully match the classic model of coastal zone development when alongshore sediment transport is disturbed by jetties (Bruun, 1995; Johnson, 1957; Komar, 1976; Kudale, 2010). In the case of the Port of Klaipėda, the course and development of the processes taking place on the northern side of the jetties caused a bay to be formed. Its development was evaluated by applying a mathematical function, namely a parabolic bay equation (Pupienis et al., 2013). On the other hand, discriminating between the effects of dredging and downdrift on the downdrift side of the port is quite a complicated task.

Meanwhile, on the updrift side of the jetties, where accretion was expected to take place, sediment barely accumulated on the nearshore after finishing the southern jetty. Moreover, in the nearest shore sector the shoreline did not migrate out to sea and even retreated inland (Figures 3–4, Table 1). Based on the investigation results (section 3), we can assume that these changes were predetermined by intensive cleaning of the entrance channel in the 20th century.

In contrast to the downdrift side of the jetties, erosion on their updrift side did not set in immediately after the end of the southern jetty's construction (Table 1). During the first half of the 20th century, when the amount of sediment dredged from the entrance channel was 100 thousand m^3 yr, some of the lost sediment was compensated for by alongshore sediment transport. During the second half of the 20th century, when the amount of dredged sediment reached 330 thousand m^3 yr, the alongshore sediment transport was unable to compensate for these losses.

This time lag is natural: at first, while the entrance channel was being deepened and widened, the sediment was replenished from the adjacent nearshore zone; therefore, the changes to the nearshore were not immediate. These processes are reflected by the slope angle dynamics across (Table 2) and along the nearshore (Figure 9).

Investigations into different underwater quarries on the northern nearshore of the Black Sea have also shown that

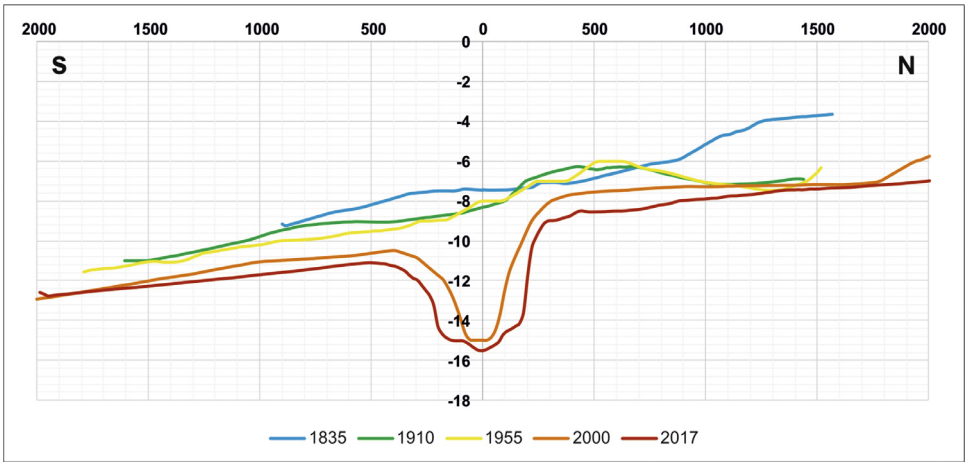

Figure 9 Nearshore depth dynamics at a distance of 400 m from the port gates in 1835–2017. Abscissa "0" on the fairway axis of entrance channel in 2001 (Figure 3).

the impact of dredging pits on the shore becomes evident only 3–4 years after the beginning of dredging works. In some cases, the impact on the shore only becomes apparent after 8 years such as, for example, in the Saxon Spit (the western part of the Crimean Peninsula) or 10 years as in Yalta Bay (the southern part of the Crimean Peninsula) (Šuiskyj et al., 1987). Presumably for this reason, M. R. Philips (2008), who investigated the nearshore in South Wales (Port Eynon and Horton Beach for 6 years and Port Penarth for 5 years), failed to establish any causality between seabed dredging and beach erosion.

Dredging the entrance channel causes changes in the wave field. Due to the wave divergence in the entrance channel, the wave height there decreases (Environmental Impact..., 2019). However, outside the entrance channel the wave refraction pattern changes along with the decrease in depth. The refraction tends to turn the waves away from the pit (Demir et al., 2004, Treloar, 1986). In the nearshore adjacent to the channel, due to the waves' convergence, the wave height increases. Bottom sediments driven by the waves settle to the bottom of the channel under the influence of gravity (Žilinskas, 1998). The bottom erosion of the nearshore adjacent to the entrance channel is also affected by the longshore sediment transport. The velocity of the longshore current is significantly reduced due to the greater depth of the entrance channel (Environmental Impact..., 2019). Therefore, sediments being transported along the shore settle in the channel. The sediment deficit increases in the coastal zone near the port, as the sediments dredged from the entrance channel are dumped in the Baltic Sea's deep water zone (Pupienis and Žilinskas, 2005).

During storms, the wave field at greater nearshore depths is subject to weaker transformations in the surf zone. Therefore, waves that are less reduced in height and that have more energy reach the shore (Brampton and Evans, 1998; Maa et al., 2001; Work, 2004). The wave set-up and the width of washed out beaches during storms are in direct dependence on the wave height (Žilinskas, 1994–1995). Therefore, the deepening of the nearshore causes the shore to erode. Investigations into the Port of Klaipėda environment have shown that intensive deepening of the entrance channel caused nearshore and shore erosion on the updrift side of the jetty, even when a sufficient sediment load was being transported by the alongshore drift.

A reconstruction of the Port of Klaipėda' entrance channel and jetties is planned to take place in 2020; therefore, negative changes to the coastal zone are expected in the future, including a more rapid retreat of the shoreline (Environmental Impact..., 2019). Based on the results of wave height modelling for westerly winds of different speeds (Environmental Impact ..., 2019; Jakimavičius et al., 2018), it is estimated that in the case of winds with a speed of 15 m/s coming from a SW and W direction, there would be significant increases in the wave height at the port gate of 0.03 and 0.66 m, respectively. For winds coming from a NW direction, the wave height would decrease by 0.51 m. For winds with a speed of 20 m/s coming from a SW and W direction, the wave height would be expected to increase by 0.80 m and 1.67 m, respectively. For winds coming from a NW direction, the wave height would decrease by 0.97 m. These estimated increases in wave height for SW and W winds would lead to significant changes to the shoreline that would be not be compensated for, even by the lower wave heights for the NW winds. According to the results of the wave height modelling (Environmental Impact..., 2019), the recurrence of winds with speeds over 10 m/s coming from a SW and W direction could reach 23.6% and 23.2%, respectively, i.e., they would be more frequent than winds coming from a NW direction (11.2%). Based on the shoreline modelling (Environmental Impact..., 2019), after the reconstruction of the Port of Klaipėda's jetties and entrance channel, the shoreline could retreat along a 50 m section on both sides of the jetties by 0.8 m/yr to the south and 1.3 m/yr to the north, respectively. A comparison of the modelled 2007–2013 shoreline dynamics with those of 1910–1990 showed the shoreline's average rate of retreat would increase to 0.11 m/yr to the south and 0.92 m/yr to the north. The modelling results confirmed the hypothesis that the erosion of the coastal zone near the Port of Klaipėda is related to the dredging of the entrance channel.

One way of mitigating the coastal zone erosion on the updrift side of the jetty would be nearshore and beach

nourishment using sand dredged from the entrance channel (Žilinskas, 1998). The previous nourishment of the nearshore at Giruliai (Karaliūnas et al., 2020; Žilinskas et al., 2003) and of the beach at Palanga (Pupienis et al., 2014; Žilinskas et al., 2008) proved and ensured the stability of the coastal sections. Also, sand dredged from the entrance channel could be used to form a sandbar along the shore (Žilinskas et al., 2010). However, as noted by Staniszewska et al. (2016), to ensure coastal zone protection from erosion, the amount of sediment used for coastal nourishment should be significantly increased.

5. Conclusion

Due to dredging works in coastal zones, lithodynamic systems lose some sediment, thus causing sediment deficiencies on the nearshore. Meanwhile, the energy potential of waves remains the same or even increases due to weaker wave transformation in surf zones. Coastal erosion intensifies. In other words, natural systems attempt to compensate for sediment loss in their coastal zones and to restore a state of equilibrium. Investigations into the Port of Klaipėda environment have shown that intensive deepening and cleaning of the entrance channel caused nearshore and shore erosion on the updrift side of the port jetty, even when the sediment load transported by the alongshore sediment drift is sufficient.

Acknowledgments

This research did not receive any specific grant from funding agencies in the public, commercial, or not-for-profit sectors. We are grateful to both reviewers for the helpful comments on an earlier version of this manuscript.

References

Babakov, A.N., Chuburenko, B.V., 2019. The Structure of the Net Alongshore Sediment Transport in the Eastern Gulf of Gdańsk. Water Res. 46 (4), 515—529, https:/doi.org/10.1134/S0097807819040031.

Bakker, W.T., 1968. The Dynamics of Coast with a Groin System. Proc. 11th Conf. Coast. Eng. 492—517.

Blackman, B., 1951. Dredging at Inlets on Sandy Coasts. Proc. 1st Conf. Coast. Eng., 169—174.

Brampton, A.H., Evans, C.D.R., 1998. Regional seabed sediment studies and assessment of marine aggregate dredging. CIRIA Rep. C505, London, 28—32.

Bruun, P., 1995. The Development of Downdrift Erosion. J. Coast. Res. 11 (4), 1242—1257, http://www.jstor.org/stable/4298427.

Demir, H., Otay, E.N., Work, P.A., Börekçi, O.S., 2004. Impacts of Dredging on Shoreline Change. J. Waterway, Port, Coast., Ocean Eng. 130 (4), 170—178, https://doi.org/10.1061/(ASCE)0733-950X(2004)130:4(170).

Eberhards, G., Lapinskis, J., 2008. Processes on the Latvian Coast of the Baltic Sea. Atlas. Riga, 64 pp.

Environmental Impact Assessment of Klaipeda State Seaport External and Internal Entrance Chanal Improvement (Dredging and Distribution), Southern and Northern Breakwater Reconstruction (Construction) and Part of the Curonian Spit Slope Reinforcement and Southern Port Gate Construction Environmental Impact Assessment., 2019. Sweco Lietuva, Vilnius, 905 pp., https://www.sweco.lt/contentassets/b18af075b8484f838a58090c1df73b55/2019-02-26-pav-ataskaita_sweco-www.pdf.

Gulbinskas, S., 1999. Anthropogenic impact and geological processes in the Baltic Sea. In: Lietuvos mokslas, Vilnius, 338—355.

Hagen, L.H., 1885. Die Seehafen in der Provinzen Preussen. II. Der Hafen zu Memel, Berlin, 133 pp.

Healy, T., Stephensa, S., Blacka, K., Gormanb, R., Cole, R., Beamsley, B., 2002. Port redesign and planned beach renourishment in a high wave energy sandy-muddy coastal environment, Port Gisborne, New Zealand. Geomorphology 48, 163—177, https://doi.org/10.1016/S0169-555X(02)00180-0.

HELCOM, 2015. Guidelines for Management of Dredged Material at Sea. HELCOM, Helsinki, 39 pp.

Jakimavičius, D., Kriaučiūnienė, J., Šarauskienė, D., 2018. Assessment of wave climate and energy resources in the Baltic Sea nearshore (Lithuanian territorial water). Oceanologia 60 (2), 207—218, https://doi.org/10.1016/j.oceano.2017.10.004.

Jarmalavičius, D., Pupienis, D., Žilinskas, G., Janušaitė, R., Karaliūnas, V., 2020. Beach-Foredune Sediment Budget Response to Sea Level Fluctuation. Curonian Spit, Lithuania. Water 12 (2), 583, 1—12, https://doi.org/10.3390/w12020583.

Jarmalavičius, D., Pupienis, D., Žilinskas, G., Karaliūnas, V., Jukna, L., 2019. The development and stability of beach-dune system on the wave-dominated coast: A case study of the Curonian Spit, Lithuania. Aeolian Res. 41, 100542. 1—7, https://doi.org/10.1016/j.aeolia.2019.100542.

Jarmalavičius, D., Satkūnas, J., Žilinskas, G., Pupienis, D., 2012. Dynamics of beaches of Lithuanian coast (the Baltic Sea) for the period 1993-2008 based on morfometric indicators. Env. Earth Sci. 65 (6), 1727—1736, https://doi.org/10.1007/s12665-011-1152-3.

Jarmalavičius, D., Žilinskas, G., Pupienis, D., Kriaučiūnienė, J., 2017. Subaerial beach volume change on a decadal time scale: the Lithuanian Baltic Sea coast. Zeitschrifft fur Geomorph 61 (2), 149—158, https://doi.org/10.1127/zfg/2017/0441.

Johnson, J.W., 1957. Littoral Drift Problem at Shoreline harbors. J. Waterways and Harbors Division, ASCE 83 (WW1) 1211-1—1211-37.

Karaliūnas, V., Jarmalavičius, D., Pupienis, D., Janušaitė, R., Žilinskas, G., Karlonienė, D.Malvárez, G., Navas, F. (Eds.), 2020. Shore nourishment impact on coastal landscape transformation: An example of the Lithuanian Baltic Sea coast. Global Coastal Issues of 2020. J. Coas. Res. 95 (SI), 840—844, https://doi.org/10.2112/SI95-163.1.

Knaps, R.B., 1965. Sediment transport along the southeastern Baltic Sea coast. Tech. Rep. 104, Latgipprom, Riga, 16 pp.

Kojima, H., Ijima, T., Nakamuta, T., 1986. Impact of offshore dredging on beaches along the Genkai Sea, Japan. In: Proc. 20th Int. Conf. on Coast. Eng. ASCE, New York, 1281—1295.

Komar, P.D., 1976. Beach Processes and Sedimentation. Prentice-Hall Inc, New Jersey, 429 pp.

Krek, A., Stont, Z., Ulyanova, M., 2016. Alongshore bedload transport in the south eastern part of the Baltic Sea under changing hydrometeorological conditions. Reg. Stud. Mar. Sci. 7, 81—87, https://doi.org/10.1016/j.rsma.2016.05.011.

Kriaučiūnienė, J., Gailiušis, B., Kovalenkovienė, M., 2006. Peculiarities of sea wave propagation in the Klaipėda Strait. Lithuanica. Baltica 19 (1), 20—29.

Kriaučiūnienė, J., Žilinskas, G., Pupienis, D., Jarmalavičius, D., Gailiušis, B., 2013. Impact of Šventoji port jetties on coastal dynamics of the Baltic Sea. J. Env. Eng. Land. Manag. 21 (2), 114—122, https://doi.org/10.3846/16486897.2012.695736.

Kudale, M.D., 2010. Impact of port development on the coastline and the need for protection. Ind. J. Geo-Mar. Sci. 39 (4), 597—604, http://nopr.niscair.res.in/handle/123456789/10808.

Maa, J.P.-Y., Hobbs III, C.H., Hardaway Jr, C.S., 2001. A Criterion for

Determining the Impact on Shorelines Caused by Altering Wave Transformation. J. Coast. Res. 17 (1), 107—113.

Marine Habitat Committee, 2000. Report of the working group on the effects of extraction of marine sediments on the marine ecosystem. Rep. No. ICES CM 2000/E:07, Gdańsk, Poland, 49 pp.

McLoughlin, L.C., 2000. Shaping Sydney Harbour: Sedimentation, dredging and reclamation 1788—1990s. Aust. Geogr. 31 (2), 183—208, https://doi.org/10.1080/713612246.

Mėžinė, J., Ferrarin, C., Vaičiūtė, D., Idzelytė, R., Zemlys, P., Umgiesser, G., 2019. Sediment Transport Mechanisms in a Lagoon with High River Discharge and Sediment Loading. Water 11 (10), 1970, 1—24, https://doi.org/10.3390/w11101970.

Mohanty, P.K., Patra, S.K., Bramha, S., Seth, B., Pradhan, U., Behera, B., Mishra, P., Panda, U.S., 2012. Impact of groins on beaches morphology: a case study near Gopalpur port, east coast of India. J. Coast. Res. 28 (1), 132—142, https://doi.org/10.2112/JCOASTRES-D-10-00045.1.

Müsset, M., 1916. Untersuchungen über die Erfolge der Dunenarbeiten auf der Kurischen Nehrung, Memel, 32 pp.

Ostrowski, R., Pruszak, Z., Babakov, A., 2014. Condition of southeastern Baltic Sea shores and methods of protecting them. Archives of Hydro-Engineering and Environmental Mechanics 61 (1—2), 17—37, https://doi.org/10.1515/heem-2015-0002.

Phillips, M.R., 2008. Beach erosion and marine aggregate dredging: a question of evidence? Geograph. J. 174 (4), 332—343, https://www.jstor.org/stable/40205253.

Pupienis, D., Žilinskas, G., 2005. Specific features of morphodynamic processes in the dumps of the Lithuanian offshore. Baltica 18 (1), 29—37.

Pupienis, D., Buynevich, I., Ryabchuk, D., Jarmalavičius, D., Žilinskas, G., Fedorovič, J., Kovaleva, O., Sergeev, A., Cichoń-Pupienis, A., 2017. Spatial patterns in heavy-mineral concentrations along the Curonian Spit coast, southeastern Baltic Sea. Estuar. Coast. Shelf Sci. 195, 41—50, https://doi.org/10.1016/j.ecss.2016.08.008.

Pupienis, D., Jarmalavičius, D., Žilinskas, G., Fedorovič, J., 2014. Beach nourishment experiment in Palanga, Lithuania. In: Green, A.N., Cooper, J.A.G. (Eds.), Proceedings 13th International Coastal Symposium (Durban, South Africa), J. Coas. Res., 70(SI), 490—495.

Pupienis, D., Jonuškaitė, S., Jarmalavičius, D., Žilinskas, G., 2013. Klaipėda port jetties impact on the Baltic Sea shoreline dynamics, Lithuania. J. Coast. Res. 65(SI), 2167—2172, https://doi.org/10.2112/SI65-366.1.

Remeikaitė-Nikienė, N., Garnaga-Budrė, G., Lujanienė, G., Jokšas, K., Stankevičius, A., Malejevas, V., Barisevičiūtė, R., 2018. Distribution of metals and extent of contamination in sediments from the south-eastern Baltic Sea (Lithuanian zone). Oceanologia 60 (2), 193—206, https://doi.org/10.1016/j.oceano.2017.11.001.

Shaw, J.R., 1978. Coastal response at Point Pelee, Lakie Erie. Rep. Symp. Tech. Environ. Spcioecon. And Regul. Aspects Coast. Zone Manag. San-Francisco 3, 1937—1953.

Simons, R., Hollingham, S., 2001. Marine aggregate dredging: A review of current procedures for assessing coastal processes and impact at the coastline. Tech. Rep. No HYD10401, Civil Environ. Eng. Dept., Univ. College London, London, 81 pp.

Šuiskyj, J.D., Vychovanec, G.B., Pedan, G.S., 1987. Results of investigations of the impact of underwater sand dredging on the dynamics of the shores of the Black Sea dynamics. In: Vasiutinskaja, L.G. (Ed.). In: Prierodnyje osnovy beregozaschity. Moskva, Nauka, 68—82.

Szmytkiewicz, M., Biegowski, J., Kaczmarek, L.M., Okroj, T., Ostrowski, R., Pruszak, Z., Rozynsky, G., Skaja, M., 2000. Coastline changes nearby harbour structures: comparative analysis of one-line models versus field data. Coast. Eng. 40, 119—139.

Staniszewska, M., Boniecka, H., Cylkowska, H., 2016. Dredging works in the Polish open sea ports as an anthropogenic factor of development of sea coastal zones. Bulletin of the Maritime Institute in Gdańsk 31 (1), 173—180, https://doi.org/10.5604/12307424.1223959.

Treloar, P.D., 1986. Spectral wave refraction under the influence of depth and current. Coast. Eng. 9, 439—452, https://doi.org/10.1016/0378-3839(86)90007-4.

Tsinker, G.P., 2004. Port Engineering. John Wiley and Sons Inc, USA, 882 pp.

Veit, H.K., 1821. Beschreibung des Memelschen Hafens und der daselbst angelegten Werke, nebst einem Situations Plane. In: Beiträge zur Kunde Preussens, 4. Königsberg, 458—516.

Work, P.A., Fehrenbacher, F., Voulgaris, G., 2004. Nearshore Impacts of Dredging for Beach Nourishment. J. Waterway, Port, Coast., Ocean Eng. 130, 303—311, https://doi.org/10.1061/(ASCE)0733-950X(2004)130:6(303).

Žaromskis, R., 2008. Baltic Sea Ports. Vilnius University, Vilnius, 432 pp.

Žaromskis, R., Gulbinskas, S., 2016. Changes of Baltic Sea nearshore bottom relief in the viciniytyi of Klaipėda harbour during the 20th century. Geologija. Geografija 2 (3), 135—150.

Žilinskas, G., 1998. The peculiarities of shoreline dynamics in the impact zone of Klaipėda port. Geografijos metraštis 31, 99—109.

Žilinskas, G., 1994. Set-up in the surf zone. Geografijos metraštis 28, 235—255.

Žilinskas, G., Jarmalavičius, D., Minkevičius, V., 2001. Eolian processes on the marine coast. GI, Vilnius, 284 pp.

Žilinskas, G., Jarmalavičius, D., Pupienis, D., 2003. The influence of nourishment of nearshore sediment supplies on the coast. Geografijos metraštis 36 (1), 89—100.

Žilinskas, G., Jarmalavičius, D., Pupienis, D., 2018. The influence of natural and anthropogenic factors on grain size distribution along the southeaster Baltic spits. Geol. Q. 62 (2), 375—384, http://dx.doi.org/10.7306/gq.1413.

Žilinskas, G., Pupienis, D., Jarmalavičius, D., 2010. Possibilities of regeneration of Palanga coastal zone. J. Env. Land. Manag. 18 (2), 95—10, http://doi:10.3846/jeelm.2010.11.

Oceanologia (2020) 62, 501—510

Available online at www.sciencedirect.com

ScienceDirect

journal homepage: www.journals.elsevier.com/oceanologia

ORIGINAL RESEARCH ARTICLE

Increases in the temperature and salinity of deep and intermediate waters in the West Spitsbergen Current region in 1997—2016

Małgorzata Merchel*, Waldemar Walczowski

Institute of Oceanology, Polish Academy of Sciences, Sopot, Poland

Received 20 February 2020; accepted 3 August 2020
Available online 13 August 2020

KEYWORDS
Climate change;
Ocean warming;
Heat content;
Deep water;
Intermediate water;
Nordic Seas

Summary This study investigated the temporal variability in the basic physical properties of deep and intermediate waters in the West Spitsbergen Current region at 76°30'N latitude from 1997 to 2016. Emphasis was placed on quantifying the changes in temperature and salinity and determining the potential drivers of these changes. Hydrographic data were obtained during annual summer cruises aboard the r/v *Oceania* in the Nordic Seas. The increase in the water temperature, which was especially strong in the western part of the investigated section, was associated with considerable changes in the water layers salinity. The temperature and salinity of the intermediate water increased much faster (0.021°C yr^{-1} and 0.0022 yr^{-1}, respectively) than those of the deep water (0.009°C yr^{-1} and 0.0004 yr^{-1}, respectively). The warming rate in the upper 2000 m was also higher than the mean warming rate of the global ocean. The source of the deep water temperature and salinity increases was the deep water inflow from the Arctic Ocean into the Greenland Sea. In contrast, the increase in these properties in the intermediate water was associated with the advection of warmer and more saline Atlantic Water from the North Atlantic to the Nordic Seas.

1. Introduction

In recent years, oceanographers and climatologists have been increasingly focused on ocean warming and the ocean's importance as a buffer that stores excess energy trapped on the Earth via the greenhouse effect. The global ocean has absorbed 93% of this additional heat since 1970 (Rhein et al., 2013), and the rate of change in the ocean heat content (OHC) is a good indicator of radiation imbalances at the top of the atmosphere (Church et al., 2013). Due to its enormous heat capacity, the global ocean is the

* Corresponding author at: Physical Oceanography Department, Institute of Oceanology Polish Academy of Sciences, Powstańców Warszawy 55, 81—712 Sopot, Poland.
E-mail address: merchel@iopan.gda.pl (M. Merchel).
Peer review under the responsibility of the Institute of Oceanology of the Polish Academy of Sciences.

Production and hosting by Elsevier

https://doi.org/10.1016/j.oceano.2020.08.001

flywheel of the climate system, absorbing, storing and redistributing heat over long time scales and large spatial scales. The average global ocean temperatures are less variable than land temperatures, which can change rapidly from year to year (Wijffels et al., 2016).

Solar radiation is absorbed in the euphotic zone of the ocean, and the absorbed heat is distributed over the mixed layer depth (MLD). In most of the ocean, the MLD does not exceed 100 m; in only the subpolar and polar zones in winter does the MLD exceed 200 m. However, recent studies have shown that heat accumulates not only in the ocean surface layer but also in intermediate and deep waters (e.g., Desbruyères et al., 2016, 2017; Levitus et al., 2012; Purkey and Johnson, 2010; Roemmich et al., 2015). According to Levitus et al. (2012), from 2003 to 2010, the heat content in the upper 700 m increased more slowly than it did in the previous decade, while the absorption of heat at depths between 700 and 2000 m did not weaken during this period. The 700–2000 m ocean layer absorbed approximately one-third of the heat absorbed by the upper 2000 m of the global ocean. This suggests that the ocean's deeper layers reduce the surface layer warming by absorbing the excess heat accumulated in the surface layer. The warming of the ocean between 700 and 2000 m depth from 2006 to 2015 accounted for 50% of the total increase in the ocean's heat content (from 0 to 2000 m) (Desbruyères et al., 2016), which is more than 20 percentage points higher than the long-term estimate (1955–2010) made by Levitus et al. (2012).

A better understanding of the temporal changes occurring in intermediate and deep waters is critical due to the important role that these layers play in the global climate system. Deep water formation processes are very important for global thermohaline circulation forcing, and these processes occur mainly at high latitudes. The Arctic Ocean and the Nordic Seas compose one of the most important regions for deep water formation in the world ocean. Thermohaline circulation plays two very important roles: it regulates climate by distributing heat globally and it supports marine life by providing well-oxygenated and nutrient-rich water (Rahmstorf, 2002).

Increases in the temperature and salinity of the intermediate and deep waters in the Nordic Seas have been observed and analyzed by, for example, Holliday et al. (2008), Latarius and Quadfasel (2010, 2016), Langehaug and Falck (2012), Rudels et al. (2012), Somavilla et al. (2013), von Appen et al. (2015), Wang et al. (2015), Walczowski et al. (2017), Jeansson et al. (2017), Lauvset et al. (2018) and Brakstad et al. (2019).

This study aims to analyze increases in temperature and salinity observed in intermediate and deep waters in the West Spitsbergen Current (WSC) region. The heat stored in this area and transported by the WSC to the Arctic Ocean may have a high influence on Arctic sea ice melting and climate change. We believe that the results described in this work complement the current understanding of the intermediate and deep water properties in this area.

2. Study area

The Nordic Seas, located north of the Greenland-Scotland Ridge and south of the Fram Strait, include the Greenland, Norwegian, and Iceland Seas (Fig. 1). The Greenland-Scotland Ridge separates the Nordic Seas from the North Atlantic, and the Fram Strait, situated between Greenland and Svalbard, is the only deep connection ($\sim$ 2600 m) between the Nordic Seas and the Arctic Ocean. The Nordic Seas are a primary region for high-latitude water mass transformation, where strong vertical mixing induced by heat loss to the atmosphere converts most of the incoming subtropical warm and saline Atlantic Water (AW) into dense overflow water (e.g., Latarius and Quadfasel, 2016). Atlantic Water inflows to the Nordic Seas with the North Atlantic Current (NAC) through the Greenland-Scotland Ridge; then, it continues as the Norwegian Atlantic Current (NwAC) (Hansen and Østerhus, 2000; Orvik and Niiler, 2002) and as two branches of the West Spitsbergen Current (WSC) (Piechura and Walczowski, 1995). The eastern WSC branch transports AW along the Barents Sea/Svalbard Shelf break into the Arctic Ocean, while the western WSC branch transports AW over the Mohn and Knipovich ridges, where it recirculates westward and southward (Piechura, Walczowski 1995). Additionally, a significant portion of the AW that inflows into the Fram Strait recirculates to the south (Schauer et al., 2004). The flows of the western branch of the WSC create the border between the Arctic-origin water masses (Arctic domain) to the west and the Atlantic-origin water masses (Atlantic domain) to the east (Swift and Aagaard, 1981; Walczowski, 2013). The border between the Atlantic domain and the Arctic domain is the Arctic front, whose location is closely related to the bottom topography. The midocean ridge system of the Mohn and Knipovich ridges creates a natural barrier separating the waters of Atlantic and Arctic origin. Located at latitudes of 70–73°N, the Mohn Ridge stretches towards the northeast. The northern extension of the Mohn Ridge – the Knipovich Ridge – stretches north towards the Fram Strait (Raj et al., 2019).

There are various definitions of Atlantic Water. In this region, it is often defined as water warmer than 0°C and more saline than 34.92 (Walczowski, 2014). The maximal thickness of the defined AW layer does not exceed 700 m in the Atlantic domain and 500 m in the Arctic domain. The Arctic Intermediate Water (AIW), located below the AW layer, is formed within the convective gyres in the Arctic domain of the Nordic Seas (Blindheim, 1990; Jeansson et al., 2017; Swift and Aagaard, 1981) as a result of the cooling of the warm, saline AW and subsequent mixing with the colder, fresher Polar Water found to the west of the Greenland Sea Gyre (Lauvset et al., 2018). Beneath the intermediate layer, Norwegian Sea Deep Water (NSDW) occurs. NSDW is formed by the mixing of Greenland Sea Deep Water (GSDW) and deep water from the Arctic Ocean. NSDW is the densest water mass in the Norwegian and Iceland seas but is also found in the northern and eastern parts of the Greenland Sea. Part of the AIW and NSDW advects from the Greenland Sea northward to the West Spitsbergen Current region, gradually changing its properties as a result of interactions with other water masses (Swift and Koltermann, 1988).

Since the 1980s, the renewal of deep water in the Greenland Sea has decreased considerably (Schlosser et al., 1991). Only the intermediate layer has been ventilated, contributing to the lower limb of the Atlantic meridional overturning circulation (Eldevik et al., 2009; Karstensen et al., 2005). The relatively cold and fresh deep

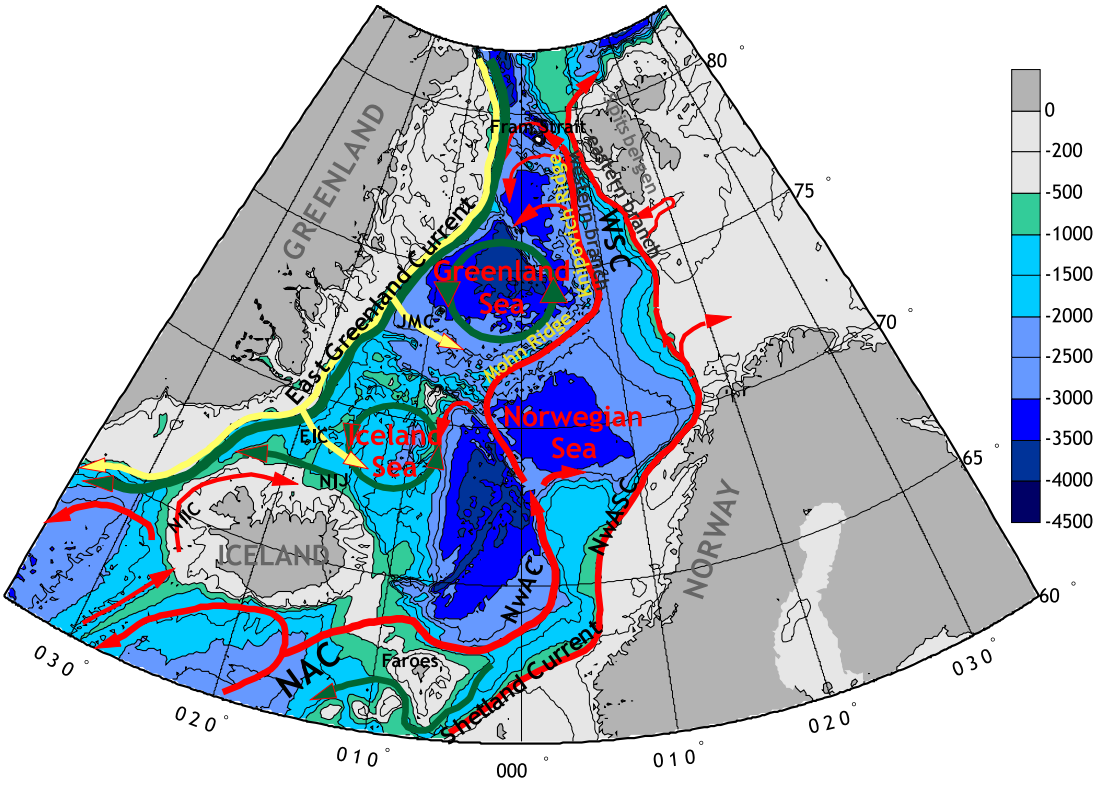

Figure 1 Map of the Nordic Seas with bathymetry and circulation patterns. Red and yellow arrows indicate warm Atlantic Water inflow and cold and fresher outflow, respectively. Green arrows indicate cold, dense water circulation. The acronyms are the East Icelandic Current (EIC), the Jan Mayen Current (JMC), the North Atlantic Current (NAC), the North Icelandic Irminger Current (NIIC), the North Icelandic Jet (NIJ), the Norwegian Atlantic Current (NwAC), the Norwegian-Atlantic Slope Current (NwASC), and the West Spitsbergen Current (WSC).

water in the Greenland Sea (GSDW) is modified by the advection of warmer and more saline deep water from the Arctic Ocean. Eurasian Basin Deep Water (EBDW) is Arctic Ocean deep water that is dense enough to mix with the deep water in the Greenland Sea and leaves the Arctic Ocean below 2000 m depth. Therefore, in the absence of deep convection providing fresher and colder waters below 2000 m, EBDW accumulates in the deep Greenland Sea, increasing the temperature and salinity (Somavilla et al. 2013).

3. Data and methods

In this work, we used data collected by the long-term AREX program. For the last 30 years, the Institute of Oceanology, Polish Academy of Sciences has performed annual cruises aboard the r/v *Oceania* to the Nordic Seas and Fram Strait (Walczowski et al., 2017). Since 2000, the data have been collected in the same array in the same season (June–July) and processed in the same way. The samples constituting the longest time series were collected from section N, situated along the 76°30'N parallel between 4°E and 14°E longitude (Fig. 2); therefore, this section was selected for further analysis.

Water masses are mainly defined based on temperature and salinity (or density) criteria, so the temporal variability in their properties strongly depends on the adopted parameterizations. Therefore, in this study, the mean temperature and salinity, as well as the heat content, were calculated for selected depth layers. Water between 0 and 500 m was defined as surface water, water between 500 and 1000 m was defined as intermediate water, and water below 1000 m was defined as deep water. The mean values of the water properties were calculated for the whole section as well for the Arctic Water and Atlantic Water domains, which are represented by stations N-8 (76°30'N, 6°E) and N-1 (76°30'N, 10°E), respectively.

The CTD measurements were performed using an SBE 911plus probe and covered the whole water column from the surface to the seafloor. The accuracy of the temperature, conductivity and pressure measurement was ± 0.001°C, ±0.0003 S/m and ±0.015% of full scale, respectively, sufficient for the analysis of the temperature and salinity changes in the intermediate and deep waters. Standard procedures provided by the manufacturer of the SeaBird system (software modules SeaSave and SBEDataProc) were used for collection, processing and quality control of the hydrographic data.

Interpolation, quantitative data analysis and statistical calculations were performed in MATLAB, while dedicated software (Ocean Data View (Schlitzer, 2015)) was used to visualize the processed data. The mean water properties

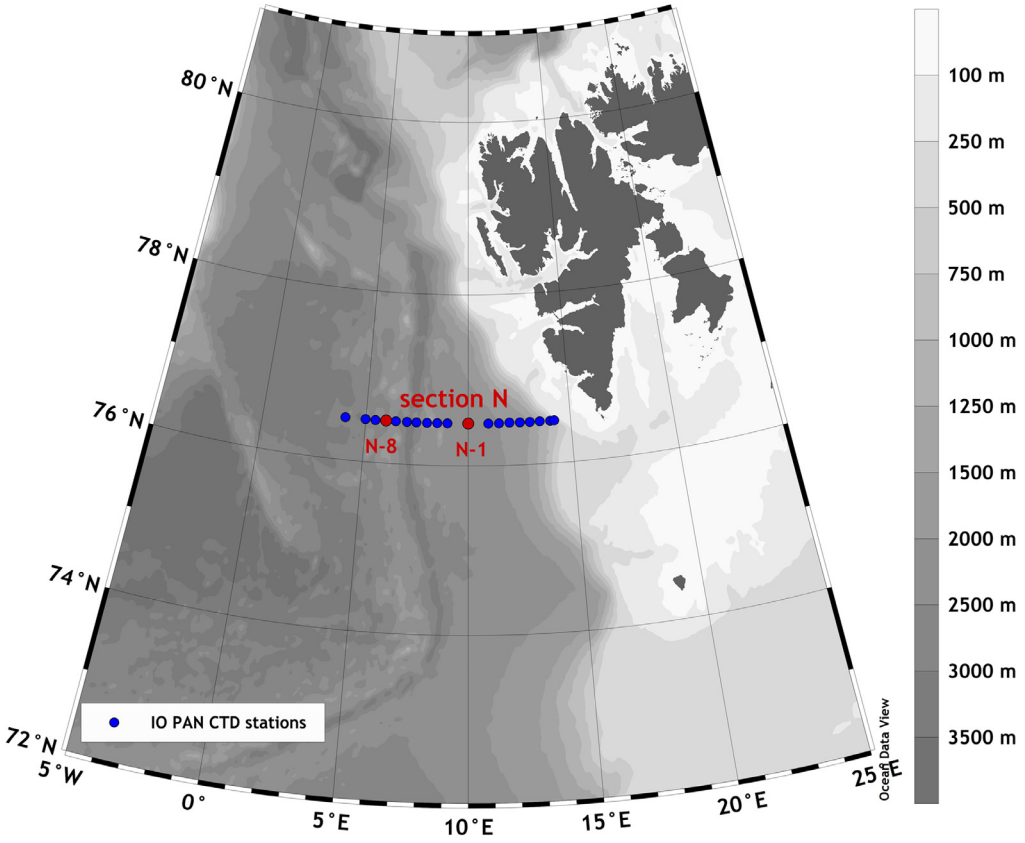

Figure 2 CTD stations along section N sampled every summer during the AREX observational program carried out by IO PAN in the period 1997–2016.

and heat content in each water layer were calculated from temperature and salinity fields interpolated onto a regular grid with the horizontal and vertical resolution of 0.1 degree and 1 m, respectively. The data were interpolated using the MATLAB griddata function, applying the linear interpolation method. All the analyzed trends presented below are statistically significant, with a p-value < 0.01.

The heat content (H) was calculated for the surface, intermediate and deep water layers, as well as the entire water column:

$$H = \int_{h2}^{h1} \rho C p \theta dz. \quad (1)$$

The average water density (ρ), heat capacity (Cp) and potential temperature (Θ) of each layer were used; $h1$ and $h2$ are the depth range over which the heat content was computed.

4. Results and discussion

The distributions of potential temperature and salinity along section N in the summer seasons of 1997 and 2016 are shown in Figure 3. The intermediate and deep waters were much warmer and more saline in 2016 than in 1997. The average −0.80°C isotherm depth was 1200 m in 1997 but 1700 m in 2016, a reduction of 500 m over 20 years. The greatest increases in potential temperature and salinity were observed in the western part of the section, in the Arctic domain.

The temporal changes in the water properties varied with depth. The potential temperature trend reached 0.045°C yr^{-1} in the surface layer (Tab. 1) (Fig. 4). The temporal variability in the surface water temperature was very high, with three pronounced maxima in 1999, 2006, and 2014. The salinity trend reached 0.0051 yr^{-1}, with clear maxima in 2006 and 2014 (Fig. 5). The potential temperature of the intermediate water increased more slowly (0.021°C yr^{-1}) than that of the surface layer, but the temporal variability was still evident. The slowest warming occurred in the deep water, with a stable linear increase of 0.009°C yr^{-1} without major interannual variations (Fig. 4). The same patterns were observed for the salinity of the intermediate water (0.0022 yr^{-1}) and deep water (0.0004 yr^{-1}) (Fig. 5). The observed trends along section N confirm the positive temperature and salinity trends observed in the eastern Nordic Seas (Larsen et al., 2016; Walczowski et al., 2017).

The changes in water properties were not uniform along the whole section. Hovmöller plots of potential temperature at stations N-8 (76°39'N, 6°E) and N-1 (76°30'N, 10°E) show differences between these two stations (Fig. 6). The changes in the intermediate and deep water temperatures in the Arctic domain occurred more quickly than those in the Atlantic domain. At the station in the Arctic domain (N-8), after 2009, the potential temperature of the deep and

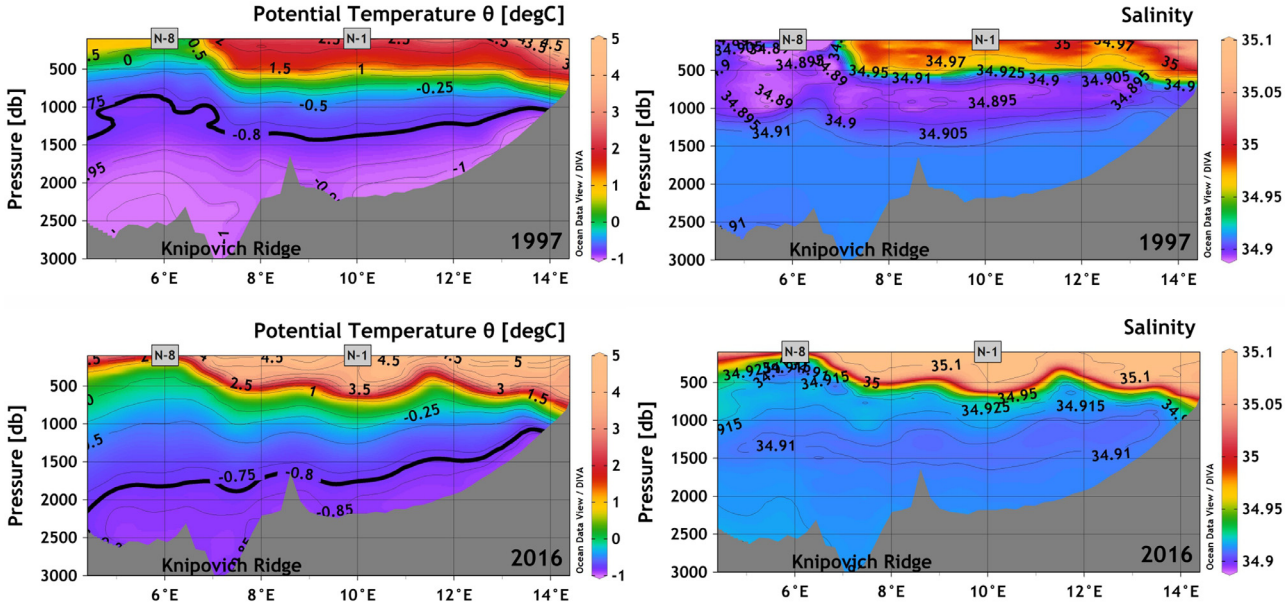

Figure 3 Distributions of potential temperature (left) and salinity (right) along section N in the summer seasons of 1997 (upper) and 2016 (lower). The bold line shows the −0.8°C isotherm.

Table 1 Trend analysis of temperature and salinity in the surface, intermediate and deep water layers from 1997 to 2016.

Pressure [db]	Temperature			Salinity		
	Slope	R^2	p-value	Slope	R^2	p-value
0–500	0.045	0.34	0.0075	0.0051	0.66	0
500–1000	0.021	0.37	0.0046	0.0022	0.73	0
1000–bottom	0.009	0.91	0	0.0040	0.44	0.0014

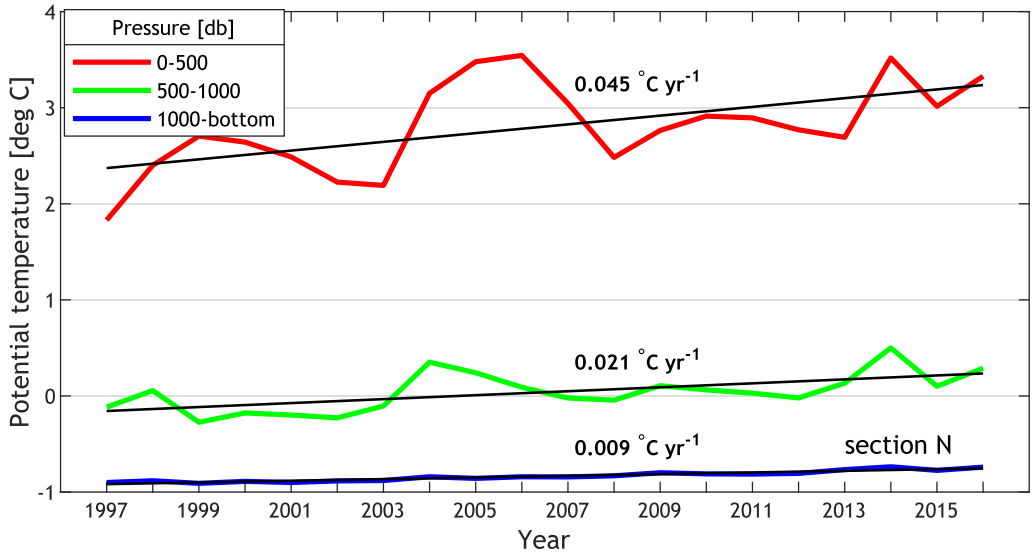

Figure 4 Mean potential temperature of the surface, intermediate and deep waters across section N from 1997 to 2016.

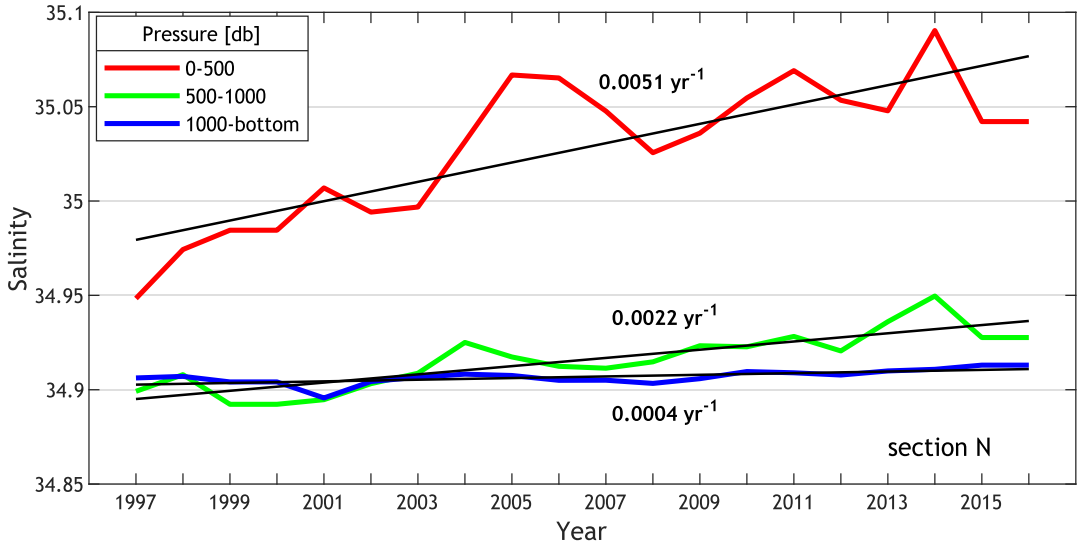

Figure 5 Mean salinity of the surface, intermediate and deep waters across section N from 1997 to 2016.

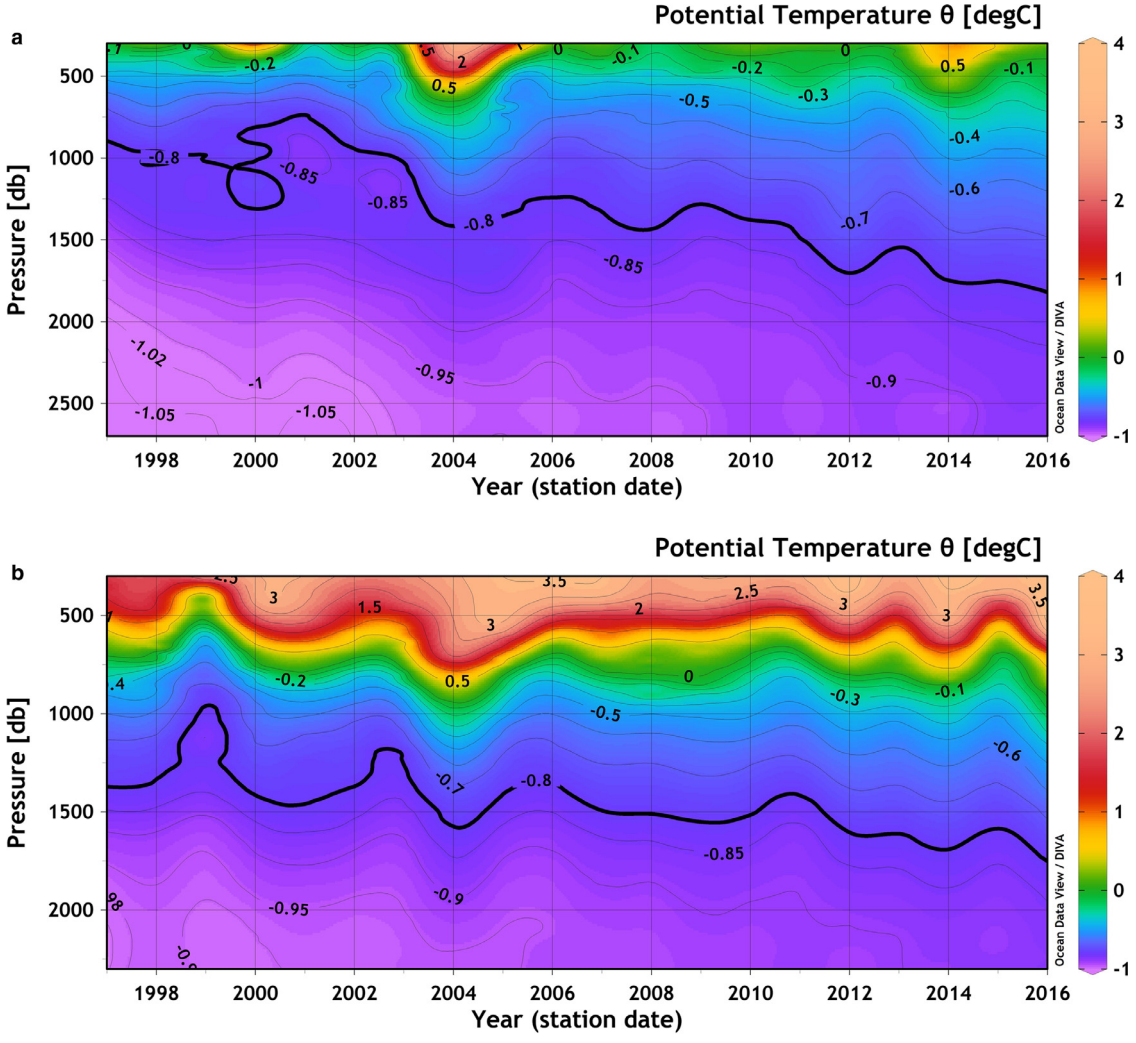

Figure 6 Hovmöller plot of potential temperature at stations N-8 (upper) and N-1 (lower) from 1997 to 2016. The bold line shows the −0.8°C isotherm.

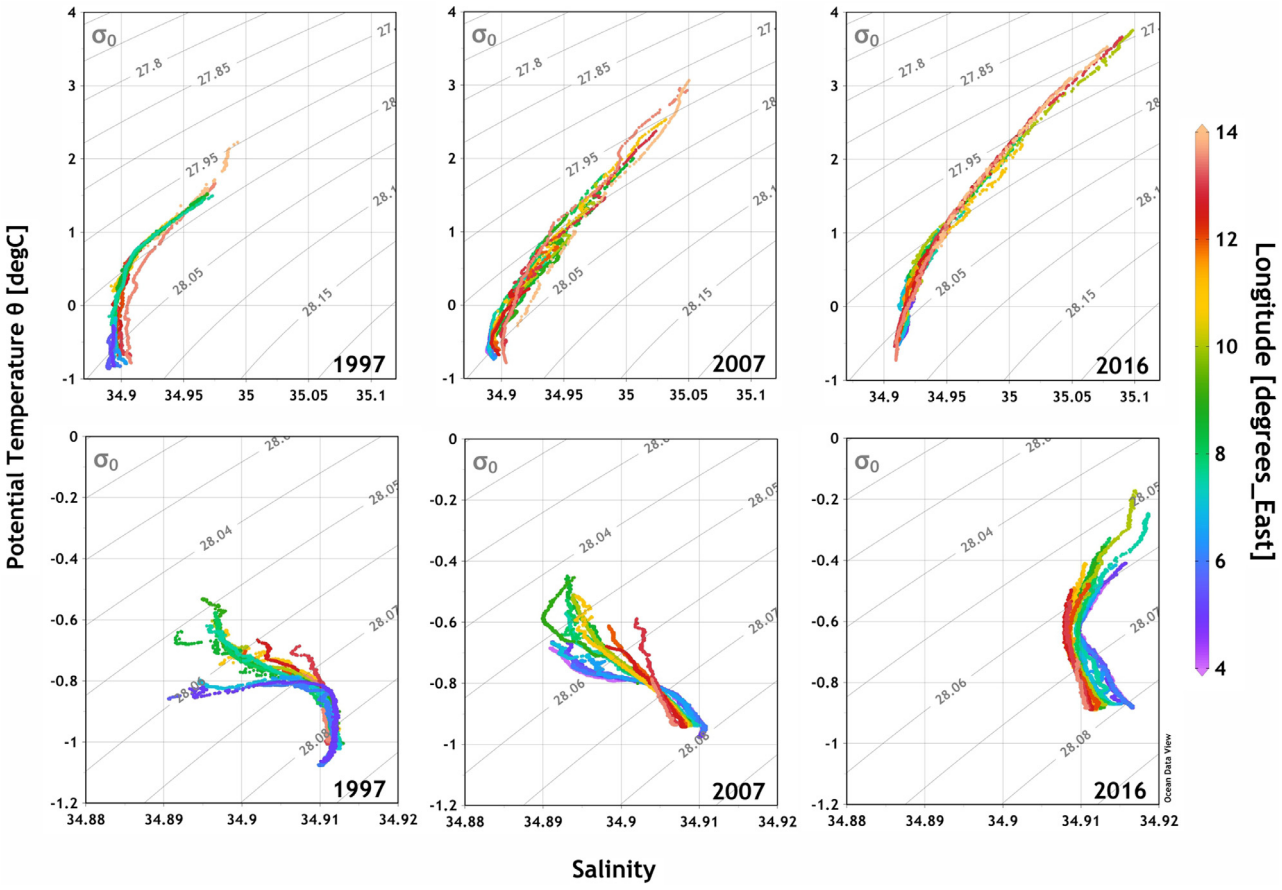

Figure 7 Θ-S diagrams of intermediate (upper panels) and deep (lower panels) water along section N in 1997, 2007 and 2016. Note the differing temperature and salinity scales between the two panels. The color scale indicates the eastern longitude.

intermediate waters did not exceed −0.95 and −0.8°C, respectively. The bottom water potential temperature was −1.08°C in 1997 and −0.87°C in 2016 (Fig. 6), reflecting an increase of 0.21°C in the last 20 years. In the Atlantic domain (N-1), the potential temperature of the deep water did not exceed −0.95°C after 2005, four years earlier than this temperature was observed in the Arctic domain (N-8), while the potential temperature of the intermediate water did not exceed −0.7°C. The lowest potential temperature of deep water was −1.01°C in 1997 and −0.87°C in 2016 (Fig. 6). This means that the lowest potential temperature at this station increased by 0.14°C in the last 20 years and was 0.07°C less than that in the Arctic domain (N-8).

The Θ-S diagrams presented in Figure 7 show the relationship between the potential temperature and salinity along section N in the intermediate (500–1000 m) and deep (> 1000 m) waters in 1997, 2007, and 2016. The upper Θ-S diagrams show the significant influence of sinking Atlantic Water on the intermediate water, especially in the eastern part of the section. In 1997, the intermediate water (500–1000 m) was characterized by salinity below 35 and potential temperatures below ~2°C. In 2007, the maximum salinity was 35.05, and the potential temperature reached 3°C, while in 2016, the maximum salinity was 35.1, and the potential temperature was almost 4°C. The lower Θ-S diagrams show that in 1997, the properties of the deep water varied among the western, central and eastern parts of section N. The western part (purple-blue dots) was the least saline and the coldest, the central part (green dots) was the warmest, and the eastern part (orange-red dots) was the most saline. In subsequent years, the deep water became more homogeneous as its potential temperature and salinity continuously increased.

This 20-year time series of continuous, consistent oceanographic data provides a valuable basis for analysis. It reveals significant summer-to-summer changes in the basic water properties in the West Spitsbergen Current region. The greatest variability occurred in the surface layer and decreased with depth. There were positive trends in both temperature and salinity in all layers. The rates of the annual salinity and temperature increases also decreased with depth. All these trends were statistically significant. However, this time series is still too short to determine the causes of these changes or to separate natural variability from that resulting from progressive climate change. The flow in the surface layer of the investigated region is dominated by the Atlantic meridional overturning circulation (AMOC), and the changes are mostly advective in nature.

The long-term changes in poleward oceanic fluxes are associated with the Atlantic multidecadal oscillation, which has a period of 60-80 years (Delworth and Mann, 2000).

The intermediate and deep waters of the studied region mostly inflow from the central part of the Greenland Sea (Swift and Koltermann, 1988). Therefore, the increases in temperature and salinity in the deep and intermediate waters along section N are closely related to the changes observed in the central part of the Greenland Sea (Brakstad et al., 2019; Latarius and Quadfasel, 2016; Lauvset et al., 2018). This is most clearly observed in the western part of the area (Arctic domain), which is located in the north-eastern part of the Greenland Sea. The water supply to this area from the west is unimpeded over the entire water column. The flow of water to the eastern part (Atlantic domain), which is located in the northern part of the Norwegian Sea, is to some extent blocked by the Knipovich Ridge. Therefore, mostly in this area, the pattern of changes in the 500–1000 m layer is similar to that in the surface layer. Nevertheless, connections with the inflow of AW to the Nordic Seas are also important for the intermediate and deep layers in the western part of the studied region. Holliday et al. (2008) found that the freshening trend in the upper ocean of the northeastern North Atlantic and Nordic Seas in the 1960s–1990s had reversed and that since that period, temperature and salinity have rapidly increased in the Atlantic Water inflow to the Nordic Seas. After 2000, stronger ventilation was observed in this area, which is associated with the advection of warmer and more saline surface water flowing from the North Atlantic (Lauvset et al., 2018). The advection of Atlantic origin water resulted in stronger ventilation in the Greenland Sea (Brakstad et al., 2019; Lauvset et al., 2018). However, convection still reached only intermediate depths, enabling ventilation and refreshing the water in the intermediate layer. This contributed to much greater increases in temperature and salinity in this layer than in the deep layer (Brakstad et al., 2019; Latarius and Quadfasel, 2016; Lauvset et al., 2018).

The source of warming in the deep Greenland Sea is the inflow of deep water from the Arctic Ocean. The relatively warm and salty Eurasian Basin Deep Water flows into the colder and less saline Greenland Sea Deep Water (Aagaard et al., 1985). This inflow is possible due to the cessation of deep convection in the central part of the Greenland Sea in the 1980s, which provided cold and deep saline water below 2000 m (Schlosser et al., 1991). The rate of deep water warming is not the same for the entire Nordic Seas region. Deep water in the central Greenland Sea warms rapidly because it has direct contact with deep water flowing from the Arctic Ocean. The deep waters of the Norwegian and Iceland Seas are warming at a slower rate because they are products of the mixing of their own ambient waters with GSDW and Arctic outflow water (González-Pola et al., 2018; Rudels et al., 2012). According to Somavilla et al. (2013), in the absence of deep convection, deep water from the Arctic Ocean will flow into the deep parts of the Greenland Sea, making them warmer and more saline until they reach the properties of the deep water from the Arctic Ocean. The rate of EBDW import from the Arctic Ocean into the central Greenland Sea increased from 0.12 Sv before the 1980s (Bönisch and Schlosser, 1995) to ~0.44 Sv in 1993–2009 (Somavilla et al., 2013). Assuming that the current trend will remain unchanged, the GSDW will have the same properties as the Arctic Ocean deep water in approximately 2025 (Langehaug and Falck, 2012; Somavilla et al., 2013).

As mentioned above, one cannot say with certainty whether the causes of these changes are natural or anthropogenic. Indisputably, we are observing an increase in temperature in the WSC region and subsequent changes in the regional ecosystem (Dąbrowska et al., 2020; Stempniewicz et al., 2007; Węsławski et al., 2011). In the context of global warming, the temperature increase in all layers is an important and concerning phenomenon. The increasing concentrations of greenhouse gases in the atmosphere warm the Earth's climate system. The ocean contains over 50 times more carbon dioxide (the main greenhouse gas) than the atmosphere, and cold deep waters serve as its main reservoir (Stewart, 2008). Warming of the deep ocean layer could release large amounts of carbon dioxide into the atmosphere, intensifying the greenhouse effect. Moreover, the thermal expansion of water (the steric effect) leads to increased sea levels and, in addition to the loss of glacial mass, accounts for approximately 75% of global sea level rise since the 1970s. From 1993 to 2010, the average global sea-level rise was estimated at ~2.8 mm yr^{-1}, of which oceanic thermal expansion accounted for ~1.1 mm yr^{-1} (Stocker et al., 2013).

The progressive increase in the OHC may suggest that, in addition to natural variability, climate change caused by the greenhouse effect is an important driver of the observed warming. The world ocean accounts for approximately 93% of the warming of the Earth system that has occurred since 1955 (Levitus et al., 2012). For the years 1955–2010, the heat content of the world ocean in the 0–2000 m layer increased by 24.0 10^{22} J, corresponding to a rate of 0.39 W m^{-2} per unit area of the world ocean and a volume mean warming of 0.09°C. This has resulted in a temperature increase of 0.006°C yr^{-1}. Over the decade (2007–2016) of continuous observations, the mean surface-to-bottom ocean warming was 0.0022°C yr^{-1}. This temperature change is equivalent to a heat uptake of 0.71 W m^{-2} over the surface of Earth, approximately 1 W m^{-2} per unit area of the world ocean. The global ocean is warming at all depths, with warming maxima at the surface, 1000 m, and 4200 m (Desbruyères et al., 2017).

The warming we observed in the West Spitsbergen Current is occurring much faster than the global ocean warming. The temperature in the 0–2000 m layer is increasing at a rate of 0.023°C yr^{-1}, which is equivalent to 5.98 W m^{-2} of heat uptake, almost 6 times more than the mean oceanic heat uptake given by Desbruyères et al. (2017). Of course, this heat was not absorbed from the sun in the studied region and is mainly the effect of ocean heat convergence. However, these data show that the investigated region is a very effective heat sink and that the warming rate is much higher than the mean warming rate for the whole ocean. The intermediate water stores 22% of the heat surplus, and the deep water stores 29%. This confirms that deep and intermediate waters, in addition to surface water, are significant heat sinks. The surplus of heat stored in the West Spitsbergen Current region and transported by the WSC to the Arctic Ocean may have an important influence on Arctic sea ice melting and climate change.

5. Conclusion

In this study, we analyzed potential temperature and salinity increases in intermediate and deep waters in the West Spitsbergen Current region from 1997 to 2016. This area is divided into two parts by the Arctic front (~7°E): the Arctic domain in the west and the Atlantic domain in the east. The increase in the potential temperature of the water was especially intense in the Arctic domain and was associated with considerable changes in the water layers salinity.

The potential temperature and salinity of the intermediate water increased much faster (0.021°C yr^{-1} and 0.0022 yr^{-1}, respectively) than those of the deep water (0.009°C yr^{-1} and 0.0004 yr^{-1}, respectively). The intermediate and deep waters in the study area flow from the central part of the Greenland Sea; therefore, the increases in the temperature and salinity of these waters are related to the changes observed in the central Greenland Sea. This is most clearly observed in the western part of the area (Arctic domain), where the direct water supply from the central Greenland Sea is not inhibited by the Knipovich Ridge, unlike in the eastern part (Atlantic domain).

The increases in salinity and temperature in the intermediate water have also been associated with the advection of anomalously warm and saline Atlantic Water in recent years, which enters the region from the North Atlantic. This has contributed to deeper convection in the Greenland Sea, ventilating the intermediate water and increasing both the temperature and salinity of this layer. The temperature and salinity increases in the intermediate water were more substantial, with considerably higher interannual fluctuations, than the variability in the deep water physical properties. The source of the increases in temperature and salinity in the deep water is the inflow of relatively warm and salty Eurasian Basin Deep Water from the Arctic Ocean to the relatively cold and fresh Greenland Sea Deep Water in the Greenland Sea.

A temperature increase of 0.46°C in the 2000 m water column causes a mean increase in the heat content of 3770 MJ m^{-2} and requires an additional 5.98 W m^{-2} of atmosphere-ocean heat flux per 20 years, almost 6 times more than the mean oceanic heat uptake.

Acknowledgments

This study was funded by the National Science Centre, Poland within the DWINS Project (2016/21/N/ST10/02920). We would like to thank the crew of the r/v *Oceania* for their support and help at sea.

References

Aagaard, K., Swift, J.H., Carmack, E.C., 1985. Thermohaline circulation in the Arctic Mediterranean seas. J. Geophys. Res-Oceans 90 (C3), 4833—4846, https://doi.org/10.1029/JC090iC03p04833.

Blindheim, J., 1990. Arctic intermediate water in the Norwegian Sea. Deep Sea Res. Pt. A 37 (9), 1475—1489, https://doi.org/10.1016/0198-0149(90)90138-L.

Bönisch, G., Schlosser, P., 1995. Deep water formation and exchange rates in the Greenland/Norwegian Seas and the Eurasian Basin of the Arctic Ocean derived from tracer balances. Prog. Oceanogr. 35, 29—52, https://doi.org/10.1016/0079-6611(95)00004-Z.

Brakstad, A., Våge, K., Håvik, L., Moore, G.W.K., 2019. Water mass transformation in the Greenland Sea during the period 1986—2016. J. Phys. Oceanogr. 49 (1), 121—140, https://doi.org/10.1175/JPO-D-17-0273.1.

Church, J.A., Clark, P.U., Cazenave, A., Gregory, J.M., Jevrejeva, S., Levermann, A., Merrifield, M.A., Milne, G.A., Nerem, R.S., Nunn, P.D., Payne, A.J., Pfeffer, W.T., Stammer, D., Unnikrishnan, A.S., 2013. Sea level change. In: Stocker, T.F., Qin, D., Plattner, G.-K., Tignor, M.M.B., Allen, S.K., Boschung, J., Nauels, A., Xia, Y., Bex, V., Midgley, P.M. (Eds.), Climate Change, The Physical Science Basis. Cambridge Univ. Press, Cambridge, UK, New York, USA, 1137—1216.

Dąbrowska, A.M., Wiktor Jr., J.M., Merchel, M., Wiktor, J.M. , 2020. Planktonic protists of the eastern Nordic Seas and the Fram Strait: spatial changes related to hydrography during early summer. Front. Marine Sci, 7, art. no. 557, 14 pp., https://doi.org/10.3389/fmars.2020.00557.

Delworth, T.L., Mann, M.E., 2000. Observed and simulated multidecadal variability in the Northern Hemisphere. Clim. Dynam. 16 (9), 661—676, https://doi.org/10.1007/s003820000075.

Desbruyères, D.G., Purkey, S.G., McDonagh, E.L., Johnson, G.C., King, B.A., 2016. Deep and abyssal ocean warming from 35 years of repeat hydrography. Geophys. Res. Lett. 43 (19), 10,356—10,365, https://doi.org/10.1002/2016GL070413.

Desbruyères, D., McDonagh, E.L., King, B.A., Thierry, V., 2017. Global and full-depth ocean temperature trends during the early twenty-first century from Argo and repeat hydrography. J. Climate 30 (6), 1985—1997, https://doi.org/10.1175/JCLI-D-16-0396.1.

Eldevik, T., Nilsen, J.E.Ø., Iovino, D., Olsson, K.A., Sandø, A.B., Drange, H., 2009. Observed sources and variability of Nordic seas overflow. Nature Geosci. 2 (6), 406—410, https://doi.org/10.1038/ngeo518.

González-Pola, C., Larsen, K. M. H., Fratantoni, P., Beszczynska-Möller, A., Hughes, S. L. (Eds)., 2018. ICES Report on Ocean Climate 2016, ICES Coop. Res. Rep. No. 339, 110 pp., https://doi.org/10.17895/ices.pub.4069.

Hansen, B., Østerhus, S., 2000. North atlantic—nordic seas exchanges. Prog. Oceanogr. 45 (2), 109—208, https://doi.org/10.1016/S0079-6611(99)00052-X.

Holliday, N.P., Hughes, S.L., Bacon, S., Beszczynska-Möller, A., Hansen, B., Lavin, A., Loeng, H., Mork, K.A., Østerhus, S., Sherwin, T., Walczowski, W., 2008. Reversal of the 1960s to 1990s freshening trend in the northeast North Atlantic and Nordic Seas. Geophys. Res. Lett, 35, art. no. L03614, 5 pp., https://doi.org/10.1029/2007GL032675.

Jeansson, E., Olsen, A., Jutterström, S., 2017. Arctic intermediate water in the Nordic Seas, 1991—2009. Deep-Sea Res. Pt. I 128, 82—97, https://doi.org/10.1016/j.dsr.2017.08.013.

Karstensen, J., Schlosser, P., Wallace, D.W., Bullister, J.L., Blindheim, J., 2005. Water mass transformation in the Greenland Sea during the 1990s. J. Geophys. Res.-Oceans 110 (C7), art. no. C07022, 18 pp., https://doi.org/10.1029/2004JC002510.

Langehaug, H.R., Falck, E., 2012. Changes in the properties and distribution of the intermediate and deep waters in the Fram Strait. Prog. Oceanogr. 96 (1), 57—76, https://doi.org/10.1016/j.pocean.2011.10.002.

Larsen, K. M. H., Gonzalez-Pola, C., Fratantoni, P., Beszczynska-Möller, A., Hughes, S.L. (Eds.), 2016. ICES Report on Ocean Climate 2015, ICES Coop. Res. Rep. No. 331, 79 pp., https://doi.org/10.17895/ices.pub.5137.

Latarius, K., Quadfasel, D., 2010. Seasonal to inter-annual variability of temperature and salinity in the Greenland Sea Gyre:

heat and freshwater budgets. Tellus A 62 (4), 497—515, https://doi.org/10.1111/j.1600-0870.2010.00453.x.

Latarius, K., Quadfasel, D., 2016. Water mass transformation in the deep basins of the Nordic Seas: Analyses of heat and freshwater budgets. Deep-Sea Res. Pt. I 114, 23—42, https://doi.org/10.1016/j.dsr.2016.04.012.

Lauvset, S.K., Brakstad, A., Våge, K., Olsen, A., Jeansson, E., Mork, K.A., 2018. Continued warming, salinification and oxygenation of the Greenland Sea gyre. Tellus A 70 (1), 1—9, https://doi.org/10.1080/16000870.2018.1476434.

Levitus, S., Antonov, J.I., Boyer, T.P., Baranova, O.K., Garcia, H.E., Locarnini, R.A., Mishonov, A.V., Reagan, J.R., Seidov, D., Yarosh, E.S., Zweng, M.M., 2012. World ocean heat content and thermosteric sea level change (0—2000 m), 1955—2010. Geophys. Res. Lett. 39 (10), art. no. L10603, 5 pp., https://doi.org/10.1029/2012GL051106.

Orvik, K.A., Niiler, P. , 2002. Major pathways of Atlantic water in the northern North Atlantic and Nordic Seas toward Arctic. Geophys. Res. Lett. 29 (19), 2-1—2-4, https://doi.org/10.1029/2002GL015002.

Piechura, J., Walczowski, W., 1995. The Arctic Front: structure and dynamics. Oceanologia 37 (1), 47—73.

Purkey, S.G., Johnson, G.C., 2010. Warming of global abyssal and deep Southern Ocean waters between the 1990s and 2000s: Contributions to global heat and sea level rise budgets. J. Climate 23 (23), 6336—6351, https://doi.org/10.1175/2010JCLI3682.1.

Rahmstorf, S., 2002. Ocean circulation and climate during the past 120,000 years. Nature 419 (6903), 207—214, https://doi.org/10.1038/nature01090.

Raj, R.P., Chatterjee, S., Bertino, L., Turiel, A., Portabella, M., 2019. The Arctic Front and its variability in the Norwegian Sea. Ocean Sci. 15, 1729—1744, https://doi.org/10.5194/os-15-1729-2019.

Rhein, M.A., Rintoul, S.R., Aoki, S., Campos, E., Chambers, D., Feely, R.A., Gulev, S., Johnson, G.C., Josey, S.A., Kostianoy, A., Mauritzen, C., Roemmich, D., Talley, L.D., Wang, F., 2013. Observations: Ocean. In: Stocker, T.F., Qin, D., Plattner, G.-K., Tignor, M.M.B., Allen, S.K., Boschung, J., Nauels, A., Xia, Y., Bex, V., Midgley, P.M. (Eds.), Climate Change, The Physical Science Basis. Cambridge Univ. Press, Cambridge, UK, New York, USA, 255—316.

Roemmich, D., Church, J., Gilson, J., Monselesan, D., Sutton, P., Wijffels, S., 2015. Unabated planetary warming and its ocean structure since 2006. Nat. Clim. Change 5 (3), 240—245, https://doi.org/10.1038/nclimate2513.

Rudels, B., Korhonen, M., Budéus, G., Beszczynska-Möller, A., Schauer, U., Nummelin, A., Quadfasel, D., Valdimarsson, H., 2012. The East Greenland Current and its impacts on the Nordic Seas: observed trends in the past decade. ICES J. Mar. Sci. 69 (5), 841—851, https://doi.org/10.1093/icesjms/fss079.

Schauer, U., Fahrbach, E., Osterhus, S., Rohardt, G., 2004. Arctic warming through the Fram Strait: Oceanic heat transport from 3 years of measurements. J. Geophys. Res.-Oceans 109 (C6), https://doi.org/10.1029/2003JC001823.

Schlitzer, R., 2015. Ocean Data View. http://odv.awi.de.

Schlosser, P., Bönisch, G., Rhein, M., Bayer, R., 1991. Reduction of deepwater formation in the Greenland Sea during the 1980s: Evidence from tracer data. Science 251 (4997), 1054—1056, https://doi.org/10.1126/science.251.4997.1054.

Somavilla, R., Schauer, U., Budéus, G, 2013. Increasing amount of Arctic Ocean deep waters in the Greenland Sea. Geophys. Res. Lett. 40 (16), 4361—4366, https://doi.org/10.1002/grl.50775.

Stempniewicz, L., Błachowiak-Samołyk, K., Węsławski, J.M., 2007. Impact of climate change on zooplankton communities, seabird populations and arctic terrestrial ecosystem—a scenario. Deep Sea Res. Pt. II 54 (23—26), 2934—2945, https://doi.org/10.1016/j.dsr2.2007.08.012.

Stewart, R., H., 2008. Introduction to physical oceanography, https://www.uv.es/hegigui/Kasper/por%20Robert%20H%20Stewart.pdf.

Stocker, T.F., Qin, D., Plattner, G.-K., Tignor, M.M.B., Allen, S.K., Boschung, J., Nauels, A., Xia, Y., Bex, V., Midgley, P.M., 2013. Climate Change 2013: The Physical Science Basis. In: Contribution of Working Group I to the Fifth Assessment Report of the Intergovernmental Panel on Climate Change. Cambridge Univ. Press, Cambridge, UK, New York, USA, 1535 pp.

Swift, J.H., Aagaard, K., 1981. Seasonal transitions and water mass formation in the Iceland and Greenland seas. Deep Sea Res. Pt. A. 28 (10), 1107—1129, https://doi.org/10.1016/0198-0149(81)90050-9.

Swift, J.H., Koltermann, K.P., 1988. The origin of Norwegian Sea deep water. J. Geophys. Res.-Oceans 93 (C4), 3563—3569, https://doi.org/10.1029/JC093iC04p03563.

von Appen, W.J., Schauer, U., Somavilla, R., Bauerfeind, E., Beszczynska-Möller, A., 2015. Exchange of warming deep waters across Fram Strait. Deep Sea Res. Pt. I 103, 86—100, https://doi.org/10.1016/j.dsr.2015.06.003.

Walczowski, W., 2013. Frontal structures in the West Spitsbergen Current margins. Ocean Sci. 9 (6), 957—975, https://doi.org/10.5194/os-9-957-2013.

Walczowski, W., 2014. Atlantic Water in the Nordic Seas. Springer, Heidelberg, New York, London, 300 pp.

Walczowski, W., Beszczynska-Möller, A., Wieczorek, P., Merchel, M., Grynczel, A., 2017. Oceanographic observations in the Nordic Sea and Fram Strait in 2016 under the IO PAN long-term monitoring program AREX. Oceanologia 59 (2), 187—194, https://doi.org/10.1016/j.oceano.2016.12.003.

Wang, X., Zhao, J., Li, T., Zhong, W., Jiao, Y., 2015. Deep waters warming in the Nordic seas from 1972 to 2013. Acta Oceanologica Sinica 34 (3), 18—24, https://doi.org/10.1007/s13131-015-0613-z.

Węsławski, J.M., Kendall, M.A., Włodarska-Kowalczuk, M., Iken, K., Kędra, M., Legezynska, J., Sejr, M.K., 2011. Climate change effects on Arctic fjord and coastal macrobenthic diversity — observations and predictions. Mar. Biodivers. 41 (1), 71—85, https://doi.org/10.1007/s12526-010-0073-9.

Wijffels, S., Roemmich, D., Monselesan, D., Church, J., Gilson, J., 2016. Ocean temperatures chronicle the ongoing warming of Earth. Nat. Clim. Change 6 (2), 116—118, https://doi.org/10.1038/nclimate2924.

Oceanologia (2020) 62, 511—524

Available online at www.sciencedirect.com

ScienceDirect

journal homepage: www.journals.elsevier.com/oceanologia

ORIGINAL RESEARCH ARTICLE

Combined impact of summer heat waves and coastal upwelling in the Baltic Sea

Ülo Suursaar*

University of Tartu, Estonian Marine Institute, Tallinn, Estonia

Received 22 May 2020; accepted 10 August 2020
Available online 21 August 2020

KEYWORDS
Global warming;
Water temperature;
Salinity;
Marine heat waves;
Satellite images;
Breeze

Summary Under warming climates, heat waves (HWs) have occurred in increasing intensity in Europe. Also, public interest towards HWs has considerably increased over the last decades. The paper discusses the manifestations of the summer 2014 HW and simultaneously occurring coastal upwelling (CU) events in the Gulf of Finland. Caused by an anticyclonic weather pattern and persisting easterly winds, CUs evolved along the southern coast of the Gulf in four episodes from June to August. Based on data from coastal weather stations, 115 days-long measurements with a Recording Doppler Current Profiler (RDCP) oceanographic complex and sea surface temperature (SST) satellite images, the partly opposing impacts of these events are analysed. Occurring on the background of a marine HW (up to 26°C), the CU-forced SST variations reached about 20 degrees. At the 10 m deep RDCP mooring location, a drop from 21.5 to 2.9°C occurred within 60 hours. Salinity varied between 3.6 and 6.2 and an alongshore coastal jet was observed; the statistically preferred westerly current frequently flowed against the wind. Locally, the cooling effect of the CUs occasionally mitigated the overheating effects by the HWs both in the sea and on the marine-land boundary. However, in the elongated channel-like Gulf of Finland, upwelling at one coast is usually paired with downwelling at the opposite coast, and simultaneously or subsequently occurring HWs and CUs effectively

* Corresponding author at: University of Tartu, Estonian Marine Institute, Mäealuse 14, 12618 Tallinn, Estonia.
E-mail addresses: ulo.suursaar@ut.ee, ys@sea.ee

Peer review under the responsibility of the Institute of Oceanology of the Polish Academy of Sciences.

Production and hosting by Elsevier

https://doi.org/10.1016/j.oceano.2020.08.003

contribute to heat transfer from the atmosphere to the water mass. Rising extremes of HWs and rapid variations by CUs may put the ecosystems under increasing stress.

1. Introduction

In the Earth system, contemporary climate change primarily manifests as 'global warming', which nevertheless is a spatially varying and complex phenomenon (IPCC, 2014). Other important interrelated effects are spatio-temporal changes in atmospheric circulation patterns and in wind characteristics, occurring from global to local scales (e.g. Easterling et al., 2000). All these forcings mingle and act on the marine environment causing changes in thermic conditions, hydrodynamics, and ultimately via various links, in biota (e.g. Hoegh-Guldberg and Bruno, 2010; Kotta et al., 2018).

This study addresses the combined effects of atmospheric heat waves and coastal wind-driven upwelling. The study focusses on the year 2014, when in the region of the Baltic Sea, a major summer heat wave (HW) was registered, and in addition, intense coastal upwelling (CU) with a cooling effect along certain, extensive coastline stretches occurred as well.

Based on reports from several scientific agencies around the world, the World Meteorological Organization (WMO) declared 2014 the hottest year on record, then. Globally, the average atmospheric air temperature (AT) was 0.68°C above the 1951–1980 baseline average, which, in turn, was about 0.3–0.4°C higher than the 1880–1920 average (Lenssen et al., 2019). In fact, the record-setting temperature anomalies have continued after 2014. Currently, according to the datasets by the NOAA and NASA, the year 2016 is considered the hottest on record, followed by 2019 and 2015 (Cole and Jacobs, 2020). Due to larger inertia in the oceanic system, the six highest global ocean heat contents have occurred in: 2019, 2018, 2017, 2015, 2016, and 2014 (Cheng et al., 2020). However, Central Europe and the Baltic Sea region has warmed in an even relatively faster pace. For instance, in recent years, the positive anomalies in the Baltic region ATs have been higher by 0.5–1.0°C than the global average (Rutgersson et al., 2015). The total warming trend in the whole Baltic Sea water mass has been 1.07°C for 35 years (1982–2016), while in the upper layer (in sea surface temperature, SST), the increase has been 1.75°C or 0.05°C/year (Liblik and Lips, 2019). While the main AT rise in the Baltic Sea region has occurred in late winter and spring, the SST increase has been faster in summer months (Liblik and Lips, 2019). This can partially be related to the increased frequency and magnitudes of summer HWs, which in turn, cause an increase in marine heat waves (MHWs) (Hobday et al., 2018; Oliver et al., 2019).

Over time, many different HW definitions have been proposed, which vary regarding the target area or study purpose (e.g. Perkins and Alexander, 2013). A HW is usually understood as a period of excessively hot weather lasting from several days to weeks and is measured relative to the weather norms in the area and for the season. Currently, the WMO defines a heat wave as 5 or more consecutive days of prolonged heat in which the daily maximum temperature is higher than the average maximum temperature by 5°C or more (Rafferty, 2020), which concurs with one of the earliest definitions proposed by Frich et al. (2002). However, some nations have come up with their own, slightly different threshold and duration criteria and more definitions and indices describing different aspects of the HW exist in scientific literature (e.g. Keevallik and Vint, 2015; Russo et al., 2014). There is no clear definition of HWs established in Estonia. For instance, while HWs are sometimes considered as periods with daily maxima over 25°C, a gradation of dangerous events includes the ones when the daily maximum exceeds 30°C in two, three, or five consecutive days (EWS, 2020; Õispuu, 2019).

Under warming climates, HWs have occurred in increasing frequencies and magnitudes in Europe (Russo et al., 2015; Schär et al., 2004). The spread and locations of HWs vary greatly. Quite naturally, the most dangerous events are those occurring in densely populated urban areas and in low latitudes. In that sense, the deadliest ones (more than ten thousand casualties per event) probably occurred in France (in 2003) and in Moscow (2010) (Smid et al., 2019). Lying in relative high latitudes, the less populous Baltic Sea region usually suffers from far less HW casualties. Nevertheless, such kind of extreme events may still pose unexpected adverse societal, economic and environmental consequences on high latitudes as well. For instance, exceptionally large cyanobacteria blooms, poisoning water both for human and animal use, have been reported in years with summer HWs in the Baltic Sea (e.g. Kononen and Nõmmann, 1992), and possible further increase in such record-breaking algal blooms have been projected by Meier et al. (2019). Effect of HWs (and MHWs) on the Baltic Sea environment have been studied e.g. by Paalme et al. (2020) and by Takolander et al. (2017). Sea surface warming trends and impacts of HW events in a wider scale have been demonstrated e.g. by Panch et al. (2013), Shaltout (2019), and Wernberg et al. (2013).

Coastal upwelling studies in the Baltic Sea form a much larger pool, including scores of scientific articles (e.g. Delpeche-Ellmann et al., 2017; Gidhagen, 1987; Kowalewski and Ostrowski, 2005; Lehmann et al., 2012; Lips et al., 2009; Myrberg and Andrejev, 2003; Uiboupin and Laanemets, 2009). The CUs in the Baltic Sea can occur site-specifically under suitable meteorological conditions, and in principle, in whatever season. For instance, 'warm' CUs exist in winter (e.g. Kowalewska-Kalkowska and Kowalewski, 2019; Suursaar, 2010). However, summer CUs are still more typical and possibly more influential with much stronger SST imprint. In case of summer CU, persistent alongshore winds (coastline on its left) bring dense,

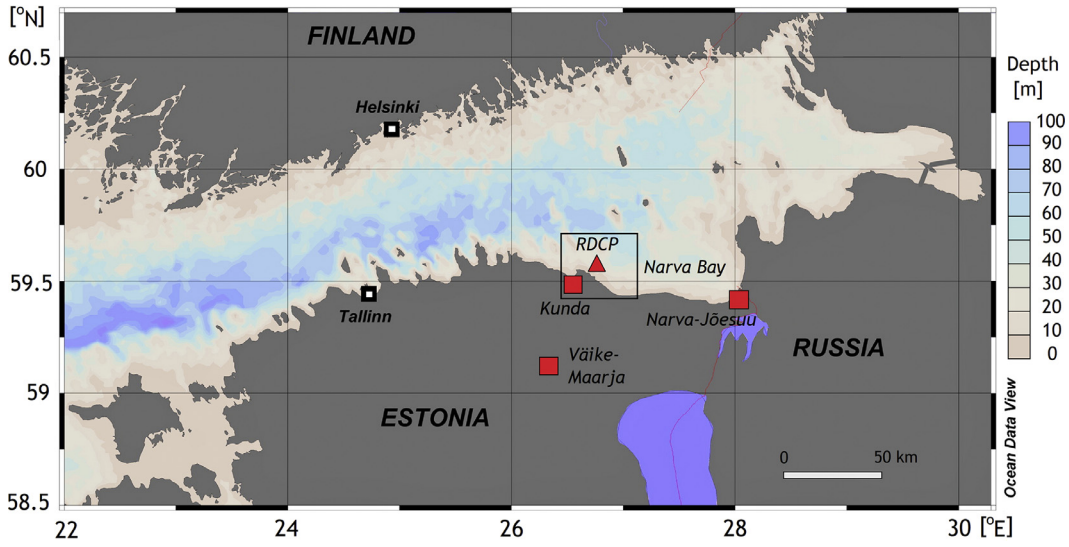

Figure 1 Bathymetric map of the Gulf of Finland (Schlitzer, 2020). Red rectangles mark weather stations by the EWS (Estonian Weather Service), the triangle marks the RDCP (Recording Doppler Current Profiler) mooring location near Letipea Peninsula.

cooler, and usually nutrient-rich water towards the sea surface (e.g. Jiang and Wang, 2018), replacing the warmer and less saline surface water.

Although occurring sometimes simultaneously in certain sea areas, the combined, and possibly opposing effects of HWs and CUs are far less studied so far. Recently, Paalme et al. (2020) studied the effects of HWs and CUs on littoral benthic communities in the Gulf of Finland based on 2018 data. However, under warming climate, study of HWs and their impacts in various conditions and environments is increasingly topical. The aim of this article is to (1) document and analyse the manifestation of the 2014 HW event in the Gulf of Finland (NE Baltic Sea), (2) present and analyse 4 months long in situ oceanographic measurements capturing an extensive CU along the southern coast of the Gulf of Finland in same summer, and (3) discuss the combined effect of simultaneously and/or subsequently occurring HW and CU events on the marine environment and coastal climate.

2. Material and methods

2.1. Study area and the meteorology

The Gulf of Finland is a longitudinally elongated fjord-like sub-basin of the Baltic Sea (Figure 1), located on the relatively high latitudes (59—60.5°N) in the temperate climate zone of prevailing westerlies (Kont et al., 2011). It has an area of 29 571 km^2, water volume of 1103 km^3, and an average depth of 37 m with maximum values reaching 123 m in the westernmost part of the Gulf (Alenius et al., 1998). It receives a relatively large (114 km^3/yr) freshwater input from rivers (mainly via the Neva, Narva, and Kymijoki) and the typical surface salinity varies between 1 and 7 PSU lengthwise and, in the deeper western part, between 6 and 12 units vertically (Alenius et al., 1998).

Our study focuses mainly on the south-eastern part of the Gulf of Finland, where the broad Narva Bay defines a roughly 100 km long, relatively straight coastal section between the Narva River mouth and Kunda-Letipea area on the southern shore (Figure 1). Owing to its elongated shape, upwelling can occur along both coasts. The relatively straight southern coast has a more suitable coastal slope for upwelling evolvement (Delpeche-Ellmann et al., 2018). On the other hand, due to statistically prevailing westerlies (Soomere et al., 2008), the occurrence of upwelling is higher on the northern shore (Lehmann et al., 2012; Myrberg and Andrejev, 2003).

Meteorological description of this study is based on data from the Estonian Weather Service (EWS, 2020; formerly the EMHI). The closest station to our oceanographic instrument mooring location near the Letipea Peninsula is at Kunda (59°31′17″N; 26°32′29″E; 8 km from the RDCP), where we used hourly average wind speed and direction data, as well as air temperature and water temperature data (measured at nearby Kunda Port). The wind data were used to analyse upwelling-favouring forcing conditions, AT data for defining HW periods, and water temperature data for describing effects of HWs and MHWs on the marine environment. From Narva-Jõesuu (59°28′06″N; 28°02′33″E; 77 km from the RDCP) we only used water temperature data. From Väike-Maarja station, (59°08′29″N; 26°13′51″E), 45 km inland from Kunda Port (Figure 1), we used air temperature data to analyse the temperature differences between the coast and an inland location. Since 2003, all the stations are equipped with MILOS-520 automated weather complexes (see: Keevallik et al., 2007).

In order to consider climatic background conditions in Estonia, we also used various web-based annual overviews by the EWS (e.g. Kallis et al., 2015), as well as its statistics on climate normals (EWS, 2020).

2.2. In situ oceanographic measurements

Studies on hydrodynamic conditions near the Letipea Peninsula and in the Narva Bay have been carried out several times since 2006. It turned out that along the straight coastline section, illustrious upwelling events can be occasionally recorded and analysed (Suursaar and Aps, 2007). Using

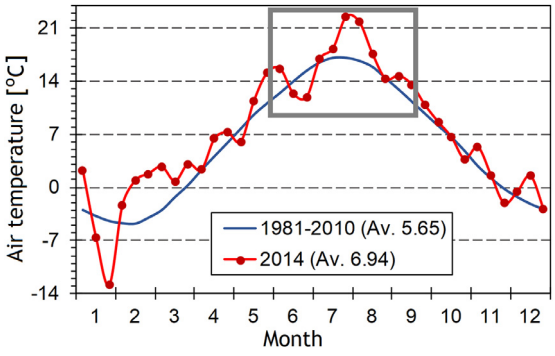

Figure 2 Variations in air temperature at Kunda weather station (10-day averages in 2014) compared with 1981–2010 long-term average (EWS data). The window defines the 4-months study period in summer 2014.

bottom-mounted current profilers, CTD-probes and other devices, more than a years' worth of recordings on various hydro-physical and chemical parameters have been obtained in that location over 2006–2010 (Suursaar, 2010, 2013). This article stems from nearly 4-month long measurements at the same location in 2014 (Figure 2), which have never been analysed and published before.

In 2014, the measurements were carried out using the oceanographic measuring complex called Recording Doppler Current profiler (RDCP-600) by AADI Aanderaa (currently YSI, a Xylem brand). The upward-looking instrument was deployed on the seabed (about 2 km off the coast at 59°33′30″N; 26°40′10″E; Figure 1) by divers from a speed boat of the Estonian Marine Institute and it started autonomous recording on 6 June 2014 at 12.00 UTC. The instrument depth was about 10–11 m (it changed a bit along with water level variations) and the recording interval was set to 60 min. The instrument was retrieved on 29 September 10.00 UTC, producing 2758 hourly records (114.9 days).

The recorded parameters were, firstly, three velocity components (u, v, z) on a multitude of depth cells. The vertical column set-up for flow measurements included a 2 m cell size with no overlap. Due to relatively shallow water, we used 3 depth intervals (3–5, 5–7 and 7–9 m). Beginning with the seabed, there was a 2 m blank distance between the instrument and the lowest measurable cell. Within the 1–3 uppermost metres, depending on sea-level variations and wave height, the flow measurements were somewhat "contaminated" and thus discarded on the grounds of high standard deviations.

In addition to Doppler effect-based current measurements, the RDCP-600 was equipped with temperature, oxygen, pressure, turbidity and conductivity (i.e. salinity) sensors, which sampled hourly the near-bottom layer (0.4 m from the seabed) in contact with the instrument (see also Suursaar, 2010). The high accuracy quartz-based pressure sensor (resolution 0.001% of full scale) enabled measurement of wave parameters, such as significant and maximum wave heights (H_s, H_{max}), as well as various derivations of wave periods (not discussed in this article). The raw data were stored on a multimedia card, processed upon retrieval by the special software by AADI, and thereafter, using packages such as Statistica. Cumulated water (and air) flow components (u-, v-) were computed for the Kunda location, temporal variations in observed parameters studied, and regression and spectral analysis performed.

2.3. SST images

In order to describe SST spatial patterns in the Gulf of Finland during HW and CU periods in 2014, satellite images processed in the Finnish Environment Institute (SYKE) were used. Based on raw data from several NASA, NOAA and EU Copernicus program instruments, SYKE Geoinformatics systems and Geoinformatics research units have produced downloadable remote sensing products (e.g. SST, turbidity, CDOM and Chl *a*). For 2014, SST images based on NOAA AVHRR (NOAA) satellite observations (mediated by the Finnish Meteorological Institute) were downloaded from SYKE TARKKA open web service (http://syke.fi/tarkka/en). In principle, the images are available on a nearly daily basis. However, their usefulness varies due to cloudiness.

Over the 4-month period (June–September), 93 images were reviewed and visually assessed. Our preliminary assortment yielded 8 particularly good SST-images for our study area (i.e. the Gulf of Finland and particularly its southern half). Additionally, 7 images were satisfactory (i.e., partially usable), while the remaining 78 were not that usable (Figure 3a). Still, both the HW and CU periods, as well as post-upwelling conditions, can be successfully illustrated by the SST images.

3. Results and discussion

3.1. Year 2014 case: air and water temperature

The summer 2014 HW, also sometimes called the "2014 Swedish heat wave" (Russo et al., 2015), was caused by a large and stable atmospheric high pressure aloft which remained over north-eastern Europe for several weeks, blocking westerlies and cyclonic activity along the polar front in this region. According to synoptic maps by EWS and SMHI, the high-pressure area covered the entire of Scandinavia and the Baltic Sea. It extended up to Svalbard and Novaya Zemlya in the North and down to Belarus and Ukraine in the South-East. Several heat records were broken in Sweden, as well as in Finland and elsewhere. According to the ranking of European record-breaking HWs in the period of 1950–2015 by Russo et al. (2015), the exceptionally long Scandinavian July–August 2014 event went to the top ten list of the 65-year period. The HW in 2014 also caused a MHW in the Baltic Sea and an overall warming of the Baltic Sea water mass. The annual mean SSTs of the entire Baltic Sea was 9°C in 2014, which was the warmest at the time and 1.14°C higher than the average in 1990–2018 (Siegel and Gerth, 2019); this anomaly was only surpassed in 2018 (which was 1.19°C higher).

According to the 2014 yearbook by the EWS (EWS, 2020; Kallis et al., 2015), the summer was unusually warm also in Estonia (Figure 2). In retrospect (1951–2018), the most influential HWs in Estonia have occurred, starting with the most influential, in 2010, 2018, 2014, and 2003 (the order may slightly vary depending on criteria). This list partly reflects the warming trend, including the 2 degrees increase

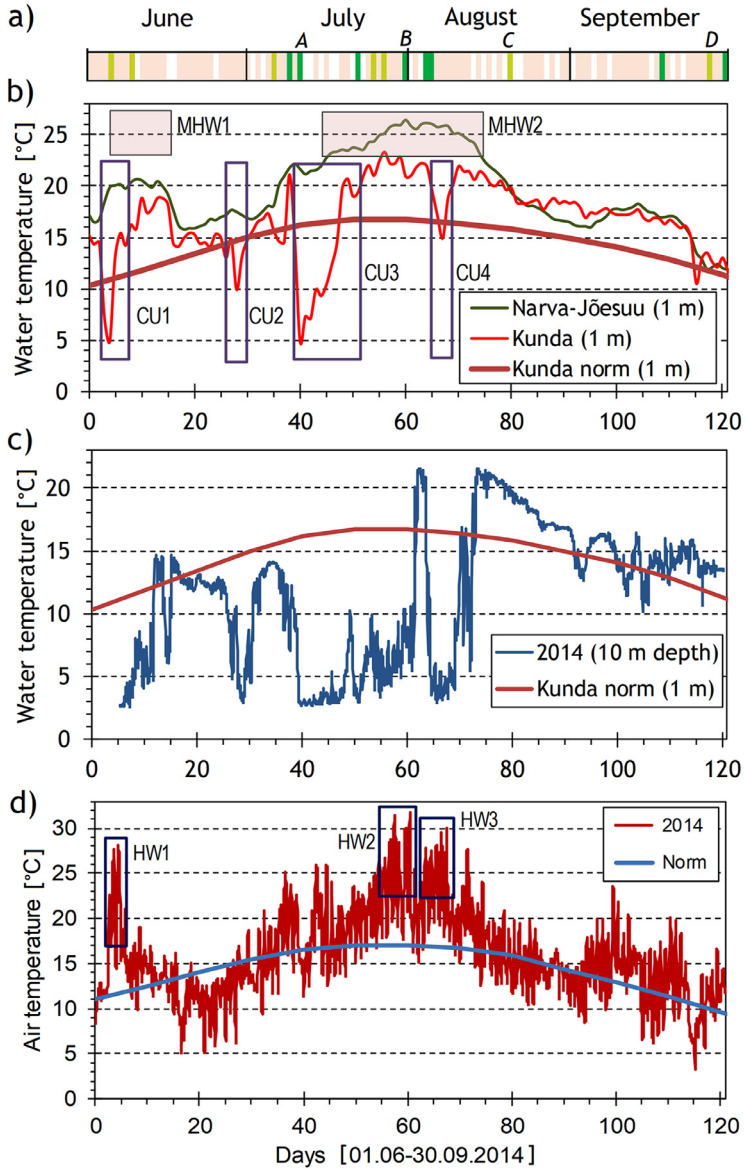

Figure 3 (a) Availability of SST images during the 4-month period; dark green — particularly good image, light green — satisfactory image, pink — limited coverage, white — no image. Letters A—D mark the chosen images on Fig. 4. (b) Water temperatures at Narva-Jõesuu and Kunda weather stations (EWS afternoon data) in 2014, Kunda long-term normal, MHW — marine heat wave events, CU — Kunda station based coastal upwelling events (Table 1). (c) Variations in water temperature measured hourly near Letipea Peninsula at 10 m depth. (d) Air temperatures measured hourly at Kunda weather station compared with long-term normal; HW — heat wave events based on Kunda weather data.

in maximum air temperatures over the same 68-year period (Õispuu, 2019). At Kunda station, July was on average 3°C warmer than the norm (16.3 vs. 19.3°C) and August was 2.4°C warmer (15.4 vs. 17.8°C). As a result, the whole year was 1.3°C warmer than the norm (1.4°C warmer in entire Estonia). Some clear HW events can be identified in the study area (Figure 3).

Considering the simple criteria (daily average exceedance by at least 5 degrees over a long-term normal on at least 5 consecutive days), there were 2 proper heat waves at Kunda location (HW2 and HW3, Figure 3) and one remarkable event which barely did not qualify (HW1). Daily maxima in this coastal town exceeded 30°C in four days. According to the EWS Kunda data, the HW1 event occurred on 4—6 June. It lasted at least 3 consecutive days (actually nearly 4 days), however, the daily average normal was exceeded by about 10 degrees on two consecutive days. HW2 occurred on 25—31 July (7 days) and HW3 on 3—7 August (5 days). The maximum value (32°C) was measured on 31 July. There were some other relatively warm periods around 13 July, 11 August, and 8 September, which were either shorter or not so extreme to be considered as HWs (Figure 3d). However, in other weather stations, the HW periods and durations could have been slightly different.

Following a similar criterion, marine heat waves (MHWs) occurred in Kunda (at port, 1 m depth) on 10—15.06 (MHW1,

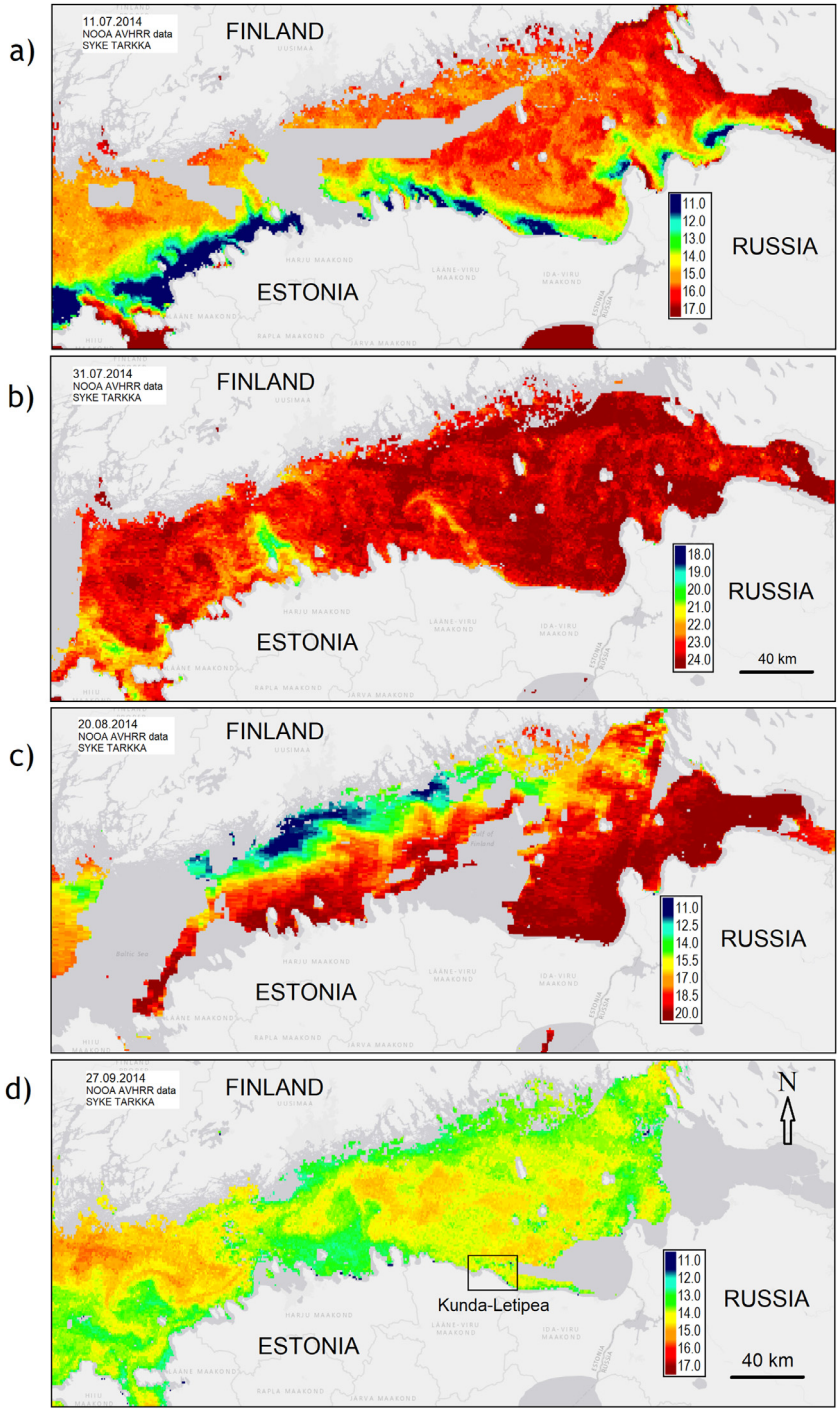

Figure 4 SST images (modified from SYKE TARKKA) during upwelling along the Estonian coast (a, 11.07), MHW (marine heat wave events) covering the entire Gulf (b, 31.07), upwelling at the Finnish coast (c, 20.08), mixing and cooling (d, 27.09).

6 days) and on 24–30.06 (MHW2, 7 days plus 3 more days after a short recession). In Narva-Jõesuu, MHW1 occurred on 4–16.06 (13 days) and MHW2 on 16.07–15.08 (31 consecutive days). MHWs at Kunda were occasionally interrupted by CU events (Figure 3b). In contact with the RDCP at 10 m depth, the summer water temperatures were obviously somewhat smaller and upwelling-influenced water temperature drops were much more extensive than at near-surface (Figure 3c). However, even there, the RDCP yielded remarkably high water temperature anomalies (defined here as exceeding by 5 degrees the 1 m depth normal; 10 m depth normal is unknown) on 2–3 August (up to 21.5°C on 2 August) and on 5 consecutive days on 13–17 August (max 21.5°C on 13 August).

The highest measured water temperature at Kunda port was 23.3°C (on 27 July). At Narva-Jõesuu, it reached 26.5°C

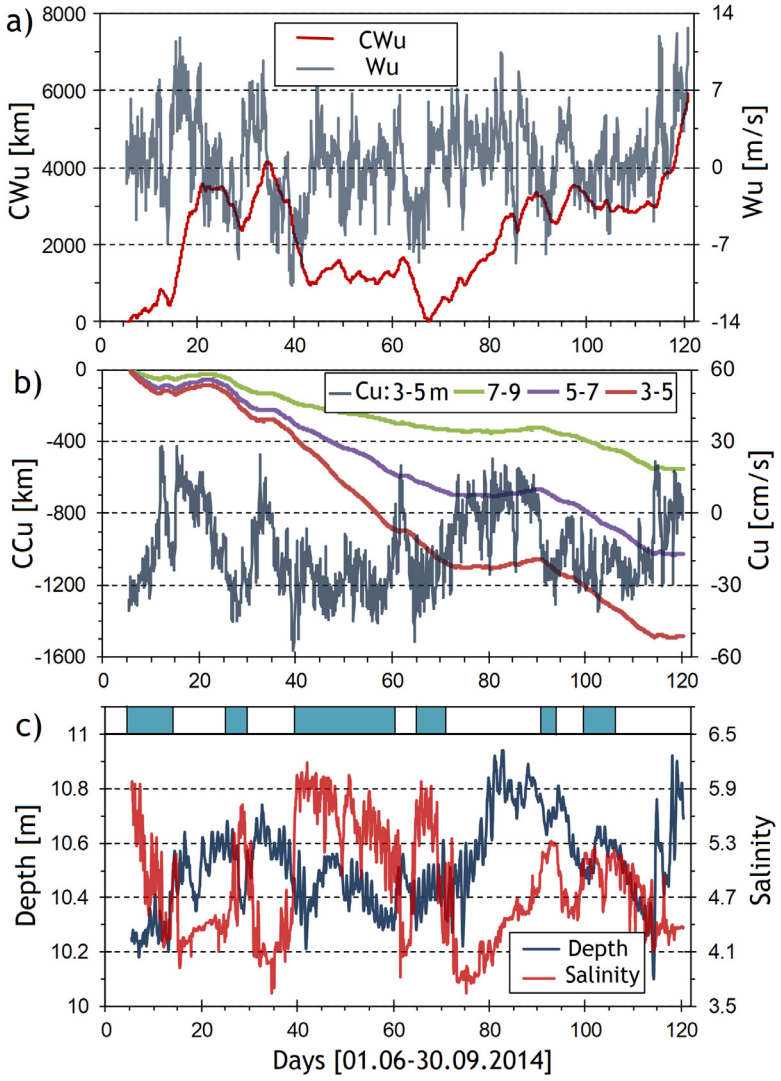

Figure 5 Variations in hourly wind u-component and cumulated u-component at Kunda station (u is nearly shore-parallel at Letipea Peninsula) positive direction of the vector is East; a); RDCP-measured flow u-component at 3–5 m depth and cumulated u-components at 7–9, 5–7, and 3–5 m layers (b); variations in salinity and instrument depth (sea level; c). Blue bar on (c) indicates upwelling impacts, including elevated salinity at 10 m depth and westerly-directed current.

Table 1 CU event durations and minimum water temperatures (WT,°C) at Kunda station (1 m) and RDCP mooring at Letipea Peninsula (10 m); see also Figure 3.

	Kunda	WT	Letipea	WT
CU1	03.06–07.06	4.7	(03.06)–12.06	2.6
CU2	26.06–29.06	8.1	26.06–01.07	2.9
CU3	10.07–17.07	4.9	09.07–01.08	2.7
CU4	05.08–07.08	14.5	04.08–12.08	2.9

on 30 July and stayed at 26.2°C for three consecutive days on 3–5 August (Figure 3b). In contrast, the water temperature at Kunda dropped down to 4.7°C during CU1, 8.1°C in CU2, 4.9°C in CU3, and 14.5°C in CU4 (Table 1), which marks nearly 20°C SST variations.

According to SST images, CU can cover the entirety of Estonia's 360 km-long northern coast from Hiiumaa Island in the West to Narva-Jõesuu in the East and extending for about 100 more km-s along the Russian coast (Figure 4a; Uiboupin and Laanemets, 2009). The cross-shore extent of the affected sea area can be up to 25 km, filaments excluded. While CU occurs on one side of the Gulf of Finland, MHW can occur in rest of the basin (Fig. 4a, c). Under unfavouring wind conditions for CUs on either coast, MHW can cover the entire Gulf. For instance, on 31 July, even the 'coldest' patches had SST around 20°C, while 90% of the Gulf's area had SSTs between 23 and 24 (or more) degrees (Figure 4b). CU duration varies depending on coastal location. The periods CU1-CU4 were identified based on Kunda SST (Figure 3b). However, the upwelling process is visible from RDCP data over a much longer period because it manifests in deeper layers before it reaches the sea surface. It also lasts longer (Figure 3c). Out of 115 measurement days, CU impact was visible on about 50 days at the 10 m depth and on 20–25 days on the sea surface near Kunda (Table 1).

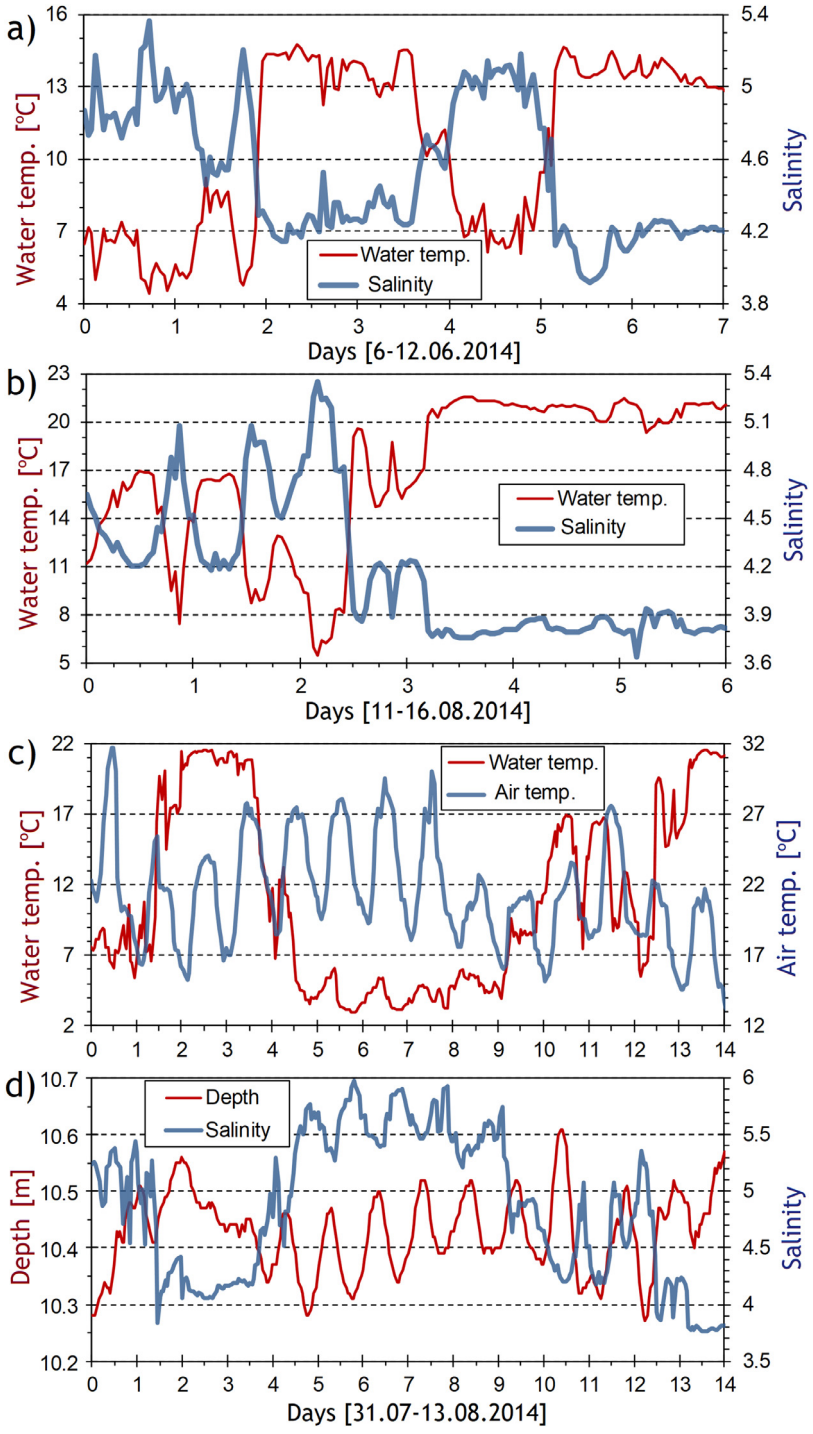

Figure 6 Contrasting variations in water temperature and salinity indicating upwelling at 10 m depth (a, b); Diurnal variations in air temperature at Kunda, also impacting (via daily switching breeze) water temperature (smaller oscillations besides large upwelling-caused variations), salinity and local sea level (c, d).

While the summer of 2014 was among the most extreme ever recorded regarding water temperatures and MHWs (Siegel and Gerth, 2019), CUs are rather common, occurring along the northern coast of Estonia roughly every other year (Uiboupin and Laanemets, 2009). In terms of extent and duration, the summer 2014 CUs probably were not among the largest. For instance, the year 2003 event and the 2006 event (e.g. Suursaar and Aps, 2007) were more extensive. However, in terms of water temperature variation, 2014 was remarkable due to opposing effects of CU and MHW, occurring on the background of very high water temperatures. For instance, at Kunda station, a 17.1°C SST drop occurred within 50 hours. At the RDCP, an 18.6°C drop (from 21.5 to 2.9°C) occurred in two and half days (60 hours), including

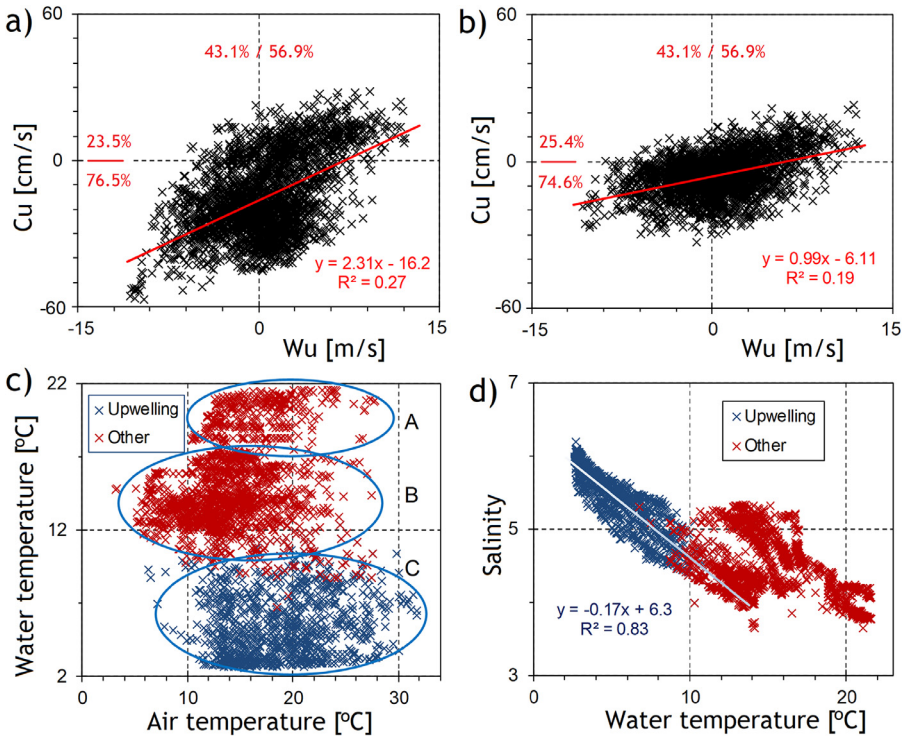

Figure 7 Plots of wind and flow u-component values at two depths (a — sub-surface, b — near-bottom) indicating preferred West-directed current occurring even in moderate West wind conditions. Plots of air versus water temperatures (c) and water temperatures versus salinity (d) indicating differently behaving data subsets under upwelling and non-upwelling conditions. Zone C (on c) marks CU, zone A mostly marks post-upwelling MHW (marine heat wave events) in August, and zone B pre-upwelling periods in June and cooling period in September.

a 24 h drop of 15.7°C. The total range was over 20°C both temporally (Figure 3) and spatially (considering maximum SSTs over 26°C; Figures 3b, 4).

3.2. Upwelling development and its effects on water column properties

It is a well-known fact that mesoscale CU is triggered by the alongshore wind component, causing Coriolis force assisted Ekman transport of surface water away from the shore, which is replaced by water that wells up from below (e.g. Gill and Clarke, 1974). It is also described that favourable alongshore winds should last for at least a few days until certain cumulative wind impulse is reached (e.g. Haapala, 1994) and upwelled water surfaces, thus becoming 'visible'. In fact, bottom-mounted instruments can show near-instantaneous changes in virtually every measured parameter (Figures. 5–6) and CUs are manifested over longer periods than on the surface (Table 1). Based on Figure 5, CU favouring conditions occur on the southern coast of the Gulf of Finland when the alongshore wind component (u-component) is mostly negative (West-directed) and cumulated u-wind decreases (Figure 5a); current u-component is negative and cumulated u- decreases, especially in sub-surface layers (Figure 5b); salinity is relatively high or increasing and water level decreases (Figure 5c).

As a result of up-flow of more saline and cooler intermediate or deep layer water of the Gulf, water temperatures and salinity graphs form distinct negatively correlated patterns (Figure 6ab, 7d). Besides dramatic (up to 20°C) fluctuations in water temperature, salinity varied between 3.6 and 6.2 (Figures 5c, 6), which is rather remarkable for this brackish water location. The correlation coefficient between water temperature and salinity was −0.82 over the entire 115-day period.

A curious feature of the Letipea coastal section is that under statistically prevailing westerly winds both above the Gulf (e.g. at Kalbådagrund; Westerlund et al., 2018) and at Kunda (Suursaar, 2013), just a relatively weak easterly is required to cause a west-directed rapid alongshore current — an upwelling-related coastal jet (Figure 5). Even more, water easily flows against the wind at Letipea (Figure 7ab). Over the 115-day study period in 2014, the wind u-component was positive in 56.9% cases. At the same time, only 23.5% of sub-surface current u-components were accordingly positive (Figure 7). The same feature has been described in previous moorings as well (Suursaar, 2010). The finding also fits with the simulation results with eddy-resolving models (Andrejev et al., 2004; Soomere et al., 2008), showing a topographically modified, quasi-permanent clockwise gyre, yielding a resultant westward current along the coast between Narva-Jõesuu and Kunda. According to modelling study by Westerlund et al. (2019), this 6–10 cm/s resultant flow occurred at Letipea throughout all seasons, being just somewhat weaker only in autumn. Based on our 293 + 115 days of in situ measurements (from previous mooring plus this study), the W current occurred on 73% of cases on the sub-surface layer (resulted u =

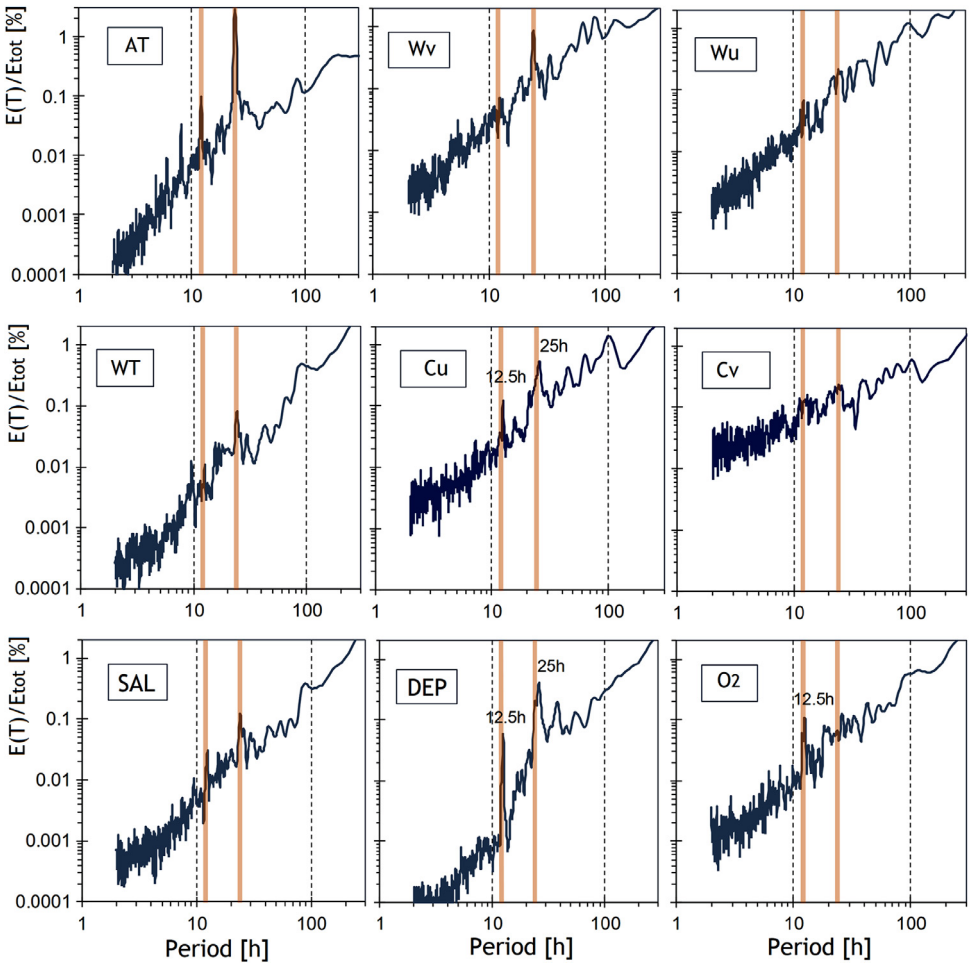

Figure 8 Normalized spectra (total energy =100%) calculated from hourly meteorological data from Kunda station (AT — air temperature, Wv and Wu — wind v- and u- component, respectively) and from hourly RDCP data measured at 10 m depth near Letipea Ps. (WT — water temperature, Cu, Cv — current u- and v-component at the lowermost cell, SAL — salinity, DEP- instrument depth, O2 — water oxygen content). Vertical lines mark diurnal (12, 24 h) periods, 12.5 and 25 h are specifically indicated, when the main peaks occur on these periods instead of strictly diurnal harmonics.

—9 cm/s), while in the near-bottom layer, W and E currents were practically balanced. While E-directed current was vertically rather homogeneous, the W-current, especially during CU, was stratified with higher values in upper layers (up to 61 cm/s at 3—5 m depth and 67 cm/s at the discarded 1—3 m depth range). Low values or even backflows occurred in deeper layers. This also appears on cumulated u-current graphs (Figure 5b), which diverge faster from each other during CU periods. Despite occasional west-storms, we have never registered a faster E current than 46 cm/s at Letipea, while the maximum W current 76 cm/s has been recorded in relatively modest (3—5 m/s, gusts up to 8 m/s) E-wind conditions, clearly indicating an upwelling-related coastal jet (Suursaar, 2010).

3.3. Combined effects of HWs and CUs on local and basin-wide scales

Several simultaneous processes with sometimes opposing effects occur in the sea. Firstly, impacts of HW and CU occasionally mingle on the local scale (Figures 3, 6). Instead of being around 20°C, water temperature may drop against seasonal norms down to 4—5°C in the surface layer and to 3—4°C at the 10—11 m depth. This can happen even in the hottest days when the air temperatures reach 25—32°C. These HW and CU-caused deformations in water temperatures are well visible in Figure 3c. Therefore, the connection between air and water temperatures is not straightforward, especially when CU is involved (Figures 6c, 7c).

In addition to these mesoscale (in temporal scale — days-weeks) processes, clear diurnal variations are visible in air and water temperatures, but also in salinity and depth (Figure 6cd). The main driving force behind these variations is daily variation in air temperature, which, under stable anticyclonic weather and HW conditions may reach 10 degrees or more (e.g. 16 vs. 32°C on 31.07, 19 vs. 30°C on 07.08) even at coastal locations. Such periodic diurnal variations also cause variations in atmospheric pressure and local winds, known as (daily) sea and (nightly) land breeze. Spectra calculated from hourly records with similar 115-days extent (Figure 8) clearly show prominent peaks and its harmonics (24 h, 12 h) in air temperature (AT, see Figure 8 for the following abbreviations). The same periods, though less prominent, also occur on WT. Further on, the 24 h peak at Wv shows the presence of cross-shore winds (breeze), while in Wu the diurnal peak was missing. Wv in turn evokes variations in alongshore current (Cu) and depth. However, these peaks did not occur strictly on diurnal periods but were somewhat modified by inertial and tidal periods, which yielded peaks at 12.5 h and 25 h, instead. Slopes of the spectra and the share of long-period (>100 h) variations (Figure 8) described atmospheric synoptic processes, including the variations due to CU and HW. The share of such motions was relatively large in wind data (Wu, -v), Cu and depth, but also in WT and salinity (due to strong CU-related variations). The gentle slope in Cv is due to the lack of freedom in cross-shore water movements in the nearshore location.

Besides the contrasting impacts on water column properties discussed above, the combined effects of CU and HW may also include some other aspects. Firstly, there is an important impact of CUs and HWs on basin-wide mixing and water column warming. Up- and downwelling are the major agents of mixing in the Gulf of Finland. Average properties of the water masses across the gulf may be substantially modified by sequences of upwellings and downwellings (Delpeche-Ellmann et al., 2017; Soomere et al., 2008; Talpsepp, 2008). In a stratified sea, heat transport from the surface to deeper layers is a slow process (Figure 9a) unless aided by vertical mixing due to surface and internal waves, shear entrainment, turbulence and upwelling (e.g. Elken et al., 2015; Strange and Fernando, 2001). Moreover, in elongated channel-like basins like the Gulf of Finland, upwelling at one coast is usually paired with downwelling at opposite coast (Figure 9b). Obviously, heat transport during HW is faster and more effective in such up/downwelling conditions rather than without it — in calm anticyclonic conditions or under non-persistent wind conditions (Figure 9).

Delayed heat transfer from the surface into deep layers is confirmed by the fact that, over the last decades, water temperature in the upper layer has increased faster in the Baltic Sea than the whole water mass (Liblik and Lips, 2019). This also means that thermal contrasts during CUs tend to increase over time.

Another impact to consider is the influence of low water temperatures due to CU on local cooling of air temperature above land. The heat exchange between the sea and land is partially maintained by the cross-shore breeze (Figure 9). The landward penetration of the daily sea breeze usually reaches 10—50 km in temperate zones while nightly land breeze may reach ca 10 km seaward (Miller et al., 2003).

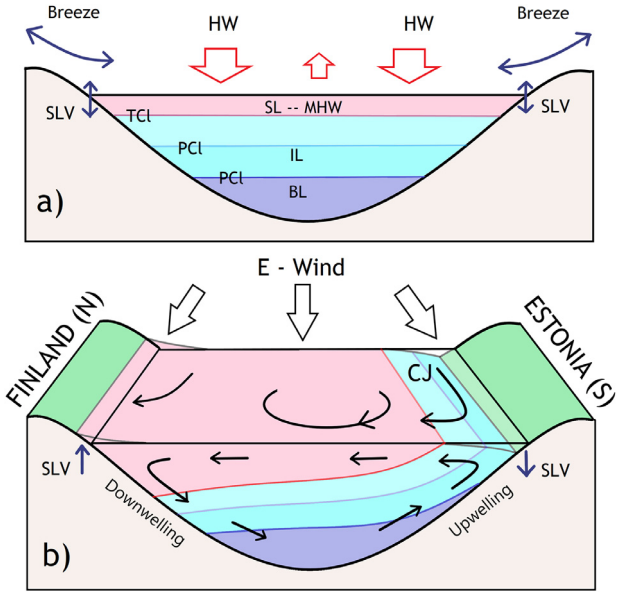

Figure 9 Scheme of HW — heat wave events (a) and wind-driven upwelling-downwelling pairing in the Gulf of Finland (b). (a): HW causes MHW (marine heat wave events) in the surface layer (SL), while the heat transfers into intermediate (IL) and bottom layers (BL) with gradually increasing salinity are restricted by thermocline (TCl) and pycnoclines (PCl). Coastal breeze mediates heat transfers between sea and land, also causing diurnal sea level variations (SLV) at the coast. (b): At the Estonian coast, easterly wind causes alongshore coastal jet (CJ), rise of pycnoclines, upwelling, and local SL lowering. Westerly would basically turn the scheme around (upwelling along Finnish coast and downwelling at Estonian coast); controlled by topography, Coriolis force and friction, the current patterns may be more complex basin-wise. Differing from the steady state (a), the simultaneous occurrence of HW and CU (or CUs slowly switching between opposing coasts) enable more effective heat transfer to the water mass (b).

Statistically, Kunda is slightly warmer than the 45 km inland Väike-Maarja station (5.7 vs. 4.9°C according to the EWS statistics). This is because Väike-Maarja is located 120 m higher than Kunda and considering environmental lapse rate, one can expect ca 0.8°C lower temperatures there. According to the comparison of air temperature differences between Kunda and Väike-Maarja stations, the cooling effect during the CU events compared to the rest of the studied period (Figure 10) was 0.9°C in terms of average temperatures and 1.5°C in daily maxima. More specifically, during the studied HW, Kunda was 1.2°C warmer than Väike-Maarja, while during HW and CU combined, the Kunda location was only 0.3°C warmer. In some CU days, instead of being 1°C warmer, the maxima at Kunda were up to 5 degrees lower than in Väike-Maarja (Figure 10). Such influence of cool nearshore currents is also known on a grander scale. For instance, cold Benguela current-affected Namib coast is climatologically ca. 3—5 degrees cooler than areas less than 100 km inland (Lancaster et al., 1984). The influence is similar in the case of the cold Humboldt current near the Chilean coast, however, without a very clear thermal pattern due to mountainous inland terrain.

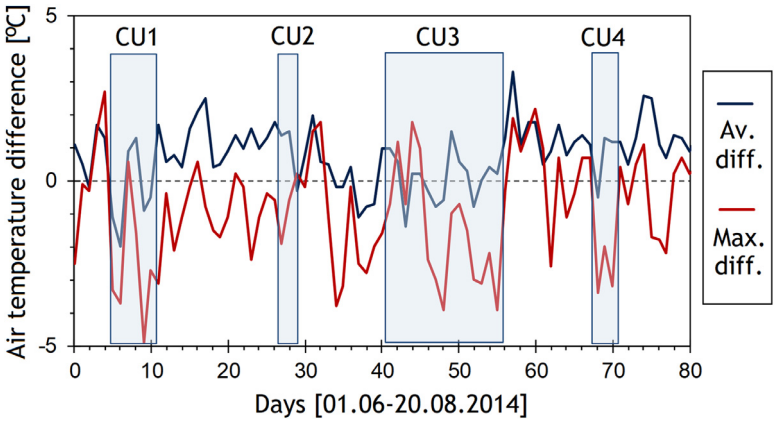

Figure 10 Temporal variations in air temperature differences between Kunda (coastal) and Väike-Maarja (inland) stations, showing cooling effect (i.e. larger negative differences) of CU events on Kunda's daily average (Av.) and maximum (Max.) air temperatures.

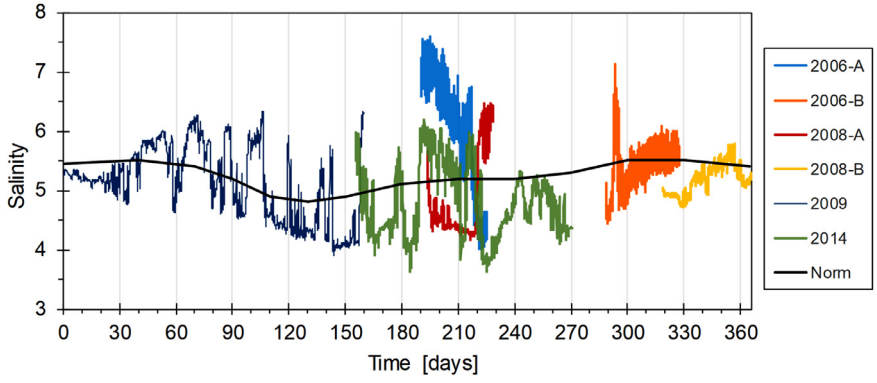

Figure 11 Salinity variations at Letipea according to RDCP measurements performed in different moorings (see also Suursaar, 2010; 2013) plotted against days in year. Always corresponding to CU events, the abrupt changes for 1–3 units mask the feeble seasonality in statistical norm (e.g. Alenius et al., 1998). Slightly higher maxima in 2006 partly occur as a result of slightly deeper mooring in that year (ca 11.5 m vs. ca 10.5 m).

Finally, the possible ecological effects of HW and CU on biota increasingly deserve attention. Generally, adverse effects of MHWs on biota are relatively well-known (Meier et al., 2019; Oliver et al., 2019; Panch et al., 2013). It is reasonable to assume that under global warming, HWs and MHWs are becoming more frequent and intense in different environments worldwide – at least relative to local climatic normals, but also in absolute terms. On a local scale, CUs may occasionally mitigate such overheating effects by cooling down the water mass (Figures 3, 9). However, CUs also serves as a nutrient pump, lifting up nutrient-rich water from the deep to surface, promoting thus productivity and triggering algal blooms (e.g. Jiang and Wang, 2018; Kononen and Nõmmann, 1992). Moreover, although introducing some variability, CUs cannot stop the overall basin-wide warming trends. Continuation of water temperature rise and intensification of MHWs in combination with CUs, causing abrupt changes in water temperature (e.g. Figure 3), salinity (e.g. Figure 11) and other interrelated parameters, put ecosystems under additional stress by challenging the established tolerance limits of species or entire communities (Paalme et al., 2020; Takolander et al., 2017; Wernberg et al., 2013).

4. Conclusions

(1) Summer 2014 HW (also called 2014 Swedish heat wave) manifested in the Gulf of Finland area by extraordinary high air and water temperatures. Air temperatures reached 32°C on 31 July and the daily normals were exceeded by 5°C at Kunda weather station (North Estonia) in several episodes lasting for 3, 5, and 7 consecutive days. At Narva-Jõesuu station, water temperatures stayed between 20 and 26.5°C during 44 consecutive days in July and August while at Kunda coastal station the MHWs were frequently interrupted by upwellings. Both HW and CU effects were captured by the RDCP measurements at Letipea Peninsula, lasting for 115 days from 6 June to 29 September 2014.

(2) Caused by a stable anticyclonic weather pattern and persisting E-winds, CUs evolved along the southern coast of the Gulf in four episodes (3–7.06, 26–29.06, 10–17.07, 5–7.08). Occurring on the background of a MHW, the maximum water temperature dropped by up to 17°C within a few days. At the 10 m deep RDCP mooring location, an 18.6°C drop (from 21.5 to 2.9°C) occurred within 60 hours on 3–5 August. In addition to up to

20°C variations in water temperatures, the CUs were also accompanied by salinity fluctuations between 3.6 and 6.2, and relatively fast West-directed alongshore current (coastal jet). The CU-related West current was especially favoured in upper layers and it was the statistically preferred current mood, which frequently flowed against the wind.

(3) In terms of local climate, the cooling effect of the CUs occasionally mitigated the overheating effects by HWs both in the sea and above the land (via breezes operating at the marine-land boundary). However, CUs cannot stop the overall basin-wide warming trends. In elongated channel-like basins like the Gulf of Finland, being major mixing agents, upwelling at one coast is usually paired with downwelling at the opposite coast. The simultaneous or subsequent occurrence of HWs and CUs effectively contributes to heat transfer from the atmosphere to the deeper water mass. Because heating of the water mass in the process of global warming begins from the sea surface and lags behind in the deeper layers, also thermal contrasts during CUs may increase in the future. Hence, rising extremes of HWs and rapid variations by CUs may increasingly put ecosystems under stress and trigger undesirable changes.

Acknowledgements

The study was financially supported by the Estonian Research Council grant PUT1439 and marine environment monitoring project LLOMI14064. We thank the EWS for the Estonian weather data and the Finnish Environment Institute (SYKE) for the SST images.

References

Alenius, P., Myrberg, K., Nekrasov, A., 1998. The physical oceanography of the Gulf of Finland: a review. Boreal Environ. Res. 3, 97—125.

Andrejev, O., Myrberg, K., Alenius, P., Lundberg, P., 2004. Mean circulation and water exchange in the Gulf of Finland — a study based on three-dimensional modelling. Boreal Environ. Res. 9 (1), 1—16.

Cheng, L., Abraham, J., Zhu, J., Trenberth, K.E., Fasullo, J., Boyer, T., Locarnini, R., Zhang, B., Yu, F., Wan, L., Chen, X., Song, X., Liu, Y., Mann, M.E., 2020. Record-setting ocean warmth continued in 2019. Adv. Atmos. Sci. 37 (2), 137—142. https://doi.org/10.1007/s00376-020-9283-7.

Cole, S., Jacobs, P., 2020. NASA, NOAA Analyses Reveal 2019 Second Warmest Year on Record. NASA Press Release 20-003, https://www.nasa.gov/press-release/nasa-noaa-analyses-reveal-2019-second-warmest-year-on-record, (accessed 22 May 2020).

Delpeche-Ellmann, N., Mingelaitė, T., Soomere, T., 2017. Examining Lagrangian surface transport during a coastal upwelling in the Gulf of Finland. Baltic Sea. J. Mar. Syst. 171, 21—30, https://doi.org/10.1016/j.jmarsys.2016.10.007.

Delpeche-Ellmann, N., Soomere, T., Kudryavtseva, N., 2018. The role of nearshore slope on cross-shore surface transport during a coastal upwelling event in Gulf of Finland. Baltic Sea. Estuar. Coast. Shelf Sci. 209, 123—135, https://doi.org/10.1016/j.ecss.2018.03.018.

Easterling, D.R., Meehl, G.A., Parmesan, C., Changnon, S.A., Karl, T.R., Mearns, L.O., 2000. Climate extremes: observations, modeling, and impacts. Science 289, 2068—2074.

Elken, J., Lehmann, A., Myrberg, K.The BACC II Author Team, 2015. Recent Change — Marine Circulation and Stratification. In: Second Assessment of Climate Change for the Baltic Sea Basin. Springer, Cham, 131—144, https://doi.org/10.1007/978-3-319-16006-1_7.

Frich, P., Alexander, L.V., Della-Marta, P., Gleason, B., Haylock, M., Klein Tank, A., Peterson, T., 2002. Global changes in climatic extremes during the 2nd half of the 20th century. Clim. Res. 19, 193—212, https://doi.org/10.3354/cr019193.

Gidhagen, L., 1987. Coastal upwelling in the Baltic Sea — satellite and in situ measurements of sea-surface temperatures indicating coastal upwelling. Estuar. Coast. Shelf Sci. 24 (4), 449—462.

Gill, A.E., Clarke, A.J., 1974. Wind-induced upwelling, coastal currents and sea-level changes. Deep-Sea Res. 21, 325—345.

Haapala, J., 1994. Upwelling and its influence on nutrient concentration in the coastal area of the Hanko Peninsula, entrance of the Gulf of Finland. Estuar. Coast. Shelf Sci. 38 (5), 507—521.

Hobday, A.J., Oliver, E.C.J., Sen Gupta, A., Benthhuysen, J.A., Burrow, M.T., Donat, M.G., Holbrook, N.J., Moore, P.J., Thomsen, M.S., Wernberg, T., Smale, D.A., 2018. Categorizing and naming marine heatwaves. Oceanography 31 (2) 162—173, https://doi.org/10.5670/oceanog.2018.205.

Hoegh-Guldberg, O., Bruno, J.F., 2010. The impact of climate change on the World's marine ecosystems. Science 328, 1523—1528.

EWS, 2020. Estonian Weather Service; http://www.ilmateenistus.ee/kliima/weather-events/?lang=en, (accessed 22 May 2020).

IPCC 2014. IPCC Fifth Assesment Report (AR5), https://www.ipcc.ch/report/ar5/.

Jiang, R., Wang, Y.-S., 2018. Modeling the ecosystem response to summer coastal upwelling in the northern South China Sea. Oceanologia 60 (1) 32—51, https://doi.org/10.1016/j.oceano.2017.05.004.

Kallis, A., Loodla, K., Tillmann, E., Krabbi, M., Pärg, R., Vint, K., Jõeveer, A., Juust, E., 2015. Yearbook of Estonian Meteorology 2014. Tallinn, 162 pp., (in Estonian), http://www.ilmateenistus.ee/wp-content/uploads/2016/02/aastaraamat_2014.pdf (Accessed on 22 May 2020).

Keevallik, S., Soomere, T., Pärg, R., Žukova, V., 2007. Outlook for wind measurement at Estonian automatic weather stations. Proc. Estonian Acad. Sci.-Eng. 13 (3), 234—251.

Keevallik, S., Vint, K., 2015. Temperature extremes and detection of heat and cold waves at three sites in Estonia. Proc. Estonian Acad. Sci. 64 473—479, https://doi.org/10.3176/proc.2015.4.02.

Kononen, K., Nõmmann, S., 1992. Spatio-temporal dynamics of the cyanobacterial blooms in the Gulf of Finland, Baltic Sea. In: Carpenter, E.J., Capone, D.G., Rueter, J.G., et al. (Eds.). In: Marine pelagic cyanobacteria: Trichodesmium and other Diazotrophs. NATO ASI Ser., vol. 362. Springer, Dordrecht, 95—113.

Kont, A., Jaagus, J., Orviku, K., Palginõmm, V., Ratas, U., Rivis, R., Suursaar, Ü., Tõnisson, H., 2011. Natural development and human activities on Saaremaa Island (Estonia) in the context of climate change and integrated coastal zone management. In: Schernewski, G., Hofstede, J., Neumann, T. (Eds.), Global change and Baltic coastal zones. Springer, Dordrecht 117—134, https://doi.org/10.1007/978-94-007-0400-8_8.

Kotta, J., Herkül, K., Jaagus, J., Kaasik, A., Raudsepp, U., Alari, V., et al., 2018. Linking atmospheric, terrestrial and aquatic environments in high latitude: Regime shifts in the Estonian regional climate system for the past 50 years. PLOS ONE 13 (12), art. no. e0209568, https://doi.org/10.1371/journal.pone.0209568.

Kowalewski, M., Ostrowski, M., 2005. Coastal up- and downwelling in the southern Baltic. Oceanologia 47 (4), 453—475.

Kowalewska-Kalkowska, H., Kowalewski, M., 2019. Combining

Satellite Imagery and Numerical Modelling to Study the Occurrence of Warm Upwellings in the Southern Baltic Sea in Winter. Remote Sens. 11 (24), art. no. 2982, https://doi.org/10.3390/rs11242982.

Lancaster, J., Lancaster, N., Seely, M.K., 1984. Climate of the central Namib Desert. Madoqua 14 (1), 5—61.

Lehmann, A., Myrberg, K., Höflich, K., 2012. A statistical approach to coastal upwelling in the Baltic Sea based on the analysis of satellite data for 1990—2009. Oceanologia 54 (3), 369—393, https://doi.org/10.5697/oc.54-3.369.

Lenssen, N.J.L., Schmidt, G.A., Hansen, J.E., Menne, M.J., Persin, A., Ruedy, R., Zyss, D., 2019. Improvements in the GISTEMP uncertainty model. J. Geophys. Res. Atmos. 124, 6307—6326, https://doi.org/10.1029/2018JD029522.

Liblik, T., Lips, U., 2019. Stratification has strengthened in the Baltic Sea — an analysis of 35 years of observational data. Front. Earth Sci. 7, art. no. 174, https://doi.org/10.3389/feart.2019.00174.

Lips, I., Lips, U., Liblik, T., 2009. Consequences of coastal upwelling events on physical and chemical patterns in the central Gulf of Finland (Baltic Sea). Cont. Shelf Res. 29, 1836—1847, https://doi.org/10.1016/j.csr.2009.06.010.

Meier, H.E.M., Dieterich, C., Eilola, K., Gröger, M., Höglund, A., Radtke, H., Saraiva, S., Wåhlström, I., 2019. Future projections of record-breaking sea surface temperature and cyanobacteria bloom events in the Baltic Sea. Ambio 48, 1362—1376, https://doi.org/10.1007/s13280-019-01235-5.

Miller, S.T.K., Keim, B.D., Talbot, R.W., Mao, H., 2003. Sea breeze: Structure, forecasting, and impacts. Rev. Geophys. 41 (3), 1—31, https://doi.org/10.1029/2003RG000124.

Myrberg, K., Andrejev, O., 2003. Main upwelling regions in the Baltic Sea — a statistical analysis based on three-dimentional modelling. Boreal Environ. Res. 8, 97—112.

Oliver, E.C.J., Burrows, M.T., Donat, M.G., Sen Gupta, A., Alexander, L.V., Perkins-Kirkpatrick, S.E., Benthuysen, J.A., Hobday, A.J., Holbrook, N.J., Moore, P.J., Thomsen, M.S., Wernberg, T., Smale, D.A., 2019. Projected Marine Heatwaves in the 21st Century and the Potential for Ecological Impact. Front. Mar. Sci. 6, art. no. 734, https://doi.org/10.3389/fmars.2019.00734.

Õispuu, T.-M., 2019. Heat waves in Estonia in 1951—2018. In: Järvet, A. (Ed.). Yearbook of Estonian Geographical Society, Vol. 44 Tallinn, 93—110, (in Estonian, English summary), http://egs.ee/wp-content/uploads/2019/12/EGS_Aastaraamat_44kd.pdf, (Accessed May 22, 2020).

Paalme, T., Torn, K., Martin, G., Kotta, I., Suursaar, Ü, 2020. Littoral benthic communities under effect of heat wave and upwelling events in NE Baltic Sea. J. Coast. Res., Spec. Issue 95, 133—137. https://doi.org/10.2112/SI95-026.1.

Panch, C., Scotti, M., Barboza, F.R., Al-Jaabi, B., Brakel, J., Briski, E., Bucholz, B., Franz, M., Ito, M., Paiva, F., Saha, M., Sawall, Y., Weinberger, F., Wahl, M., 2013. Heat waves and their significance for temperate benthic community: A near-natural experimental approach. Glob. Chang. Biol. 24, 4357—4367, https://doi.org/10.1111/gcb.14282.

Perkins, S.E., Alexander, L.V., 2013. On the measurement of heat waves. J. Clim. 26, 4500—4517, https://doi.org/10.1175/JCLI-D-12-00383.1.

Rafferty, J.P., 2020. Heat wave. Britannica online: https://www.britannica.com/science/heat-wave-meteorology, (accessed 22 May 2020).

Russo, S., Dosio, A., Graversen, R.G., Sillmann, J., Carrao, H., Dunbar, M.B., Singleton, A., Montagna, P., Barbola, P., Vogt, J.V., 2014. Magnitude of extreme heat waves in present climate and their projection in a warming world. J. Geophys. Res. Atmos. 119 (22), 12,500—12,512, https://doi.org/10.1002/2014JD022098.

Russo, S., Sillmann, J., Fischer, E.M., 2015. Top ten heatwaves since 1950 and their occurrence in the coming decades. Environ. Res. Lett. 10, art. no. 124003, https://doi.org/10.1088/1748-9326/10/12/124003.

Rutgersson, A., Jaagus, J., Schenk, F., Stendel, M., Bärring, L., Briede, A., Claremar, B., Hanssen-Bauer, I., Holopainen, J., Moberg, A., Nordli, Ø., Rimkus, E., Wibig, J.The BACC II Author Team, 2015. Recent Change — Atmosphere. In: Second Assessment of Climate Change for the Baltic Sea Basin. Springer, Cham, 69—97, https://doi.org/10.1007/978-3-319-16006-1_4.

Schlitzer, R., 2020. Ocean Data View, https://odv.awi.de.

Schär, C., Vidale, P.L., Lüthi, D., Frei, C., Häberli, C., Liniger, M.A., Appenzeller, C., 2004. The role of increasing temperature variability in European summer heatwaves. Nature 427, 332—336.

Shaltout, M., 2019. Recent sea surface temperature trends and future scenarios for the Red Sea. Oceanologia 61 (4), 484—504, https://doi.org/10.1016/j.oceano.2019.05.002.

Siegel, H., Gerth, M., 2019. Sea Surface Temperature in the Baltic Sea in 2018. HELCOM Baltic Sea Environment Fact Sheets 2019 https://helcom.fi/baltic-sea-trends/environment-fact-sheets/hydrography/sea-surface-temperature-in-the-baltic-sea-in-2018/, (accessed May 22, 2020).

Smid, M., Russo, S., Costa, A.C., Granell, C., Pebesma, E., 2019. Ranking European capitals by exposure to heat waves and cold waves. Urban Clim. 27, 388—402, https://doi.org/10.1016/j.uclim.2018.12.010.

Soomere, T., Myrberg, K., Leppäranta, M., Nekrasov, A., 2008. The progress in knowledge of physical oceanography of the Gulf of Finland: a review for 1997—2007. Oceanologia 50 (3), 287—362.

Strange, E., Fernando, H., 2001. Entrainment and mixing in stratified shear flows. J. Fluid Mech. 428, 349—386.

Suursaar, Ü., Aps, R., 2007. Spatio-temporal variations in hydro—physical and -chemical parameters during a major upwelling event off the southern coast of the Gulf of Finland in summer 2006. Oceanologia 49 (2), 209—228.

Suursaar, Ü., 2010. Waves, currents and sea level variations along the Letipea—Sillamäe coastal section of the southern Gulf of Finland. Oceanologia 52 (3), 391—416, https://doi.org/10.5697/oc.52-3.391.

Suursaar, Ü., 2013. Locally calibrated wave hindcasts in the Estonian coastal sea in 1966—2011. Est. J. Earth Sci. 62 (1), 42—56, https://doi.org/10.3176/earth.2013.05.

Takolander, A., Cabeza, M., Leskinen, E., 2017. Climate change can cause complex responses in Baltic macroalgae: A systematic review. J. Sea Res. 123, 16—26, https://doi.org/10.1016/j.seares.2017.03.007.

Talpsepp, L., 2008. On the influence of the sequence of coastal upwellings and downwellings on the surface water salinity in the Gulf of Finland. Estonian J. Eng. 14 (1), 29—41.

Uiboupin, R., Laanemets, J., 2009. Upwelling characteristics derived from satellite sea surface temperature data in the Gulf of Finland, Baltic Sea. Boreal Environ. Res. 14 (2), 297—304.

Westerlund, A., Tuomi, L., Alenius, P., Miettunen, E., Vankevich, R.E., 2018. Attributing mean circulation patterns to physical phenomena in the Gulf of Finland. Oceanologia 60 (1), 16—31, https://doi.org/10.1016/j.oceano.2017.05.003.

Westerlund, A., Tuomi, L., Alenius, P., Myrberg, K., Miettunen, E., Vankevich, R.E., Hordoir, R., 2019. Circulation patterns in the Gulf of Finland from daily to seasonal timescales. Tellus A 71, art. no. 1627149, https://doi.org/10.1080/16000870.2019.1627149.

Wernberg, T., Smale, D.A., Tuya, F., Thomsen, M.S., de Langlois, T.J., Bettignies, T., Bennett, S., Rousseaux, C.S., 2013. An extreme climatic event alters marine ecosystem structure in a global biodiversity hotspot. Nat. Clim. Chang. 3, 78—82, https://doi.org/10.1098/rspb.2012.2829.

Oceanologia (2020) 62, 525—537

Available online at www.sciencedirect.com

ScienceDirect

journal homepage: www.journals.elsevier.com/oceanologia

ORIGINAL RESEARCH ARTICLE

Dissolved oxygen variability in the southern Baltic Sea in 2013—2018

Daniel Rak[a,*], **Waldemar Walczowski**[a], **Lidia Dzierzbicka-Głowacka**[a], **Sergey Shchuka**[b]

[a] *Institute of Oceanology, Polish Academy of Sciences, Sopot, Poland*
[b] *Shirshov Institute of Oceanology, Russian Academy of Sciences, Moscow, Russia*

Received 7 May 2020; accepted 17 August 2020
Available online 26 August 2020

KEYWORDS
Inflows;
Cod;
Spermatozoa;
Physical variability;
Oxygenation

Summary This paper discusses changes in the dissolved oxygen concentration (DOC) in the southern Baltic Sea. The oxygenation of the whole water column was estimated. Monthly mean DOCs, as well as a detailed description of the annual surface layer dissolved oxygen (DO) cycle, are presented. The DO cycle at the surface is characterized by two maxima in March/April and November, and by two minima in July/August and December. The DO decline time after the major Baltic inflow (MBI) in 2014 was estimated at about 10 months for the Bornholm Deep and Słupsk Furrow. Whereas the Bornholm Basin was relatively well oxygenated, low oxygen concentrations (<4 mg l^{-1}) were measured in the deep layer of the Gdańsk Deep throughout the inflow period. In addition, the cod spermatozoa activation layer together with the neutral egg buoyancy layer for the Bornholm Basin and Słupsk Furrow are discussed on the basis of the measured DOCs and the variability in hydrographic conditions.

1. Introduction

Dissolved oxygen concentration (DOC) is an important property of sea water, affecting the structure and intensity of marine life. In the surface layer, the primary source of dissolved oxygen is air-sea exchange: this leads to near saturation of this layer. Oxygen in the marine environment is also derived from photosynthesis — primary production depends strongly on light availability and water temperature (Woźniak et al., 1989). Whereas the water in the upper layer is well oxygenated, the instantaneous DOC is subject to seasonal fluctuations. This results from the different solubility of oxygen at different temperatures and the seasonal inten-

* Corresponding author at: Institute of Oceanology, Polish Academy of Sciences, Powstańcow Warszawy 55, 81—712 Sopot, Poland.
E-mail addresses: rak@iopan.gda.pl (D. Rak), walczows@iopan.gda.pl (W. Walczowski), dzierzb@iopan.gda.pl (L. Dzierzbicka-Głowacka), s_shchuka@mail.ru (S. Shchuka).
Peer review under the responsibility of the Institute of Oceanology of the Polish Academy of Sciences.

Production and hosting by Elsevier

https://doi.org/10.1016/j.oceano.2020.08.005

sity of photosynthesis. One of the main processes responsible for the decline in the amount of oxygen is consumption by bacteria during the decomposition and mineralization of organic matter (Walker, 1980). In addition, oxygen is used by marine organisms during respiration, while chemical reactions involving oxygen, such as the oxidation of methane or ammonia, play an important role in its depletion.

The extent of oxygenation of sea water is also affected by its excessive eutrophication (Carlson, 1997). Enrichment of water with nutrients, especially phosphorus, nitrogen and carbon in the surface layer, results in elevated biological production (Jarvie et al., 2018). The very rapid growth of phytoplankton causes algal blooms and reduces water transparency. The accumulation of algae on such a massive scale increases the mortality not only of these organisms but of marine fauna as well. The descending transport of decomposing organic detritus to the sea bed increases oxygen consumption in the deep layers, and exhaustion of oxygen resources in the bottom layer leads to the disappearance of deep-sea fauna, including relict species. In addition, some fish cease spawning, as a result of which valuable species vanish.

The Baltic Sea is currently one of the largest dead zones in the world (Conley et al., 2009; Diaz and Rosenberg, 2008). Indeed, the extents of hypoxia and anoxia zones have been expanding in the Baltic Proper, the Gulf of Finland and the Gulf of Riga (Hansson and Andersson, 2016). The coverage of these zones increased from ca 5% between 1960 and 1995 up to ca 17% from 2000 to 2016. According to Meier et al. (2006), the decade-long stagnation periods without Major Baltic Inflows (MBIs), with decreasing oxygen and increasing hydrogen sulphide levels, may have been caused by large freshwater inputs and anomalously high zonal wind speeds. According to Mohrholz (2018), the main driver of the temporal and spatial spread of suboxic and anoxic conditions is most probably the increased eutrophication during the last century.

The varied bathymetry of the Baltic Sea severely hampers water exchange between its basins. Vertical water exchange is also limited: wind-driven and convective mixing are restricted by the pycnocline. The main processes ensuring water exchange in the deep layer of the Baltic Sea are the MBIs from the North Sea (Feistel et al., 2006; Fischer and Matthäus, 1996; Lass and Matthäus, 1996; Lehmann et al., 2004; Matthäus and Frank, 1992; Reissmann et al., 2009). Since 1983, an MBI has occurred once every 10 years (Dahlin et al., 1993; Jakobsen, 1995; Liljebladh and Stigebrandt, 1996; Matthäus and Lass, 1995; Mohrholz et al., 2015; Piechura and Beszczyńska-Möller, 2004; Rak, 2016). However, the only pathway along which inflowing highly saline and oxygen-rich water can enter the central and northern Baltic is the area of the Słupsk Furrow. Therefore, this region in the southern Baltic is extremely important as regards the hydrology and biology of the entire Baltic.

Depending on the type of forcing, one distinguishes between barotropic and baroclinic inflows. Barotropic inflows are forced by the difference in sea levels between the Baltic and the North Sea (Feistel et al., 2003; Fischer and Matthäus, 1996; Franck et al., 1987; Matthäus and Franck, 1992). One factor promoting the generation of major inflows is the decrease in river discharges (Schinke and Matthäus, 1998). Appearing mainly in autumn and winter, waters from barotropic inflows are rich in oxygen and salt. The weaker, baroclinic inflows are forced by the baroclinic pressure gradient (Feistel et al., 2003; Fischer and Matthäus, 1996; Franck et al., 1987; Matthäus and Franck, 1992) and usually occur in late summer. Those waters are also rich in oxygen, though less so than waters from barotropic inflows. Winter and spring inflows increase salinity and oxygen content, while reducing temperature in the bottom layers. Summer and autumn inflows increase salinity and temperature, but oxygen levels are lower. The main inflows were characterized by Matthäus and Franck (1992), who pointed out that inflows of medium or greater intensity occur much less frequently than weak intensity inflows.

Forming at the base of the surface layer, the dicothermal layer is specific to the Baltic Sea and to other seasonally ice-covered seas. It appears in spring, when the surface layer is warmed from above while the temperature of the layer beneath is still near freezing. On the other hand, the deep, bottom layer remains at ca 3–6°C, but because of its higher salinity is much denser than the layer above it. The dicothermal layer persists throughout the summer, ultimately disappearing only as a result of autumn convection. Because of the nature of its formation, this layer is also known as 'old winter water' or the *Cold Intermediate Layer (CIL)*.

All the above factors influence the complex spatial structure of DO in the Baltic Sea, which has a marked effect on marine life. Oxygen loss is increasingly being recognized as a major threat to marine ecosystems, altering habitat conditions in many parts of the global ocean (Oschlies, 2018). Hypoxia with a combination of reduced prey availability along with increased parasite burdens have contributed to a worsening Baltic cod (*Gadus morhua*) population status (Casini et al., 2016; Eero et al., 2015). Cod in the Baltic are assessed and managed as two distinct stocks. The eastern cod stock lives to the east of the island of Bornholm while the western stock inhabits the area from west of Bornholm to the Sound and the Danish Belts (Bagge et al., 1994). The differences between the two populations have been established by tagging, phenotypic and genetic programmes (Berner and Borrmann, 1985; Müller, 2002; Nielsen et al., 2005; Nielsen et al., 2003; Otterlind, 1985). However, the tagging programme indicates that the eastern and western stocks co-occur in the Arkona Basin (Aro, 1989; Nielsen et al., 2013). The eastern Baltic stock is about five times larger than the western one (Eero et al., 2015). Identification of the cod's spawning areas is based on ichthyoplankton surveys. However, two major problems crop up with this approach to identification. Firstly, the natural buoyancy layer may change as a result of salinity changes in the area. Quantitative sampling is therefore demanding, because it is impossible to sample close to the seabed, near the greatest concentration of eggs. Secondly, the distribution of eggs and early larvae can change or switch their spawning origin owing to the highly variable environmental conditions. Eastern Baltic cod utilize the deep basins (Bornholm Basin, Gdańsk Deep and Gotland Basin) as spawning habitats (Köster et al., 2001), but the most important spawning ground in the Baltic is in the Bornholm Basin (Bagge et al., 1994). Low salinity can

limit the fertilization of fish eggs by inhibiting the activation of spermatozoa (Hüssy, 2011). The minimum salinity required by Baltic cod differs between stocks, from S≥11—12 PSU in the eastern Baltic to S>15—16 PSU in the western Baltic (Nissling et al., 1994; Nissling and Westin, 1997). At lower salinities, the eggs will sink and fail to hatch (Westernhagen, 1970). Because of the low oxygen content at the depth where the eggs sink, the cod cannot reproduce. Superimposed on this primary driver, oxygen content and temperature have a significant effect on egg/larva development and survival. The whole spawning season for all stocks lasts for 6—7 months. However, peak spawning is limited to no longer than two months, with a pronounced trend towards progressively later spawning along a gradient from northwest to east (Bleil et al., 2009; Vitale et al., 2008). The cod in the Kattegat are the first to start spawning, peaking in January/February (Vitale et al., 2005). In the Bornholm Basin, cod spawning peaks in July/August (Bleil et al., 2009; Wieland et al., 2000). Generally, small fish are rather stationary, whereas adult cod migrations are associated with spawning (Rose et al., 2018).

The aim of this study was to describe the recent variability of DO in southern Baltic sea water. The locations of the study area were chosen because of their significance for the hydrography of the entire Baltic, especially under the influence of MBIs. MBIs transport large amounts of DOC into the Baltic: as Mohrholz et al. (2015) pointed out, the total amount of oxygen transported into the Baltic during MBI 2014 was estimated at 2.04×10^6 t. It takes approximately 30 years for the Baltic Sea waters to be fully exchanged (Stigebrandt, 2001). However, no direct calculations about the time scale of the impact of MBI on DO have been performed to date. We therefore investigated this impact in the deepest regions of the Bornholm Basin, Słupsk Furrow and Gdańsk Deep. The two MBIs in 1976 were responsible for the greatest landings of cod ever recorded in the Baltic (Matthäus et al., 2008). Accordingly, the link between MBIs and cod reproduction is unquestionable. Therefore, based on the findings of this work as well as on the critical values of physicochemical parameters for cod egg fertilization and survival, we assessed the cod fertilization layer as well as the egg neutral buoyancy layer in the basins surveyed. Finally, we examined the changes in those layers under the influence of MBIs.

2. Methodology

2.1. Study area

With a total surface area of 420 000 km^2, the Baltic is one of the largest brackish water bodies in the world. However, this large sea is relatively isolated from the ocean. The only connection with the North Sea is through the Sound and the Belt Seas. Bringing oxygen and salt, saline waters enter the Baltic mainly during winter storms, thereby improving oxygen conditions in the Baltic deeps. The freshwater input to the Baltic from rivers corresponds to about one fortieth of the total water volume per year (Bergström et al., 2001). This complex hydrological situation creates a characteristic brackish water gradient: whereas the surface salinity is about 15—18 PSU in the Sound, it falls to 7—8 in the Baltic Proper and to 0—3 in the Gulf of Finland. The upper fresher and deep saline waters are separated by a halocline. Simultaneously, the strong halocline coincides with the pycnocline, which limits the vertical range of wind mixing and convection (Feistel et al., 2006; Lehmann et al., 2004; Matthäus and Franck, 1992; Matthäus and Lass, 1995; Reissmann et al., 2009).

This paper focuses on three areas in the southern Baltic Sea: the Bornholm Basin (BB), the Słupsk Furrow with the Słupsk Sill (SF), and the Gdańsk Deep (GD). These areas are distinguished by the 70 m isobath (Figure 1). They are also delimited by longitude: BB — 15° and 16.35°; SF — 16.76° and 17.95°; GD — 18.37° and 19.28°.

Situated to the north-east of the island of Bornholm, the Bornholm Basin is connected to the Arkona Basin via the Bornholm Gate. Oxygen-rich, inflowing waters can move through the Bornholm Gate towards the Bornholm Deep. The shallow Rønne, Odra and Orla banks restrict the advection of saline water on the southern side. On the eastern side, the route for MBIs flowing in from the Bornholm Basin is towards the Słupsk Furrow. These areas are separated by a 50 m deep threshold known as the Słupsk Sill.

An elongated, parallel-sided basin with an asymmetrical cross-sectional shape, the Słupsk Furrow has a total length of ca 115 km and a width of 25 km. The greatest depth of the furrow is about 90 m. The Słupsk Furrow is limited by two thresholds: the Western and Eastern Słupsk Sills. The Słupsk Furrow is a highly dynamic area and, because it provides a transit for inflow waters, is decisive for the hydrography of the entire Baltic Sea.

The Gulf of Gdańsk and the Gdańsk Deep form the Gdańsk Basin, the greatest depth of 115 m being in the central part. The Gdańsk Basin is separated from the Słupsk Furrow and Gotland Basin by an 85 m deep diagonal sill. Both models and measurements indicate that the Gdańsk Deep does not actively participate in the inflow of waters to the deep areas of the Baltic Sea, but acts as a buffer (Elken, 1996; Jankowski and Livingstone, 2003).

2.2. Field Data

The hydrographic data used in this paper were obtained by the Institute of Oceanology, Polish Academy of Sciences (IO PAN) and the Institute of Oceanology, P.P. Shirshov Russian Academy of Sciences (IO RAN).

IO PAN used towed CTD (Conductivity, Temperature, Depth) and Oxygen probes to acquire high-resolution transect records along the main profile in the southern Baltic (Rak and Wieczorek, 2012). This transect runs along the main axis of the deep basins in the southern Baltic, from the Bornholm Basin through the Słupsk Furrow to the Gdańsk Deep (Figure 1). The data were collected during regular cruises of r/v *Oceania* in 2013—2017 (Table 1). A total of 15 transects with over 12 000 casts were recorded. The spatial resolution of measurements was ca 200—500 m in the horizontal and 3 cm (30 measurements per metre) in the vertical.

IO RAN used a moored Aqualog System (Ostrovskii, 2013) located at 55°12.7'N 16°41.2'E to gather data on the eastern slope of the Słupsk Sill (Figure 1). The mooring was redeployed during three expeditions in order to maintain continuity of measurements. The record started on 12 May 2016 and ended on 13 May 2017. This long-term, continuous

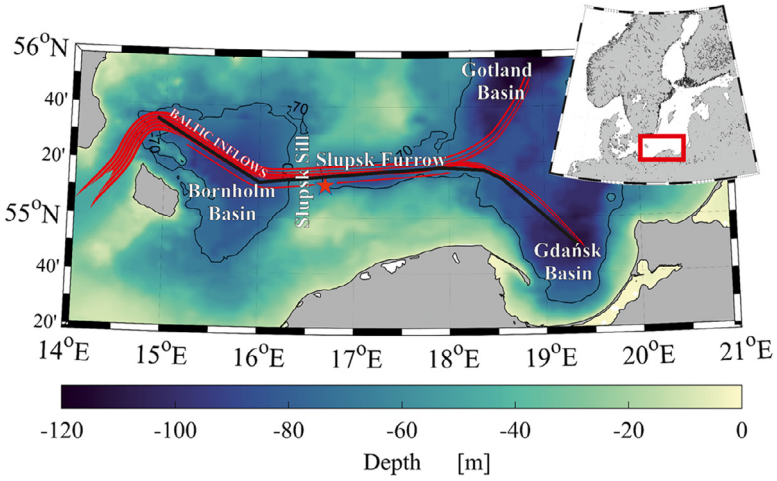

Figure 1 Location of measurements in the southern Baltic Sea. The solid black line represents the main course taken by r/v *Oceania*, and the star shows the position of the Aqualog. The red lines indicate the routes taken by MBIs.

Table 1 Specification of measurement methods.

Platform	Data measurement period (dd.mm.yyyy)	Sensors used		Data acquisition type
		CTD	DO	
r/v *Oceania*	03 04.01.2015, 02–03.01.2017; 24–26.02.2015; 01–03.03.2013; 22–26.04.2013; 22–24.05.2016, 11–14.05.2017; 12–13.09.2016; 09–13.10.2013, 09–12.10.2014, 01–04.10.2015; 26–29.11. 2014, 26–27.11.2015, 22–25.11.2016; 09–12.12. 2013;	SBE 49 FastCAT	JFE Advantech Rhinko probe	Towed probe
Argo float	06.02.2018–18.07.2018;	SBE 41	AANDERAA OPTODE 4330	Autonomous floats
Aqualog	12.05.2016–13.05.2017;	SBE 19plus	SBE 43F sensor	Moored system

vertical profiling system gathered hydrographic information about CTD and DO from the water column from 15 m below the sea surface to 68 m depth (3 m above the seabed). The temporal resolution of this system was about 2 hours, the time taken by Aqualog to move down to the end of the wire and back up to its original position.

The third type of data came from the autonomous profiling Argo float (Argo, 2018). This was set up by IO PAN in the Bornholm Basin on 6 February 2018. For the next five months, the float measured CTD and DO in the southern Baltic. The deployment position and trajectory are shown in Figure 2. The autonomous float spent most of the time drifting at the parking depth about 60 m. The float performed a full profile from bottom to surface every 2 days, while at the surface it transmitted data via satellites and determined the geographic position of the unit. The vertical resolution of the transmitted data was 1 m. The first measurements by the Argo floats in the Baltic were performed by Finnish oceanographers in the Bothnian Sea (Haavisto et al., 2018) and in the Gotland Deep (Siiriä et al., 2019). The IO PAN experiments proved the usefulness of Argo floats for the monitoring in the Southern Baltic.

The raw data collected from r/v *Oceania* was averaged into 0.5 m vertical layers, the data collected from Aqualog into 1 m layers. For the analysis, the data was gridded in Matlab into fixed vertical and horizontal layers. Data averaged into 1 m layers were used for the seasonal analysis of the DO cycle. To study the variability of the CIL, the halocline and thermocline depths were determined by the maximum temperature and salinity gradient in the water column. The spermatozoa activation layer and natural buoyancy layers were determined on the basis of critical values for salinity and DO (Hüssy, 2011). The spermatozoa activation layer was established for salinities of 11 PSU or higher with a minimum DOC of 5 mg l^{-1}. The natural buoyancy layer was located for a salinity of 14.5+1.2 PSU and a DOC of 2 mg l^{-1}. The critical DOC for egg survival during incubation is 2 mg l^{-1}.

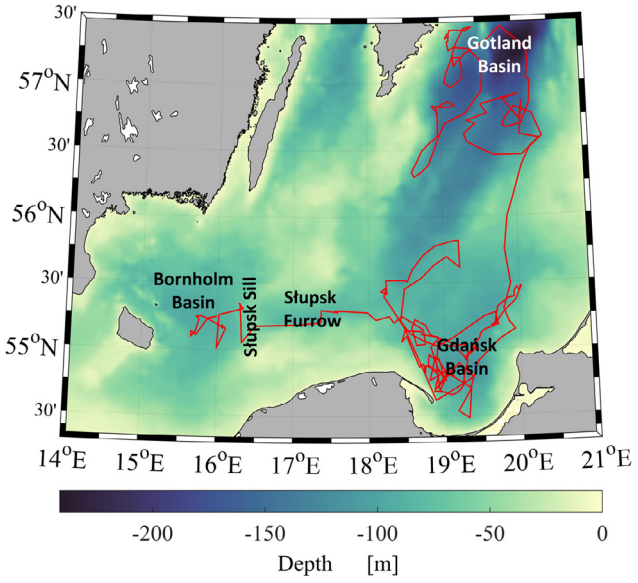

Figure 2 Deployment position and trajectory of the Argo float in the southern Baltic Sea. The float was launched in the Bornholm Basin in February 2018.

3. Results

3.1. Spatial variations in DO stratification

The highest DOCs in the Bornholm Basin, Słupsk Furrow and Gdańsk Deep are found in the surface layer (Figure 3): they are no greater than 14.5 mg l^{-1}. The upper layer is relatively homogeneous with a standard deviation of DO up to 2 mg l^{-1}. DO variation in the upper layer (ca 55 m thick) is due to large fluctuations of water temperature, which affect oxygen solubility, and to the seasonality of oxygen production during photosynthesis. The oxygen content in the oxycline is ca 8 mg l^{-1} less, and the thickness of this layer is determined by the position of the upper boundary of the halocline with respect to the seabed. The range of changes as well as the content of dissolved oxygen in the deep waters of the Baltic Proper depend directly on the advection of dense, saline waters from the North Sea. Both the DOC in the bottom layer and its variability decrease with distance from the Danish Straits. The oxygen content in the 25 m-thick deep layer of the Bornholm Basin is ca 4 ± 3 mg l^{-1} (Table 1); the oxygenation of this layer takes extreme values, from relatively well oxygenated to anoxic. The Słupsk Furrow is fairly well oxygenated for most of the time, but periodically, the less well oxygenated waters contain ca 2.6 mg l^{-1} of dissolved oxygen. In the Gdańsk Deep, poor oxygenation (< 4 mg l^{-1}) is the rule: there, the average oxygen content within the ca 20 m-thick bottom layer is 2 ± 1 mg l^{-1}.

The annual changes in DOCs are presented as monthly averages along the main axis of the deep basins in the southern Baltic Sea (Figure 4). Because of the insufficient number of surveys, the transects from June to August are not shown. Generally, the vertical DO distribution reflects the salinity pattern (dashed blue line). Therefore, two layers of DO, separated by the steep oxycline, can normally be distinguished. In the upper layer, DO also seasonally reflects temperature changes (solid red line): owing to the greater impact of the CIL on the oxygen content, a three-layered structure of DO then becomes recognizable. From January to May there is almost homogeneous oxygenation of the upper layer. As the oxygen content decreases with increasing temperature, the lowest annual oxygen content in the measured time series was in September and October, as the summer months are missing from the dataset. Moreover, when oxygenation of the upper layer is at a minimum, greater vertical gradients of DO are noticeable at a depth of 50 ± 10 m. The lower temperature of the dicothermal layer in the surrounding water causes differences in the oxygen content. The least oxygenation of the CIL can be expected in the vicinity of the Danish Straits and increases with distance towards the deeps of the Baltic Sea. After November, with increasing DOC, the upper layer becomes homogeneous. The maximum oxygen concentration in the upper layer in March/April reaches ca 14 mg l^{-1}. Further oxygenation of the upper layer and the penetration of oxygen into the deeper layer closes the annual cycle.

The dense waters of the Baltic Sea below the halocline (50–60 m) are isolated from the sources of oxygen: therefore, anaerobic conditions often prevail in the deep basins. Only the advection of dense, well-oxygenated water can transport oxygen efficiently into the deepest basins. Some of the results presented here were obtained during the 2015 inflow, which affected the conditions in the deep layer of the Bornholm Basin. From January to March, DOC in this re-

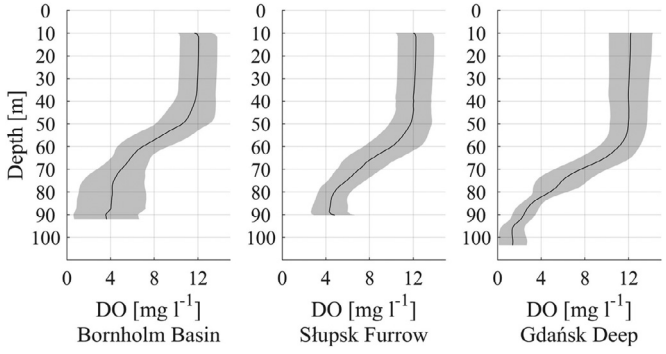

Figure 3 The average, long-term oxygen content with associated standard deviation in the Bornholm Basin, Słupsk Furrow and Gdańsk Deep.

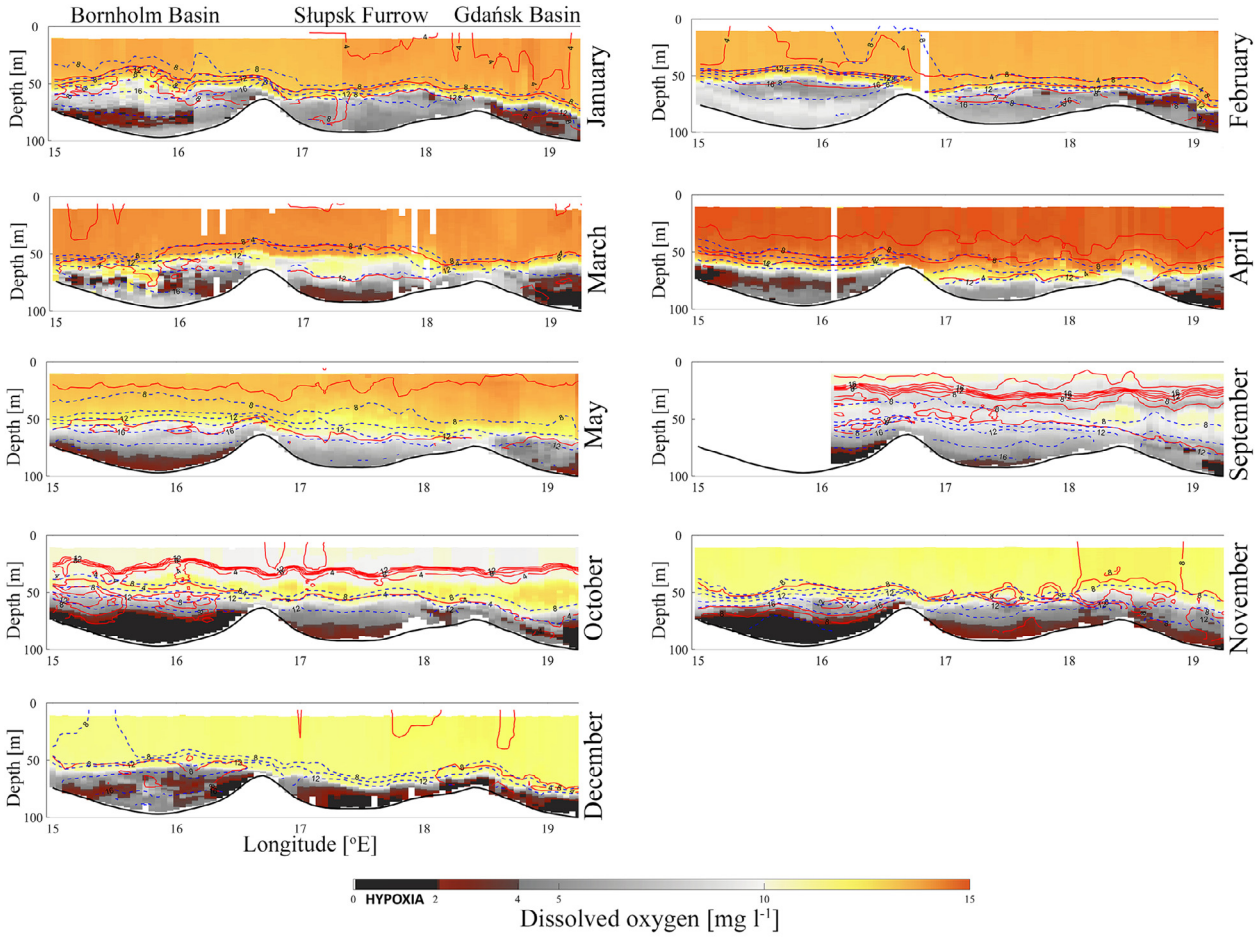

Figure 4 Monthly distributions of dissolved oxygen along the main transect in 2013–2017. Based on data from 2 cruises in January, 1 each in February, March and April, 2 in May, 1 in September, 3 in October, 3 in November and 1 in December. Temperature (solid red line), salinity (dashed blue line).

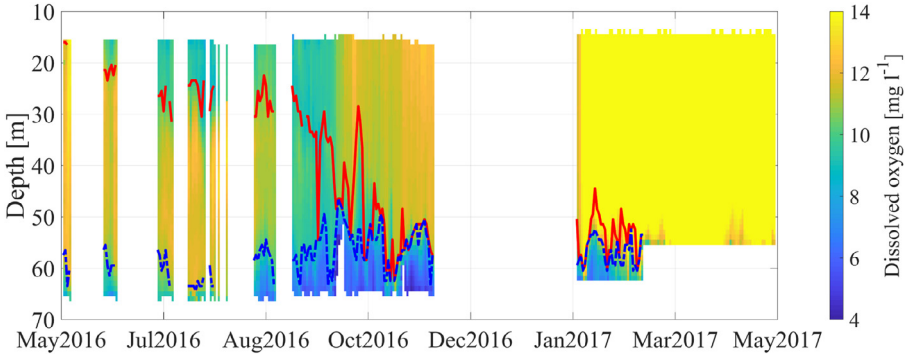

Figure 5 The Aqualog system measurements 12 May 2016–13 May 2017. Thermocline (red line), halocline (blue line).

gion was thus very high, > 8 mg l^{-1} (Figure 4). As shown in the previous section, the average for the Bornholm Basin is ca 5 mg l^{-1}.

3.2. DO and CIL transformation

The transformation of the CIL with respect to DOC in the southern Baltic is shown in Figures 5 and 6. Although the CIL forms in winter, it is most noticeable in summer, when the remnants of cold winter water become covered by warmer surface water. The thermocline, the upper limit of the CIL, starts to form in May/June and persists until late November/December. The CIL slowly erodes by mixing with warmer, overlying waters. Therefore, the maximum value of the temperature gradient slowly falls at a rate of ca 10 m depth per month, reaching the halocline in winter. Winter storms align the temperature in the upper layer and thus

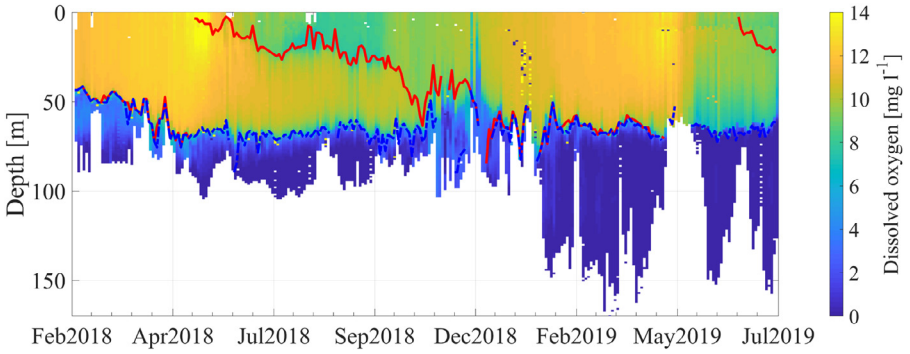

Figure 6 Argo float measurements from 6 February to 18 July 2018. Thermocline (red line), halocline (blue line).

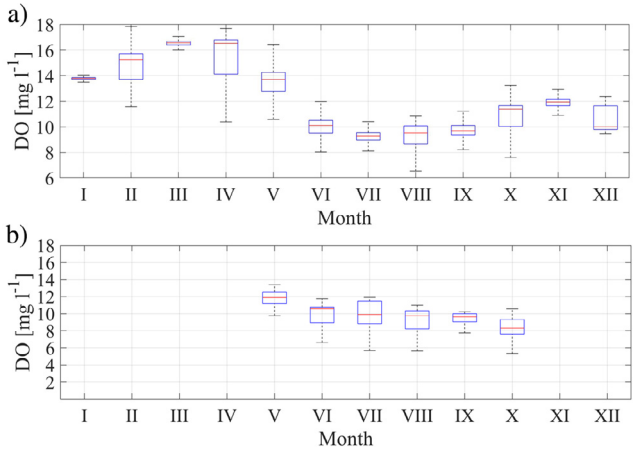

Figure 7 Seasonal DO in the 0–20 m layer (upper plot) and in the CIL (lower plot) in the southern Baltic Sea. The results for 2013–2018 were obtained during cruises of r/v *Oceania*, from the Aqualog mooring system and from Argo float data.

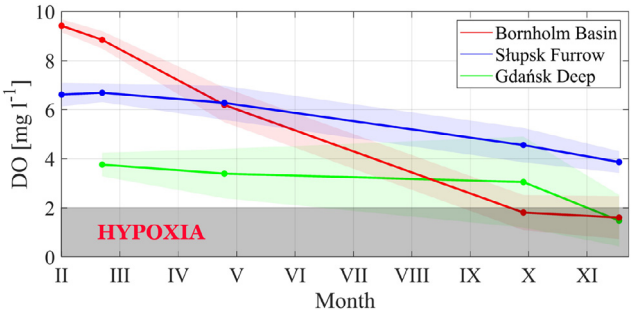

Figure 8 Dynamics of DO decline after MBI 2014, measured in 2015 (average DO below 70 m depth in the Bornholm Basin, Słupsk Furrow and Gdańsk Deep). The shaded areas indicate standard deviations.

close the annual CIL cycle. The halocline, the lower limit of the CIL, lies at about 55 m depth. The upward and downward movement of the halocline is associated with near-bottom advection, so variation in the vertical can reach up to 15 m.

The seasonal changes in DO in the southern Baltic are presented as the average for the 0–20 m layer and for the CIL (Figure 7). Surface water oxygenation (upper plot) peaks in March/April. Having achieved this spring maximum, the oxygen in the water column is then systematically consumed until the first oxygenation minimum is reached in July. With falling temperatures, the oxygen content again rises continually to the second maximum in November, after which it again drops to a minimum in December, thus closing the annual DO cycle in the southern Baltic.

At the depth of the CIL (lower plot), the oxygen content differs from that in the surface layer. The differences arise during the warmest months, when the first minimum is reached at the surface. The difference in DOC between the surface layer and CIL can be as high as 4 mg l^{-1} in summer. In the CIL, moreover, there is a constant decrease in DOC with only one maximum (May) and minimum (October). As a result of mixing and diffusion at the upper and lower limits of the CIL, a decrease in DOC can be expected. DO is transported from the edge of the CIL (ca 10 m depth) to the upper and lower layers. The CIL thus acts as a reservoir of oxygen for the less oxygenated layers.

3.3. Influence of inflows on deep layer oxygenation

The average DOC and its standard deviation were calculated in order to estimate the changes in DO after MBI 2014. Figure 8 shows the temporal evolution of DO in the layer below 70 m depth for three areas in the Baltic Proper. The highest values (ca 9.5 mg l^{-1}) were recorded in January/February 2015 in the Bornholm Basin. The monthly DO decrease in this region was ca 1 mg l^{-1}. Thus, just 10 months from the beginning of the inflow, anoxic conditions returned to the layer below the halocline. In the Słupsk Furrow, the decrease in DO was slightly slower: this depletion took 11 months, and the lowest oxygen concentration in this region was ca 4 mg l^{-1}. However, during the entire inflow period, low DO water was not expelled from the deep layer of the Gdańsk Deep. In the intermediate layer (the upper value of STD in the figure), at a depth of ca 70 m, the oxygen content increased slightly to ca 4.8 mg l^{-1}.

Figure 9 compares the temperature and salinity of MBI 2014 (recorded in January and May 2015) with the corresponding values for the weak inflows in November 2014 and 2016. Overall, MBIs are characterized by a higher density and lower temperature than baroclinic inflows. However, the temperatures of the inflows depend on the season in which they occur. During MBIs, higher DOCs are measured

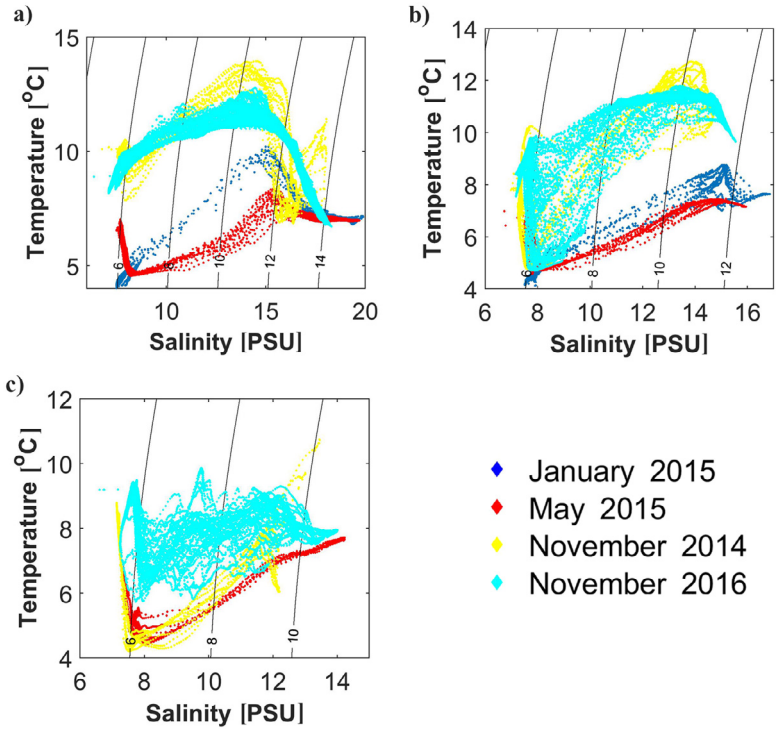

Figure 9 Comparison of the TS diagrams for MBI 2014 recorded in January and May 2015 with the weak inflows recorded in November 2014 and 2016. The figures represent the Bornholm Basin (a), Słupsk Furrow (b) and Gdańsk Deep (c).

in the deepest layers in Bornholm Deep and Słupsk Furrow (Figure 10).

During November 2014 and 2016, intrusions of warm waters below the halocline were recorded in the Bornholm Basin. Having passed the Słupsk Sill, they sank to the sea bed. The sinking was accompanied by increased mixing, so the lower limits of the transition layers (thermocline/oxycline) reached 75 m depth in the Słupsk Furrow (Figure 10). In the Gdańsk Deep the upper limit of the oxycline lay at 47–57 m, the lower one at 74–83 m.

3.4. Cod spermatozoa activation and natural buoyancy layers

A very interesting aspect is the possible effect of DO on the eggs of Baltic cod. Based on the mean salinity and mean DO data from 2013–2017 along the main axis in the southern Baltic, we were able to distinguish the Baltic cod's egg fertilization (Figure 11) and neutral egg buoyancy layers. The spermatozoa activation layer lay at 52–73 m depth in the Bornholm Basin and 62–81 m in the Słupsk Furrow. Conditions in the Gdańsk Deep were not appropriate for spermatozoa activation.

After fertilization, the egg enters the optimum depth determined by its neutral buoyancy. The neutral egg buoyancy layer in the Bornholm Basin lies within the range of the spermatozoa activation layer. However, in the Słupsk Furrow, a fertilized egg can sink to reach the optimum buoyancy depth.

The spermatozoa activation and neutral egg buoyancy layers overlap in the Bornholm Deep throughout the measurement period (Figure 12). In the Słupsk Furrow, these layers are sometimes separated: eggs can be fertilized in the transition layer but will sink to the deeper layers. If the oxygen conditions are suitable, cod eggs will survive in the deep water of the Słupsk Furrow. For most of the time, however, conditions in the Gdańsk Deep do not ensure cod egg survival there. Stronger advection can bring saline, oxygenated waters to this region, which will guarantee the existence of the spermatozoa activation and neutral buoyancy layers. After MBI 2014, these layers were separated in the Gdańsk Deep.

4. Discussion

This paper characterizes oxygen variability in the three basins of the Baltic Proper: the Bornholm Basin, Słupsk Furrow and Gdańsk Deep. It describes the average DO in those basins and the monthly distributions of DOC along the main transect. This paper estimates the time scale of the DO change after an MBI. Finally, the spermatozoa activation layer as well as the natural buoyancy layer of the Baltic cod has been determined. The analysis is based on measurements of CTD and DO performed during regular cruises of r/v *Oceania* across the Baltic in 2013–2017, the moored Aqualog system (2016–2017) and the autonomous Argo float deployed in 2018. This is the first time that changes in DO have been estimated for an Baltic inflow period. This research is also the first attempt to estimate the depth that meets the conditions required for the survival of cod eggs in the early stages of their existence.

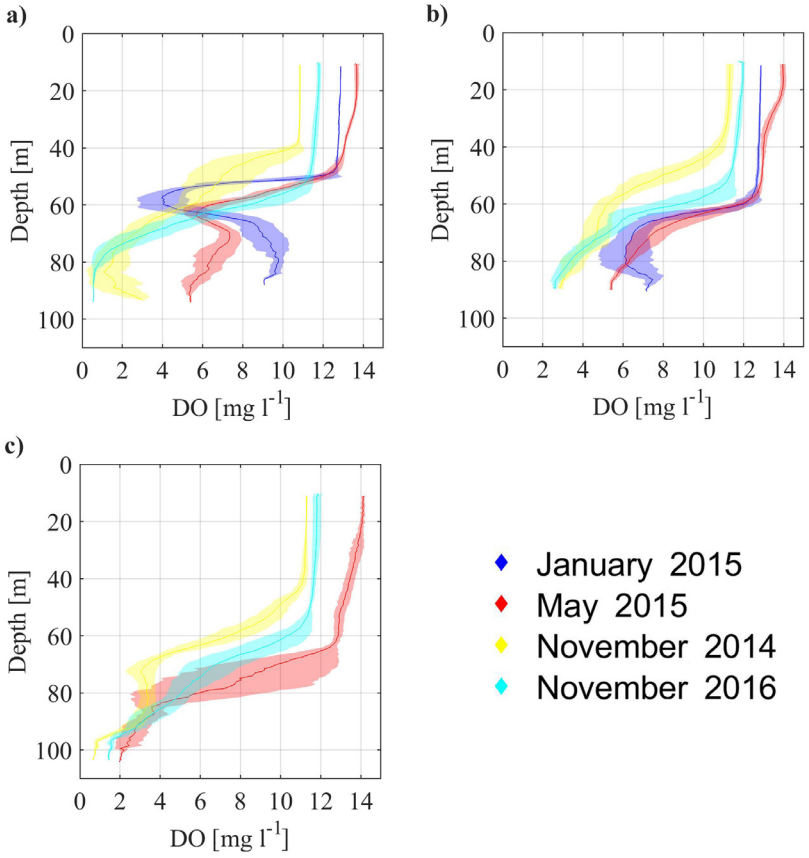

Figure 10 Comparison of DO during MBI 2014 recorded in January and May 2015 with the weak inflows recorded in November 2014 and 2016. The figures represent the Bornholm Basin (a), Słupsk Furrow (b) and Gdańsk Deep (c).

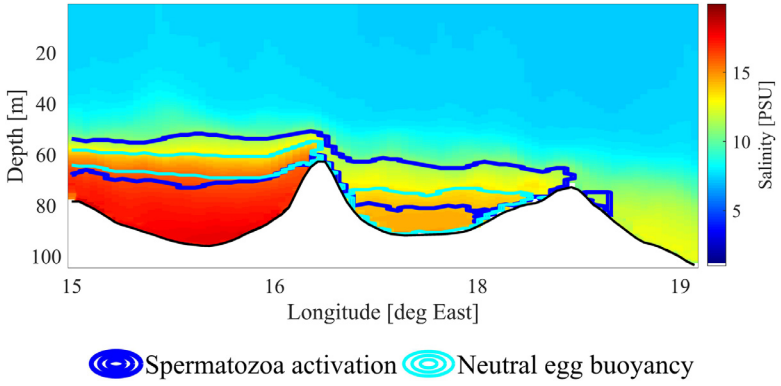

Figure 11 Cod spermatozoa activation layer (dark blue lines) and the neutral egg buoyancy layer (light blue lines) along the main axis in the southern Baltic Sea.

4.1. DO variability in the southern Baltic Sea

Steep spatial gradients and DO stratification occur in the deeper layers of the Baltic Sea. The stratification of DO in the southern Baltic reflects the salinity distribution. One can therefore recognize a two-layered structure: an upper (euphotic) zone and a lower one, separated by the oxycline. However, the DO distribution partly reflects the temperature pattern, just as it reflects the salinity field, so a seasonally three-layered DO structure occurs.

The highest oxygen content is in the layer in contact with the atmosphere, where photosynthesis also takes place. As this layer is relatively homogeneous to the depth of the oxycline, a seasonal DO cycle is distinguishable in the surface layer of the southern Baltic. This cycle has two maxima and two minima. The first DO maximum, occurring in spring, is related to the increased rate of photosynthesis at this time (Renk, 1974; Woźniak, 1989). There are variants when the first maximum appears in March or April. The second maximum falls in November. The first minimum falls in

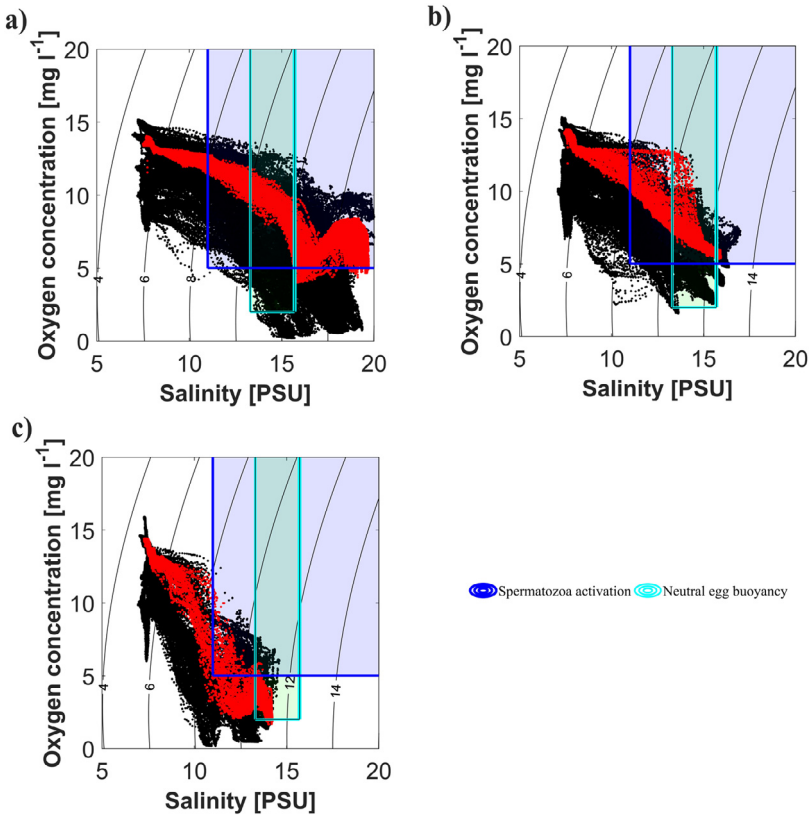

Figure 12 OS diagrams for the Bornholm Basin (a), Słupsk Furrow (b) and Gdańsk Deep (c). The red dots represent the MBI, May 2015.

July/August, and the second in December, closing the annual cycle of oxygenation changes of the surface layer.

The CIL has a great impact on the DO structure in the southern Baltic. Owing to the greater solubility of oxygen in colder waters, the CIL is a reservoir of oxygen for the less oxygenated upper and lower layers. Furthermore, steady decreases of oxygen are recorded in the CIL from May to October. The smallest thickness of the CIL can be expected in the vicinity of the Danish Straits. Moving from the Straits towards the deeps of the Baltic, the thickness of the CIL increases. Therefore, a greater DO content in this layer can be expected in the Gdańsk Basin than in the Bornholm Deep.

4.2. DO variability in the near-bottom layer

Below the halocline, where dense waters are separated from the direct source of oxygen, one of the main processes capable of transporting oxygen into the Baltic deep waters is advection. Therefore, one can expect the greatest oxygenation of the deep layer to be in the vicinity of the Danish Straits. The oxygenation of the near-bottom layer in the Bornholm Basin takes extreme values, from relatively well oxygenated during inflow periods to anaerobic during stagnation periods. Monitoring data (Mohrholz, 2018) indicate, however, that during stagnation periods before and after MBI 2014, oxygen in the Bornholm Deep increased several times. With increasing distance from the Straits, oxygenation of the deep waters decreases. In the Gdańsk Deep, where advection is severely limited by the Słupsk Sill, oxygen-deficient conditions (< 4 mg l^{-1}) are permanent.

4.3. Water oxygenation during inflows

The greatest volume of oxygen pushed into the Baltic's deepest basins originates from barotropic inflows. With a total saline water volume of 198 km^3, MBI 2014 transported 2.04×10^6 t of oxygen into the Baltic (Mohrholz et al., 2015). Two months after the inflow, DOC in the Bornholm Basin was ca 9 mg l^{-1}, while in the Słupsk Furrow it was ca 7 mg l^{-1}. However, 9 months after the start of the inflow, anaerobic conditions (2 mg l^{-1}) returned to the deep layer of the Bornholm Basin and 10 months later to the Słupsk Furrow (< 4 mg l^{-1}). Moreover, despite the large volume of MBI 2014, oxygen-deficient conditions persisted in the Gdańsk Deep.

The very high rate of oxygen consumption in the anaerobic layers in the Baltic Proper after MBI 2014 can be explained by biological production, which used up the newly supplied oxygen. Oxygen is also consumed during the decomposition of dead organisms. With declining oxygen, phosphorus is released from the sediments (Stigebrandt and Kalén, 2013) and transported to the upper layers (Viktorsson et al., 2012), thus stimulating biological production and consequently intensifying oxygen consumption in the bottom layer.

The advection of dense MBI waters in the Baltic propagates them over the seabed. The inflow volume of ca

198 km^3 and mixing processes enhanced the oxygenation of the bottom layer. An exceptional feature of the last inflow was the mixing of three water masses in the Bornholm Basin: the MBI waters, the warm intrusion and the waters previously occupying the Bornholm Deep. The MBIs in December 2002 (Meier et al., 2004) and 2014 (Rak, 2016) were preconditioned by weaker inflows. Those inflows moved some way towards the Słupsk Sill and partially mixed with anoxic deep waters in the Bornholm Deep. The inflow in the Bornholm Deep therefore took the form of intrusions as a result of being pushed upwards by the MBI. Thus, in January and February 2015, a warm, poorly oxygenated layer was recorded above the deep, well-oxygenated water in the Bornholm Basin.

The advection of weaker inflows propagates in the form of an intrusion, raising the oxycline and halocline in the Bornholm Basin; the movement of inflow waters over the Słupsk Sill was thus possible. This warm, relatively well-oxygenated intrusion passed the Słupsk Sill and sank. The sinking was accompanied by increased mixing, so the lower limit of the transition layer (oxycline) extended to 75 m depth in the Słupsk Furrow.

Advection of DO during an MBI leads from the deep layer of the Bornholm Basin to the Słupsk Furrow. During weaker inflows, DO advection extends from the intermediate layer in the Bornholm Basin.

4.4. Baltic cod spermatozoa activation and natural buoyancy layers

Dissolved oxygen and the requisite salinity in the sea are important requirements for survival. For the Baltic cod, oxygen is necessary from the early stages of its life. In order to begin spawning, the physical properties of the water have to match the cod's requirements. In the Bornholm Basin the critical salinity for spermatozoa activation is S>11–12 PSU (Nissling and Westin, 1997). Neutral egg buoyancy is maintained at ca 14.5±1.2 PSU. During incubation, cod eggs can survive when DOC $>$ 2 mg l^{-1} (Rohlf, 1999; Wieland et al., 1994). However, at DOC $<$ 5 mg l^{-1} the cod stock begins to decline (Köster et al., 2005). In the Bornholm Basin the waters enabling spermatozoa activation lie in a 21 m-thick layer at an average depth of ca 62 m, while in the Słupsk Furrow they are in a 19 m-thick layer at an average depth of 71 m. The differences between the lower limit of the spermatozoa activation layer in the Bornholm Basin and the Słupsk Furrow results from the deep layer DO conditions. After fertilization, the egg enters the optimum depth determined by its neutral buoyancy. In the Bornholm Basin the neutral buoyancy layer (65±5 m) lies within the spermatozoa activation layer. However, in the Słupsk Furrow, fertilized eggs can be found at depths from 75 m to the seabed, whereby only the upper limit is within the range of spermatozoa activation. Therefore, fertilized eggs can sink to reach the optimum depth. Based on average values of salinity and DO, no cod spermatozoa activation layer and no egg neutral buoyancy layer exist in the Gdańsk Deep. However, inflows from the North Sea can guarantee the existence of those layers.

Recapitulating, cod eggs can survive in the layer where they were fertilized in the Bornholm Basin. In the Słupsk Furrow, the eggs can leave the fertilization layer and sink to the bottom, because the neutral buoyancy layer only partly overlaps the spermatozoa activation layer. After fertilization, eggs can survive in the bottom layer of the Słupsk Furrow. During stagnation, there are no conditions which can guarantee egg survival in the Gdańsk Deep. Only during inflow periods do the fertilization layer and neutral buoyancy layer reappear.

Fertilized eggs from the Bornholm Deep can be transported to the Słupsk Furrow by deep currents. Owing to the position of the neutral buoyancy layer at the intermediate layer depth, movement above the sill is limited by the upward movement of the halocline. One factor which can shift the halocline upwards is the strong advection of saline, well-oxygenated waters from the North Sea (Mohrholz et al., 2015). Unlike weak inflows, MBIs refresh the deep layer of the Bornholm Basin, allowing cod to fertilize their eggs in the whole water layer from the halocline to the seabed. On the other hand, weaker inflows increase the transition layer thickness and have a great impact on the upward movement of the halocline.

5. Conclusions

1. At the surface layer the DO seasonal cycle has two maxima and two minima. The first maximum appears in March or April, the second in November. The first minimum appears in July/August, the second in December.
2. The CIL is a reservoir of oxygen for the less oxygenated upper and lower layers. A steady decrease in DO can therefore be expected from May to October.
3. The DOC at the bottom of the Bornholm Basin varies between well oxygenated to anaerobic.
4. Oxygen deficient conditions with DO $<$ 4 mg l^{-1} at the bottom of the Gdańsk Deep are permanent.
5. Nine months after MBI 2014, anaerobic conditions returned to the deep layer of the Bornholm Basin, but oxygen-deficient conditions persisted in the Gdańsk Deep.
6. Cod eggs can survive in the layer where they were fertilized in the Bornholm Basin. The eggs can leave the fertilization layer and sink to the bottom in the Słupsk Furrow. There are no conditions which can guarantee egg survival during the stagnation period in the Gdańsk Deep.
7. Only advection of water from the North Sea can guarantee the existence of the cod spermatozoa activation layer and the egg neutral buoyancy layer in the Gdańsk Deep.

Acknowledgement

This work was supported by the National Centre for Research and Development within the BIOSTRATEG III programme (project WaterPUCK, No. BIOSTRATEG3/343927/3/NCBR/2017); the European Union through the European Regional Development Fund within the Pomorskie Voivodeship Regional Operational Programme for 2014–2020 (project FindFISH, No. RPPM.01.01.01-22-0025/16-00); the Ministry of Sciences and Higher Education – the Polish contribution to the EuroArgo project (Decision

DIR/WK/2016/12); IO RAS state assignment (Theme No. 0149-2019-0004); the Russian Foundation for Basic Research (Grant No. 17-05-41196); the Polish National Science Centre, funded under project No. 2013/11/N/ST10/00804.

References

Argo, 2018. Argo float data and metadata from Global Data Assembly Centre (Argo GDAC) - Snapshot of Argo GDAC of December 8st 2018. SEANOE, https://doi.org/10.17882/42182#60707.

Aro, E., 1989. A review of fish migration patterns in the Baltic. Rapports et Procès-Verbaux des Réunions du Conseil International pour l'Exploration de la Mer 190, 72—96.

Bagge, O., Thurow, F., Steffensen, E., Bay, J., 1994. The Baltic cod. Dana 10, 1—28.

Bergström, S., Carlsson, B., Gardelin, M., Lindström, G., Pettersson, A., Rummukainen, M., 2001. Climate change impacts on runoff in Sweden — Assessments by global climate models, dynamical downscalling and hydrological modelling. Climate Res. 16, 101—112, https://doi.org/10.3354/cr016101.

Berner, M., Borrmann, U., 1985. Zum saisonalen Längenwachstum des Dorsches der Mecklenburger Bucht nach Wiederfangdaten von Markierungsexperimenten und Bestandsvergleichen. Fischerei-Forschung Wissenschaftliche Schriftenreihe 23, 63—69.

Bleil, M., Oeberst, R., Urrutia, P., 2009. Seasonal maturity development of Baltic cod in different spawning areas: importance of the Arkona Sea for the summer spawning stock. J. Appl. Ichthyol. 25, 10—17, https://doi.org/10.1111/j.1439-0426.2008.01172.x.

Casini, M., Käll, F., Hansson, M., Plikshs, M., Baranova, T., Karlsson, O., Lundström, K., Neuenfeldt, S., Gårdmark, A., Hjelm, J., 2016. Hypoxic areas, density-dependence and food limitation drive the body condition of a heavily exploited marine fish predator. Roy. Soc. Open Sci. 10 (3), https://doi.org/10.1098/rsos.160416.

Conley, D.J., Björck, S., Bonsdorff, E., Carstensen, J., Destouni, G., Gustafsson, B.G., Hietanen, S., Kortekaas, M., Kuosa, H., Meier, M., Müller-Karulis, B., Nordberg, K., Norkko, A., Nürnberg, G., Pitkänen, H., Rabalais, N.N., Rosenberg, R., Savchuk, O.P., Slomp, C.P., Voss, M., Wulff, F., Zillén, L., 2009. Controlling Eutrophication: Nitrogen and Phosphorus. Environ. Sci. Technol. 43 (10), 3412—3420.

Diaz, R.J., Rosenberg, R., 2008. Spreading dead zones and consequences for marine ecosystems. Science 321 (5891), 926—929, https://doi.org/10.1126/science.1156401.

Eero, M., Hjelm, J., Behrens, J., Buchmann, K., Cardinale, M., Casini, M., Gasyukov, P., Holmgren, N., Horbowy, J., Hüssy, K., Kirkegaard, E., Kornilovs, G., Krumme, U., Köster, F.W., Oeberst, R., Plikshs, M., Radtke, K., Raid, T., Schmidt, J., Tomczak, M.T., Vinther, M., Zimmermann, C., Storr-Paulsen, M., 2015. Eastern Baltic cod in distress: biological changes and challenges for stock assessment. ICES J Mar. Sci. 72 (8), 2180—2186, https://doi.org/10.1093/icesjms/fsv109.

Elken, J., 1996. Deep water overflow, circulation and vertical exchange in the Baltic Proper. Estonian Marine Institute, Tallinn, 691 pp.

Feistel, R., Nausch, G., Hagen, E., 2006. Unusual inflow activity in 2002—2003 and varying deep-water properties. Oceanologia 48 (S), 21—35.

Feistel, R., Nausch, G., Mohrholz, V., Lysiak-Pastuszak, E., Seifert, T., Matthäus, W., Krüger, S., Sehested, H.I., 2003. Warm waters of summer 2002 in the deep Baltic Proper. Oceanologia 45 (4), 571—592.

Fischer, H., Matthäus, W., 1996. The importance of the Drogden Sill in the Sound for major Baltic inflows. J. Marine Syst. 9 (3—4), 137—157, https://doi.org/10.1016/S0924-7963(96)00046-2.

Franck, U., Matthäus, H., Sammler, R., 1987. Major inflows of saline water into the Baltic Sea during the present century. Gerl. Beitr. Geophys. 96 (6), 517—531.

Haavisto, N., Tuomi, L., Roiha, P., Siiriä, S-M., Alenius, P., Purokoski, T., 2018. Argo Floats as a Novel Part of the Monitoring the Hydrography of the Bothnian Sea. Front Mar. Sci. 5, 324 pp, https://doi.org/10.3389/fmars.2018.00324.

Hansson, M., Andersson, H., 2016. Oxygen Survey in the Baltic Sea 2016 — Extent of Anoxia and Hypoxia, 1960—2016, Report Oceanography No. 58.

Hüssy, K., 2011. *Review of western Baltic cod (*Gadus morhua*) recruitment dynamics*. ICES J Mar. Sci. 68 (7), 1459—1471, https://doi.org/10.1093/icesjms/fsr088.

Jankowski, T., Livingstone, D.M., 2003. Consequences of the 2003 European heat wave for lake temperature profiles, thermal stability, and hypolimnetic oxygen depletion: Implications for a warmer world. Limnol. Oceanogr. 51 (2), 815—819, https://doi.org/10.4319/lo.2006.51.2.0815.

Jarvie, H.P., Smith, D.R., Norton, L.R., Edwards, F.K., Bowes, M.J., King, S.M., Scarlett, P., Davies, S., Dils, R.M., Bachiller-Jareno, N., 2018. Phosphorus and nitrogen limitation and impairment of headwater streams relative to rivers in Great Britain: A national perspective on eutrophication. Sci. Total. Environ. 621, 849—862, https://doi.org/10.1016/j.scitotenv.2017.11.128.

Köster, F.W., Hinrichsen, H-H., St John, M.A., Schnack, D., MacKenzie, B.R., Tomkiewicz, J., Plikshs, M., 2001. Developing Baltic cod recruitment models. 2. Incorporation of environmental variability and species interaction.. Can. J. Fish Aquat. Sci. 58, 1534—1556, https://doi.org/10.1139/f01-093.

Köster, F.W., Möllmann, C., Hinrichsen, H-H., Wieland, K., Tomkiewicz, J., Kraus, G., Voss, R., 2005. Baltic cod recruitment — the impact of climate variability on key processes. ICES J. Mar. Sci. 62, 1408—1425, https://doi.org/10.1016/j.icesjms.2005.05.004.

Lehmann, A., Lorenz, P., Jacob, D., 2004. Modelling the exceptional Baltic Sea inflow events in 2002—2003. Geophys. Res. Lett. 31, https://doi.org/10.1029/2004GL020830.

Matthäus, W., Franck, H., 1992. Characteristics of major Baltic inflows — a statistical analysis. Cont. Shelf Res. 12 (12), 1375—1400, https://doi.org/10.1016/0278-4343(92)90060-W.

Matthäus, W., Nehring, D., Feistel, R., Nausch, G., Mohrholz, V., Lass, H., 2008. The Inflow of Highly Saline Water into the Baltic Sea. In: Feistel, R., Nausch, G., Wasmund, N. (Eds.), State and Evolution of the Baltic Sea, 1952—2005, https://doi.org/10.1002/9780470283134.ch10.

Meier, H.E.M., Doscher, R., Broman, B., Piechura, J., 2004. The major Baltic inflow in January 2003 and preconditioning by smaller inflows in summer/autumn 2002: a model study. Oceanologia 46 (4), 557—5794.

Meier, H.E.M., Feistel, R., Piechura, J., Arneborg, L., Burchard, H., Fiekas, V., Golenko, N., Kuzmina, N., Mohrholz, V., Ch., Nohr, Paka, V.T., Sellschopp, J., Stips, A., Zhurbas, V., 2006. Ventilation of the Baltic Sea deep water: A brief review of present knowledge from observations and models. Oceanologia 48 (S), 133—164.

Mohrholz, V., 2018. Major Baltic Inflow Statistics — Revised. Front. Mar. Sci. 5, Art. 384, https://doi.org/10.3389/fmars.2018.00384.

Mohrholz, V., Naumann, M., Nausch, G., Krüger, S., Gräwe, U., 2015. Fresh oxygen for the Baltic Sea — An exceptional saline inflow after a decade of stagnation. J. Marine Syst. 148, 152—166, https://doi.org/10.1016/j.jmarsys.2015.03.005.

Müller, H., 2002. The distribution of 'Belt Sea cod' and 'Baltic cod' in the Baltic Sea from 1995 to 2001 estimated by discriminant analysis of the number of dorsal fin rays. ICES Document CM 200/L, 16, pp.

Nielsen, E.E., Grønkjær, P., Meldrup, D., Paulsen, H., 2005. Retention of juveniles within a hybrid zone between North Sea and Baltic Sea Atlantic cod (Gadus morhua). Can. J. Fish Aquat. Sci. 62, 2219—2225, https://doi.org/10.1139/f05-139.

Nielsen, E.E., Hansen, M.M., Ruzzante, D.E., Meldrup, D., Grønkjær, P., 2003. Evidence of a hybrid-zone in Atlantic cod (Gadus morhua) in the Baltic and the Danish Belt Sea revealed by individual admixture analysis. Mol. Ecol. 12, 1497—1508, https://doi.org/10.1046/j.1365-294x.2003.01819.x.

Nielsen, J.R., Lundgren, B., Kristensen, K., Bastardie, F., 2013. Localisation of Nursery Areas Based on Comparative Analyses of the Horizontal and Vertical Distribution Patterns of Juvenile Baltic Cod (Gadus morhua). PloS one 11 (2), https://doi.org/10.1371/journal.pone.0148721.

Nissling, A., Westin, L., 1997. Salinity requirements for successful spawning of Baltic and Belt Sea cod and the potential for cod stock interactions in the Baltic Sea. Mar. Ecol. Prog. Ser. 152, 261—271, https://doi.org/10.3354/meps152261.

Oschlies, A., Brandt, P., Stramma, L., Schmidtko, S., 2018. Drivers and mechanisms of ocean deoxygenation. Nat. Geosci. 11, 467—473, https://doi.org/10.1038/s41561-018-0152-2.

Ostrovskii, A.G., Zatsepin, A.G., Soloviev, V.A., Tsibulsky, A.L., Shvoev, D.A, 2013. Autonomous system for vertical profiling of the marine environment at a moored station. Oceanology+ 53 (2), 233—242, https://doi.org/10.1134/S0001437013020124.

Otterlind, G., 1985. Cod migration and transplantation experiments in the Baltic. Z. Angew Ichthyol. 1, 3—16.

Piechura, J., Beszczyńska-Möller, A., 2004. Inflow waters in the deep regions of the southern Baltic Sea — transport and transformations. Oceanologia 46 (1), 113—141.

Rak, D., 2016. The inflow in the Baltic Proper as recorded in January—February 2015. Oceanologia 58 (3), 241—247, https://doi.org/10.1016/j.oceano.2016.04.001.

Rak, D., Wieczorek, P., 2012. Variability of temperature and salinity over the last decade in selected regions of the southern Baltic Sea. Oceanologia 54 (3), 339—354, https://doi.org/10.5697/oc.54-3.339.

Reissmann, J., Burchard, H., Feistel, R., Hagen, E., Lass, H.U., Mohrholz, V., Nausch, G., Umlauf, L., Wieczorek, W., 2009. State-of-the-art review on vertical mixing in the Baltic Sea and consequences for eutrophication. Prog. Oceanogr. 82, 47—80, https://doi.org/10.1016/j.pocean.2007.10.004.

Renk, H., 1974. Primary production and chlorophyll content of the Baltic Sea. Part III. Primary production in the Baltic, Hydrobiologia 21, 191 pp.

Rohlf, N., 1999. Verhaltensänderungen der Larven des Ostseedorsches (Gadus morhua callarias) während der Dottersackphase. Berichte aus dem Institut für Meereskunde, 312 pp.

Rose, A.G., Marteinsdottir, G., Godø, O., 2018. *Atlantic Cod: A Bio-Ecology*. Chapter 7. Wiley and Sons Ltd., 287—336.

Schinke, H., Matthäus, W., 1998. On the causes of major Baltic inflows — an analysis of long time series. Cont. Shelf Res. 18, 67—97.

Siiriä, S., Roiha, P., Tuomi, L., Purokoski, T., Haavisto, N., Alenius, P., 2019. Applying area-locked, shallow water Argo floats in Baltic Sea monitoring. J. Oper. Oceanogr. 12 (1), 58—72, https://doi.org/10.1080/1755876X.2018.1544783.

Stigebrandt, A., Kalén, O., 2013. Improving oxygen conditions in the deeper parts of Bornholm Sea by pumped injection of winter water. Ambio 42 (5), 587—595, https://doi.org/10.1007/s13280-012-0356-4.

Viktorsson L., Almroth-Rosell E., Tengberg A., Vankevich R., Neelov I., Isaev A., Kravtsov V., Hall POJ. Benthic phosphorus dynamics in the Gulf of Finland, Baltic Sea. Aquat. Geochem. 18, 543—564, https://doi.org/10.1007/s10498-011-9155-y.

Vitale, F., Börjesson, P., Svedäng, H., Casini, M., 2008. The spatial distribution of cod (Gadus morhua L.) spawning grounds in the Kattegat, eastern North Sea. Fish. Res. 90, 36—44, https://doi.org/10.1016/j.fishres.2007.09.02.

Vitale, F., Cardinale, M., Svedäng, H., 2005. Evaluation of the temporal development of the ovaries in *Gadus morhua* from the Sound and Kattegat, North Sea. J. Fish Biol. 67 (3), 669—683, https://doi.org/10.1111/j.0022-1112.2005.00767.x.

Walker, J.C.G., 1980. The oxygen cycle in the natural environment and the biogeochemical cycles. Springer-Verlag, Berlin, 87—104.

Wieland, K., Jarre-Teichmann, A., Horbowa, K., 2000. Changes in the timing of spawning of Baltic cod: possible causes and implications for recruitment. ICES J. Mar. Sci. 57, 452—464, https://doi.org/10.1006/jmsc.1999.0522.

Wieland, K., Waller, U., Schnack, D., 1994. Development of Baltic cod eggs at different levels of temperature and oxygen content. Dana 10, 163—177.

Woźniak, B., Hapter, R., Dera, J., 1989. Light curves of marine plankton photosynthesis in the Baltic. Oceanologia 27, 61—78.

Oceanologia (2020) 62, 538—555

Available online at www.sciencedirect.com

ScienceDirect

journal homepage: www.journals.elsevier.com/oceanologia

ORIGINAL RESEARCH ARTICLE

A turning point in the development of phytoplankton in the Vistula Lagoon (southern Baltic Sea) at the beginning of the 21st century

Janina Kownacka*, Joanna Całkiewicz, Ryszard Kornijów

Department of Fisheries Oceanography and Marine Ecology, National Marine Fisheries Research Institute, Gdynia, Poland

Received 24 February 2020; accepted 17 August 2020
Available online 27 August 2020

KEYWORDS
Multiannual changes;
Zooplankton/
phytoplankton ratio;
Phytoplankton
community shift;
Nutrients;
Transparency

Summary Phytoplankton community structure was studied from 2002 to 2016 in the Vistula Lagoon (southern Baltic Sea) in the context of the 2010 shift in its population, as well as the reason for this shift and its environmental impact. This evident shift was indicated by Multidimensional Scaling at the Bray Curtis similarity level of 31%. Before 2010, the primary components of phytoplankton were Cyanobacteria (up to 98% of the biomass, October 2007) and Chlorophyta (40%, July 2002). After 2010, the contribution of Cyanobacteria considerably decreased, and the proportions of other phyla increased. The total phytoplankton biomass positively correlated with phosphorus, and Cyanobacteria biomass with silica. Evident changes were also observed in the seasonal dynamics of phytoplankton. Before 2010, the highest values of biomass occurred in autumn, and were related to high biomass of Cyanobacteria. Higher biomass has been recently reached in spring, during the dominance of Ochrophyta associated with Chlorophyta, Charophyta, and Cryptophyta. Generalised additive models showed a significant decreasing trend of the total phytoplankton biomass, Cyanobacteria, Chlorophyta, and flagellates, suggesting a decrease in eutrophication. This trend is concurrent with a considerable increase in the ratio of zooplankton to phytoplankton biomass since 2010. The increased ratio, however, did not result from elevated zooplankton biomass, but from the drop in phytoplankton biomass. Therefore,

* Corresponding authors at: Department of Fisheries Oceanography and Marine Ecology, National Marine Fisheries Research Institute, Kołłątaja 1, 81—332 Gdynia, Poland
E-mail addresses: janina.kownacka@mir.gdynia.pl (J. Kownacka), jcalkiewicz@mir.gdynia.pl (J. Całkiewicz), rkornijow@mir.gdynia.pl (R. Kornijów).
Peer review under the responsibility of the Institute of Oceanology of the Polish Academy of Sciences.

Production and hosting by Elsevier

https://doi.org/10.1016/j.oceano.2020.08.004

the most probable reason for the decrease in phytoplankton biomass was the simultaneous decrease in the concentration of all nutrients. The potential additional impact of filtration by a new alien bivalve *Rangia cuneata* G. B. Sowerby I, 1832 is also discussed.

1. Introduction

Lagoons are coastal marine ecosystems under a strong direct influence of land and rivers. Consequently, they are characterised by high productivity (Newton et al., 2014; Viaroli et al., 2008). The trophic status of lagoons shows considerable temporal inertia due to nutrient loads originating from both auto- and allochthonous matter accumulated over several years in sediments (Schernewski et al., 2011; Verdonschot et al., 2013). The gradual release of nutrients from sediments to the water column occurs under worsening oxygen conditions (Zilius et al., 2015), as well as through resuspension (Sondergaard et al., 1992). The latter phenomenon is common in lagoons due to the shallow depth of the water bodies and their high exposure to wind action. Phytoplankton is the primary beneficiary of a higher than the average level of nutrients (Eyto et al., 2018). The role of phytoplankton as a primary producer in lagoons is usually considerably greater than that of macrophytes, which predestines the systems to remain in a phytoplankton-dominated regime (Kornijów, 2018). This process bears consequences for the habitat conditions (worse light conditions, strong supply of organic matter to sediments, and periodical oxygen deficits), as well as for ecosystem services benefitting the human economy (Newton et al., 2014). The 2000s seem to have had the particular anthropogenic impact on the Vistula Lagoon (VL). Firstly, the economic transformation that commenced in the early 1990s (Eriksson et al., 2007) resulted in a considerable decrease in the nutrient load in the lagoon during the 2000s. It can be assumed to have caused a gradual decrease in the phytoplankton biomass and a transformation of its taxonomic composition as the bottom-up effect. At the same time, the food-web structure changed in the lagoon. In addition to the numerous alien species of invertebrates and fish already present in the lagoon (Grabowski et al., 2006; Jablonska-Barna et al., 2013), a new efficient bivalve filter-feeder appeared (Rudinskaya and Gusev, 2012; Warzocha et al., 2016).

Research on the phytoplankton of the Polish section of the lagoon has been occasionally conducted since the early 1950s (Kruk et al., 2016; Margoński and Horbowa, 2003; Margoński et al., 2003; Nawrocka and Kobos, 2011; Piwosz et al., 2016; Pliński, 1972; Pliński and Simm, 1978; Szarejko-Łukaszewicz, 1957). Previous research had been usually based on relatively short and non-continuous data series. The research shows that for more than half a century, the phytoplankton of the lagoon has been characterised by the dominance of blue-green algae (Cyanobacteria). Cyanobacterial blooms involved the appearance of species constituting potential producers of cyanobacterial toxins (Mazur-Marzec et al., 2010; Rybicka, 2005). These blooms occurring from May to October formed one vast peak lasting almost throughout the vegetation season, suggesting a disturbance of the typical order of seasonal phytoplankton succession in the waters of the temperate zone, usually consisting of spring, late spring, summer, and autumn peaks (Gasiūnaitė et al., 2005; Pliński and Simm, 1978; Wasmund et al., 1998; Witek et al.,1993). Whereas seasonal changes in the phytoplankton of the lagoon have been quite thoroughly investigated, publications concerning the long-term transformations occurring in the community are scarce. This publication shows changes in the phytoplankton structure in the Vistula Lagoon in the period 2002—2016, both in the seasonal and long-term aspect, as well as the verification of the hypotheses regarding causes of such changes and their effect for the environment. First, we hypothesised that the observed decrease in the concentration of nutrients in the lagoon should lead to changes in the seasonal development of phytoplankton, limiting the development of Cyanobacteria in the summer period and to a progressing decrease in its biomass in a long-term cycle (bottom-up effect).

Moreover, we verified whether the underlying causes were related to the pressure of filter-feeding zooplankton on the phytoplankton community as a top-down effect.

Finally, we assumed that water quality would considerably improve in terms of the concentrations of chlorophyll *a* and Cyanobacteria biomass.

2. Material and Methods

2.1. Study area

The Vistula Lagoon (VL), second largest coastal lagoon in the southern Baltic Sea (Witek et al., 2010), extends over approximately 90 km along the Polish and Russian coast of the Gulf of Gdańsk (Figure 1). Its width ranges from 8 to 19 km, and its depth reaches up to 5.1 m, averaging 2.4 m. To the north, the lagoon is separated from the open sea by the Vistula Spit, a shallow belt of sandy land with a width of 1—2 km and length of approximately 50 km. This estuarine system is exposed to strong land (inflow of fresh waters via rivers) and marine (intrusion of salt waters from the Baltic Sea via the Strait of Baltiysk) impacts. The annual freshwater influx is approximately 4 km^3, and the water retention time is approximately 4 months (Witek et al., 2010). Salinity decreases from 6.5 psu at the Baltiysk Strait to <1 psu at the mouths of the larger rivers.

In comparison to the water surface area (838 km^2) of the lagoon, its drainage area (23,871 km^2) is exceptionally large (Łomniewski, 1958). More than half of the area is under agricultural use, and approximately 25% is covered by forests. The total number of residents in the lagoon's catchment slightly exceeds one million. The industry is not extensive.

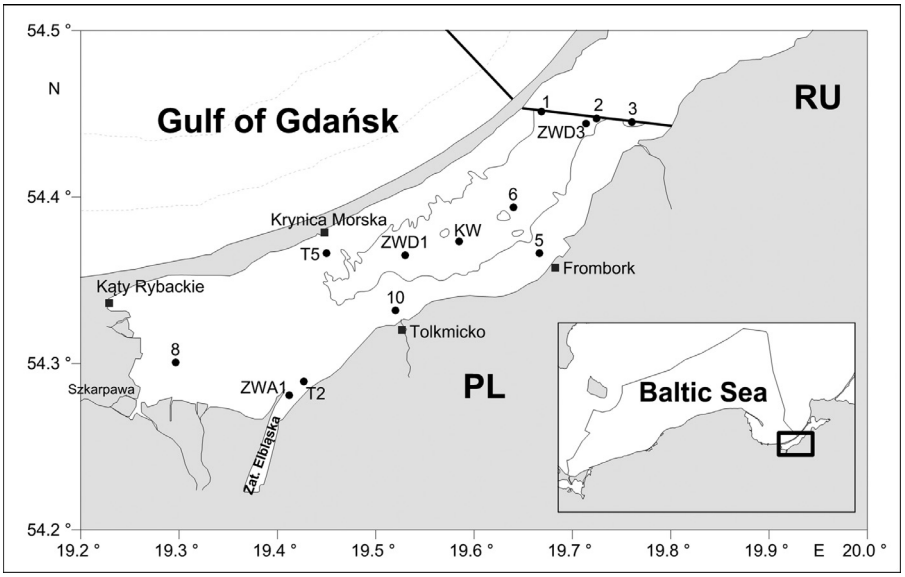

Figure 1 Location of sampling stations in the Polish part of the Vistula Lagoon.

The water level in the lagoon is subject to considerable fluctuations with an amplitude of up to 1.2 m, particularly in the period of autumn-winter storms (Chubarenko et al., 2012). Wave-induced mixing results in a continuous resuspension and homogeneous temperature distribution in the lagoon during the ice-free period (Chubarenko et al., 2017). The lagoon is under the influence of both maritime and continental climates, with air temperature reaching high annual amplitudes from −31°C to 36°C. During winter, VL may become covered by ice. Depending on the year, the ice may remain from several days to several months.

2.2. Physico-chemical parameters

Water temperature and salinity were measured *in situ* by means of a CTD probe. Transparency was measured with a Secchi disc as the Secchi disc depth (SDD). Physical parameters were measured simultaneously with phytoplankton sampling. Concentrations of nutrients (N-NO_3, N-NO_2, N-NH_4, total nitrogen (N_{tot}), P-PO_4, total phosphorus (P_{tot}), and dissolved silicate DSi) were determined using methods applied for the Baltic Sea to meet the objectives of the HELCOM monitoring programme (HELCOM, 2013). According to the HELCOM guidelines, the determination of nutrients is based on colorimetric methods (c.f. Grasshoff et al., 1983; Kirkwood, 1996). N/P ratio was calculated as N_{tot} to P_{tot} ratio.

2.3. Phytoplankton

2.3.1. Chlorophyll *a*

Chlorophyll *a* (Chl *a*) concentrations were analysed in accordance with the HELCOM recommendations for the fluorometric method (Edler, 1979; Evans et al., 1987; HELCOM 1988, 2015; Strickland and Parsons, 1968). Although all measurements were performed using the same method as that applied in the monitoring programme, the data for the period 2007–2017 were a raw database, and those for the period 2002–2006 were obtained from the study by Kobos and Nawrocka (2018).

2.3.2. Species composition, abundance, and biomass

The data shown in this study come from the analysis of 443 samples collected monthly from April to November during the period 2002–2016 with one gap in 2004, when phytoplankton monitoring was not conducted. In some years (2011, 2014–2015), samples were also collected in winter (Supplement Table 1).

The research was conducted at 13 stations relatively evenly distributed in the Polish part of the lagoon (Figure 1).

Surface water was collected by means of a 5–10 litre bathometer or another plastic container, and 250 ml samples were immediately fixed with acidic Lugol's solution to a final concentration of 0.5%. Subsamples of 2, 10, or 20 ml were analysed using an inverted microscope following the method of Utermöhl (Edler and Elbrächter, 2010; Utermöhl, 1958). Individual phytoplankton cells were counted in accordance with the HELCOM recommendations (HELCOM, 1988, 2006). The wet weight biomass and carbon content in the phytoplankton cells were calculated in accordance with Olenina et al. (2006). Phytoplankton organisms were identified to the lowest possible taxonomic rank. Their names and classification complied with the accepted binomial nomenclature of the World Register of Marine Species (version 2016).

Flagellates and *Others* were differentiated as artificial groups aggregating cells impossible to identify, divided into size classes.

As the samples were collected over a period of almost 20 years (a period of numerous changes in the phytoplankton taxonomy due to the development of molecular biology techniques), and analysed in various research centres, harmonisation of the data was necessary at the initial stage (Derolez et al., 2020; Munitz et al., 2020). This process resulted in a unified database for further analysis. The harmonisation of the database involved the unification of the

names of taxa often occurring as synonyms of the same species. Then the organisms were aggregated to higher taxonomic units, phyla, classes, orders, and genera. The calculation of annual average values was always preceded by the calculation of the monthly average.

2.4. Zooplankton

Zooplankton data were needed for the determination of the potential impact of zooplankton on phytoplankton. Water sampling and quantitative and qualitative laboratory analysis of the samples were conducted in accordance with the HELCOM COMBINE methodology applied in the monitoring of the Baltic Sea (HELCOM, 2017; Hernroth, 1985).

Zooplankton in the mezo-size fraction, i.e. 0.2—20 mm, was sampled at the same time and place as phytoplankton, by means of single vertical tows performed with the HydroBios (Germany) limnological standard plankton net (25 cm in diameter and a mesh size of 100 μm). The samples were preserved in ~4% formaldehyde solution buffered to pH 8—8.2 with disodium tetraborate (borax).

To highlight certain mechanisms of food-web interactions, the ratio between zooplankton and phytoplankton biomass (Bzoo/Bphyto) was calculated. This ratio is considered sensitive to changes in the top-down control through cascading trophic interactions (Carpenter et al., 1985) from fish to zooplankton and from zooplankton to phytoplankton (Gyllstrom et al., 2005; Hessen et al., 2003; Jeppesen et al., 2000). The ratio was calculated based on the analysis of samples collected at station KW during the period 2003—2016. Average annual biomasses of phytoplankton and zooplankton were used. The total zooplankton biomass covered *Copepoda, Cladocera, Rotifera*, and others that comprised meroplankton organisms.

2.5. Statistical analysis

The statistical significance of the differences in the taxonomic structure of phytoplankton was determined with the application of a one-way ANOSIM test. Multidimensional scaling (MDS) and cluster analyses were performed for the visualisation of the similarity of the structure of phytoplankton communities in years and seasons (months). Both the ANOSIM test and the MDS procedure were based on the Bray-Curtis distance matrix calculated based on the biomass of individual phylum (log(x+1) transformed data). The analysis was performed in the PRIMER 6 Version 6.1.15 package.

At least 10-year time series for the biomass of phytoplankton phyla were analysed for six selected months by means of generalised additive models (GAMs) (*gam* function, R package "mgcv", Wood, 2014). GAMs were run separately for each response variable vs. year. The possible autocorrelation between years was modelled with AR1 (autocorrelation structure with lag 1). Curves estimated with GAMs and 95% confidence limits were plotted on the data to visualise the direction of statistically significant long-term changes (i.e. decreasing, increasing, or non-linear trends). The total phytoplankton biomass and biomass of each phylum served as variables in the first stage of GAMs analysis. At the second stage, the biomass of each genus (or aggregation at class or order level) within the phylum was analysed.

The Pearson rank correlation (r) was used to evaluate the relations between environmental variables and phytoplankton biomass (at the level of total biomass, phylum, and genus) as well as between phytoplankton and zooplankton biomass. The Pearson correlation and statistical significance of correlations were determined (*cor* and *cor.test*, functions, R package "stats").

The statistical significance of temporal changes in the physico-chemical parameters was confirmed or rejected after the verification of whether the coefficient of the slope of the regression line was significantly different from 0. Such analysis permits trend detection. A test probability value of $p<0.05$ was considered for rejecting the hypothesis of the lack of a trend (*lm* function, R package "stats").

3. Results

3.1. Physical and chemical water properties

3.1.1. Temperature

The mean water temperature recorded during the growing season (March—November) of the period 2002—2016 was 15.6°C (Figure 2). Statistically, no evident trends occurred over the analysed years. There were, however, slight differences in the two periods. Before 2010, the mean temperature was 16.3°C, with the highest values in July and June. After 2010, the warmest months were August and July, and the mean temperature dropped to 14.7°C (Figure 2).

3.1.2. Salinity

The mean water salinity measured at station KW, located in the centre of the Polish part of VL and providing the longest time series of data, was 3.6 psu throughout the study period, and showed minor fluctuations (Figure 2). Linear regression showed a slight although not statistically significant increasing trend ($p>0.05$) in time. Moreover, the comparison of the years before and after 2010 showed the same mean values for both differentiated periods and multiannual means. In November, the salinity was the highest (5.5 psu), and slightly higher during the second period.

3.1.3. Transparency

The mean water transparency (SDD) recorded during the period 2002—2016 was 0.57 m. During the first period, 2002—2009, values of SDD readings were relatively uniform and always lower than the multiannual value. Later, considerable fluctuations occurred with a strongly increasing tendency in the years 2013—2016 (Figure 3, top panel). The increasing trend of water transparency in time, in terms of maximum, average, as well as the minimum values, was statistically significant ($p<0.05$).

During the first period, the lowest average values occurred in early spring and in autumn (Figure 3, middle panel), while during the second period (Figure 3, bottom panel), they occurred in summer from May to July as well as in late autumn (November). Then, very high maximum values of up to 2 m were recorded. These values were at least twice as high as the maximum values during the first period.

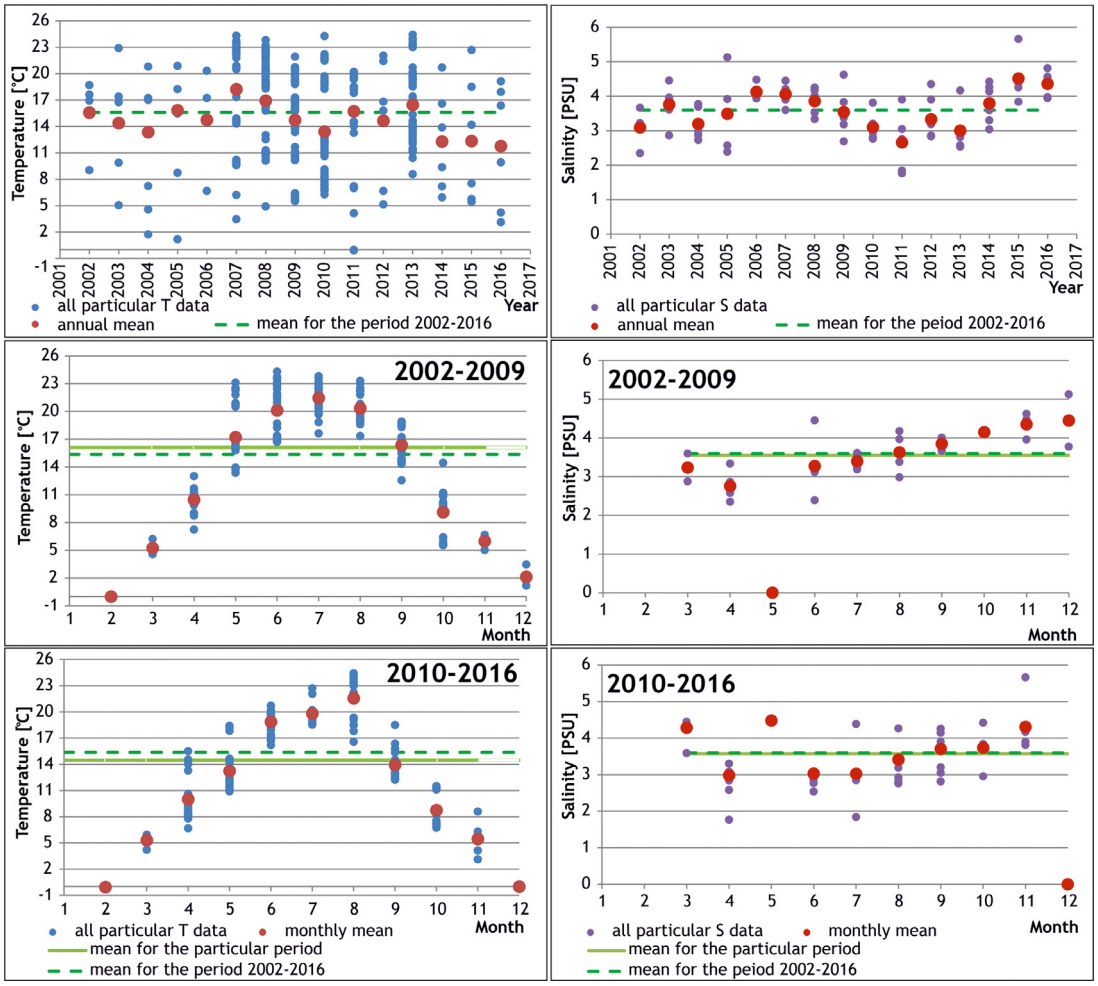

Figure 2 Temperature and salinity in VL. Multiannual changes during the study period (top panel) and seasonal changes during the two differentiated periods (middle and bottom panels).

3.1.4. Nutrients

The course of the mean annual concentrations of total nitrogen showed considerable fluctuations (Figure 4a), with the highest values (up to 328 μmol L^{-1}) between 2007 and 2009 and in 2013. The comparison of both periods revealed a decrease in the monthly mean N_{tot} concentrations below the multiannual average (127 μmol L^{-1}) during the period 2010–2016, and in the mean value for that period (112 μmol L^{-1}) compared to the multiannual average. Moreover, in the case of P_{tot} (Figure 4b) and Si (Figure 4c) concentrations, the comparison of data from before 2010 with data after 2010 showed a decrease in nutrient concentrations in recent years. It is worth emphasising that over the multiannual course of changes, a statistically significant downward trend occurred in P_{tot} concentration ($p < 0.05$), whereas for N_{tot}, Si, and N_{tot}/P_{tot}, the value of $p > 0.05$ for linear regression indicated no trends.

Until 2006, the ratio between total nitrogen and phosphorus remained at an even level close to or slightly above the Redfield ratio. Between 2007 and 2016, the N/P ratio showed fluctuations analogous to those of the total nitrogen concentrations, with maximum values in 2009 and 2013, and values approximately equal to the initial values in 2012 and 2015 (Figure 4d).

The mean annual silicon concentrations were maintained at a level approximately equal to the multiannual mean value for the entire study period (96 μmol L^{-1}). Silicon concentrations only decreased in recent years (2014–2016), in 2015 by almost 50% in comparison to the multiannual average (Figure 4c).

3.1.5. Abiotic variables as drivers of phytoplankton biomass

The Pearson rank correlation (r) demonstrated positive correlations between the total phytoplankton biomass and (i) phosphorus (P-PO4 and P_{tot}) concentration, (ii) suspension, and (iii) Chl *a* concentration. In contrast, the total biomass was negatively correlated with transparency. A considerably higher correlation of transparency with suspension than with the total phytoplankton biomass or Chl *a* concentration deserves particular attention. A positive correlation occurred between transparency and *Mesodinium rubrum* Lohmann, 1908 (Ciliophora), and a negative correlation was determined between transparency and Cyanobacteria and Chlorophyta.

No significant correlations were determined between the phytoplankton biomass and water temperature, the concentration of total nitrogen and its different forms, or

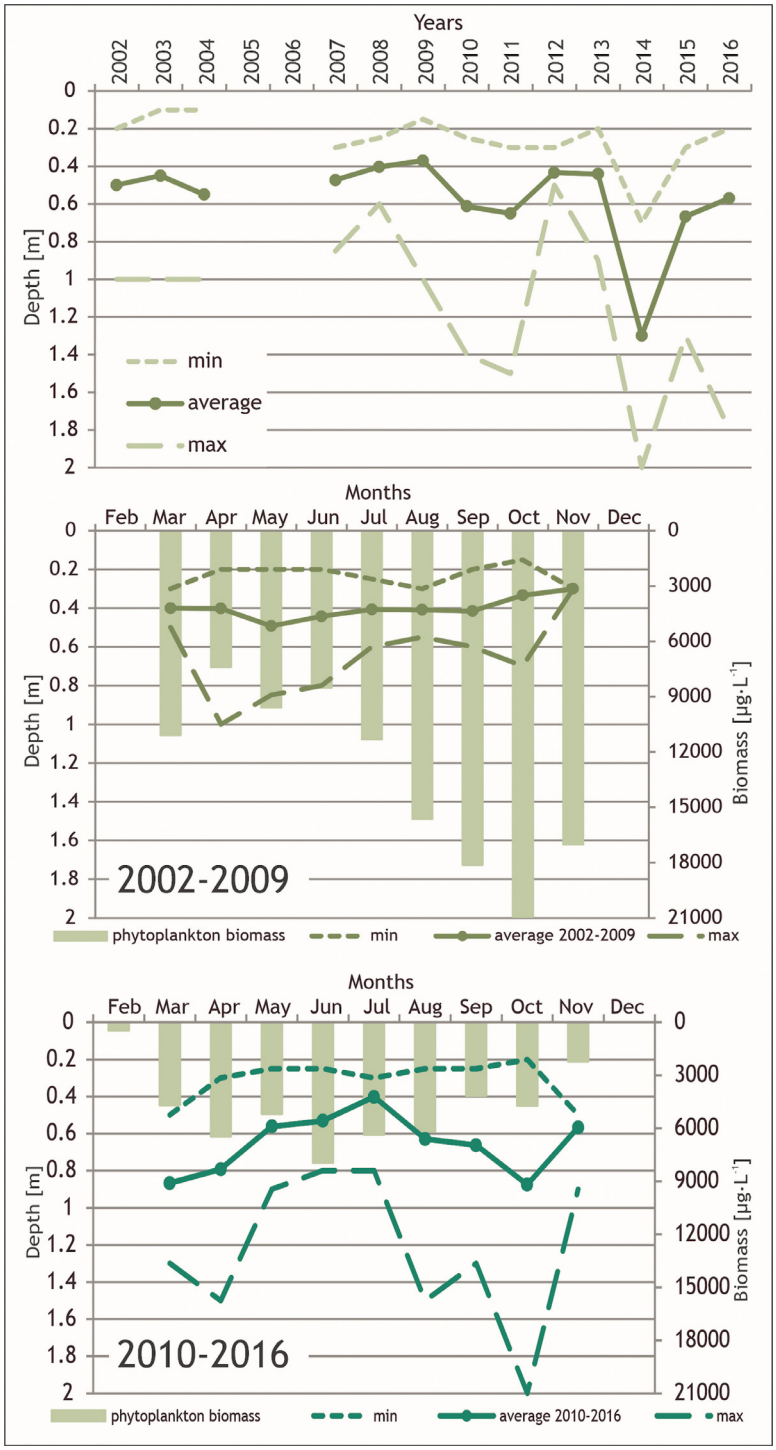

Figure 3 Transparency (SDD) versus phytoplankton biomass in VL. Multiannual changes during the study period (top panel) and seasonal changes during the two differentiated periods (middle and bottom panels).

the N/P ratio (with the exception of Chlorophyta which was positively correlated with N_{tot}). Silica was positively correlated with Cyanobacteria biomass, including genera such as *Snowella* Elenkin, 1938 and *Woronichinia* Elenkin, 1933, as well as genera belonging to Chlorophyta, namely, *Planctonema* Schmidle, 1903 and *Ankistrodesmus* Corda, 1838. The highest number of genera was correlated with total phosphorus and phosphate phosphorus (*Ankistrodesmus*, *Aphanotheceae/Anatheceae*, *Gleocapsopsis* Geitler ex Komárek, 1993, *Lemmermanniella* Geitler, 1942, *Monoraphidium*, Komárková-Legnerová, 1969, *Planctonema*, *Snowella*, and *Woronichinia* and biomass of Cyanobacteria, *Chlorophyceae* and *Oscillatoriales*). Cyanobacteria showed a positive correlation with salinity, including those from genera *Snowella* and *Woronichinia*, and a negative correlation was found for Ochrophyta (*Nitzschia* A.H. Hassall,

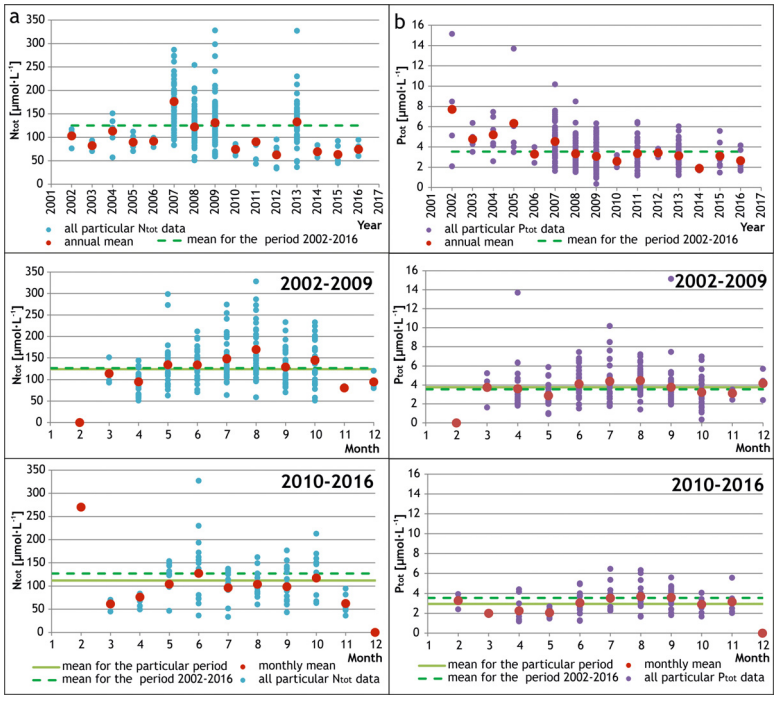

Figure 4 Total nitrogen (a), phosphorus (b), and silicon (c) concentrations and N/P ratio (d) in VL. Multiannual changes throughout the study period (top panel) and seasonal changes during the two differentiated periods (middle and bottom panels).

1845), and a representative of Chlorophyta genus *Desmodesmus* (R. Chodat) S.S. An, T. Friedl & E. Hegewald, 1999 (Supplement Table 2).

3.2. Phytoplankton

3.2.1. Chlorophyll *a* (Chl *a*)

Although mean Chl *a* concentrations (range: 21–70 mg m^{-3}) showed no significant differences ($p>0.05$) throughout the period (2002–2017), considerable differences were observed in the maximum concentrations between the years (Figure 5). Maximum Chl *a* concentrations reached values of more than 100 mg m^{-3}, particularly during the period 2002–2008 (up to 520 mg m^{-3} in 2002). The amplitude of the fluctuations considerably decreased after 2009, not exceeding 100 mg m^{-3} (except for 2013). The described changes, however, were of periodical character, with no statistically significant trend ($p>0.05$).

3.2.2. Species composition and dominance structure

A total of 170 taxa were identified before 2010, and approximately twice more (323) during the period 2010–2016. During the period 2002–2009, no Myzozoa such as *Prorocentrum cordatum* (Ostenfeld) J.D. Dodge, 1975, *Heterocapsa triquetra* (Ehrenberg) F. Stein, 1883, or *Oblea rotunda* (Lebour) Balech ex Sournia, 1973 were observed in VL. Among Ochrophyta, no genera such as *Chaetoceros* C.G. Ehrenberg, 1844, *Diploneis* (C.G. Ehrenberg) P.T. Cleve, 1894, *Achnanthes* Bory, 1822, or *Dinobryon* Ehrenberg, 1834 were documented, either.

Phytoplankton in VL was dominated by picoplanktonic (diameter <2 μm) Cyanobacteria-forming colonies belonging to genera *Anatheceae (Aphanotheceae* C. Nägeli, 1849*), Cyanodictyon* (Komárek & Anagnostidis) Komárek, Kastovsky & Jezberová, 2011, *Lemmermanniella, Woronichinia, Aphanocapsa* C. Nägeli, 1849, and *Merismopedia* Meyen, 1839, particularly during summer and autumn. During the period 2002–2009, the abundance of coccal Cyanobacteria reached $1.7 \cdot 10^{10}$ cells L^{-1}. At the same time, the mean abundance of nano- and microplanktonic Cyanobacteria was $6 \cdot 10^{8}$ cells L^{-1}, and the abundance of other components of phytoplankton ranged between $6 \cdot 10^{5}$ and $7 \cdot 10^{8}$ cells L^{-1}. During the period 2010–2016, the abundance of picoplanktonic Cyanobacteria decreased by an order of magnitude (10^{9} cells L^{-1}), but still exceeded the abundance of the remaining phytoplankton components (nano- and microplanktonic Cyanobacteria abundance was $1.7 \cdot 10^{6}$ cells L^{-1}, and the abundances of the remaining components were between $5 \cdot 10^{5}$ and $7 \cdot 10^{8}$ cells L^{-1}).

The dominant taxa were recognised as those with biomass exceeding 30% of the total phytoplankton biomass in a sample (Supplement Table 3). Among such established dominants, only six dominated throughout the study period (2002–2016), namely: *Dolichospermum* (Ralfs ex Bornet & Flahault) P. Wacklin, L. Hoffmann & J. Komárek, 2009 with coiled trichomes, *Microcystis aeruginosa* (Kützing) Kützing, 1846, *Microcystis* Lemmermann, 1907, *Snowella* spp., *Aphanizomenon* spp., and *Cyclotella* (F.T. Kützing) A. de Brébisson, 1838. During the initial period of the study (2002–2009), along with these taxa, dominants included 9 others, whereas after 2010, the presence of 29 other periodically dominant taxa was recorded (Supplement Table 3).

3.2.3. Long-term changes in the taxonomic composition and phytoplankton biomass

Statistical analyses aimed at the assessment of the effect of station location on the distribution of phytoplankton in the Polish part of VL showed no significant differences. There-

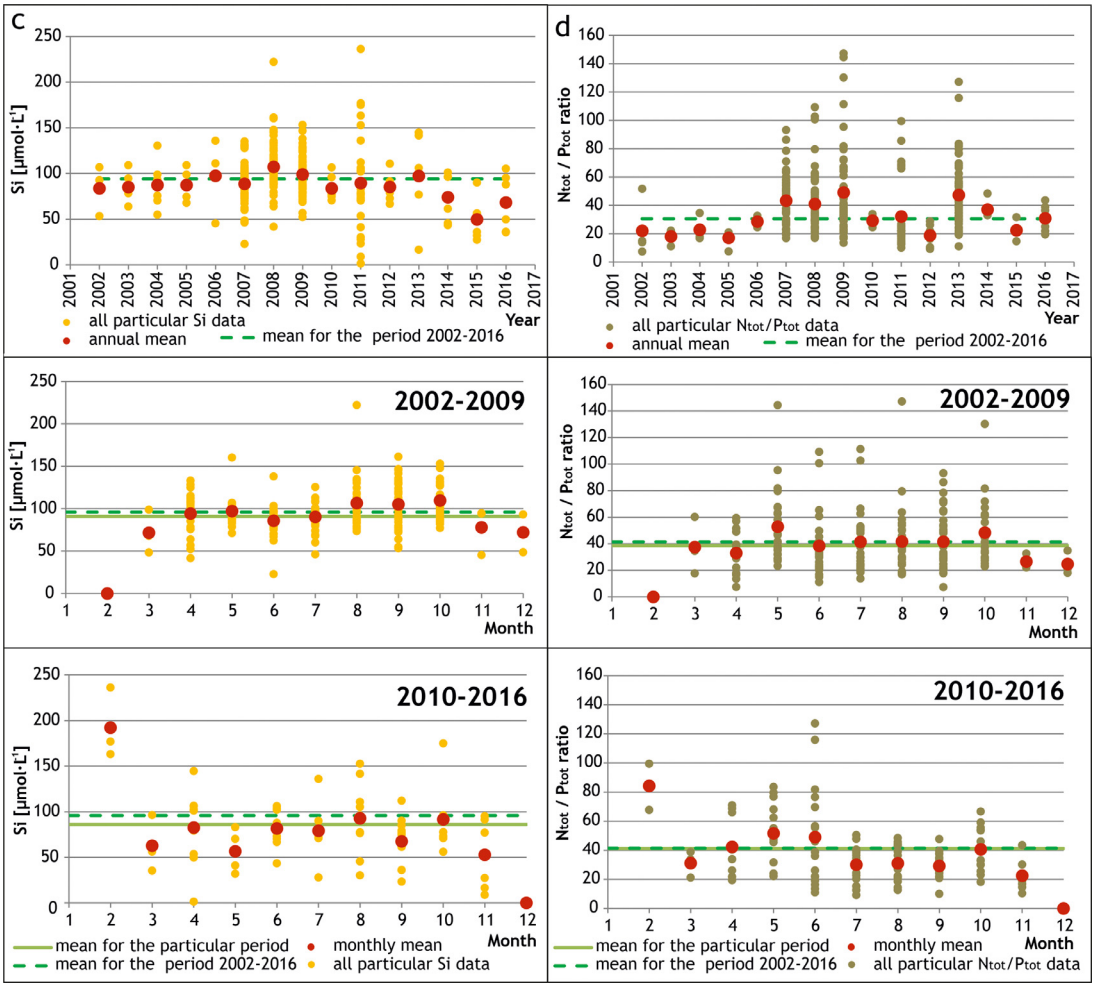

Figure 4 *Continued.*

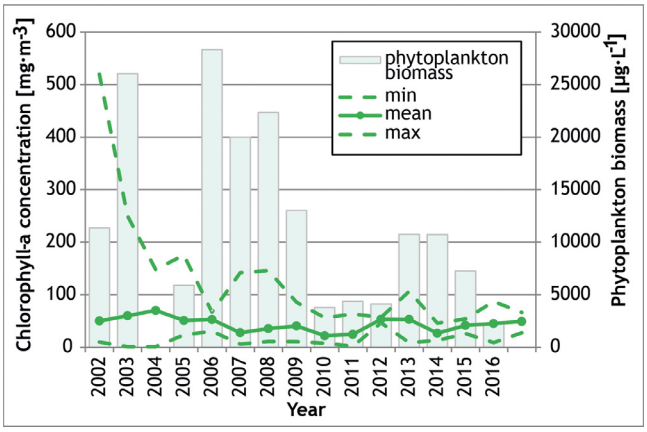

Figure 5 Multiannual changes in Chl *a* concentrations.

fore, the spatial distribution of phytoplankton will not be subject to further analysis. In contrast, a significant effect of time (year) on phytoplankton biomass was determined (one-way ANOSIM, p=0.001). It was revealed in a significant decrease in the total biomass and evident reorganisation of the taxonomic structure of the phytoplankton community (Figure 6).

For better visualisation of the observed changes in phytoplankton biomass during the period 2002–2016, the MDS analysis with phytoplankton biomass at the level of genus was applied. The analysis revealed two groups of data (Bray Curtis similarity at 31%), marked in Figure 7. One of the groups covers data from years 2002–2009, and the other from the period 2010–2016. Therefore, all further analyses were conducted with consideration of the division into these two time periods.

Before 2010, the primary components of the phytoplankton community were Cyanobacteria, accounting for 53–98% of the total phytoplankton biomass, and Chlorophyta, with a contribution of 14–40%. Other phytoplankton groups only occasionally reached a higher share of the total biomass, e.g., diatoms in 2002 and cryptophytes in 2007 (15% and 20% of the total biomass, respectively). The highest total phytoplankton biomass of $6{\cdot}10^4$ µg L−1 was observed in 2006 and 2008. Ten times lower total biomass was observed in 2010. In 2011 and 2012, the maximum values of phytoplankton biomass did not exceed $2 \cdot 10^4$ µg L^{-1}. Subsequently, until the end of 2015, they did not exceed $4 \cdot 10^4$ µg L^{-1}. The lowest biomass was recorded in 2016, not exceeding $3 \cdot 10^3$ µg L^{-1}.

The taxonomic reorganisation of the phytoplankton community resulted in an equalisation of the contribution of

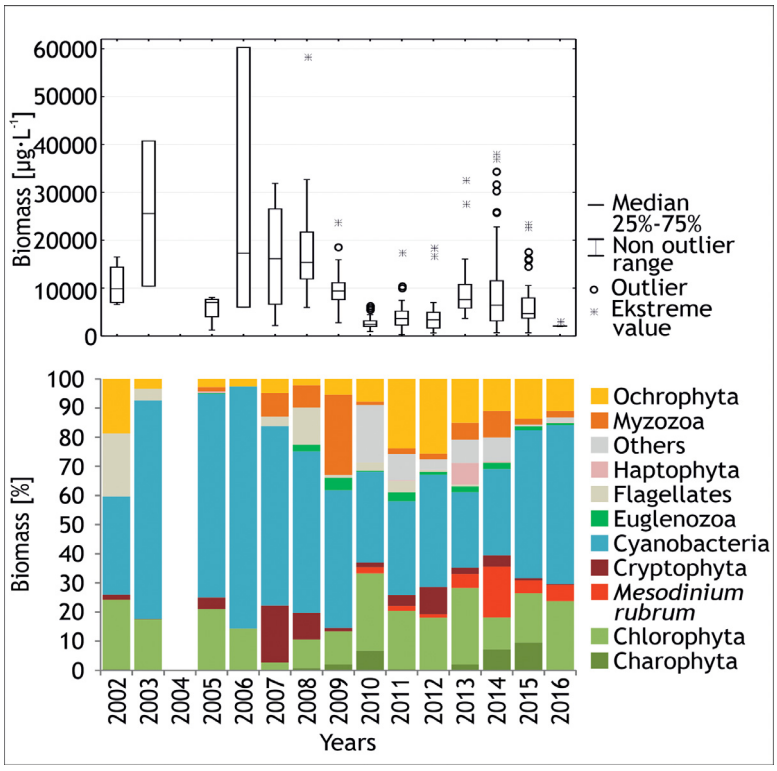

Figure 6 Multiannual changes in phytoplankton biomass (top panel) and its structure shown as percentages of the main groups (bottom panel) during the period 2002–2016.

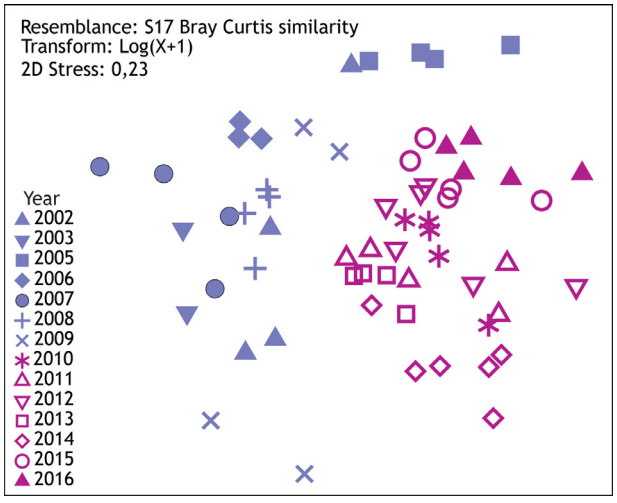

Figure 7 Multidimensional scaling (MDS) for phytoplankton biomass (at genus level) at station KW during the period 2002–2016.

particular phyla to the total phytoplankton biomass after 2010 (Figure 6, bottom panel). The most important changes included (i) the reduction of the proportion of Cyanobacteria biomass almost by half; (ii) an increase in the proportion of Ochrophyta, Charophyta, and Chlorophyta; (iii) the appearance of the mixotrophic ciliate *Mesodinium rubrum* with a proportion in certain events in autumn 2014 reaching 98% in the eastern part of VL, but with an average share of 21%.

3.2.4. Seasonal changes in phytoplankton biomass

Phytoplankton biomass underwent statistically significant monthly changes (one way ANOSIM, $p=0.001$). MDS analysis covered phytoplankton biomass at the genus level. It showed that all monthly data from the period 2002–2009 were mixed without grouping into seasons (Figure 8). In contrast, during the period 2010–2016, data from summer months formed one group, while those from spring months formed a second group. The results from autumn months were less pronounced. September data were combined with summer data, October data with spring data, and November data remained separate. The division of data was not as strong as that in the case of years (Bray Curtis similarity >50%), but it pointed to at least three seasons in the annual vegetation cycle in comparison with the period 2002–2009, when the data were mixed with no pattern. The analysis of phytoplankton biomass at the phylum level during the period 2002–2009, however, showed seasonal succession consisting of two stages (Figure 9). The stage lasting from March to April was followed by the stage from May to November. In early spring, there was a small peak of biomass of the complex primarily consisting of cryptomonads and Chlorophyta, diatoms, euglenids, and flagellates, with a small share of cyanobacteria. At the second stage of succession, phytoplankton biomass dominated by Cyanobacteria gradually increased, culminating in October.

During the period 2010–2016, phytoplankton succession showed three stages of development (Figure 9). The first spring stage lasted from March to May with a maximum in April. At that time, the community was primarily composed of diatoms and representatives of Charophyta, Chlorophyta, Cryptophyta, Myzozoa, and inconsiderable quantities of

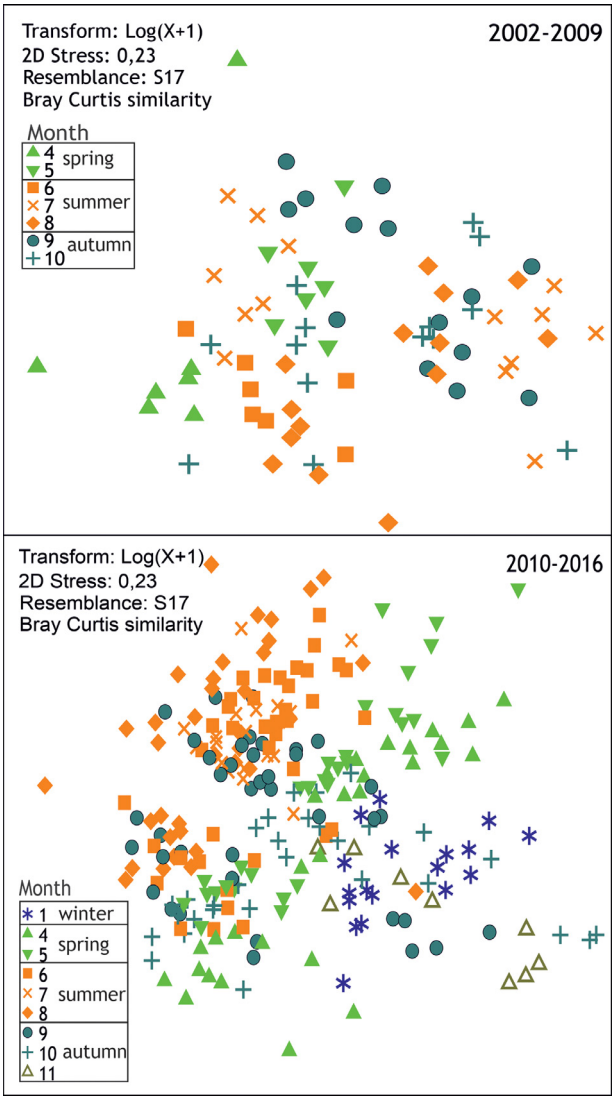

Figure 8 Multidimensional scaling (MDS) for phytoplankton biomass (at genus level) in two periods: 2002–2009 (top panel) and 2010–2016 (bottom panel).

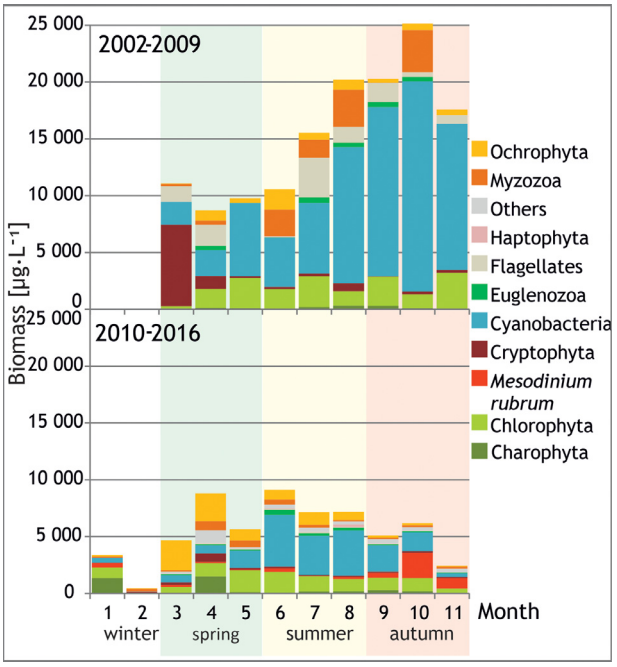

Figure 9 Seasonal changes in monthly biomass of the main taxonomic groups in VL during the periods 2002–2009 and 2010–2016. The values are means for all the analysed stations.

Cyanobacteria. The summer stage of the succession lasted from June to August, with a maximum in June, and was dominated by Cyanobacteria, primarily accompanied by Chlorophyta and Ochrophyta. During the autumn stage, lasting from September to November, the taxonomic composition was similar to that in summer, with an additional considerable share of *Mesodinium rubrum* (Ciliophora). The biomass peaked in October, although its mean value was 5 times lower than during the period 2002–2009.

The above observations were also confirmed by the results of the GAMs analysis used for the detection of long-term trends in phytoplankton biomass and structure (Figure 10, Supplement Table 4). GAMs indicated a decreasing trend of the total phytoplankton biomass in August, September, and October (Figure 10a), and a similarly decreasing trend for Cyanobacteria (Figure 6**b**). This group was the most important component of phytoplankton biomass (20–63% depending on the season).

Chlorophyta (with a share of total phytoplankton biomass ranging from 14 to 23% depending on the season) and flagellates (1–8%) also showed a decreasing trend. In the case of Chlorophyta, it was recorded in July and October (Figure 10d, Supplement Table 4), and for flagellates (Figure 10c) also in April. In both cases, in autumn, the trend was non-linear, with a significant decrease during the period 2002–2008 followed by stabilisation until 2016.

At the same time, ciliate *Mesodinium rubrum* (0.1–8% of the total phytoplankton biomass in different seasons), Cryptophyta (1–14%), and Myzozoa (1–6%) showed an increasing tendency. Whereas in the case of *M. rubrum* this trend was evident in spring and autumn, in the case of Cryptophyta and Myzozoa a regular trend occurred in September and October (Figure 10e–f, Supplement Table 4). The GAMs analysis was also used to detect the long-term trends in Cyanobacteria and Chlorophyta biomass and taxonomic structure, i.e. the most important components of the phytoplankton community in VL (Supplement Table 5 and Table 6). Decreasing trends occurred in the months from August to October for the following genera dominant in the total biomass of Cyanobacteria: *Woronichinia*, *Snowella*, *Cyanodictyon*, and *Aphanotheceae (Anatheceae)*, as well as for the order of Oscillatoriales, primarily represented by *Planktolyngbya capillaris* (Hindák) Anagnostidis & Komárek, 1988 /*contorta* (Lemmermann) Anagnostidis & Komárek, 1988 (Supplement Table 3 and Table 5). No significant trends occurred in the biomass of potentially toxic diazotrophic Cyanobacteria causing blooms in June–July–August from genera *Aphanizomenon* and *Dolichospermum* (with the exception of *Aphanizomenon* in August, when an increasing trend occurred).

The decreasing trends occurred during months from July to October for the following genera: *Tetraëdron* Kützing,

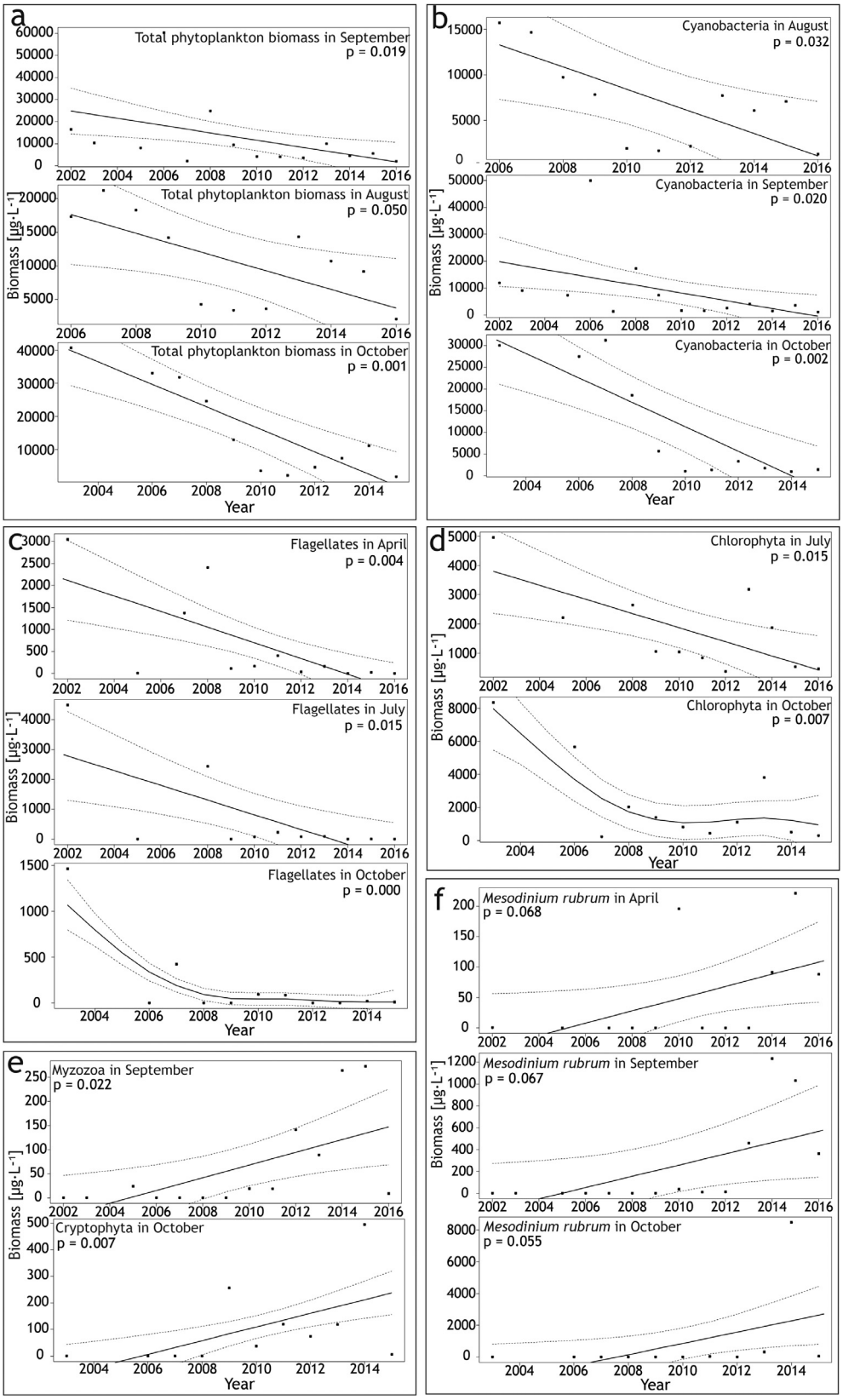

Figure 10 Significant long-term trends in total phytoplankton biomass (a) and biomass of Cyanobacteria (b), flagellates (c), Chlorophyta (d), Myzozoa and Cryptophyta (e), and *Mesodinium rubrum* (f) in VL. For variables with a statistically significant trend ($p < 0.05$), a GAM curve (solid line) is plotted with a 95% confidence interval (dashed line). Annual averages are plotted as filled squares.

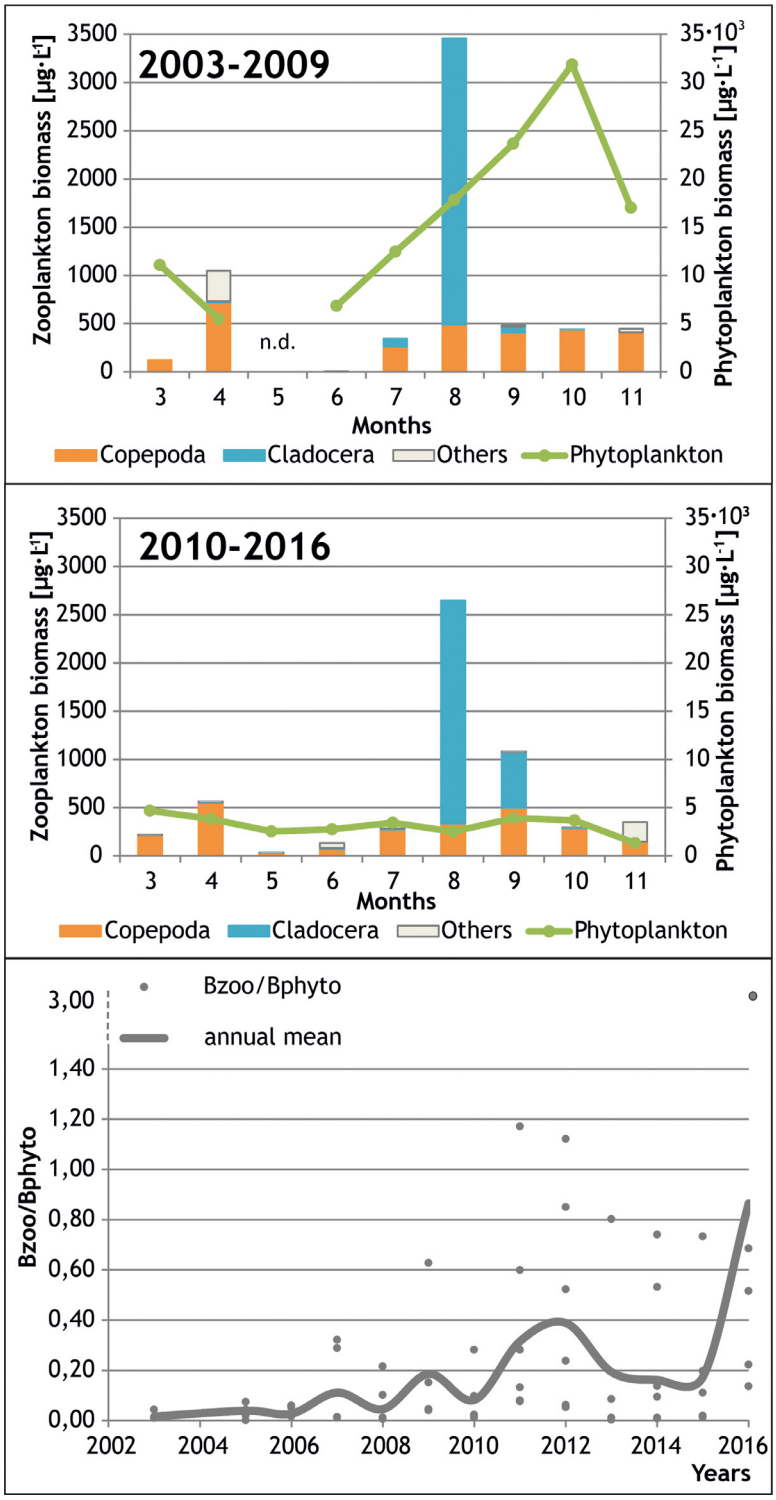

Figure 11 Comparison of monthly mean phyto- and zooplankton biomass at station KW in the differentiated periods (top and middle panels). Zooplankton to phytoplankton biomass ratio (B_{zoo}/B_{phyto}) in subsequent years (bottom panel). n.d.= no data.

1845, *Scenedesmus* Meyen, 1829, *Acutodesmus* (Hegewald) Tsarenko, 2001, and *Monoraphidium* belonging to phylum Chlorophyta. Among them, only *Tetraëdron* was included in the dominant taxa (Supplement Table 3). In April, a decreasing trend was determined for the dominant genus *Desmodesmus*. In summer months, however, this genus showed an increasing trend similar to those of *Dictyosphaerium* Nägeli, 1849 and *Tetrastrum* Chodat, 1895. Among the genera dominant in phylum Chlorophyta, *Pediastrum* Meyen, 1829 and *Oocystis* Nägeli ex A. Braun, 1855 showed no trend, and *Crucigenia* Morren, 1830 exhibited an increasing or decreasing trend depending on the month.

3.2.5. Ratio between zoo- and phytoplankton biomass

Throughout the study period, zooplankton biomass ranged between 4 $\mu g\ L^{-1}$ in June 2005 and 64 000 $\mu g\ L^{-1}$ in August 2016. The highest biomass was always observed in August. In spite of the evident seasonal variability of zooplankton, no significant variability was determined between years. During the period 2003–2009 in March, June, and September, zooplankton biomass was usually lower than in the years 2010–2016. In April, August, October, and November, the opposite dependency was observed (Figure 11, top and middle panels). The mean values of zooplankton biomass in the first and second period were very approximate, and reached 874 and 882 μgL^{-1}, respectively. During both study periods, i.e. 2002–2009 and 2010–2016, considerable differences occurred in the structure of the phytoplankton community (Subchapters "*Long-term changes in the taxonomic composition and phytoplankton biomass*" and "*Seasonal changes in phytoplankton biomass*"), but no substantial changes were observed in the development of the zooplankton community. These observations suggest that changes in the B_{zoo}/B_{phyto} ratio were associated with changes in phytoplankton biomass rather than zooplankton (Figure 11, bottom panel).

During the period 2003–2009, the B_{zoo}/B_{phyto} ratio gradually increased from 0.02 to 0.19. In 2010, it decreased to a value of 0.08, and from 2011, its further increase was observed until it reached a maximum value of 0.86 in 2016.

The Pearson rank correlation (r), used to evaluate the relations between zooplankton and phytoplankton biomass, demonstrated that total phytoplankton biomass was not correlated with the total zooplankton biomass or with any of the identified groups of zooplankton (Supplement Table 7). A correlation was determined for the total zooplankton biomass, including superorder *Cladocera*, with colony-forming coccal cyanobacteria from genera *Aphanocapsa*, *Cyanodictyon*, and *Lemmermanniella*, and the Chlorophyta *Monoraphidium*. *Rotifera* was correlated with phytoplankton phylum Euglenozoa and genus *Coelastrum* Nägeli, 1849 (Chlorophyta), whereas *Copepoda* was correlated with a very rarely occurring genera *Anabaenopsis* V.V.Miller, 1923 and *Phacotus* Perty, 1852.

4. Discussion

4.1. Abiotic and biotic variables as the potential drivers of the long-term changes in the structure of the phytoplankton community

A rapid improvement in water quality in the Polish part of VL since 2010 is suggested by SDD measurements showing an outstanding increase in water transparency. SDD measurements reveal not only the effect of plankton on water transparency, but also the effect of suspension originating from periodical intensive resuspension. Therefore, these are not the mean annual SDD measurements as such, but rather the amplitude of their values that are useful for the assessment of the trophic status of a water body (Kornijów, 2018; Margoński and Horbowa, 2003; Margoński et al., 2003). This interpretation is confirmed by results of the present study indicating a higher negative correlation of SDD with the total suspension (coefficient −0.71) than with the total phytoplankton biomass (coefficient −0.25) or Chl *a* concentration (coefficient −0.34).

Margoński and Horbowa (2003) observed significant changes in SDD measurements in the Polish part of VL between the 1950s and 1990s. The range of the recorded SDD was much broader (0.2–1.7 m) and the mean values higher during the 1950s than 1990s (0.1–1.1 m). An analogous situation occurred in the compared periods 2002–2009 and 2010–2016. The former period shows a continuation of the situation from the 1990s, with a characteristic low amplitude of the measurement values and highest transparency in April (maximum up to 1 m). The latter period (2010–2016) reflects the situation from the 1950s, with two peaks of the maximum transparency: a smaller one (approximately 1.5 m) in spring, and a higher one (even up to 2 m) in autumn.

Considerable differences between the two analysed periods also occurred in the taxonomic composition and biomass of phytoplankton, as well as Chl *a* concentration. The question arises as to what the cause of the observed changes in phytoplankton after 2010 could have been. Potential causes include abiotic factors (temperature and nutrients) as well as trophic interactions occurring in food webs.

The mean water temperature in the study period 2002–2016 (15.6°C) was 2.1°C higher than the mean value in 1953 (Szarejko-Łukaszewicz, 1957). This finding corresponds with the observations of Dailidienė et al. (2011), who estimated the warming trend of the mean surface water temperature in the lagoons of the southern and eastern Baltic Sea at 0.03°C $year^{-1}$ (during period 1961–2008). An increase in temperatures, however, proved not to be significantly correlated with the phytoplankton biomass. Moreover, an increase in temperature occurred gradually; hence, this factor cannot be attributed to the considerable changes in phytoplankton observed at the turn of 2009 and 2010.

Changes in nutrient concentrations involved a gradual decrease in phosphorus, whereas changes in nitrogen fluctuated with no evident trend. In 2010, very low concentrations of both elements overlapped, including the mean as well as maximum values. Moreover, according to Burska et al. (2018), a significant decrease in the concentrations of not only total N and P but also their inorganic undissolved forms occurred during this period. Furthermore, the maximum concentrations of Si in 2010 proved the lowest in comparison to previous years. Therefore, the changes can be presumed to have been at least one of the causes of a decrease in the phytoplankton biomass in the Polish part of VL. This conclusion is confirmed by a statistically significant correlation between the total phytoplankton biomass and its different components, primarily showing a decreasing trend (Cyanobacteria, *Chlorophyceae*, *Woronichinia*, *Snowella*, *Oscillatoriales*, *Aphanotheceae*/*Anatheceae*) and phosphorus concentrations (as $P\text{-}PO_4$ and P_{tot}), and to a lower degree also with Si and N_{tot} concentrations. This confirms our first hypothesis that one of the causes of the changes observed in the phytoplankton community could have been a decrease in the concentration of nutrients.

Among biotic factors controlling the development of phytoplankton from the top of the trophic pyramid (top-down effect), the greatest role is traditionally ascribed to grazing by filter-feeders, including zooplankton (Jeppesen et al., 1994; Moss, 1994). The comparison of phyto- and zooplank-

ton biomass presented in this study, however, suggest no significant role of zooplankton as a factor controlling phytoplankton development. The determined positive correlation of Cladocera biomass with colony-forming coccal cyanobacteria points only to the promotion of the growth of colonial cyanobacteria through the selective eating of competitive phytoplankton by selective filter-feeder cladocerans (Haney, 1987). It is, however, necessary to find a factor that would limit rather than promote the development of cyanobacteria with the strongest decreasing trend.

The feeding pressure exerted by zooplankton on phytoplankton can be determined based on the B_{zoo}/B_{phyto} ratio. The values of the coefficient provided for the Baltic lagoons refer to relatively short periods (Dmitrieva and Semenova, 2011; Kornijów et al., 2020; Krylova, 1985). They still correspond with the values measured by us for the same years of research.

The study results indicate a considerable increase in the B_{zoo}/B_{phyto} ratio beginning in 2010. A more thorough analysis of both components of the indicator, however, shows that the increased B_{zoo}/B_{phyto} ratio observed in recent years did not result from the elevated biomass of zooplankton. The zooplankton biomass was very similar in subsequent years of both compared periods. In contrast, the phytoplankton biomass during the second period was considerably lower than during the preceding period. Therefore, our second hypothesis regarding the limiting effect of zooplankton on the development of phytoplankton in the second study period was not supported.

Other efficient filter-feeders consuming phytoplankton may include e.g. bivalves (Derolez et al., 2020, Strayer et al., 1999). Until 2010, these organisms were represented only by *Dreissena polymorpha* Pallas, 1771 in VL. Their abundance, however, shows strong decreasing tendencies, and their current occurrence is scarce, patchy and limited to near-shore hard substrates (Rychter and Jabłońska-Barna, 2018). Therefore, it is difficult to attribute the effect on phytoplankton and suspension at the scale of the entire ecosystem to the bivalve.

The opposite conclusions can be drawn for another bivalve clam *Rangia cuneata* G.B. Sowerby I. 1832, a non-intentionally introduced alien species originating from the Gulf of Mexico. *R. cuneata* probably arrived in VL in the years of 2007–2008, and was first observed in the Russian part of VL in 2010 (Rudinskaya and Gusev, 2012). The clams probably appeared in the Polish part of the lagoon in 2008 or 2009, because the first reports concerning their presence originate from 2012 when it was already 30–40 mm in length (Warzocha et al., 2016).

During the period 2012–2016, the clam spread over the Polish part of VL, where it became the dominant component of the benthos. Its biomass periodically reached up to 1750 g/m^2 (Kornijów et al., 2018; Warzocha et al., 2016). Such high biomass had not been previously reported for any benthic invertebrate in VL.

The literature provides examples of the strong controlling effect of *R. cuneata* on phytoplankton, resulting in an improvement of water transparency and recovery of submerged vegetation at the biomass several times lower than in VL (e.g., Cerco and Noel, 2010 in oligohaline and tidal fresh regions of the Chesapeake Bay; Wong et al., 2010 in the coastal lakes of south-eastern Louisiana).

The appearance of *R. cuneata* in VL coincided with a decrease in the phytoplankton biomass and considerable structural changes in the community, particularly in the case of Cyanobacteria. These changes could have been both directly caused by the clam through filtration, and indirectly through the utilisation of phosphorus compounds deposited in bottom sediments (Tenore et al., 1968). In addition to detritus, sand, organic matter, remnants of vascular plants, and bacteria derived directly from the sediments, several dozen species of phytoplankton (Hopkins et al., 1973; Olsen, 1976), including cyanobacteria as well as diatoms (Rudinskaya and Gusev, 2012) have been identified in the stomachs of *R. cuneata*.

It is worth mentioning, however, that after the appearance of the *R. cuneata* population, changes in the phytoplankton of the Russian part of the lagoon were different. They involved a considerable decrease in the contribution of Chlorophyta and diatoms in the total phytoplankton biomass (Semenova and Dmitrieva, 2013). At the same time the contribution of Cyanobacteria in the total phytoplankton biomass considerably increased, resulting in a competitive advantage when the biomass of Chlorophyta decreased.

Next to a drop in nutrient concentration, the sudden appearance and rapid development of the *R. cuneata* population at the end of the first decade of the 21st century could have likely been an additional cause of a decrease in the phytoplankton biomass at the turn of 2009 and 2010. After all, both factors (nutrients and *R. cuneata*) could have permitted a new balance between phytoplankton and filtering invertebrates, including zooplankton. As a result, the current values of the B_{zoo}/B_{phyto} ratio are a promising predictor for the efficient control of phytoplankton by zooplankton, especially that it is accompanied by a gradual decrease in nutrient load.

4.2. Impact on the environment quality

The phenomena described above, observed in the environment of VL (a decrease in nutrient concentration, and particularly P_{tot}; increase in water transparency; decrease in phytoplankton biomass, and increase in the B_{zoo}/B_{phyto} ratio), point to the improvement of its ecological state since 2010, i.e. from the moment of appearance of *Rangia cuneata*. Other consequences of the changes also deserve attention, such as a decrease in Cyanobacteria biomass and decrease in Chl *a* maximum concentration.

According to Wasmund et al. (1998), nitrogen-fixing Cyanobacteria can be considered as “blooms” at a biomass concentration of approximately 200 μg L^{-1}. Current calculations revealed that even after 2010, the average biomass of nitrogen-fixing Cyanobacteria is still much higher than 200 μg L^{-1} (1016 μg L^{-1}), although it decreased 3.6 times in comparison to those from the period 2002–2009. Statistical analyses showed no significant trends in the biomass of potentially toxic diazotrophic cyanobacteria causing blooms from genus *Dolichospermum*, but an increasing trend occurred in August for *Aphanizomenon*. The shift in the occurrence of blooms in months is very interesting. Before 2010, diazotrophic Cyanobacteria occurred from June to November with a maximum in September, but after 2010, they started blooming earlier, from May to September, with a

maximum in June and August. This phenomenon is probably related to the filtration activity of *R. cuneata* during the summer season, or to the ongoing climate change in the Northern Hemisphere. Both experimental results and models have indicated that cyanobacteria respond more strongly to the climate change than do diatoms or Chlorophyta (De Senerpont Domis et al., 2007; Moore et al., 2008).

In addition to nitrogen-fixing Cyanobacteria, a significant seven-fold decrease in biomass after 2010 occurred in orders Chroococcales and Synechococcales. These orders were abundant in VL year round, with particular intensity between March and November. Within the aforementioned orders, decreasing trends in months from August to October were observed in the following genera dominant in the total cyanobacterial biomass: *Woronichinia, Snowella, Cyanodictyon*, and *Aphanotheceae (Anatheceae)*. Genus *Woronichinia* and morphologically similar genus *Snowella* are characteristic of standing-water ecosystems. The *Woronichinia compacta* (Lemmermann) Komárek & Hindák, 1988 complex was predominant in the Polish part of VL, and is known as a dominant species in eutrophic ecosystems, including lakes (Nowicka-Krawczyk and Żelazna-Wieczorek, 2017) and the Curonian Lagoon connected to the Baltic Sea (Krevs et al., 2007). According to Sagert et al. (2008), *W. compacta* occurring along the German coast of the Baltic Sea can be considered a species indicating an increase in eutrophication. Therefore, a considerable decrease in the biomass of the species in the Polish part of VL confirms a decrease in the level of eutrophication in the water body. A decrease in the biomass of *Woronichinia* could have also had a positive effect on zooplankton invertebrates. Representatives of the genus often blooming in the plankton of meso-eutrophic to eutrophic water bodies have been found to be able to produce toxins (microginin FR3) active towards invertebrate zooplankton (Bober and Bialczyk, 2017).

Mean Chl *a* concentrations did not differ significantly between the start and end of the study period, and were maintained at the same level as concentrations recorded by Margoński and Horbowa (2003), Renk et al. (2001) and Witek et al. (2010) throughout the period 1970–2000. This stability of the mean Chl *a* concentrations over more than 45 years is interesting in the context of evident changes in phytoplankton biomass. Although the Pearson rank correlation (r) demonstrated positive correlations between total phytoplankton biomass and Chl *a* concentration, maximum Chl *a* concentrations were better harmonised with phytoplankton biomass (Figure 5). This was not the exact relationship, however, because the highest peak of Chl *a* in 2002 did not correspond to the highest phytoplankton biomass recorded in 2006. This is because the concentration of Chl *a* depends on the phytoplankton species composition, development stage, and environmental conditions. A particularly large discrepancy between the Chl *a* concentration and phytoplankton biomass is observed at the high abundance of picoplankton organisms in the environment (Albertano et al., 1997; Hawley and Whitton, 1991), as is the case for VL. The picoplankton fraction cannot be properly analysed by means of the Utermöhl method applied in this study, because the colonies of very small cells, solitary Cyanobacteria, and Chlorophyta in the picoplankton range are often overlooked (Albrecht et al., 2017). Reliable quantitative counting of the picoplankton fraction requires fluorescence microscopy or flow cytometry (HELCOM, 2017). The decreasing tendency of the maximum Chl *a* concentrations indicates a less intensive or shorter duration of phytoplankton blooms. From this point of view, Chl *a* concentrations found in VL also suggest better environmental quality of this estuary during the second study period. Based on the above, our third hypothesis regarding the progressive improvement of water quality in the Vistula Lagoon was confirmed.

5. Conclusions

1. The turn of 2009 and 2010 marked a breakthrough in the recent history of the phytoplankton community (its biomass and taxonomic structure) in the Vistula Lagoon.
2. The range of variability of phytoplankton biomass was considerable in time, in both the multiannual and seasonal aspect, and inconsiderable in space.
3. Evident decreasing trends of changes occurred in summer and autumn months from July to October, and were determined for Cyanobacteria and Chlorophyta, reaching the highest contribution in the total biomass.
4. The most probable factors that caused a decrease in the phytoplankton biomass included a simultaneous decrease in the concentrations of all nutrients (N, P, Si) in 2010, and the occurrence of a new filter-feeder *Rangia cuneata* at the same time. Due to the lack of availability of specific data on the development dynamics of the clam in VL, however, its impact on phytoplankton remains largely undetermined. Final confirmation of this conclusion requires further research.
5. A decrease in phytoplankton biomass triggered a decrease in the Chl *a* concentration, increase in the water transparency, and increase in the B_{zoo}/B_{phyto} ratio. The observed changes point to an improvement of the ecological state of the Polish part of VL.

Acknowledgments

This publication is the result of project P9-7/15 'Ecology of an invasive clam *Rangia cuneata* in the Vistula Lagoon' funded by the National Marine Fisheries Research Institute (NMFRI). The paper is based on the results of monitoring of phytoplankton, zooplankton, as well as physical and chemical variables by the Chief Inspectorate of Environmental Protection in Warsaw and the Regional Inspectorate of Environmental Protection in Elbląg within the framework of the Polish National Monitoring Programme funded by the National Fund for Environmental Protection and Water Management. The study also employed data collected in the scope of project P1-2/2011 'Coexistence of freshwater and marine populations in the Vistula Lagoon on the example of selected groups of bacteria' funded by the NMFRI. The authors would like to thank their colleagues from the Department of Fisheries Oceanography and Marine Ecology of NMFRI – Sławomira Gromisz for assistance in statistical one-way ANOSIM and MDS analyses and preparation of boxplots, Tycjan Wodzinowski for preparing a map, and Jan Warzocha for constructive discussions concerning the ecology of the

Vistula Lagoon. Finally, we thank the Reviewer and the Editor for their valuable comments on the first version of this manuscript.

Supplementary materials

Supplementary material associated with this article can be found, in the online version, at https://doi.org/10.1016/j.oceano.2020.08.004.

References

Albertano, P., Di Somma, D., Capucci, E., 1997. Cyanobacterial picoplankton from the Central Baltic Sea: cell size classification by image-analyzed fluorescence microscopy. J. Plankton Res. 10, 1405—1416, https://doi.org/10.1093/plankt/19.10.1405.

Albrecht, M., Pröschold, T., Schumann, R., 2017. Identification of Cyanobacteria in a Eutrophic Coastal Lagoon on the Southern Baltic Coast. Front. Microbiol. 8, 1—16, https://doi.org/10.3389/fmicb.2017.00923.

Bober, B., Bialczyk, J., 2017. Determination of the toxicity of the freshwater cyanobacterium *Woronichinia naegeliana* (Unger) Elenkin. J. Appl. Phycol. 29, 1355—1362, https://doi.org/10.1007/s10811-017-1062-1.

Burska, D., Pryputniewicz-Flis, D., Bolałek, J., Zalewski, M., 2018. Nutrients in the waters of the Vistula Lagoon. In: Bolałek, J. (Ed.), Vistula Lgoon. Wydawnictwo Naukowe PWN SA, Warszawa, 190—210 (in Polish).

Carpenter, S.R., Kitchell, J.F., Hodgson, J.R., 1985. Cascading trophic interactions and lake productivity. Bioscience 35, 634—639, https://doi.org/10.2307/1309989.

Cerco, C.F., Noel, M.R., 2010. Monitoring, modeling, and management impacts of bivalve filter feeders in the oligohaline and tidal fresh regions of the Chesapeake Bay system. Ecol. Model. 221, 1054—1064, http://dx.doi.org/10.1016/j.ecolmodel.2009.07.024.

Chubarenko, B., Domnin, D., Navrotskaya, S., Stont, Z., Chechko, V., Bobykina, V., Pilipchuk, V., Karmanov, K., Domnina, A., Bukanova, T., Topchaya, V., Kileso, A., 2017. Transboundary Lagoons of the Baltic Sea. In: Kosyan, R. (Ed.), Diversity of Russian Estuaries and Lagoons Exposed to Human Influence, 149—189.

Chubarenko, B.V., Leitsina, L.V., Esiukova, E.E., Kurennoy, D.N., 2012. Model analysis of the currents and wind waves in the Vistula Lagoon of the Baltic Sea. Oceanology 52, 748—753, https://doi.org/10.1134/S000143701206001X.

Dailidienė, I., Baudler, H., Chubarenko, B., Navrotskaya, S., 2011. Long term water level and surface temperature changes in the lagoons of the southern and eastern Baltic. Oceanologia 53 (1-TI), 293—308, https://doi.org/10.5697/oc.53-1-TI.293.

De Senerpont Domis, L.N., Mooij, W.M., Huisman, J., 2007. Climate-induced shifts in an experimental phytoplankton community: a mechanistic approach. Hydrobiologia 584, 403—413, https://doi.org/10.1007/s10750-007-0609-6.

Dmitrieva, O.A., Semenova, A.S., 2011. Seasonal dynamics of phyto and zooplankton and their interactions in the hypertrophic reservoir. Inland Water Biol 4, 308—315, https://doi.org/10.1134/S1995082911030059.

Derolez, Valé., Soudant, D., Malet, N., Chiantella, C., Richard, M., Abadie, E., Aliaume, C., Bec, B., 2020. Two decades of oligotrophication: Evidence for a phytoplankton community shift in the coastal lagoon of Thau (Mediterranean Sea, France). Estuar. Coast. Shelf S. 241, https://doi.org/10.1016/j.ecss.2020.106810.

Edler, L., 1979. Recommendations on methods for marine biological studies in the Baltic Sea. Phytoplankton and chlorophyll. The Baltic Marine Biologists 5, 1—38.

Edler, L., Elbrächter, M., 2010. The Utermöhl method for quantitative phytoplankton analysis. Intergovernmental Oceanographic Commission Manuals and Guides 55. In: Karlson, B., Cusack, C., Bresnan, E. (Eds.), Microscopic and molecular methods for quantitative phytoplankton analysis. UNESCO, Paris, 13—20.

Eriksson, H., Pastuszak, M., Löfgren, S., Mörth, C.-M., Humborg, C., 2007. Nitrogen budgets of the Polish agriculture 1960—2000 — Implication for riverin nitrogen loads to the Baltic Sea. Biogeochemistry 85, 153—168, https://doi.org/10.1007/s10533-007-9126-y.

Evans, C.A., O'Reilly, J.E., Thomas, J.P., 1987. A handbook for the measurement of chlorophyll-a and primary productivity. BIOMASS Sci. Ser. 8, Texas A & M University, 114 pp.

Eyto, E., Kelly, S., Ryder, E., Dillane, M., Archer, L., O'Cathain, D., Daly, S., Lyons, K., Obrador, B., Brentrup, J., Naumoski, A., Poole, R., Lucey, F., Jennings, E., 2018. High frequency monitoring reveals fine scale spatial and temporal dynamics of the deep chlorophyll maximum of a stratified coastal lagoon. Estuar. Coast. Shelf S. 218, 278—291, https://doi.org/10.1016/j.ecss.2018.12.010.

Gasiūnaitė, Z.R., Cardoso, A.C., Heiskanen, A.S., Henriksen, P., Kauppila, P., Olenina, I., Pilkaitytė, R., Purina, I., Razinkovas, A., Sagert, S., Schubert, H., Wasmund, N., 2005. Seasonality of coastal phytoplankton in the Baltic Sea: influence of salinity and eutrophication. Estuar. Coast. Shelf S. 65, 239—252, https://doi.org/10.1016/j.ecss.2005.05.018.

Grabowski, M., Konopacka, A., Jazdzewski, K., Janowska, E., 2006. Invasions of alien gammarid species and retreat of natives in the Vistula Lagoon (Baltic Sea, Poland). Helgoland Mar. Res. 60, 90—97, https://doi.org/10.1007/s10152-006-0025-8.

Grasshoff, K., Erhardt, M., Kremling, K. (Eds.), 1983. Methods of seawater analysis. Verlag Chemie, Germany, 419 pp., https://doi.org/10.1002/iroh.19850700232.

Gyllstrom, M., Hansson, L.A., Jeppesen, E., Garcia-Criado, F., Gross, E., Irvine, K., Kairesalo, T., Kornijów, R., Miracle, M.R., Nykanen, M., Nõges, T., Romo, S., Stephen, D., Van Donk, E., Moss, B., 2005. The role of climate in shaping zooplankton communities of shallow lakes. Limnol. Oceanogr. 50, 2008—2021, https://doi.org/10.4319/lo.2005.50.6.2008.

Haney, J., 1987. Field studies on zooplankton-cyanobacteria interactions. New Zeal. J. Mar. Fresh. 21, 467—475, https://doi.org/10.1080/00288330.1987.9516242.

Hawley, G.R., Whitton, B.A., 1991. Seasonal Changes in Chlorophyll-containing Picoplankton Populations of Ten Lakes in Northern England. Int. Revue ges. Hydrobiol. 76, 545—554, https://doi.org/10.1002/iroh.19910760407.

HELCOM, 1988. Guidelines for Baltic Monitoring Programme for the third stage. Part D. Biological determinands. In: Baltic Sea Environment Proceedings No. 27 D.

HELCOM, 2006. Manual for marine monitoring in the COMBINE programme of HELCOM. Part C. Programme for monitoring of eutrophication and its effects. Annex C-6: Phytoplankton species composition, abundance and biovolume, Helsinki, http://www.helcom.fi/Lists/Publications/Manual%20for%20Marine%20Monitoring%20in%20the%20COMBINE%20Programme%20of%20HELCOM.pdf, (accessed on 29.04.2019).

HELCOM, 2013. Manual for Marine Monitoring in the COMBINE Programme of HELCOM. Part C. Programme for monitoring of eutrophication and its effects, Annex C-2, Hydrographic and hydrochemical variables, Helsinki, https://helcom.fi/media/publications/Manual-for-Marine-Monitoring-in-the-COMBINE-Programme-of-HELCOM.pdf.

HELCOM, 2015. Manual for Marine Monitoring in the COMBINE Programme of HELCOM, Helsinki, http://helcom.fi/Documents/Action%20areas/Monitoring%20and%20assessment/Manuals%20and%20Guidelines/Manual%20for%20Marine%20Monitoring%20in%20the%20COMBINE%20Programme%20of%20HELCOM.pdf.

HELCOM, 2017. Manual for Marine Monitoring in the COMBINE Programme of HELCOM: Guidelines for monitoring of mesozooplankton. Helsinki, 11 pp., http://www.helcom.fi/Documents/Action%20areas/Monitoring%20and%20assessment/Manuals%20and%20Guidelines/Guidelines%20for%20monitoring%20of%20mesozooplankton.pdf.

Hernroth, L., 1985. Recommendations on methods for marine biological studies in the Baltic Sea. Mesozooplankton assessment. BMB Publication 10, 1–32.

Hessen, D.O., Faafeng, B.A., Brettum, P., 2003. Autotroph: herbivore biomass ratios; carbon deficits judged from plankton data. Hydrobiologia 491, 167–175, https://doi.org/10.1023/A:1024456825718.

Hopkins, S.H., Anderson, J.W., Horvath, K., 1973. The brackish water clam Ranqia cuneata as indicator of ecological effects of salinity changes in coastal water. U.S. Corps of Engineers Rep. H-23-l., 250 pp.

Jablonska-Barna, I., Rychter, A., Kruk, M., 2013. Biocontamination of the western Vistula Lagoon (south-eastern Baltic Sea, Poland). Oceanologia 55 (3), 751–763, https://doi.org/10.5697/oc.55-3.751.

Jeppesen, E., Lauridsen, T.L., Mitchell, S.F., Christoffersen, K., Burns, C.W., 2000. Trophic structure in the pelagial of 25 shallow New Zealand lakes: changes along nutrient and fish gradients. J. Plankton. Res. 22, 951–968, http://dx.doi.org/10.1093/plankt/22.5.951.

Jeppesen, E., Sondergaard, M., Kanstrup, E., Petersen, B., Eriksen, R.B., Hammershoj, M., Mortensen, E., Jensen, J.P., Have, A., 1994. Does the impact of nutrients on the biological structure and function of brackish and fresh-water lakes differ? Hydrobiologia 275, 15–30, https://doi.org/10.1007/BF00026696.

Kirkwood, D.S., 1996. Nutrients: Practical notes on their determination in sea water. ICES Techniques in Marine Environmental Sciences (17), https://repository.oceanbestpractices.org/bitstream/handle/11329/696/TIMES17%281%29.pdf?sequence=1&isAllowed=y.

Kobos, J., Nawrocka, L., 2018. Phytoplankton of the Vistula Lagoon. In: Bolałek, J. (Ed.), Vistula Lgoon Wydawnictwo Naukowe PWN SA, Warszawa, 241–251 (in Polish).

Kornijów, R., 2018. Ecosystem of the Polish part of the Vistula Lagoon from the perspective of alternative stable states concept, with implications for management issues. Oceanologia 60 (3), 390–404, https://doi.org/10.1016/j.oceano.2018.02.004.

Kornijów, R., Karpowicz, M., Ejsmont-Karabin, J., Nawrocka, L., de Eyto, E., Grzonkowski, K., Magnuszewski, A., Jakubowska, A., Wodzinowski, T., Woźniczka, A., 2020. Patchy distribution of phyto- and zooplankton in large and shallow lagoon under ice cover and resulting trophic interactions. Mar. Freshwater Res., https://doi.org/10.1071/MF19259.

Kornijów, R., Pawlikowski, K., Drgas, A., Rolbiecki, L., Rychter, A., 2018. Mortality of post-settlement clams *Rangia cuneata* (Mactridae, Bivalvia) at an early stage of invasion in the Vistula Lagoon (South Baltic) due to biotic and abiotic factors. Hydrobiologia 811, 207–219, https://doi.org/10.1007/s10750-017-3489-4.

Krevs, A., Koreiviene, J., Paskauskas, R., Sulijiene, R., 2007. Phytoplankton production and community respiration in different zones of the Curonian lagoon during the midsummer vegetation period. Transit. Waters Bull. 1, 17–26, https://doi.org/10.1285/i1825229Xv1n1p17.

Kruk, M., Jaworska, B., Jablonska-Barna, I., Rychter, A., 2016. How do differences in the nutritional and hydrological background influence phytoplankton in the Vistula Lagoon during a hot summer day? Oceanologia 58 (4), 341–352, https://doi.org/10.1016/j.oceano.2016.05.004.

Krylova, O.I., 1985. Activity of plankton and benthos in the Kurshskii and Vislinskii gulfs of the Baltic Sea related with their ecological deviations, 21.10.85, TsNI ITEIRKh No. 714–RKh (AtlantNIIRO, Kaliningrad), (in Russian).

Łomniewski, K., 1958. The Firth of Vistula. PWN, Warsaw 106 pp., (in Polish, English summary).

Margoński, P., Horbowa, K., 2003. Are there trends in water quality, chlorophyll a and zooplankton of the Vistula Lagoon (Southern Baltic Sea) as a result of changes in nutrient loads? Diffuse Pollution Conf. Dublin, ECSA 9 Nutrients 6, 162–169, https://www.ucd.ie/dipcon/docs/theme06/theme06_32.PDF.

Margoński, P., Horbowa, K., Gromisz, S., Różański, S., Różańska, Z., Wątroba, K., Niemirycz, E., 2003. Long-term changes in the water quality and biota in Vistula Lagoon and its drainage basin. Mantra-East, 45, pp.

Mazur-Marzec, H., Browarczyk-Matusiak, G., Forycka, K., Kobos, J., Plinski, M., 2010. Morphological, genetic, chemical and ecophysiological characterisation of two Microcystis aeruginosa isolates from the Vistula Lagoon, southern Baltic. Oceanologia 52 (1), 127–146, http://dx.doi.org/10.5697/oc.52-1.127.

Moore, S.K., Trainer, V.L., Mantua, N.J., Parker, M.S., Laws, E.A., Backer, L.C., Fleming, L.E., 2008. Impacts of climate variability and future climate change on harmful algal blooms and human health. Env. Health 7 (Suppl. 2), S4, https://doi.org/10.1186/1476-069X-7-S2-S4.

Moss, B., 1994. Brackish and freshwater shallow lakes — different systems or variations on the same theme? Hydrobiologia 275–276/Dev. Hydrobiol. 94, 1–14, http://dx.doi.org/10.1007/BF00026695.

Muñiz, O., Rodríguez, J.G., Revilla, M., Laza-Martínez, A., Seoane, S., Franco, J., 2020. Inhomogeneity detection in phytoplankton time series using multivariate analyses. Oceanologia 62 (3), 243–254, https://doi.org/10.1016/j.oceano.2020.01.004.

Nawrocka, L., Kobos, J., 2011. The trophic state of the Vistula Lagoon: an assessment based on selected biotic and abiotic parameters according to the Water Framework Directive. Oceanologia 53 (3), 881–894, https://doi.org/10.5697/oc.53-3.881.

Newton, A., Icely, J., Cristina, S., Brito, A., Cardoso, A.C., Colijn, F., Riva, S.D., Gertz, F., Hansen, J.W., Holmer, M., Ivanova, K., Leppakoski, E., Canu, D.M., Mocenni, C., Mudge, S., Murray, N., Pejrup, M., Razinkovas, A., Reizopoulou, S., Perez-Ruzafa, A., Schernewski, G., Schubert, H., Carr, L., Solidoro, C., Viaroli, P., Zaldivar, J.M., 2014. An overview of ecological status, vulnerability and future perspectives of European large shallow, semi-enclosed coastal systems, lagoons and transitional waters. Estuar. Coast. Shelf S. 140, 95–122, https://doi.org/10.1016/j.ecss.2013.05.023.

Nowicka-Krawczyk, P.B., Żelazna-Wieczorek, J., 2017. The genus Woronichinia (Cyanobacteria) in natural lakes of Drawa National Park (Poland). Polish Bot. J. 62, 253–263, https://doi.org/10.1515/pbj-2017-0020.

Olenina, I., Hajdu, S., Andersson, A., Edler, L., Wasmund, N., Busch, S., Göbel, J., Gromisz, S., Huseby, S., Huttunen, M., Jaanus, A., Kokkonen, P., Ledaine, I., Niemkiewicz, E., 2006. Biovolumes and size-classes of phytoplankton in the Baltic Sea. HELCOM Balt.Sea Environ. Proc. No. 106, 144 pp., https://epic.awi.de/id/eprint/30141/1/bsep106.pdf.

Olsen, L.A., 1976. Ingested material in two species of estuarine bivalves: *Rangia cuneata* (Gray) and *Polymesoda caroliniana* (Bosc). Proceedings of the National Shellfish Association 11, 103–104.

Piwosz, K., Kownacka, J., Ameryk, A., Zalewski, M., Pernthaler, J., 2016. Phenology of cryptomonads and the CRY1 lineage in a coastal brackish lagoon (Vistula Lagoon, Baltic Sea). J. Phycol. 52, 626–637, https://doi.org/10.1111/jpy.12424.

Pliński, M., 1972. Badania nad glonami południowego Bałtyku oraz Zalewu Szczecińskiego i Wiślanego. Zeszyty Naukowe UG, ser. Oceanografia 1, 59—72 (in Polish).

Pliński, M., Simm, A., 1978. Seasonal fluctuations in the composition, distribution and quantity of phytoplankton in the Vistula Lagoon in 1974 and 1975. Stud. Mater. Oceanol., Biol. Morza 4 (21), 53—80, (in Polish).

Renk, H., Ochocki, S., Zalewski, M., Chmielowski, H., 2001. Environmental factors controlling primary production in the Polish part of the Vistula. Bull. Sea Fisheries Inst. 1 (152), 77—95.

Rudinskaya, L.V., Gusev, A.A., 2012. Invasion of the North American wedge clam *Rangia cuneata* (G.B. Sowerby I, 1831) (Bivalvia: Mactridae) in the Vistula Lagoon of the Baltic. Sea. Russ. J. Biol. Invasions 3, 220—229, https://doi.org/10.1134/S2075111712030071.

Rybicka, D., 2005. Potentially toxic blue-green algae [Cyanoprokaryota] in the Vistula Lagoon. Oceanol. Hydrobiol. St. 34 (Suppl. 3), 161—176.

Rychter, A., Jabłońska-Barna, I., 2018. Macozoobentos of the Vistula Lagoon. In: Bolałek, J. (Ed.), Vistula Lagoon PWN., Warszawa, 271—287 (in Polish).

Sagert, S., Rieling, T., Eggert, A., Schubert, H., 2008. Development of a phytoplankton indicator system for the ecological assessment of brackish coastal waters (German Baltic Sea coast). Hydrobiologia 611, 91—103, https://doi.org/10.1007/s10750-008-9456-3.

Schernewski, G., Neumann, T., Behrendt, H., 2011. Sources, dynamics and management of phosphorus in a southern Baltic estuary. In: Harff, J., Bjorck, S., Hoth, P. (Eds.), The Baltic Sea Basins. Springer, Berlin: Heidelberg, 373—388.

Semenova, A.S., Dmitrieva, O.A., 2013. Impact of invasive species *Rangia cuneata* (Sowerby I, 1832) on the plankton community of the Vistula Lagoon (Baltic Sea). IV International symposium "Invasion of alien species in Holarctic" 22—27 September 2013, Borok, Book of abstracts, p. 154.

Sondergaard, M., Kristensen, P., Jeppesen, E., 1992. Phosphorus release from resuspended sediment in the shallow and wind-exposed Lake Arreso. Denmark. Hydrobiologia 228, 91—99, https://doi.org/10.1007/BF00006480.

Strayer, D.L., Caraco, N.F., Cole, J.J., Findlay, S., Pace, M.L., 1999. Transformation of freshwater ecosystems by bivalves — A case study of zebra mussels in the Hudson River. Bioscience 49, 19—27, https://doi.org/10.1525/bisi.1999.49.1.19.

Strickland, J.D.H., Parsons, T.R., 1968. A practical handbook of seawater analysis. Fish. Res. Board of Canada Bull. 169, Ottawa.

Szarejko-Łukaszewicz, D., 1957. Qualitative investigations of phytoplankton of Firth of Vistula in 1953. Prace Morskiego Instytutu Rybackiego w Gdyni 9, 439—451.

Tenore, K.R., Horton, D.B., Duke, T.W., 1968. Effects bottom substrate on the brackish water bivalve *Rangia cuneata*. Chesapeake Science 9, 238—266, https://doi.org/10.2307/1351314.

Utermöhl, H., 1958. Zur Vervollkommnung der quantitativen Phytoplankton-Methodik. Verhandlungen der Internationalen Vereinigung für Theoretische und Angewandte Limnologie 9, 1—38.

Verdonschot, P.F.M., Spears, B.M., Feld, C.K., Brucet, S., Keizer-Vlek, H., Borja, A., Elliott, M., Kernan, M., Johnson, R.K., 2013. A comparative review of recovery processes in rivers, lakes, estuarine and coastal waters. Hydrobiologia 704, 453—474, https://doi.org/10.1007/s10750-012-1294-7.

Viaroli, P., Bartoli, M., Giordani, G., Naldi, M., Orfanidis, S., Zaldivar, J.M., 2008. Community shifts, alternative stable states, biogeochemical controls and feedbacks in eutrophic coastal lagoons: a brief overview. Aquat. Conserv. 18, 105—117, https://doi.org/10.1002/aqc.956.

Warzocha, J., Szymanek, L., Witalis, B., Wodzinowski, T., 2016. The first report on the establishment and spread of the alien clam *Rangia cuneata* (Mactridae) in the Polish part of the Vistula Lagoon (southern Baltic). Oceanologia 58 (1), 54—58, https://doi.org/10.1016/j.oceano.2015.10.001.

Wasmund, N., Nausch, G., Matthaus, W., 1998. Phytoplankton spring blooms in the southern Baltic Sea - spatio-temporal development and long-term trends. J. Plankton. Res. 20, 1099—1117, https://doi.org/10.1093/plankt/20.6.1099.

Witek, Z., Bralewska, J., Chmielowski, H., Drgas, A., Gostkowska, J., Kokacz, M., Knurowski, J., Krajewska—Sołtys, A., Lorenz, Z., Maciejewska, K., Mackiewicz, T., Nakonieczny, J., Ochocki, S., Warzocha, J., Piechura, J., Renk, H., Stopiński, M., Witek, B., 1993. Structure and function of marine ecosystem in the Gdańsk Basin on the basis of studies performed in 1987. Stud. Mater. Oceanol. 63, 1—124.

Witek, Z., Zalewski, M., Wielgat-Rychert, M., 2010. Nutrient stocks and fluxes in the Vistula Lagoon at the end of the twentieth century. Wyd. Nauk. Akademii Pomorskiej w Słupsku, Słupsk and NMFRI, Gdynia, 186 pp., https://wydawnictwo.apsl.edu.pl/biologia/31-nutrient-stocks-and-fluxes-in-the-vistula-lagoon.html.

Wong, W.H., Rabalais, N.N., Turner, R.E., 2010. Abundance and ecological significance of the clam Rangia cuneata (Sowerby, 1831) in the upper Barataria Estuary (Louisiana, USA). Hydrobiologia 651, 305—315, https://doi.org/10.1007/s10750-010-0310-z.

Wood, S.N., 2014. mgcv: GAMs with GCV/AIC/REML Smoothness Estimation and GAMMs by PQL. R Package Version 1.8-2, http://cran.r-project.org/package=mgcv.

Zilius, M., Giordani, G., Petkuviene, J., Lubiene, I., Ruginis, T., Bartoli, M., 2015. Phosphorus mobility under short-term anoxic conditions in two shallow eutrophic coastal systems (Curonian and Sacca di Goro lagoons). Estuar. Coast. Shelf S. 164, 134—146, https://doi.org/10.1016/j.ecss.2015.07.004.

Oceanologia (2020) 62, 556—556

Available online at www.sciencedirect.com

ScienceDirect

journal homepage: www.journals.elsevier.com/oceanologia

Corrigendum to "The inflow in the Baltic Proper as recorded in January—February 2015" [Oceanologia 58 (2016) 241—247]

Daniel Rak*

Institute of Oceanology, Polish Academy of Sciences, Sopot, Poland

The author regrets that the following information was omitted from the acknowledgements section:
The article is funded by the National Science Centre in Poland under the project no. 2013/11/N/ST10/00804.

DOI of original article: 10.1016/j.oceano.2016.04.001
* Corresponding author at: Institute of Oceanology, Polish Aycademy of Sciences, Powstańców Warszawy 55, 81—712 Sopot.
E-mail address: rak@iopan.gda.pl
Peer review under the responsibility of the Institute of Oceanology of the Polish Academy of Sciences.

https://doi.org/10.1016/j.oceano.2020.09.001